UNIVERSITAT POLITÈCNICA
DE CATALUNYA
BARCELONATECH

ICFO
The Institute of Photonic Sciences

Polarized super-resolution fluorescence microscopy

César Augusto VALADÉS CRUZ

Under the supervision of

Prof. Pablo Loza-Álvarez
Prof. Sophie Brasselet

submitted this thesis in partial fulfillment
of the requirements for the degree of

Doctor

by the
Universitat Politècnica de Catalunya

Barcelona, July, 2014

Abstract

While super-resolution microscopy has brought a significant improvement in nanoscale imaging of molecular assemblies in biological media, its extension to imaging molecular orientation using fluorescence anisotropy has not yet been fully explored. Providing orientational order information at the nanoscale would be of considerable interest for the understanding of biological functions since they are intrinsically related to structural fundamental processes such as in protein clustering in cell membranes, supra-molecular polymerization or aggregation. In this thesis, we propose a super-resolution polarization-resolved microscopy technique able to image molecular orientation behaviors in static and dynamic environments, in order to report structural information at the single molecule level and at nanometric spatial scale. Using direct Stochastic Optical Reconstruction Microscopy (dSTORM) in combination with polarized detection, fluorescence anisotropy images are reconstructed at a spatial resolution of a few tens of nanometers. We analyze numerically the principle of the method in combination with models for orientational order mechanisms, and provide conditions for which this information can be retrieved with high precision in biological samples based on fibrillar structures. Finally, we propose an alternative technique based on stochastic fluctuations of single molecules: polarized super-resolution optical fluctuation imaging (polar-SOFI), and compare this approach with the previous one in terms of information gained and spatial resolution. We illustrate both techniques on molecular order imaging in actin stress fibers and tubulin fibers in fixed cells, DNA fibers and insulin amyloid fibrils.

Keywords : fluorescence, polarization, super-resolution

Résumé

Alors que la microscopie super-résolue a apporté une amélioration considérable en imagerie des assemblages moléculaires dans les milieux biologiques à l'échelle nanométrique, son extension à l'imagerie de l'orientation moléculaire, utilisant l'anisotropie de fluorescence, n'a pas encore été complètement explorée. Apporter une information sur l'orientation moléculaire à l'échelle nanométrique aurait un intérêt considérable pour la compréhension des functions biologiques, puisque celles-ci sont fortement reliée à la structure des assemblages de protéines dans les membranes cellulaires, la polymérisation ou l'aggrégation supramoléculaire par exemple. Dans cette thèse, nous proposons une technique de microscopie super-résolution résolue en polarisation, capable d'imager les comportements d'orientation moléculaire dans des environnements statiques et dynamiques, dans le but de rapporter une information structurale à l'échelle de la molécule unique et à des échelles spatiales nanométriques. En utilisant la microscopie par reconstruction stochastique (dSTORM) en combinaison avec une détection polarisée, des images d'anisotropie de fluorescence sont reconstruites avec une résolution spatiale de quelques dizaines de nanomètres. Nous analysons numériquement le principe de la méthode en combinaison avec des modèles des mécanismes d'orientation moléculaire, et donnons les conditions auxquelles cette information peut être obtenue avec une grande précision dans des échantillons biologiques basés sur des structures fibrillaires. Enfin, nous proposons une technique alternative basée sur l'émission de molécules uniques en fluctuations stochastiques: l'imagerie super-résolue polarisée par fluctuations (polar-SOFI), et comparons cette approche avec la précédente en terme d'information gagnée et de résolution spatiale. Nous illustrons les deux techniques pour l'imagerie de l'ordre moléculaire dans des fibres de stress d'actin et de tubuline dans des cellules fixées, des fibres d'ADN et des fibrilles d'amyloid à base d'insuline.

Mots clefs : fluorescence, polarisation, super-résolution

Resumen

La microscopía de súper resolución ha aportado una mejora significativa en la imagen, a escala nanométrica, de ensambles moleculares en medios biológicos. Sin embargo, su extensión, mediante la utilización de la anisotropía de fluorescencia para la obtención de imágenes de orientación molecular, aún no ha sido explorada a fondo. El proporcionar información sobre la orientación molecular a escala nanométrica es de gran interés para la comprensión de las funciones biológicas. Esta información está intrínsecamente relacionada con la estructura de los ensamblajes de proteínas en las membranas celulares, la polimerización y la agregación supra molecular, entre otros. En esta tesis, proponemos una técnica de microscopía de luz polarizada de súper resolución, la cual permite visualizar el comportamiento de la orientación molecular en ambientes dinámicos y estáticos. El objetivo final es el de poder reportar información estructural a nivel de molécula única y escala espacial nanométrica. Utilizando microscopía de reconstrucción óptica estocástica (dSTORM) en combinación con detección polarizada, las imágenes de anisotropía de fluorescencia son reconstruidas con una resolución espacial de varias decenas de nanómetros. Además, el principio del método ha sido validado numéricamente en combinación con modelos de mecanismos de orientación molecular y delimitando las condiciones en que esta información se puede obtener con una precisión alta en muestras biológicas, principalmente en estructuras fibrilares. Así también, se propone una técnica alternativa basada en la emisión de fluctuaciones estocásticas de moléculas individuales: imagen de polarización con súper resolución de fluctuaciones (polar-SOFI). Además comparamos esta técnica con la anterior, en términos de la información obtenida y la resolución espacial. Finalmente,, ilustramos ambas técnicas para la obtención de imágenes del orden molecular de fibras de estrés de actina y tubulina en células fijas, fibras de ADN y fibrillas de insulina amiloide.

Palabras clave: fluorescencia, polarización, súper-resolución

Contents

Introduction

Single molecule microscopy is now widely exploited for biological imaging, taking advantage of the unique opportunity to retrieve information on isolated molecules without ensemble averaging, possible statistical analysis, and furthermore reveal static and dynamic processes which would be hindered otherwise if detected in ensemble averaging.

One of the most expanded use of single molecule imaging today is the reconstruction based super-resolution imaging with various modalities among which Photo Activation Light Microscopy (PALM) [1] and direct Stochastic Optical Reconstruction Microscopy (dSTORM) [2]. While significant progresses have been made in these methods, with respect to sample preparation and optical conditions optimization, quantification of the resolution gained by the technique, limitations concerning the photo-physics of the involved dye molecules and experimental conditions, another aspect of the techniques has been so far poorly exploited, which consists in using the polarized nature of the emission of fluorescence by those single molecules. It is known that when excited under depolarized or circularly polarized light, all single molecules in a medium act as emission dipoles which direction can be pointed. Methods used to report such direction use a simple analyzer oriented in a known direction, when the 2D projection of the dipole direction in the sample plane is required. More complex schemes have been developed in order to retrieve a 3D information, using for instance defocused imaging [3] or more recently an analysis requiring image acquisition at different depth of focus in the sample [4].

Numerous studies have been undertaken to report single molecule's orientation in media where they are all randomly oriented, either in a fixed environment for fundamental analyzes [4,5], or in environment where they can angularly fluctuate, giving access to local viscosity information such as in traditional fluorescence anisotropy techniques [6].

A recent work has reported the application of such an approach combined with super-resolution imaging, where changes of orientational behaviors could be detected in membrane proteins clusters of actin stress fibers [7]. There is

however no quantitative analysis done yet on processes where molecules undergo an angular constraint. This case represents nevertheless an important class of bio-molecular organization, since a vast range of biological phenomena in cells and tissues occur in assemblies of proteins which are not only spatially but also angularly structured.

Imaging orientation behaviors in ensemble measurements has been introduced in the early 90's with the help of polarization control fluorescence imaging. This process is based on the fact that the incident light polarization is strongly coupled with molecular excitation dipoles orientation when they are parallel to this polarization, while the emission dipoles directions can be detected along a selective analyzer direction. Varying either the analysis direction (anisotropy) or the excitation polarization (linear dichroism) have been implemented to retrieve orientational information in lipid probes in cell membranes [8–10] or in actin fibers labeled directly [11] or via phalloidin-labeled interaction [12, 13], but also in intercalation dyes in DNA double strand fibers [14]. A combination of anisotropy and linear dichroism techniques has also shown to be able to report finer details in the orientational behavior, including dynamics information or 3D orientation information [11].

In this work, we demonstrate the possibility to image orientational behavior of orientationally constraint molecules at a sub-diffraction scale, combining an anisotropy measurement scheme with the stochastic reconstruction technique dSTORM. We show, based on numerical modeling and simulations, that the determination of both molecule's orientation and localization can be performed with high precision, only under strict conditions with respect to signal and background levels. This numerical study shows that the choice of reporting a 2D information only using simple anisotropy monitoring is primarily governed by the restriction on the parameters' estimation precision. The major difficulty of the techniques combining both linear dichroism and anisotropy, when transposed to single molecule detection, is indeed the loss of signal resulting from the filtering by both excitation or detection polarizations. We illustrate the polarization super-resolution imaging capabilities on highly structured samples such as tubulin networks and single actin stress fiber bundles in fixed cells, as well as deposited double strand DNA fibers and amyloid fibers in vitro. An alternative to dSTORM imaging has been recently introduced, based on the measurement of fluorescence time fluctuations. This method called SOFI (Super-resolution Optical Fluctuation Imaging) [15] has been explored in this work for an adaptation to polarized detection.

The core of this thesis is the development, characterization and validation of a novel method of super resolution microscopy, in combination with a polarized detection. In particular, we developed a validation, which allow us to use the information from the super-resolution microscopy method in a quanti-

tative way. This method is able to image molecular orientation behaviors in static and dynamic environments, in order to report structural information at the single molecule level and at nanometric spatial scale. Finally, we explored the possibility to extend the same concept on another super resolution technique (polar-SOFI) based on the use of cross-cumulant estimation.

This thesis is organized as follows:

In Chapter 1, basic information of structure and biological function of filamentous structures of the cytoskeleton and other filament structures as DNA and amyloid fibrils is given. In Chapter 2, we described the principle of fluorescence. In addition, it presents the principle of super-resolution techniques, focusing on direct Stochastic Optical Reconstruction Microscopy (dSTORM). It introduces the fluorescence anisotropy technique and shows its applications in solution and in ordered structures such as actin fibers, DNA fibers and amyloid fibrils. Then, it presents an overview of the state of the art of quantification of molecular orientational order in fibers with classical fluorescence anisotropy. In Chapter 3, we describe the experimental implementation of a polar-dSTORM set up. In addition, the polar-dSTORM method is introduced. In Chapter 4, we evaluate the capacities of the polar-dSTORM technique to estimate the orientational behavior of single molecules and report super-resolution anisotropy images. In addition simulations are done, in order to define the limitations and efficiency range of the algorithm. Chapter 5 summarizes the experiments and results of polar-dSTORM application in filamentous biological samples. Chapter 6 describes the experimental implementation and validation of the polar-SOFI method.

Chapter 1

Biological filaments

Since we study filamentous structures of the cytoskeleton at nanoscale, some basic information on the cytoskeleton is given in this section. Structure and function of microtubules and microfilaments are introduced.

Other biological filament structures with size below the diffraction limit are described. General characteristics of DNA and amyloid fibrils are given.

1.1 Cytoskeleton

Looking through a microscope, we can observe a wide diversity of cells in nature, including a variety of cell shapes and movements. In this variety, we can observe some cells, such as vertebrate spermatozoid, or flagellates such as Chlamydomonas, which are able to swim rapidly, propelled by cilia and flagella. Other cells, such as amoeba and human macrophages, move more slowly, without an external propulsion system (appendage) but by synchronized movement of the cell itself. In addition, focusing in the internal organization of cells, we observe that organelles have special locations; for example the Golgi apparatus is usually near the central nucleus. To have more clear idea about the importance of a specific shape and the internal organization in cell, we can consider two different examples of cell types with very different functions and organization.

First, the epithelial cell that contours the intestine, which function is to import nutrients (such as glucose) from the intestinal lumen through the apical (top) plasma membrane and transfer them through the basolateral (bottom-side) plasma membrane, to the bloodstream (Fig. 1.1). To achieve this directional transport, the apical and basolateral parts of the plasma membranes of epithelial cells need to have different protein compositions. In addition, the apical membrane has a particular morphology, with fingerlike projections (microvilli). So,

to accomplish this organization, epithelial cells need to have internal structure to provide them shape and to deliver appropriate proteins to the correct membrane surface.

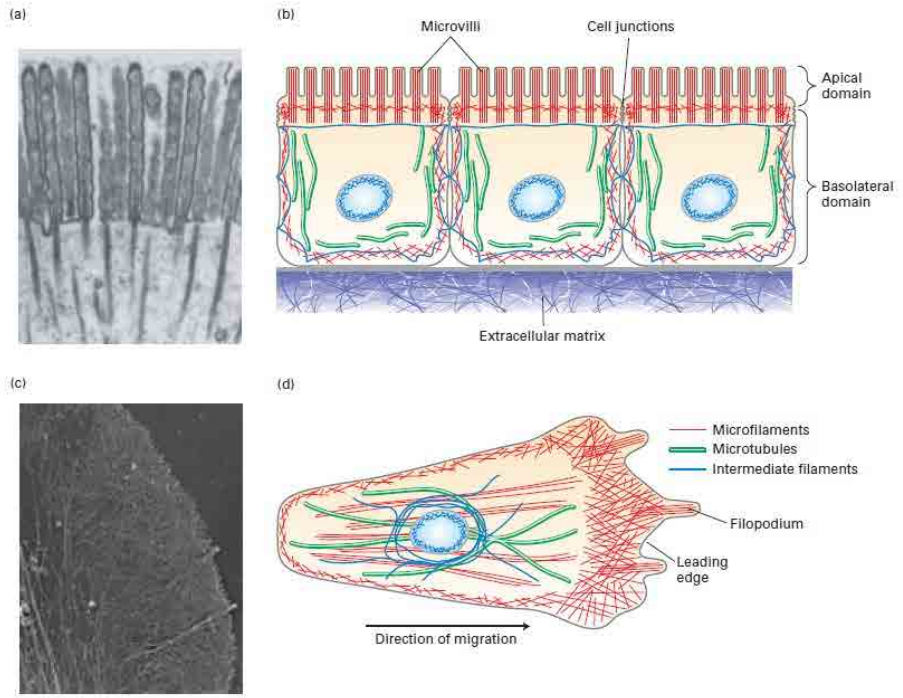

Figure 1.1: Overview of the cytoskeleton of an epithelial cell and a migrating cell. (a) Transmission electron micrograph of a thin section of an epithelial cell from the small intestine, showing the cytoskeletal components of the microvilli. (b) Epithelial cells are highly polarized, with distinct apical and basolateral domains. (c) Transmission electron micrograph of part of the leading edge of a migrating cell. (d) A migrating cell, such as a fibroblast or a macrophage, has morphologically distinct domains, with a leading edge at the front. Microfilaments are shown in red, microtubules in green and intermediate filaments in dark blue. The position of the nucleus (light blue oval) is also displayed. [Obtained from Lodish et al. (2012) [16]]

The second example is macrophages, a type of white blood cell or leukocyte, which has the function to look for infectious agents and destroy them by a process called phagocytosis. Bacteria liberate chemicals, which attract the macrophage and guide it to the infection. Since the macrophage follows this chemical gradi-

ent, constantly reorganization of its cell locomotion machinery is necessary. Its internal motile machinery is always oriented in the direction of the crawl (Fig. 1.1).

These are just two examples of "cell polarity", which can be defined as the ability of cells to generate functionally distinct regions [16]. The cytoskeleton is a three-dimensional filamentous protein network, which gives shape, internal organization and functional polarity to cell. The cytoskeleton ranges through the cell and is attached to the plasma membrane and internal organelles, therefore providing a structure for cellular organization. In addition, the cytoskeleton can be very dynamic, with mechanisms capable of reorganization in less than a minute or it can be pretty stable for hours at a time.

The cytoskeleton is divided in three major filament systems, shown in Fig. 1.2. Then, each filament system is integrated into a polymer of assembled subunits. These subunits give to the cell flexibility to assemble or dissemble different types of structures. The three systems are [16]:

- Microfilaments. They are polymers of the actin protein. They are organized into functional bundles and networks by actin-binding proteins. They are especially important in the organization of the plasma membrane, giving shape to surface structures. In addition, they can function on their own or work as tracks for ATP-powered myosin motor proteins, which offer a contractile function or ferry cargo along microfilaments.

- Microtubules are tubes formed by the tubulin protein and organized by microtubule-associated proteins. They spread through the cell, giving an organizational framework for associated organelles. The cargo function is indeed more due to microtubules than microfilaments, with the kinesin and dynein molecular motors. In addition, they give structural support to cilia and flagella. As well, they are also involved in the machine for separating duplicated chromosomes at mitosis.

- Intermediate filaments are tissue-specific filamentous structures, which have different functions, including lending structural support to the nuclear membrane, giving structural integrity to cells in tissues, and providing structural and barrier functions. One important difference comparing with the previous systems is there are no motors, which utilize this type of filament as tracks.

The importance of the cytoskeleton for normal cell function and motility can be observed when a defect in a cytoskeletal component or in regulation results on a disease. Metastatic cancer cells exhibit unregulated motility due to bad regulation of the cytoskeleton, breaking away from their original tissue and migrating to new places to form new colonies of uncontrolled growth [16].

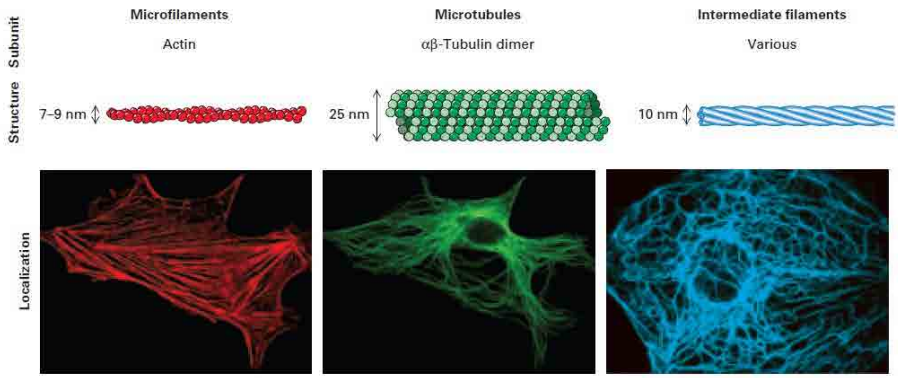

Figure 1.2: Cytoskeleton components. Top panels show structure subunits of the three type of filaments. Bottom panels show localization of the three filament systems in cultured cells as seen by immunofluorescence microscopy of actin, tubulin, and an intermediate filament protein, respectively. [Obtained from Lodish et al. (2012) [16]]

Since we are focusing in this thesis on microfilaments and microtubules, a brief description of them is given in the next subsections.

1.1.1 Microfilaments (actin filaments)

Microfilaments can be assembled into different types of structures within a cell (Fig. 1.3). These structures have particular cell functions. Microfilaments can provide support and organization (cell cortex) or strength to the epithelium ("adherens belt"). In addition, many cells have contractile microfilaments ("stress fibers"), which attach to the external substratum over specific regions called focal adhesions or focal contacts.

At late stage of animal cell division, once the organelles have been duplicated and segregated, a contractile ring shapes and restricts to generate two daughter cells (cytokinesis). Therefore actin filaments can be used in cells in different ways: in a structural role or as tracks for myosin motors. It is possible to see different arrangements of microfilaments within a single cell, as shown in Fig. 1.3c.

Actin monomer (G-actin) is the basic building unit of microfilaments. In addition, actin has the notable property of reversibly assembling into a polarized filament with ends, which have different functions. Microfilament refers to polymerized or filamentous actin (F-actin).

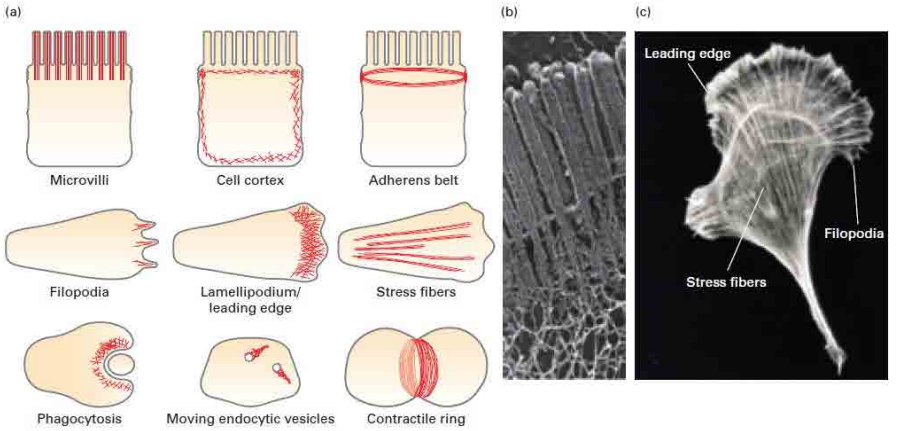

Figure 1.3: Examples of microfilament-based structures. (a) Microfilament structures. (b) Scanning electron micrograph of the apical region of a polarized epithelial cell, showing the bundles of actin filaments that make up the cores of the microvilli. (c) A cell moving toward the top of the page, stained for actin with fluorescently labelled phalloidin (a drug that specifically binds to F-actin). [Obtained from Lodish et al. (2012) [16]]

Actin

In eukaryotic cells, actin is the most abundant protein.

Actin isoforms can be classified into three classes: the α-actin, β-actin, and γ-actin. Each of them has different functions: α is related to contractile structures, γ accounts for filaments in stress fibers, and β-actin is developed in the cell cortex and leading edge of motile cells.

Actin can exist as a globular monomer (G-actin) and as a filamentous polymer (F-actin) that is a linear chain of G-actin subunits. The polymerization of G-actin into F-actin is reversible: F-actin depolymerizes into G-actin when the ionic strength of the solution is decreased. The F-actin filaments are the major component of microfilaments.

Based on x-ray diffraction studies of actin filaments and the actin monomer structure (Fig. 1.4), it has been determined that the subunits in actin filaments are arranged in a helical structure [16]. The subunits in a single strand bend around the back of the other strand and repeat after 14 actin subunits (72 nm). Considering there are two strands, the actin filament seems to repeat every 36 nm (Fig. 1.4b). For electron microscopy, when F-actin is negatively stained with uranyl acetate, it seems as a twisted string with diameter between 7 and 9

nm [17].

Subunits in an actin filament are oriented in the same way. Therefore, a filament displays polarity; that is, one end is different than the other. One end of the filament is preferred for the addition of actin subunits and is called the (+) end, while the other end is preferred for subunit dissociation, called the (-) end. (Fig. 1.4)

Another important property of actin filaments is that the motor protein myosin binds specifically to them.

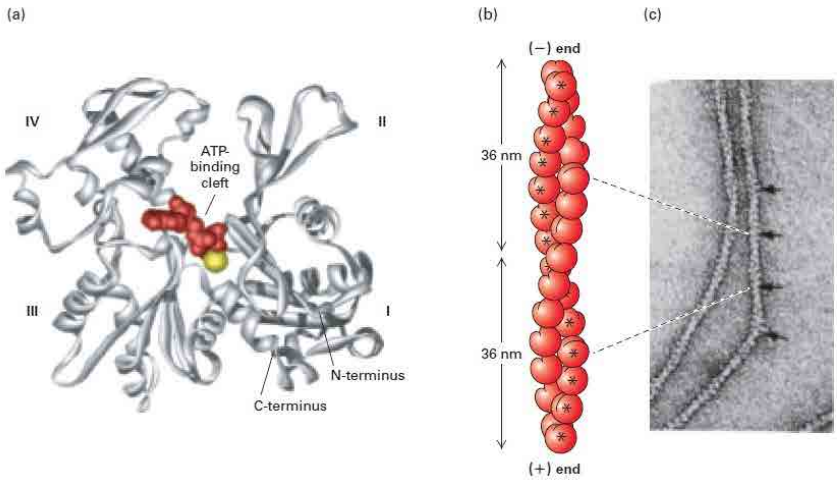

Figure 1.4: Structures of monomeric G-actin and F-actin filaments. (a) Model of actin monomer. (b) An actin filament appears as two strands of subunits. One repeating unit consists of 28 subunits, covering a distance of 72 nm. (c) In the electron microscope, negatively stained actin filaments appear as long, flexible, and twisted strands of beaded subunits. Because of the twist, the filament appears alternately thinner (7-nm diameter) and thicker (9-nm diameter) (arrows). [Obtained from Lodish et al. (2012) [16]]

Phalloidin is a toxin, which binds F-actin. The effects of phalloidin on actin are to prevent filament depolymerization and shift the equilibrium from monomer to filament. Fluorescent derivatives of phalloidin have been used for localizing actin filaments in fixed cells [18, 19] and visualizing individual actin filaments in vitro [20]. However, phalloidin do not permeate cell membranes and consequently they are not useful in experiments with living cells [21]. Fig. 1.5 shows the theoretical prediction on how rhodamine phalloidin binds to F-Actin.

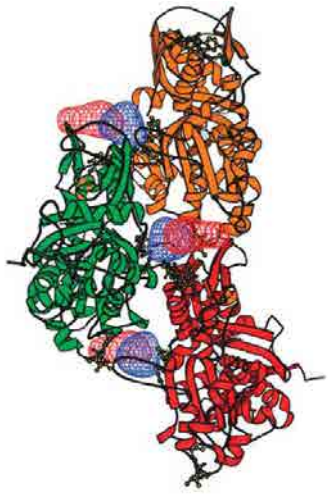

Figure 1.5: Electron densities corresponding to phalloidin (blue) and rhodamine (red) determined in the rhodamine phalloidin F-actin complex (Image taken from [22]).

1.1.2 Microtubules

Microtubules are rigid tubes that can be found as a single structure with length up to 20 μm in cells, or also in bundled arrangements, such as those observed in specialized cell structures like cilia and flagella.

One important characteristic of microtubules is the ability to generate pulling and pushing forces without buckling. They can also extend large distance within a cell and bundles. This last property with their polarity can be exploited by microtubules-dependence motors that use the microtubules as tracks for long-range transport of organelles.

Additionally, microtubules can be highly dynamic, giving flexibility to the cell, based on the ability to change the microtubule organization if it is needed.

Initially analyzed by electron microscopy, cell biologist observed long tubules in the cytoplasm that they called microtubules [16]. Similar microtubules were observed in the mitotic spindle, as components of axons and in cilia and flagella (Fig. 1.6a,b). Later examination of single microtubules shows that they are made up of 13 longitudinal repeating units, protofilaments (Fig. 1.6c). Microtubules consist of a protein called tubulin and microtubule-associated proteins (MAPs) [16].

Tubulin is a dimer consisting of two closely related subunits called α- and

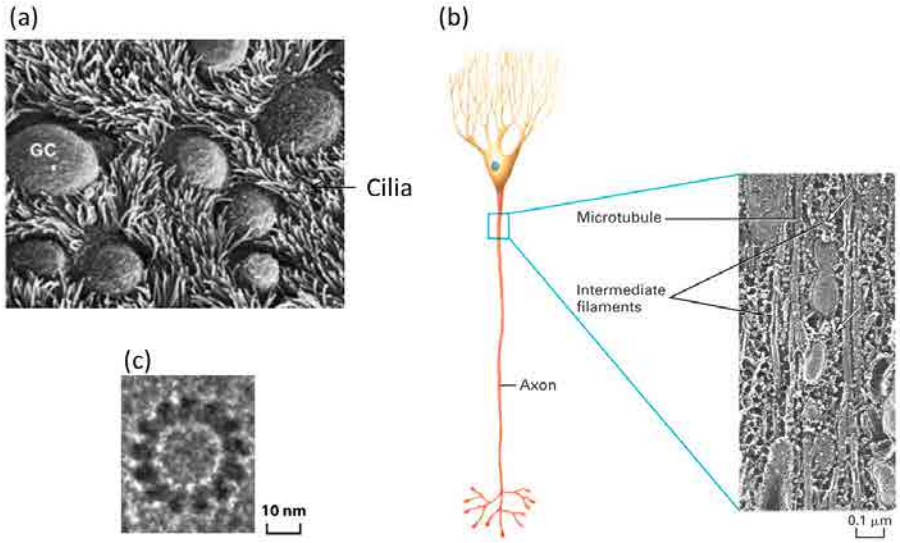

Figure 1.6: Microtubules structures, (a) Surface of the ciliated epithelium lining a rabbit oviduct viewed in a scanning electron microscope. (b) Microtubules and intermediate filaments in a quick-frozen and deep-etched frog axon visualized in a transmission electron microscope, (c) High-magnification view of a single microtubule showing 13 repeating units known as protofilaments [obtained from Lodish et al. (2012) [16]].

β-tubulin, each with a molecular weight of about 55 kDa. In addition, a third type of tubulin (γ-tubulin) is specifically localized to the centrosome, where it plays a critical role in initiating microtubule assembly [23]. The α and β-tubulin can each attach to one molecule of GTP (Fig. 1.7b).

As mentioned previously, microtubules are composed of 13 protofilaments, which assemble in a tubule form with external diameter of 25 nm (Fig. 1.7b). Each protofilaments is a string of α or β-tubulin, arranged so that the subunits alternate, with each subunit type repeating every 8 nm (Fig. 1.7b). The distance of 8 nm is similar as the kinesin (motor protein) step size. Each protofilament has intrinsic polarity, that means it has α-subunit in one end and β in the other.

Immunofluorescence microscopy is used to localize microtubules in cells, using specific antibodies to tubulin (Fig. 1.8a).

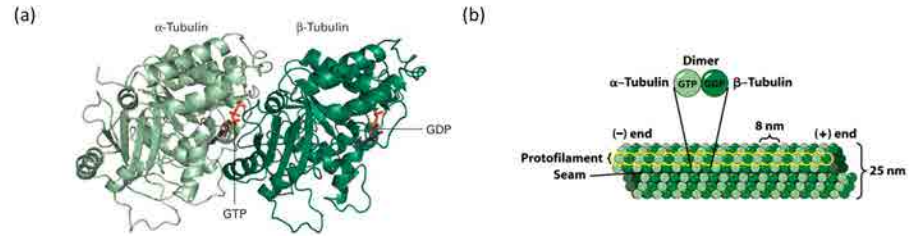

Figure 1.7: Structure of tubulin dimers and their organization into microtubules . (a) Ribbon diagram of the tubulin dimer. (b) The organization of tubulin subunits in a microtubule. The dimmers are aligned end to end into protofilaments. The microtubule displays a structural polarity in that subunits are added preferentially at the end where β-tubulin monomers are exposed. [Obtained from Lodish et al. (2012) [16]].

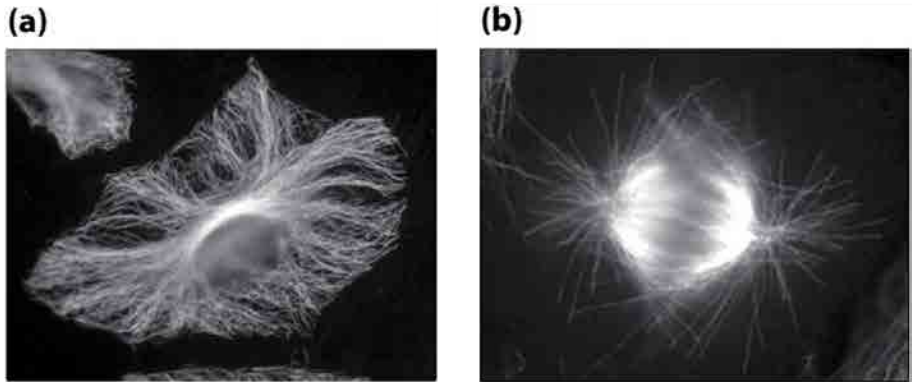

Figure 1.8: The distribution of microtubules in cultured cells as seen by immunofluorescence microscopy using antibodies to tubulin in an interphase cell (a) and a cell in mitosis (b) [Obtained from Lodish et al. (2012) [16]].

1.2 Other biological filaments

Apart of the analysis in the two of the cytoskeleton filament structures: microfilaments and microtubules, this thesis analyzes the molecular orientation of other two important biological filaments: DNA and amyloid fibrils. Briefly, their structure and functions are introduced in what follows.

1.2.1 DNA

During the cell division, the hereditary information is passed on from a cell to its daughter cells and from generation to next generation in multicellular organisms by the reproductive cells. These instructions are contained within every living cell in its genes, which are the information-containing elements that define the characteristics of species as a whole and of the individuals within it [24].

In the 1940s, based on studies in simple fungi, it was discovered that genetic information is composed primarily of instruction for making proteins [24]. Proteins are macromolecules, which achieve most of the cell's functions, like serving as building blocks for cell structures, forming enzymes that catalyze the cell's chemical reactions, regulating gene expression and they enable cells to move and communicate with other cells.

The deoxyribonucleic acid (DNA) is the carrier of the genetic information in the cell. The structure published by James Watson and Francis Crick [25] revealed how DNA can be copied or replicated and it gave the first evidences about how a molecule of DNA can encode instructions for making proteins.

Structure and function of DNA

In the nineteenth century, Chromosomes were discovered. They were observed as strain like structures in the nucleus of the eukaryotic cell, when the cell division begins (Fig. 1.9). Chromosomes contain both DNA and proteins.

Early in the 1950s, DNA was analyzed by X-ray diffraction analysis, determining the three-dimensional atomic structure of a molecule [26]. These results showed that DNA is composed of two strands wound into a helix.

A molecule of DNA consists of two long polynucleotide chains (strands). Each of these strands is composed of four types of nucleotide subunits, and the two strands are held together by hydrogen bonds between the base portions of the nucleotides (Fig. 1.10).

Nucleotides consist of a five-carbon sugar to which are bound one or more phosphate groups and a nitrogen-containing base. For the nucleotides in DNA, the sugar is deoxyribose attached to a single phosphate group and the base can be adenine (A), cytosine (C), guanine (G) or thymine (T). The nucleotides are covalently attached together in a strand through the sugars and phosphates, which therefore form a "backbone" of alternating sugar-phosphate-sugar-phosphate (Fig. 1.10B).

Due to the way in which the nucleotide subunits are linked, DNA strands have a chemical polarity. Representing the nucleotide has a knob (phosphate) and a hole (see Fig. 1.10A), each strand will have all of its subunits lined up in the same orientation. Furthermore, the two ends of the chain can be simply

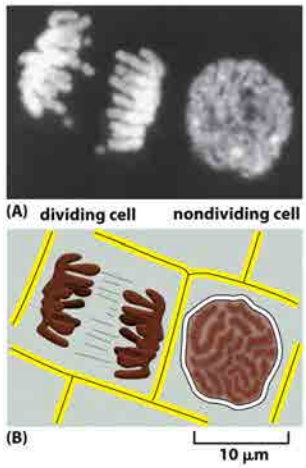

Figure 1.9: Chromosomes become visible as cells prepare to divide. (a) Two adjacent plant cells photographed through a light microscope. DNA is fluorescing brightly with a dye (DAPI) that binds to it. The DNA is observed in chromosomes, which become visible as distinct structures in the light microscope only when they condense in preparation for cell division, as shown on the left. The cell on the right, which is not dividing, contains the identical chromosomes; they cannot be distinguished as individual chromosomes in the light microscope at this phase in the cell's life cycle because the DNA is in a much more extended conformation. (B) Schematic diagram of the outlines of the two cells along with their chromosomes [obtained from Alberts (2009) [24]].

identified, as one will have a hole (the 3' hydroxyl) and the other a knob (the 5' phosphate).

The two polynucleotide strands in the DNA double helix are held together by hydrogen-bonding between the bases. In consequence, all the bases are on the inside of the helix, with the sugar-phosphate backbones on the outside (Fig. 1.10D). Importantly, only few combinations of bases are allowed: A-T and G-C (Fig. 1.11). In each case, a bulkier two-ring base (a purine) is combined with a single-ring base (a pyrimidine). Each purine-pyrimidine pair is called a base pair, and this complementary base-pairing allows them to be packed in the energetically most favorable arrangement in the interior of the double helix.

The antiparallel sugar-phosphate strands twist around each other to create a double helix having 10 base pairs per helical turn (see Fig. 1.12). The diameter of the double-stranded DNA is roughly 2 nm.

DNA encodes information in the order, or sequence, of the nucleotides along

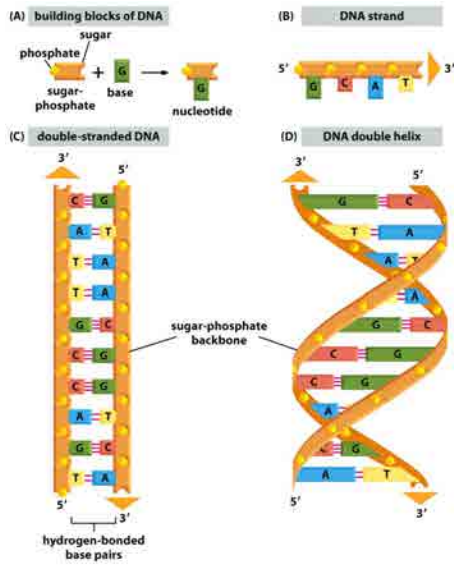

Figure 1.10: DNA is made of four nucleotide building blocks. (A) Each nucleotide is composed of a sugar-phosphate covalently linked to a base. (B) The nucleotides are covalently linked together into polynucleotide chains, with a sugar-phosphate backbone from which the bases (A, C, G, and T) extend. (C) A DNA molecule is composed of two polynucleotide chains (DNA strands) held together by hydrogen bonds between the paired bases. The arrows on the DNA strands indicate the polarities of the two strands, which run antiparallel to each other in the DNA molecule. (D) Although the DNA is shown straightened out in (C), in reality, it is wound into a double helix, as shown here [obtained from Alberts (2009) [24]].

each strand considered as a letter in a four-letter alphabet (A, C, T and G). Genes carry the code that represents the primary structure of proteins. The building blocks of proteins are amino acids. Amino acids are encoded by three consecutive nucleotides from the four-letter DNA alphabet. The sequence of nucleotides regulates the sequence of amino acids in a protein, called the primary protein structure. The differentiated chemistry of the amino acids determines how the linear amino-acid polymer folds into a defined 3D structure.

In general, two different binding modes between external dyes and DNA can be found: (a) minor or major groove-binding or (b) intercalation. YOYO-1, an intercalating dye, is widely used to label DNA.

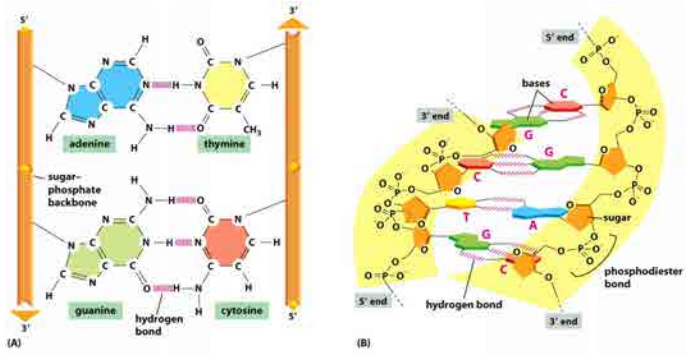

Figure 1.11: The two strands of the DNA double helix are held together by hydrogen bonds between complementary base pairs. (A) The shapes and chemical structure of the bases allow hydrogen bonds to form efficiently only between A and T and between G and C. (B) A short section of the double helix viewed from its side. Four base pairs are shown. The nucleotides are linked together covalently by phosphodiester bonds through the 3'-hydroxyl (-oh) group of one sugar and the 5'-phosphate (-PO_4) of the next [obtained from Alberts (2009) [24]].

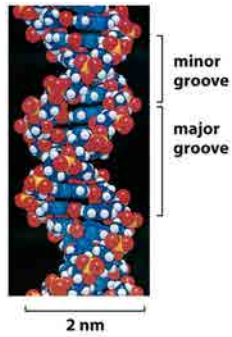

Figure 1.12: A space-filling model shows the conformation of the DNA double helix. The two strands of DNA wind around each other to form a right-handed helix with 10 bases per turn. Shown here are 1.5 turns of the DNA double helix. The coiling of the two strands around each other creates two grooves in the double helix. The wider groove is called the major groove and the smaller one the minor groove. The colors of the atoms are: N, blue; O, red; P, yellow; and H, white [obtained from Alberts (2009) [24]].

1.2.2 Amyloid fibrils

Amyloid fibrils are formed by generally soluble proteins that assemble to form insoluble fibers. These fibers are resistant to degradation. Their formation is related to disease and each disease is characterized by a specific protein or peptide that aggregates. Examples of amyloid diseases are Alzheimer's disease, Diabetes type 2 and the spongiform encephalopathies (Mad cow disease) [27].

The amyloid fibrils are deposited extracellularly in the tissues and they are believed to have a pathogenic effect [28]. The fibrillar assemblies are intrinsically stable and structural studies have shown that they are mainly composed of β-sheet structure in a characteristic cross-β conformation [27].

In the mid-19^{th} Schleiden and then Virchow has been used the term "amyloid" to described the iodine stained deposits seen in liver at autopsy. Congo Red dyes can specifically bind to amyloid. Additionally, this dye produces an apple green birefringence when amyloid is observed between cross polarizers in a light microscopy [29] (see Fig. 1.13). This discovery suggested that amyloid was a fibrillar structure. Later, it was possible to isolate amyloid fibrils from tissues and their characteristic cross-β structure was obtained from X-ray fiber diffraction patterns [30].

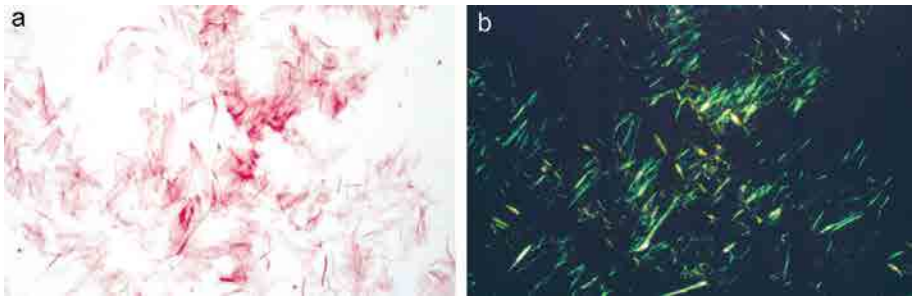

Figure 1.13: Isolated amyloid fibrils composed of A_α chain fragment of fibrinogen (a) stained with Congo red and visualized by light microscopy and (b) between crossed polarizers, showing characteristic apple-green birefringence [obtained from [27]].

Later studies probed that each amyloid disorder is associated with a particular protein or peptide. For example, Aβ, the peptide related to amyloid disorder in Alzheimer's disease [31].

In early nineties, Aβ(1-42) started to be used to produce amyloid-like fibrils, based on phase protein synthesis techniques. After that, different techniques including nuclear magnetic resonance(NMR), circular dichroism (CD), X-ray fiber diffraction, atomic force and electron microscopy(AFM and EM), Fourier trans-

form infrared spectroscopy(FTIR) have contributed to understanding at molecular level the structure of amyloid fibrils [27].

Electron and atomic force microscopy have shown that amyloid fibrils are long, straight and unbranching (Fig. 1.14 A) and are made up of individual subunits named "protofilaments" [32]. Cross-β structure of amyloid fibrils have been shown by the X-ray diffraction pattern. This X-ray diffraction pattern shows that these fibrous molecules share a particular core structure of β-sheet conformation in which the hydrogen bonding direction is parallel to the fiber axis and the β-strands are perpendicular (Fig. 1.14).

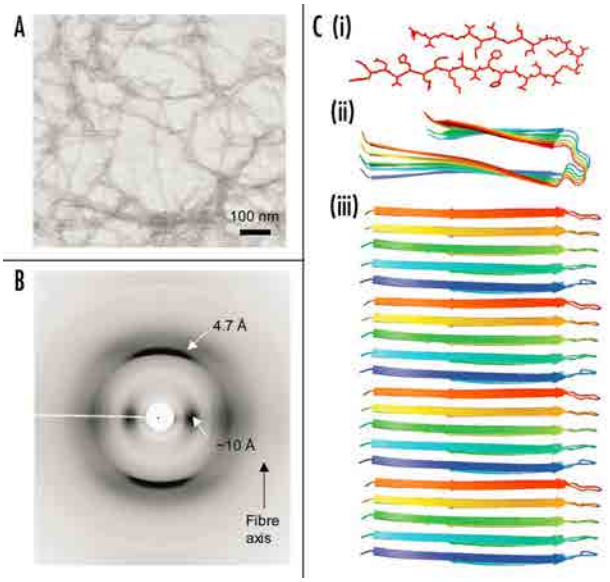

Figure 1.14: Synthetic amyloid fibrils made from Aβ peptide (A) electron micrograph showing long, straight, unbranching fibrils. (B) X-ray fiber diffraction pattern from partially aligned amyloid fibrils showing the characteristic "cross-β" diffraction pattern. (C) The structure of the Aβ amyloid fibril interpreted from ssNMR data, showing the top view of the fiber (i and ii) with side chains (i). The side view (iii) revealing the β-strands running perpendicular to the fiber axis [obtained from [27]].

Based on atomic force microscopy analysis, it was possible to observe two or three fibrillar species that vary in diameter of amyloid. The smallest, protofilaments, have a uniform height, while the larger species, protofibrils and fibrils, have morphologies that are indicative of multiple protofilaments intertwining. One hierarchical assembly model was proposed based on the mechanism of as-

sembly for all amyloid fibrils (Fig. 1.15) [33].

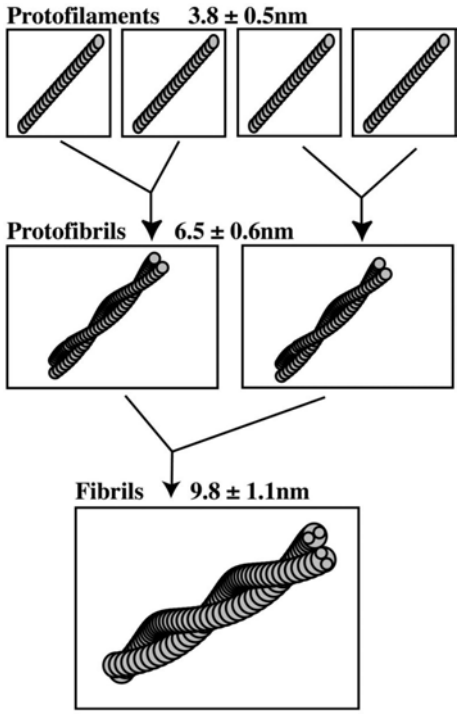

Figure 1.15: A model for the hierarchical assembly of α-synuclein into amyloid fibrils. Protofilament pairs wind together to form protofibrils, and each two protofibrils wind to form a fibril [obtained from [33]].

Another dye, benzothiazole dye, thioflavin T (ThT), is commonly used for the identification and quantification of amyloid fibrils in vitro, and it is the premier technique used to monitor fibrillation kinetics in real-time. When ThT is added to samples containing β-sheet-rich deposits, such as the cross-β-sheet structure of amyloid fibrils, it fluoresces strongly with excitation and emission maxima at approximately 440 and 490 nm, respectively. However, free ThT in an aqueous environment has only weak fluorescence, with lower (blue-shifted) excitation and emission maxima at 350 and 440 nm, respectively [34].

Even though the mechanism of interaction between ThT and amyloid fibrils remains unwell understood, the most accepted theory involves the intercalation of ThT molecules within grooves between solvent-exposed side chains of the amyloid fibril that run parallel to the fibril axis [35].

1.3 Conclusion

In this chapter we have presented the basic knowledge on cytoskeleton filaments, particularly: microfilaments and microtubules. Their structure and main functions were mentioned, as well as their importance in different cell's functions. Another biological filaments as DNA and amyloid fibrils were also introduced. Although these different filamentous structures have particular characteristics, all of them have diameters below the diffraction limit of few nanometers. For this reason, later analysis will be performed based on super-resolution microscopy techniques.

Chapter 2

Polarization-resolved fluorescence - a tool to study orientational order at the nanoscale level.

This chapter describes the principle of fluorescence. It presents the principle of super-resolution techniques, focusing on direct Stochastic Optical Reconstruction Microscopy (dSTORM). It introduces the fluorescence anisotropy technique and shows its applications in solution and in ordered structures such as actin fibers, DNA fibers and amyloid fibrils. Finally, it presents an overview of the state of the art of quantification of molecular orientational order in fibers with classical fluorescence anisotropy.

2.1 Principle of fluorescence

Fluorescence is the absorption and the following emission of a photon by a molecule. The fluorescent molecule, called fluorophore, is exposed to the electric field E of an electromagnetic wave, then an electron can be moved from an orbital in the ground state (S_0) to an orbital of higher energy level S_1. This process is called absorption (Fig. 2.1a). If the excitation energy is higher than the resonant energy between S_1 and S_0 states, the electron can be further transferred to higher energy levels, for example S_2, and therefore undergo internal conversion and vibrational relaxation.

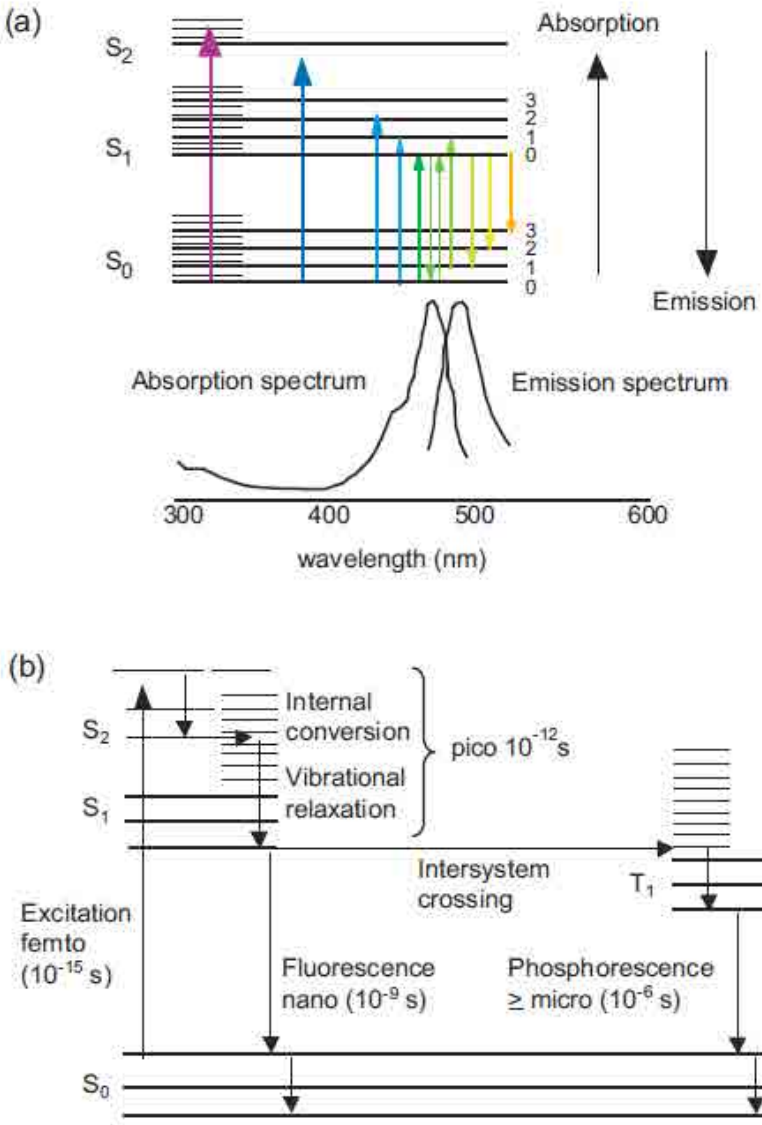

Figure 2.1: Principle of fluorescence. (a) The resulting absorption and emission spectra due to transitions between different electronic (S_0, S_1 and S_2) and vibrational states. (b) Involved energy states of a fluorescence process with their average lifetimes: S0, S1 and S2 are the electronic states and T_1 is the triplet state. Adapted from [36].

Internal conversion involves the transition of the electron from the lower vibrational level of S_2 to excited vibrational level of S_1. This excited vibration promotes a movement of the atoms and part of the fluorophore's energy is transferred to nearby molecules. During the vibrational relaxation, the electron goes down to the state S_1 and the following photon emission transfers the molecule to its ground electronic state S_0. The lifetimes of internal conversion and vibrational relaxation are in the range of picoseconds and the emission process is in the range of nanoseconds (see Fig. 2.1b).

The spectral shift of the emission spectrum to higher wavelengths, due to the vibrational relaxation is called Stokes shift. The absorption and emission spectra represent the energy levels within a molecule. These spectra can overlap, due to the fact that a fraction of the fluorophore population is in the excited vibrational state S_0 and the emitted photon can have enough energy to be transferred into the excited electronic state S_1.

The Stoke's shift is important in fluorescent techniques, because the excitation and emission light can be separated. This characteristic permits to visualize and measure molecules without the background from the incident light in the fluorescence techniques. One large Stoke's shift allows a better wavelength separation in the experiment.

The absorption and emission spectra frequently have similar shape because the difference between the vibrational levels are similar in S_1 and S_0.

In addition to the described radiative process, another radiative process called phosphorescence occurs due to intersystem crossing. Intersystem crossing is not a radiative transition and implies a forbidden electron spin transition. It has much lower efficiency than the other radiative process, but still it can be observed. The Pauli exclusion principle states that two electrons can have only opposite spins. During the excitation into S_1 states, the two electrons in S_0 and S_1 possess opposite spins. The overlap between vibrational energy levels of the triplet state T_1 and the lowest energy level of S_1 permits the intersystem crossing and the spin conversion. For the reason that the two electrons have parallel spins, the relaxation back to the S_0 state has very low efficiency [37].

Figure 2.1 presents the involved energy states of the fluorescence process. Each electronic state (ground S_0 and excited S_1 single state and the triplet state T_1) has ground and excited vibrational levels. The average lifetimes of the involved states are in the range of femtoseconds and microseconds.

2.1.1 Life time

The fluorescence lifetime τ_f is the average time that the fluorophore remains in the excited state. Generally, the lifetime is given as average value because the photon emission is a random process within a timescale of nanoseconds. Fluorescence is

an incoherent radiation process because of this random photon emission. Then each emitted photon has an emission time and phase, which are decorrelated from the earlier and subsequent ones. The fluorescence lifetime can be decreased by the non-radiative processes of the fluorophore, like phosphorescence. The fluorescence lifetime (τ_f) is defined as [37]:

$$\tau_f = \frac{1}{k_r + k_{nr}} \tag{2.1}$$

where k_r is the radiative and k_{nr} is the non-radiative decay rate. The fluorescence lifetime is an important parameter to know for measuring the rotational properties of molecules (see below).

2.1.2 Quantum yield

The quantum yield Q_f determines the brightness of the fluorophore. It is defined as the ratio between emitted and absorbed photons, consequently it represents the competition between the radiative k_r and non-radiative k_{nr} processes.

$$Q_f = \frac{k_r}{k_r + k_{nr}} \tag{2.2}$$

The quantum yield Q_f of a fluorophore depends on its environment. An increase in temperature results in a decrease in Q_f and τ_f due to the increase of non-radiative processes at higher temperatures [38].

2.2 Polarized light

Based on the classical view of light, light can be defined as electromagnetic wave consisting of an electric field E and a magnetic field B perpendicular both to each other and to the direction of propagation and they are oscillating in phase. Generally, these fields have no favored orientation in the so-called natural light, but for linearly polarized light, the oscillation of the electric field is along a given direction (polarization direction).

We can define a general case where the electric field of the propagating wave is elliptically polarized. Then two extreme cases of this elliptical polarization are linear and circular polarization.

Generally, the absorption probability of chromophores is a function of the orientation of the absorption dipole μ_{abs} ("excitation transition dipole moment") with respect to the electric field [38], determined by its electronic states. In contrast, the emission transition dipole moment μ_{em} does not depend of the excited

state reached by the molecule at the time of excitation due to the internal conversion. It rather depends on the molecule conformation in the lowest vibrational state of S_1.

Assuming linear polarization, the probability of excitation of a chromophore is proportional to $cos^2\theta_A$, θ_A being the angle between the electric vector E of the incident light and the absorption transition moment μ_{abs}. Therefore, the maximum probability is when E is parallel to μ_{abs}, and it is zero when it is perpendicular to μ_{abs}. This selectivity due to the incident polarization light is called photoselection (Fig. 2.2).

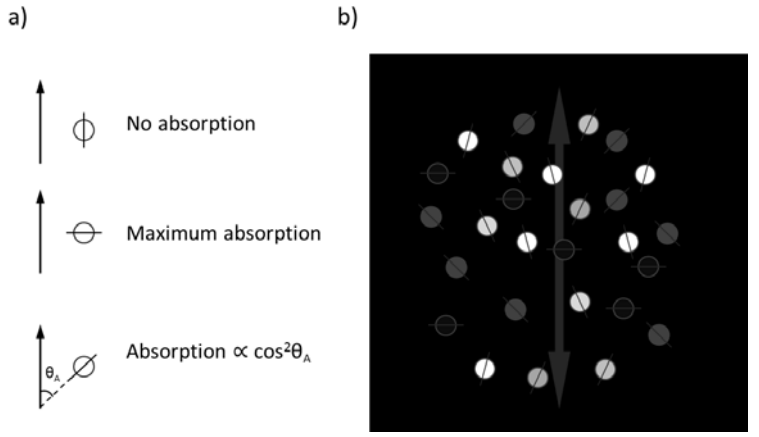

Figure 2.2: Principle of photoselection. (a) The absorption is proportional to $\cos^2\theta_A$. (b) The fluorophores whose transition moments are oriented in a direction close to that of the electric vector of the incident beam are preferentially excited, largely contributing to emission fluorescence. Adapted from [38].

The distribution of the excited fluorophores is anisotropic; therefore the emitted fluorescence is also anisotropic. This anisotropy can decrease because any change in direction of the transition moment during the lifetime of the excited state. This will induce a partial or total depolarization of the fluorescence. The main reasons of fluorescence depolarization are [38]:

- Brownian motion
- internal motion
- non-parallel absorption and emission transition moments
- transfer of the excitation energy to another molecule.

Fluorescence polarization measurements can consequently provide useful information on size, molecular mobility, viscosity and temperature of the medium, order parameters, shape and flexibility of molecules [38].

2.2.1 Characterization of the polarization state of fluorescence

The fluorescence can be analyzed as the result of three independent sources of polarized light along three perpendicular axes O_x, O_y and O_z, without any phase relation between them. The intensities along these axes are defined as: I_x, I_y and I_z and the total intensity $I_T = I_x + I_y + I_z$. The values of these intensities are defined as a function of the polarization of the incident light and the depolarization processes.

If the incident light is vertically polarized and the medium is isotropic (no preferential orientational order for the molecules), then the vertical axis Oz is a symmetry axis for the fluorescence emission, that means $I_x = I_y$. Usually, the components of the fluorescence intensity which are parallel and perpendicular to the incident electric field are denoted as $I_\parallel$ and $I_\perp$. For vertically polarized light, $I_\parallel = I_z$ and $I_\perp = I_x = I_y$ (Fig. 2.3).

If the fluorescence signal is detected along the O_x or O_y axis, then the intensity measured using a polarizer along O_z (vertical) is $I_z = I_\parallel$. For the horizontal position of the polarizer, the intensity measured with a polarizer along O_x is $I_y = I_\perp$ and along O_y is $I_x = I_\perp$.

Usually, the fluorescence is measured in the direction of the O_x axis, as show in Fig. 2.3 . The total intensity is :

$$I_T = I_x + I_y + I_z = I_\parallel + 2I_\perp \tag{2.3}$$

The polarization state of the fluorescence can be characterized by the polarization ratio p or the emission anisotropy r.

The polarization ratio is defined as:

$$p = \frac{I_\parallel - I_\perp}{I_\parallel + I_\perp} \tag{2.4}$$

The emission anisotropy is given as:

$$r = \frac{I_\parallel - I_\perp}{I_\parallel + 2I_\perp} \tag{2.5}$$

The denominator in the polarization ratio denotes the total fluorescence intensity in the observation direction. For the emission anisotropy, the denominator denotes the total fluorescence intensity in all observation directions.

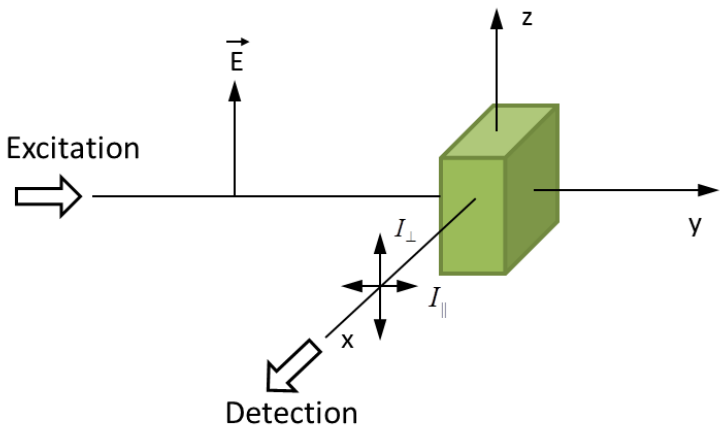

Figure 2.3: Conventional experimental scheme for measuring fluorescence anisotropy.

The relation between r and p is:

$$r = \frac{2p}{3-p} \tag{2.6}$$

In the following chapters, the term anisotropy "A" will refer to the polarization ratio.

We indeed use the term "anisotropy" in contrast to polarization in order to avoid confusion with the polarization state of light.

2.3 Fluorescence anisotropy in isotropic media

Fluorescence anisotropy is a technique used to retrieve orientational information on fluorophore in solution and isotropic biological samples. The measurement of steady-state fluorescence anisotropy involves excitation of fluorescent solution with polarized light and detection of the intensities $I_\parallel$ and $I_\perp$ (Fig. 2.3).

The fluorescence anisotropy (r) is calculated as described at Eq. 2.4 . In what follows, we will express r as a function of molecular characteristics, such as rotational diffusion time.

In the conventional scheme to measure fluorescence anisotropy r involves the excitation of fluorescent solution with linearly polarized light (Fig. 2.3). The detection is parallel or perpendicular to the excitation polarization. We denote

μ_{abs} and μ_{em} transition dipole moments involved respectively in the absorption and emission processes.

Assuming μ_{abs} and μ_{em} being parallel to each other, their projection is defined as:

$$\mu_{abs} = \mu_{em} = \begin{bmatrix} \mu_X \\ \mu_Y \\ \mu_Z \end{bmatrix} = \begin{bmatrix} \sin\theta\cos\phi \\ \sin\theta\sin\phi \\ \cos\theta \end{bmatrix} \tag{2.7}$$

We also suppose that the molecule rotates with a motion slow enough to consider that the emitted photon is radiated prior to the molecule rotation. The considered medium is therefore a "static" isotropic ensemble of molecules.

The excitation electric field E component along the z direction is defined as:

$$E_Z = E_0 \begin{bmatrix} 0 \\ 0 \\ 1 \end{bmatrix} \tag{2.8}$$

The absorption probability P_{abs} of fluorophore is defined as [39]:

$$P_{abs} \propto |\mu_{abs} \cdot E|^2 \tag{2.9}$$

In what follows, for more clarity, we omit the vector sign on all μ and E quantities.

Then the emission probability P_{em} along a certain analyzing direction i is :

$$P_{em} \propto |\mu_{em} \cdot u_i|^2 \tag{2.10}$$

where u_i is the normalized vector along i.

The fluorescence intensity can be defined as a function of the emission and absorption probabilities. For an ensemble of molecules, the intensity of all molecules is summed, accounting for their orientational distribution function $f(\theta, \phi)$. $f(\theta, \phi)$ represents the probability to find a molecule within an angle of orientation (θ, ϕ) (Fig. 2.4). This distribution can be normalized such as $\int_0^{2\pi}\int_0^{\pi} f(\theta,\phi)\sin\theta d\theta d\phi = 1$. Then the fluorescence parallel intensity ($I_\parallel$) to the excitation polarization in z direction can be written as:

$$I_\parallel = I_z = \int_0^{2\pi}\int_0^{\pi} |\mu_{abs} \cdot E|^2 |\mu_{em} \cdot Z|^2 f(\theta,\phi)\sin\theta d\theta d\phi \tag{2.11}$$

In this expression, we omit the proportionality coefficients. The expressions for the other intensities $I_\perp = I_x = I_y$ are likewise based on the eq. 2.11.

Based on the previous equations we can define the fluorescence anisotropy r as:

$$r = \frac{3\langle \cos^2\theta \rangle - 1}{2} \tag{2.12}$$

with

$$\langle \cos^2\theta \rangle = \int_0^{2\pi} \int_0^{\pi} \cos^2\theta f(\theta,\phi) \cos^2\theta \sin\theta d\theta d\phi \tag{2.13}$$

For solutions, the orientation distribution function $f(\theta,\phi)$ is $\frac{1}{4\pi}$. Therefore the term $\langle \cos^2\theta \rangle$ can be rewritten for solutions as:

$$\langle \cos^2\theta \rangle = \frac{1}{4\pi} \int_0^{2\pi} \int_0^{\pi} \cos^2\theta f_{exc}(\theta,\phi) d\theta d\phi \tag{2.14}$$

where f_{exc} represents the probability density function of the excited molecules, and it is defined as:

$$f_{exc}(\theta,\phi) d\theta d\phi = \cos^2\theta \sin\theta d\theta d\phi \tag{2.15}$$

The distribution function in the eq. 2.13 can be substituted by the eq. 2.15. Then $\langle \cos^2\theta \rangle$ is equal to $\frac{3}{5}$. The emission anisotropy r is calculated based on $\langle \cos^2\theta \rangle = \frac{3}{5}$ in the eq. 2.12, getting $r = \frac{2}{5} = 0.4$. Considering the highest possible value of $r = 1$, 0.4 appears like a low anisotropy value. This low value indicates the presence of a fraction of the excited molecules close to $x - y$ plane.

2.3.1 Applications of fluorescence anisotropy in solutions

The anisotropy "r" can decrease because different factors. In what follows, we describe two of them and how they can be used.

Different angles between the absorption and emission transition dipole moments

The angle β between the absorption μ_{abs} and emission μ_{em} transition dipole moments induces a depolarization of the fluorescence emission(Fig. 2.4). Generally, these transition dipole moments are along specific directions within the molecule's structure, such as its conjugated backbone. Nevertheless, $\beta \neq 0°$ can be induced by different molecular conformations in the highest and lowest excited states. In this case, r is rewritten into the fundamental anisotropy r_0 as [38]:

$$r_0 = \frac{2}{5}\left(\frac{3\cos^2\beta - 1}{2}\right) \tag{2.16}$$

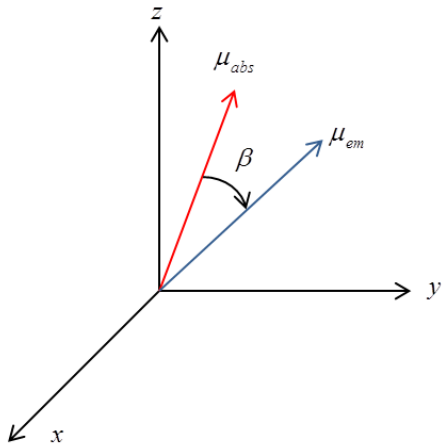

Figure 2.4: Dipole orientation and angle between absorption and emission transition dipole moments.

The fundamental anisotropy r_0 is the anisotropy of the molecule without any other depolarizing processes, like energy transfer or rotational diffusion. A β angle that is different than zero will decrease the anisotropy.

The theoretical values of r_0 are in the range from - 0.2 for perpendicular transition moments and 0.4 for parallel transition moments. A value close to - 0.2 has been observed still in the case of aromatic molecules, for example perylene [38]. The value of r_0 is zero for $\beta = 54.7°$ and negative for $\beta > 54.7°$.

The measurement of the β angle represents one of the possible application of the fluorescence anisotropy methods.

Rotational diffusion

If the excited fluorophore can rotate during its excited-state lifetime, the emitted fluorescence is depolarized. The favored orientation of emitting molecules at time zero is certainly affected as a function of time by the rotational Brownian motions.

This happens if the fluorescence lifetime τ_f is longer than the rotational correlation time τ_{rot}. In this case, after absorption of a photon, the molecule has enough time to rotate before its fluorescence emission. Therefore, the absorption and emission orientations are decorrelated, and the polarization information is lost. On another hand, if the rotational correlation time τ_{rot} is longer than the fluorescence lifetime τ_f, then the excited molecules will present polarized emission. Fast rotational diffusion induces light depolarization that can be quantified by fluorescence anisotropy.

The relation between the rotational correlation time τ_{rot}, lifetime τ_f and the fundamental (r_0) and measured (r) anisotropies is defined by the Perrin equation [40]:

$$\frac{1}{r} = \frac{1}{r_0}\left(1 + \frac{\tau_f}{\tau_{rot}}\right) \tag{2.17}$$

The quantitative information can be obtained only if the timescale of rotation motions is similar to the range of the lifetime τ_f. Consequently, if motions are slow $r_f \sim r_0$ or fast $r_f \sim 0$, then anisotropy measurements cannot give information on these motions because they occur out of the experimental time window [38].

Rotational diffusion can be estimated by measuring the steady-state fluorescence anisotropy or an anisotropy decay in time-resolved experiments [39].

The rotational correlation time τ_{rot} of a fluorophore is written as:

$$\tau_{rot} = \frac{\eta V}{RT} \tag{2.18}$$

where η is the viscosity of the solvent, V is the hydrodynamic volume of the rotating fluorophore, R is the gas constant and T is the temperature.

Since many factors like the viscosity of the solvent, or size and shape of the fluorophore affect the rotational diffusion, the measured anisotropy can give information about them if the other contributing parameters are known.

Consequently, fluorescence anisotropy methods are widely used in biochemical research studying the denaturation of proteins (which induces conformational changes leading to modifications of the rotational behavior) or their association with other macromolecules [37].

2.4 Fluorescence anisotropy in fibers - state of the art

Ordered media are defined by structures (e.g. fibers, aggregates, lipid membranes) in which fluorescent molecules are oriented with respect to each other due to some orientational constraint. This is illustrated in Fig. 2.5. Studying ordered samples requires developing different approaches than the one previously presented in the context of isotropic media. Indeed fluorescence anisotropy favors two privileged directions ($\parallel$ and $\perp$) that are not necessarily correlated with the ordered sample.

In the most simple models, a molecular order is defined by its angular aperture (ψ) and its average orientation (ρ) in the sample plane (Fig. 2.5). These two parameters cannot be measured independently using a single measurement such as fluorescence anisotropy. To circumvent this problem, several options exist. The

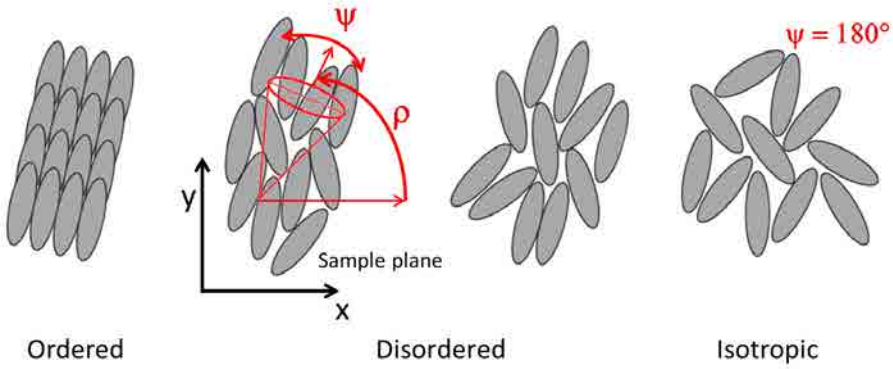

Figure 2.5: Schematic representation of molecular order (the grey ellipsoids represent fluorescent molecules), from highly ordered to totally isotropic. The angles ρ and ψ quantify the average orientation of the molecular orientation distribution, and its angular aperture (here assuming a cone).

simplest is to make the hypothesis that the observed structure (e.g. action fiber) is an axis of symmetry of the molecular angular distribution, and to infer the orientation of the distribution (ρ) from the image observation, using fluorescence anisotropy [12, 13]. The second option is to add more measurements, such as tuning also the incident polarization using the two $\parallel$ and $\perp$ states [41] or many incident polarization angles [42, 43].

Different works have been done based on analysis direction (anisotropy) or the excitation polarization (linear dichroism) in biological filaments, such as in actin fibers labeled directly [11] or via phalloidin-labeled interaction [12,13], but also in intercalation dyes in DNA double strand fibers [14]. More recent studies performed in mosaic group based on polarization resolved fluorescence microscopy have been done to study insulin amyloid fibrils [44]. Note that in fluorescence microscopy, the geometry is a little different than in Fig. 2.3: we will define (X, Y) as the sample plane and the field E propagates along Z (see Fig. 2.5). The molecular angular distribution on $f(\theta, \phi)$ is thus expected to lye in the sample plane and the measured intensity along the X polarization axis becomes:

$$I_X = \int\int |\mu_{abs} \cdot E|^2 \cdot |\mu_{em} \cdot X|^2 f(\theta, \phi) \cdot J(\theta, \phi) \cdot \sin\theta d\theta d\phi \tag{2.19}$$

where E is the incident polar, J: a factor accounting for high aperture collection which might mix slightly detected polarization states [8]. X: horizontal axis sample plane.

Similarly I_Y would be written using $|\mu_{em} \cdot Y|^2$. More detail will be given in Chapter 4.

Note that to get information on the 3D orientation of this distribution, different schemes are needed such as Z polarization excitation [45] or highly tilted excitation [46]. Some examples are presented in more details in what follows.

2.4.1 Molecular orientational order of actin

Borejdo et al. studied the orientation of phalloidin labeled actin fibers in cells (intestinal microvilli) based on ensemble measurements [12]. These studies were performed with two incident polarizations in the excitation path and two in the detection one. To model the orientational distribution, a helix-random model was proposed (Fig. 2.6 b). In this model a fraction of molecules are constraint on a helical array, characterized by polar angle Θ_H around F-actin, and the rest is randomly oriented [12]. Later in 1994, Borejdo et al. used this helix-random model and another Gaussian model to study phalloidin labeled actin in vitro, attached to a surface or free in solution [13]. The Gaussian model presented in this last study was based on fluorophore dipoles spread with Gaussian probability around a mean Θ_G angle with a standard deviation δ (Fig. 2.6c). The molecular orientation of fluorophores in actin in vitro was described with $\Theta_G \sim 49°$ (immobilized on a surface) and $\Theta_G \sim 51°$ (free in solution from a filament not attached to the surface), and $\delta \sim 1 - 4°$, based on the Gaussian model. In the case of helix-random model, the orientation of fluorophores in actin in vitro was constraint to $\Theta_H \sim 49°$ in actin on a surface (with a 1% portion being randomly oriented) and $\Theta_H \sim 51°$ for actin in solution (with a 35% portion being randomly oriented), showing consistence with the results based on the Gaussian model.

Note that due to the polarized fluorescence process itself (Eq. 2.19), these measurements cannot make the difference between the Helix-random and Gaussian model. Some attempts to do so have been made using single molecular detection.

Forkey et al. have analyzed the orientation of directly labeled F-actin (at a Cys residue) by Total Internal Reflection Fluorescence Polarization Microscopy [11]. The study was performed on single molecules using a high tilt angle of illumination in order to reach 3D information. The model used is very similar to the Gaussian model of Fig. 2.6c. The observed single molecules showed a constant tilt relative to the actin fiber ($\beta \sim 49°$ corresponding to the Θ_G angle), with a variable azimuthal angle (α rotating around the fiber axis) and a wobbling motion slower than 10 ms, within an angle $\delta \sim 20 - 40°$. The cone model used in [11] is shown in Fig. 2.7 where it shows that single molecule observation can in addition bring information on the α angle using a 3D orientation detection.

Recently, orientational order of phalloidin-stained stress fibers (mostly bun-

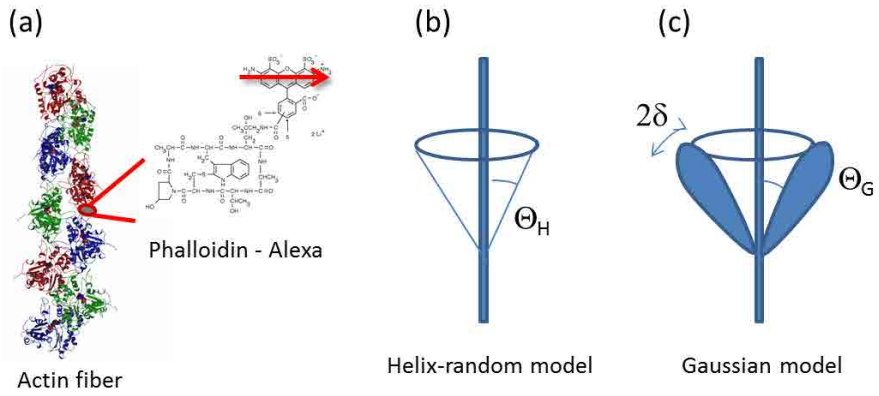

Figure 2.6: Orientation model proposed by Borejdo et al. for actin fibers labelled via phalloidin. (a) Structure of an actin fiber and of phalloidin, labelled with an alexa dye. (b) Helical-random model proposed for actin fibers in cell [12] and vitro [13]. (c) Gaussian model proposed for actin in vitro fibers [13].

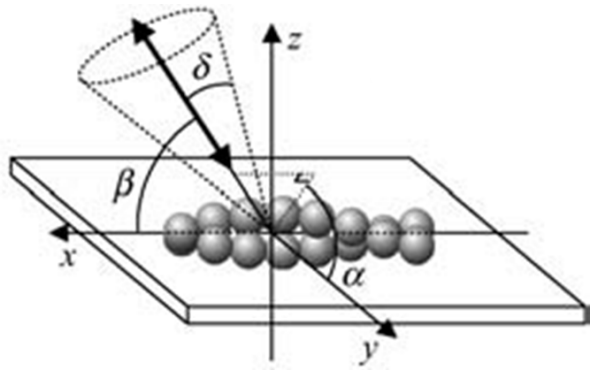

Figure 2.7: Actin coordinate system and angles introduced for single molecule investigations. β, α and δ angles are shown relative to the axis of the actin filament. The arrow is a single molecule abs/em dipole. Adapted from [11] .

dles) in COS 7 cells has been measured by polarization-resolved fluorescence ensemble measurements on a confocal microscope [43]. In these studies, the molecules were supposed to undergo an angular constraint within a filled cone aperture of total angle ψ and oriented along the average direction ρ (Fig. 2.8). For densely packed actin bundles, ψ was measured to be about 137° (Fig. 2.8) [43].

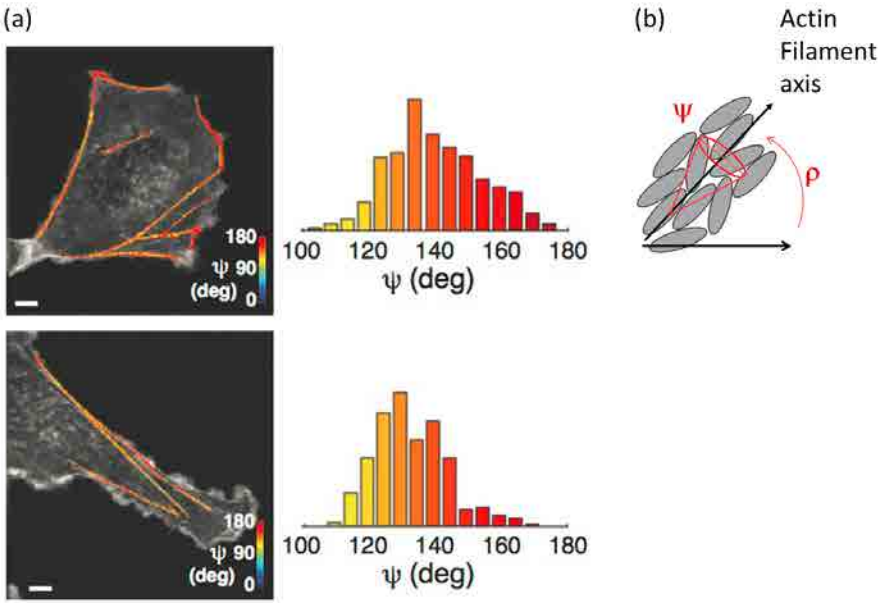

Figure 2.8: Polarization-resolved fluorescence measurements on a confocal microscope of actin stress fibers labelled with phalloidin-dye in fixed cells. (a) Representative composite images of Alexa Fluor phalloidin intensity (grey) and ψ angles. The respective histograms of ψ are shown. (b) Constraint distribution defined by a cone of orientation ρ and aperture angle ψ. Scale bar: 5 μm. Adapted from [43].

2.4.2 Molecular orientational order in amyloid fibrils

Duboisset et al. have reported recently the potential of Congo Red and Thioflavine-T (ThT) dyes to be used as structural reporters of insulin amyloid fibrils [44]. They implemented this study using polarization resolved fluorescence microscopy.

The angular constraint of these dyes was quantified by an angle ψ. The distribution of molecules was modeled as a 3D filled cone, of full width ψ and orientation ρ (Fig. 2.9 c). Values of ψ measured were either around 80° or around 120° (Fig. 2.9), showing the possible existence of two forms for the orientation behavior of ThT in insulin amyloid fibrils in consistence with their known polymorphism.

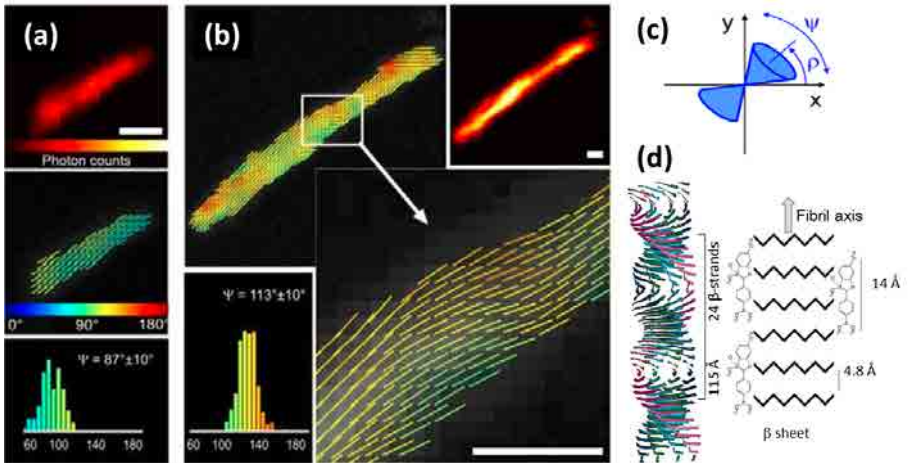

Figure 2.9: Polarization-resolved fluorescence measurements performed on insulin amyloid fibrils labeled with Congo Red (a) and ThT (b). The red/yellow color map indicates the total fluorescence intensity recorded. The composite image summarizes the mean orientation ρ (indicated by an orientated stick) and the angular aperture ψ of the fluorophores as they have been measured by the method. A histogram gives an overview of the distribution of the obtained ψ values. Scale bars are 1 μm. (c) Scheme of the angular distribution of dipoles in the plane. Adapted from [44]. (d) Structure of Thioflavine dye and model for the generic amyloid fibril structure. A number of β-sheets (4 represented here) make up the protofilament structure. The dye inserts along the perpendicular direction to the β-sheets. Adapted from [47].

2.4.3 Molecular orientational order in DNA fibers

In 1994, Larsson et al. studied the orientation of the YOYO dye into dsDNA (double stranded DNA) fibers [48]. They found two different binding behaviors depending of the mixing dye ratios, either intercalating or external binding. For mixing ratios below 0.124 dye/bp (bp=base pair), they observed that the long axis of the chromophore is approximately perpendicular to the DNA helix axis (orientation consistent with intercalation) and for the high mixing ratios dye the chromophore is aligned perpendicular to the pitch of the grooves. NMR solution structure of the TOTO-1 dye, which is similar to YOYO-1 dye, bound to DNA is shown in Fig. 2.10.

In addition, other studies have led to various interpretations of polarized data in YOYO-1 DNA systems. The most used model is a global orientation of the dyes with a mean orientation of 75° to 90° relative to the DNA fiber axis [49–51]

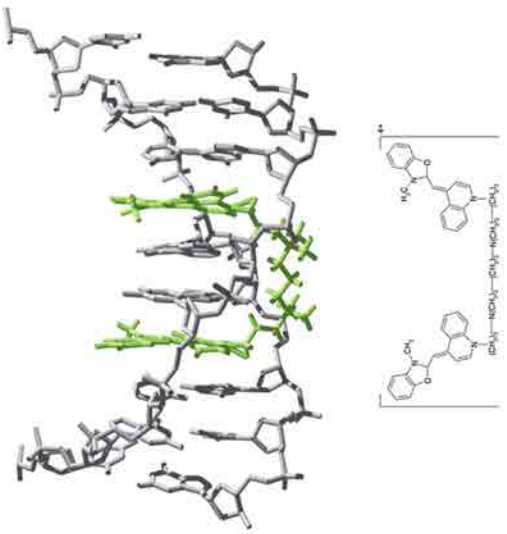

Figure 2.10: NMR solution structure of the TOTO-1 (similarly to YOYO-1) dye (green) bound to DNA (grey), derived from data submitted to the Protein Data Bank (number PDB 108D, www.rcsb.org/pdb/). Insert : chemical structure of YOYO-1.

(similarly to an helix model of Fig. 2.6b with $\Theta_H \sim 75° - 90°$).

Recently, Van Mameren et al. have refined this model using more polarization states of excitation [14] in dsDNA fibers immobilized between optical tweezers. A fast wobbling of $\psi \sim 50°$ has been found with a mean orientation of 90° relative to the fiber axis which is more consistent with a filled cone.

In all these studies, we see the importance of having a dye which is as much as possible rigidly connected to the macro-molecule of interest. It can be ensured either by a short linker (phalloidin for instance) or an intercalation (amyloid or DNA for instance). Still, the high angle of disorder observed is the signature of residual wobbling or structural disorder. Polarized single molecule spatial investigations such as the one developed here should be able to give more insight in this issue.

2.5 Super resolution microscopy.

Fluorescence microscopy has been playing an important role in biological research. Nevertheless, its spatial resolution is limited due to the diffraction of

light. Ernst Abbe established a quantitative estimation of this limit given by the size of a focussed spot [52]:

$$\begin{aligned} \delta_{x,y} &= \frac{\lambda}{2NA} \\ \delta_z &= \frac{2\lambda}{NA^2} \end{aligned} \tag{2.20}$$

where the lateral resolution of the focussed spot under a numerical aperture NA is given by δ_x, δ_y and the axial resolution δ_z. λ is the wavelength of the fluorescence emission. This limit usually lies between 200-300 nm (lateral resolution) and 500-800 nm (axial resolution).

Later on, Rayleigh defined a more adequate limit for the diffraction limit. According to Rayleigh criteria, the resolution is limited by the ability to distinguish two spots, given by [53] (Fig. 2.11):

$$\begin{aligned} \delta_{x,y} &= 0.61\frac{\lambda}{NA} \\ \delta_z &= \frac{2\lambda n}{NA^2} \end{aligned} \tag{2.21}$$

where the lateral resolution is given by δ_x, δ_y and the axial resolution δ_z. λ is the wavelength of the fluorescence emission, n is the refractive index of the medium and NA is the numerical aperture.

Recently, there are two different types of far-field fluorescence microscopy techniques which have been developed to overpass this limitation. The first type includes the techniques that use patterned illumination to sharpen the excitation PSF, possibly combined with nonlinear response of the emission behavior of the molecules, such as Stimulated Emission Depletion (STED) [54], Ground State Depletion (GSD) [54], Reversible Saturable OpticaL Fluorescence Transitions (RESOLFT) [55], Structured Illumination Microscopy (SIM) [56] and Saturated Structured Illumination Microscopy (SSIM) [57].

The second type relies on the use of precise single-molecule localization of photo-switchable fluorescence probes. This type includes the Stochastically Optical Reconstruction Microscopy (STORM) [58], direct Stochastically Optical Reconstruction Microscopy (dSTORM) [2], Photoactivated localization microscopy (PALM) [1], Fluorescence Photoactivation Localization Microscopy(FPALM) [59], and other methods using similar principles. These techniques require fluorophores that can be photoactivated or reversibly photoswitched by light. These fluorophores have a fluorescent (ON state), a non-fluorescent (OFF state) and a transition state. They can be photoconvertible fluorescent proteins in PALM

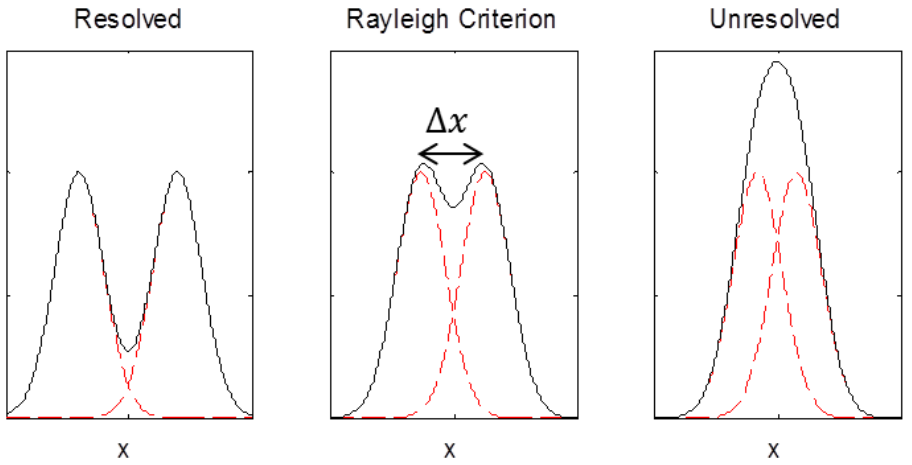

Figure 2.11: Rayleigh criterion: only signals with a greater distance than Δ_x are resolvable (dashed line shows individual lateral sections of focussed spots).

[1] and FPALM [59]; pairs of organic fluorophores, a combination of activator and reporter fluorophores in STORM [60] ; or standard organic fluorophores in dSTORM [2].

The basic principle of these methods is first to have a target structure which is densely labeled. Then few of the total population of fluorophores are switched to short-live ON state, such as they are not overlapping. Then the position of the centroid can be precisely estimated for each molecule by fitting their image, assuming a Gaussian distribution. After the few bright molecules go to the OFF state, another statistically different set of fluorophores is activated and localized. This process is repeated continuously until the structure of interest is appropriately sampled (usually 10 000 to 40 000 frames). Then the final super-resolution image is reconstructed by plotting the localizations obtained from all switching cycles or by rendering them as a 2D Gaussian peak.

2.6 direct Stochastic Optical reconstruction microscopy dSTORM.

As the other localization based super resolution techniques, dSTORM is based on the precise localization of isolated individual blinking molecules. In dSTORM, the photoswitching of small organic fluorophores (Alexa Fluor and ATTO dyes) is promoted by adding millimolar concentrations of reducing agent, such as β-

mercaptoethylamine (MEA) [2] (Fig. 2.12).

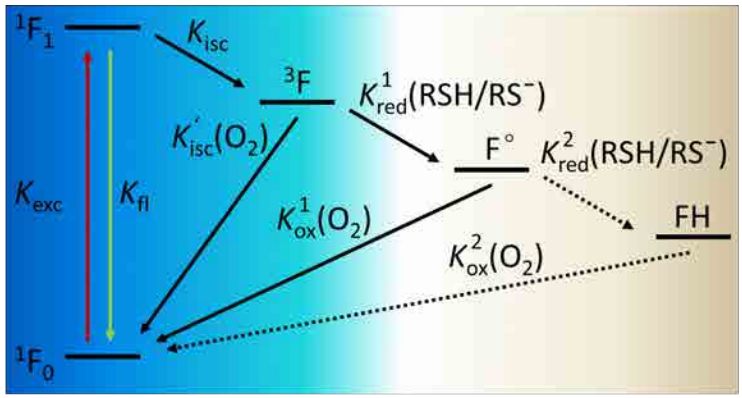

Figure 2.12: The Jablonski diagram associated with the photo-switching on dSTORM. The left blue part is the normal Jablonski diagram with the ground state $^1F_0$, excited state $^1F_1$ and triplet state^3F. Rates are the excitation rate k_{exc}, fluorescence rate (k_{fl}) and inter-system-crossing rate k_{isc}. The F° denotes the radical anion, and the FH is the fully reduce leuco-form ("colorless"). Transition to theses state occurs by reduction by a thiol with rates k^1_{red} and k^2_{red} . Transition from the dark-state to the ground state occurs by oxidation by molecular oxygen at a rate k_{ox}. Adapted from [2].

The reversible photoswitching of Alexa Fluor and ATTO dyes due to the presence of thiols is the fundamental mechanism of dSTORM [2]. The fluorophore is either switching between its singlet ground state and the excited state emitting fluorescence photons or can go through intersystem crossing with rate k_{isc} upon irradiation. Then, the triplet state (^3F) can react with molecular oxygen to go back to the singlet ground state and generate singlet oxygen or react with the thiolate with rate k_{red} to produce the radical anion of the fluorophore (F°) and the corresponding thiyl radical. The radical anion can be oxidized by oxygen with rate k_{ox} to go to the singlet ground state. Since radical anions of most rhodamine and oxazine derivatives have absorption at excitation wavelength of $\sim$ 400 nm, then illumination at 405 nm promotes recovery of the fluorescent form [2]. However the thiyl radicals react with molecular oxygen to generate superoxide radicals and hydrogen peroxides, the fluorophore radical anion is unreactive and survives for up to several seconds. Fluorophores such as ATTO 655 and ATTO 680 can accept a second electron to produce the fully reduced leuco-form (FH). Oxidation of FH recovers the ON state [2].

The principle of dSTORM is show in the Fig. 2.13.

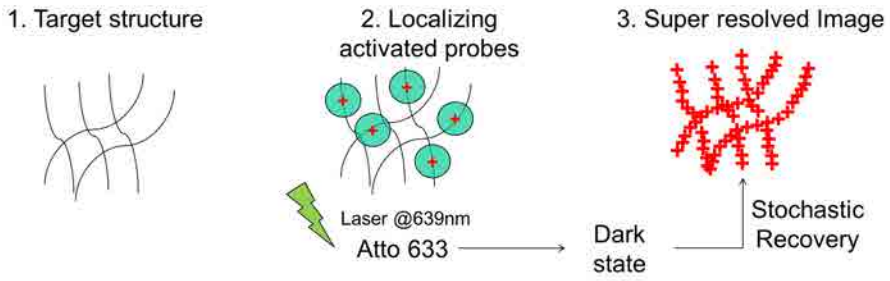

Figure 2.13: dSTORM principle. First a target structured is densely labeled. Then the fluorophores are photoactivated into a fluorescing state by a flash of light. Because photoactivation is stochastic, only a few, well-separated molecules "turn on." Then Gaussians are fit to their PSFs to high precision. After the few bright dots photobleach, another flash of the photoactivating light activates random fluorophores again and the PSFs are fit of these different well-spaced objects. This process is repeated many times, building up an image molecule-by-molecule; and, because the molecules were localized at different times, the "resolution" of the final image can be much higher than that limited by diffraction.

Figure 2.14 shows a clear improvement of resolution, which permits to see more details of the microtubules network.

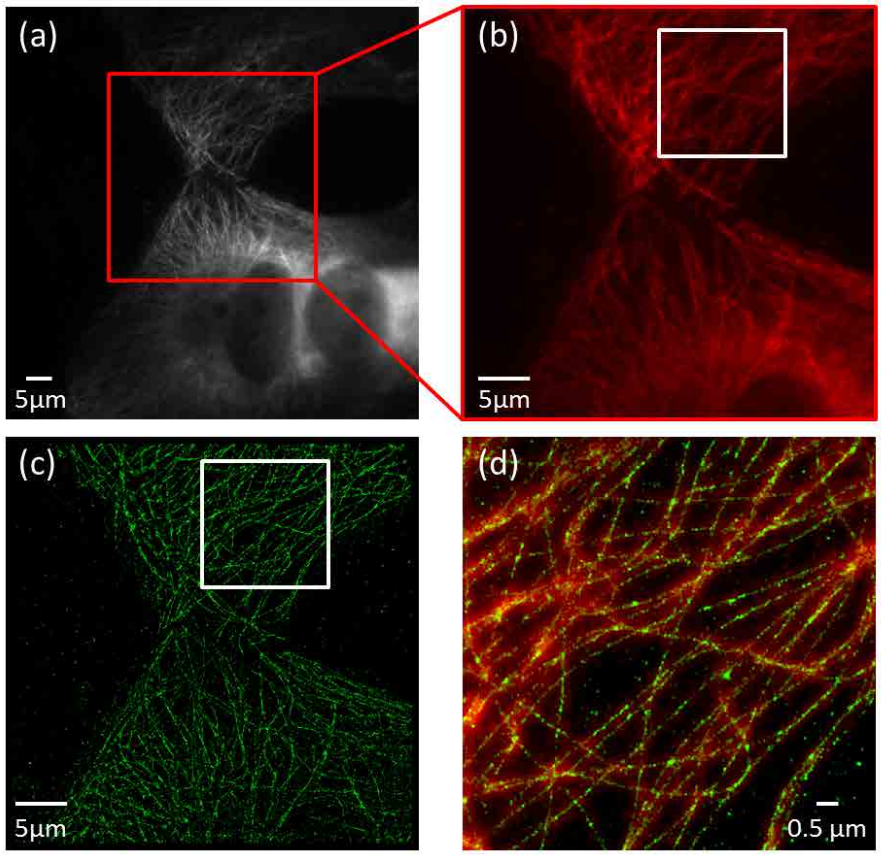

Figure 2.14: dSTORM imaging of microtubules in a COS 7 cell. (a) Conventional indirect immunofluorescence image of microtubules labeled with photo-switchable Alexa 647 in a large area. Pixel size: 157 nm. (b) Small selected region from a. (c) dSTORM image of a selected region from a. Pixel size: 19.5 nm, Gaussian blur: 20 nm. (d) Composite image of widefield (red) and dSTORM (green). Images recorded at ICFO, Barcelona.

2.7 Fluorescence anisotropy at the nanoscale

2.7.1 Fluorescence polarized detection of single molecules

Knowing that the absorption and fluorescence emission processes are sensitive to molecular orientation, and that single molecule detection provides nanoscale super resolved imaging capabilities, it seems interesting to investigate how single molecule detection dedicated to super-resolution imaging can be combined with polarized information. Single molecule polarized detection has been studies in a few works. The simplest version is to excite molecules with a circular polarization, ensuring a uniform photo-selection for all molecules lying in the sample plane (this photo-selection decreases indeed dramatically for molecules pointing their excitation dipole off plant). The retrieval of the orientation of their emission dipole in the plane of the sample (or more generally its projection in this plane) can be obtained by a polarized detection in two perpendicular directions [5]. This method has been used for instance to detect rotational mobilities (at the ms time scale) of single molecules confined in gels or glasses [61], to visualize orientational motions of single molecules attached to actin filaments sliding over myosin molecules [62].

More complex schemes using tilted excitation and two excitation/detection polarizations have been developed to decipher the complete 3D orientational behavior of fluorophores labeling F-actin fibers, following the time sequence of polarized intensities of molecules one by one [11]. Similar approaches have been used on Q rod-conjugated myosin V sliding on actin filaments, using a circular incident polarization and four states of detected polarization [63]. Note that even though this techniques offers the most complete set of measurement, it is limited by poor statistics. It is also limited by the time sequence necessary for the excitation polarization in multiple states and the splitting of the fluorescence signal in multiple channels, and therefore suffers from slow dynamics, low signal to noise levels and therefore to low precision in the angular measurements. Note that other techniques allow retrieving 3D orientation information from single molecules have been developed, based on the measurement of the deformation of their emission pattern by defocused imaging [64] or using more refined tilted image projections [65].

Combining single molecule orientation detection with super-resolution microscopy requires in principle accounting for the fact that single molecule orientation affects its localization precision. Indeed any anisotropic emission pattern caused by an oriented dipole leads to a deformation of its point spread function and therefore alters the fitting of the single molecule image by a simple Gaussian function [66]. Typically, a 10 nm error in the localization precision can occur when molecules are tilted above 45° with respect to the sample plane, this localization error increasing dramatically for slightly defocused conditions. This

effect has been investigated in the case of fixed [4] and dynamically rotating single molecules within an angular constraint angle [67], where a correction is proposed based on a double helix point spread function. While this localization error is detrimental for studies willing to image several depths of focus for 3D spatial imaging, the use of single plane imaging such as developed in this work is less affected by such localization error. Moreover highly off-plane tilted molecules are naturally not detected since both excitation and collecting efficiencies are very low. Rotational mobility (which is partly the context of this work) is also known to cause a decrease of this error effect, especially for high angular cone apertures [67].

2.7.2 Polarized FPALM imaging

Gould et al. have proposed a method called Polarization Fluorescence Photoactivation Localization Microscopy (P-FPALM) to calculate the anisotropy from single molecules at the nanoscale and report it in super-resolution images [7]. This method is based on the combination of a super-resolution imaging and anisotropy estimation using an incident linear polarization, similarly as for solution measurements (Fig. 2.3). The information gained is thus purely about existence of depolarization mechanisms. Changes of orientational behaviors have been detected on membrane proteins clusters of actin stress fibers based on local changes of single molecule's anisotropy (Fig. 2.15). There was however no quantitative analysis performed on this study. Also the measurement of single molecule anisotropy was probably affected by a lot of bias due to the method chosen on the cross-correlation on $\parallel$ and $\perp$ images. In our work we propose an alternative which is compatible with the sub-pixel localization precision.

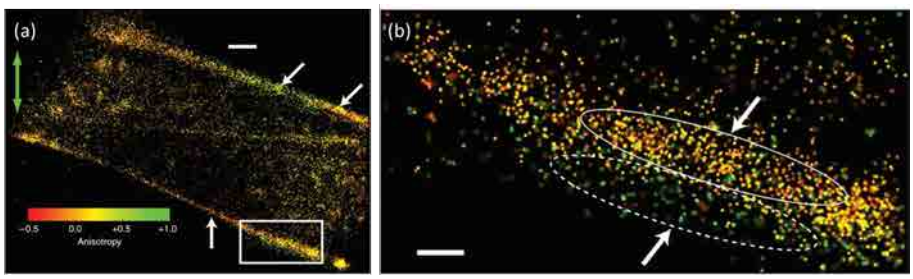

Figure 2.15: P-FPALM imaging of a fixed fibroblast expressing Dendra2-actin. Scale bars: 1 μm. Adapted from [59] .

Almost at the same time, Testa et al. published a combination of PALM microscopy with polarization-sensitive fluorescence detection using a similar analy-

sis [68].

2.8 Conclusion

In this chapter we have presented the basics of the fluorescence anisotropy methods, as well as their possible applications. We have described the state of the art of the fluorescence anisotropy in biological fibers, including actin fibers, DNA and amyloid fibrils.

In addition, super-resolution techniques based on localization microscopy have been introduced, focusing on dSTORM.

Chapter 3

Experimental set-up and methodology for polar-dSTORM

The methodology described in this chapter is based on the dSTORM microscopy, that uses standard organic fluorophores (Alexa fluor or Atto-dyes) as reversible photostable probes [69]. In this case, no activator is required as in the case of STORM or PALM. The photoswitching is induced by light and an aqueous buffer in a presence of a reducing thiol compound as mercaptoethylamine (MEA) [69].

Our goal is to use the polarization information of single molecules signal to measure their orientational behavior. For this purpose, we propose a combination of direct Stochastic Optical Reconstruction Microscopy (dSTORM) [2] in combination with polarized detection. The system proposed called "polar-dSTORM" is able to generate simultaneous images in two perpendicular directions of polarization emission, along the horizontal ("parallel") and vertical ("perpendicular") directions of the sample plane. This scheme has been used a long time ago for single molecule anisotropy analysis [5] and recently in PALM [7]. In this chapter, we describe the experimental implementation of a polar-dSTORM set up compatible with excitations by two different wavelengths and focus stabilization. The polar-dSTORM algorithm is proposed to precisely determine the anisotropy of the detected single molecule. This algorithm allows to determine lateral positions and intensity of single molecules with nanometer accuracy in parallel and perpendicular polarized emission images. In addition, a post-processing analysis is described, including lateral drift correction, molecules selection and anisotropy display. A more refined analysis is finally introduced to address the specific case of

fiber structures such as actin, tubulin, DNA and amyloids. Using this approach, we are able to reconstruct anisotropy images with a localization precision of less than 50 nm. This development allowed to retrieve a molecular order information that will be further interpreted in the next chapter.

3.1 Experimental setup

The experimental setup is based on an epifluorescence widefield microscope which has been adapted for polarization dSTORM imaging. It is described in details in what follows.

3.1.1 Optical setup

Measurements are carried out on a custom epifluorescence microscope system, adapted to retrieve the perpendicular (called "$\perp$" in what follows, corresponding to the vertical axis of the sample plane) and parallel ("$\parallel$", corresponding to the horizontal axis of the sample plane) polarization states of the fluorescence images. The general principle of the super resolved microscope proposed for this work follows the principle of dSTORM [2]. The excitation light source is a polarized continuous wave laser (Genesis, Coherent) emitting at 639 nm wavelength with a typical averaged power density of about 5 kW/cm^2 before the objective. The laser beam is expanded by a telescope in order to achieve a diameter of about 100 mm. Then it is circularly polarized by a quarter waveplate (WPQ10M-633, Thorlabs). A mirror reflects the beam towards the microscope, followed by a large focal length lens (f = 400 mm) to focus the beam in the backfocal plane of the objective. This provides a widefield illumination of diameter of about 100 μm in the sample plane. The reflection mirror and lens are mounted on a translation stage in order to provide the possibility for tilted excitation. After the reflection on a dichroic mirror (FF 500/646, Semrock Rochester NY), the excitation light is focused onto the sample by an oil immersion objective lens (TIRF Plan Apo 60×, NA = 1.45, or ×100, NA = 1.45 Nikon). The emitted fluorescence is collected by the same objective lens in an epi-geometry, passes through the dichroic mirror and a band pass emission filter (FF01-535/675, Semrock Rochester NY). The tube lens provides a total magnification of ×90 or ×150. After the microscope exit, imaging lenses are used with a ×1 magnification(f_1=f_2=50mm) to leave space for polarization separation. This polarized analysis is provided by a Wollaston prism (WP10, Thorlabs) placed just before the EMCCD camera(Quantem 512sc, Photometrics: 512 × 512 pixels), such as to fill the CCD chip with two perpendicularly polarized images. The size of these images is set by a diaphragm placed in the first image plane (see Fig. 3.1). A single molecule spot size is

typically 3 pixels which is compatible with the diffraction limited spot size and the pixel size of the CCD (16 μm $\times$ 16 μm).

Another similar excitation pathway has been built on another entrance port (upper stage) of the microscope for excitation of molecules at 488 nm (also circular polarized), using an Argon laser (power $\sim$ 8 kW/cm^2), the dichroic mirror introduced at this level is not affecting the other functions of microscope.

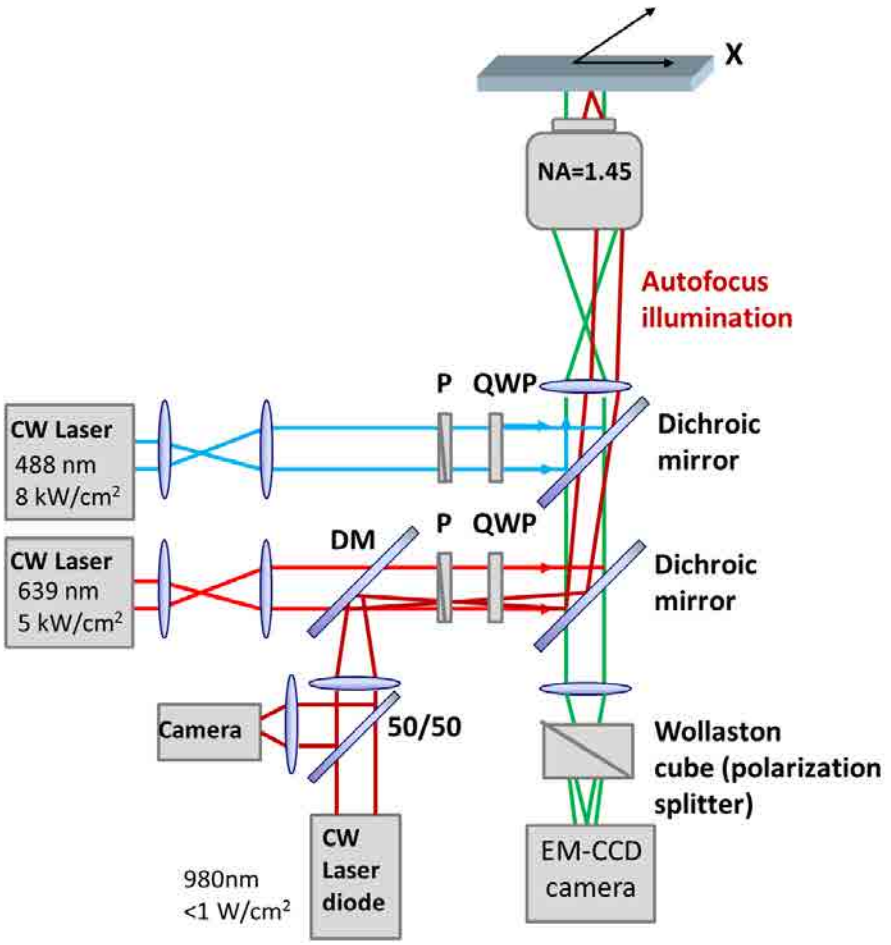

Figure 3.1: Experimental Setup. The 980 nm laser is used for defocus correction in real time, the 639 nm laser is used to excite the fluorescence molecules in dSTORM. The Wollaston prism is used to separate the two polarized images, on two areas of the EMCCD camera.

For the measurement of anisotropy in dynamic samples, the incident polarization is changed from circular to linear by removing the $\lambda/4$ waveplate. At last, an additional feasibility has been added to the setup to provide the possibility to heat regions of the sample by metallic substrates. For this configuration, a continuous laser at 532 nm (Coherent Verdi) and varying power around 0.01-0.1 W is used and focused to image a small region of ($\sim$ 80 μm^2) the sample (see Fig. 3.2).

3.1.2 Focus drift correction

Axial drift of the sample-objective distance can considerably affect the size of the single molecules point spread functions (PSF) leading to a low single-molecule localization precision. To correct for the axial drift between the cover glass of the sample and the objective lens, one system to maintain an accurate focal position during the experiment was implemented based on an earlier development by S. Monneret in the mosaic team (Fig. 3.1).

This defocus correction is performed based on a closed loop feedback system that maintains the focus. The goal is to detect how the reflection of a reference beam focused on the coverslip is spatially displaced when the coverslip drifts away or towards the objective. By imaging this displacement it is possible to use a pre-calibration information to know how much the sample or objective should be moved back to its initial position. Here the sample is mounted on a piezo-electric stage (MCL Nano-T Series). This system is based on a laser diode emitting at 980 nm coupled in an optical fiber. It is 50/50 transmitted through a first beam splitter and reflected by a dichroic mirror (FF 720-SDi01, Semrock Rochester NY) which permits to combine this beam with the 639 nm excitation pathway. A lens is used to adapt the beam divergence such as to focus this beam on the sample interface whatever the sample position chosen for fluorescence imaging. The beam diameter is narrow (2 mm) and laterally displaced such as to be focused in a tilted incidence by the objective. The laser reflection is collected though the same optical path. The signal reflected by the 50/50 beam splitter is detected by a camera (CMOS camera, Thorlabs) before which an imaging lens (f= 100 mm) is placed. In the occurrence of axial drift, the position of the beam is shifted by a value to which corresponds a z-displacement of the sample (pre-calibration curve, see Fig. 3.3b). To correct this shift, the piezo stage is changed in Z-position up/down to the original focal position following the calibration curve. This system maintains the focus with a precision which is set by the user depending on the pre-calibration curve obtained (typically 20 to 80 nm). All the procedure is performed and controlled by a labview program. Note that additionally lateral drift correction is applied afterwards by data analysis (Section 3.4).

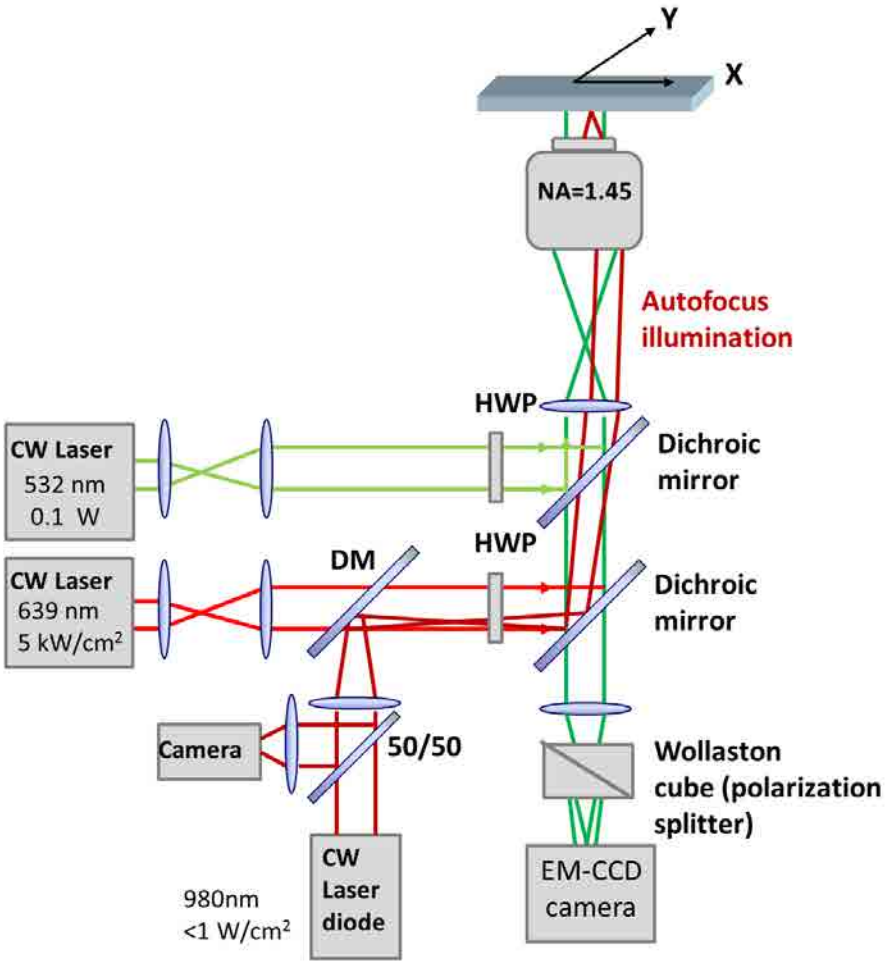

Figure 3.2: Experimental Setup for thermal imaging. A 532 nm laser is used to heat the gold nanoparticles, while the 639 nm laser is used to excite the fluorescence molecules in dSTORM.

3.2 Camera Calibration

In order to guarantee the precise quantitative data analysis, the response of the camera has been investigated. First, the camera response was analyzed in dark conditions showing a systematic offset of 1000 counts, irrespectively of the gain

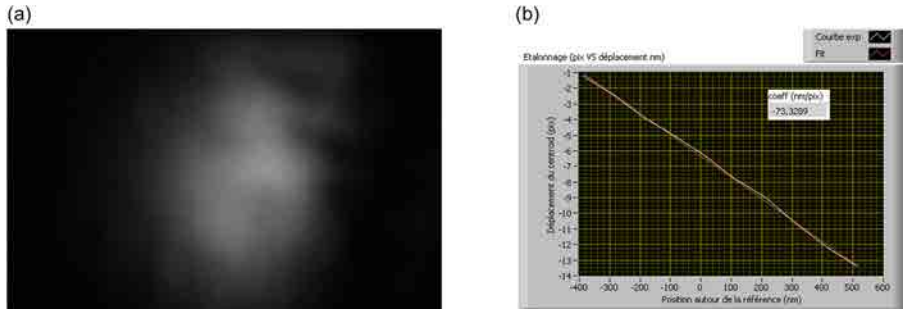

Figure 3.3: Calibration of the defocus correction system. (a) Image of the laser reflection. (b) Precalibration curve.

and exposure time. This offset value will be subtracted from all data acquisitions, including calibrations below.

3.2.1 Linearity of camera response

To investigate the linearity of the camera response for different acquisition settings, images of an illuminated white object (piece of paper) have been recorded under several excitation powers, going between 0.5 mW and 3.5 mW, in order to produce a widespread range of signal. During each test 100 fluorescence images were recorded and averaged to reduce the influence of fluctuations. For each condition, different regions of interest have been chosen, over which the response has been averaged. For this analysis, two different camera gain settings were considered (Gain=100, 300). We observed a trend on nonlinear intensity dependance for a measured signal above 20 000 counts.

Signal values below this threshold clearly show a linear relationship between the recorded signal and the excitation power, which guarantees that the measurements can be analyzed with a quantitative approach.

3.2.2 Camera noise analysis

The signal retrieved by the camera has been analyzed in detail, in consideration that EMCCD differs from pure photon counters. Using a white object (piece of paper), as an imaged sample, different measurements conditions of gain and power have been tested. For each case, 500 images were recorded, allowing to analyze the standard deviation σ_I as a function of the mean value of the signal $< I >$. A global analysis performed for different configurations demonstrates that σ_I depends on the mean signal following to :

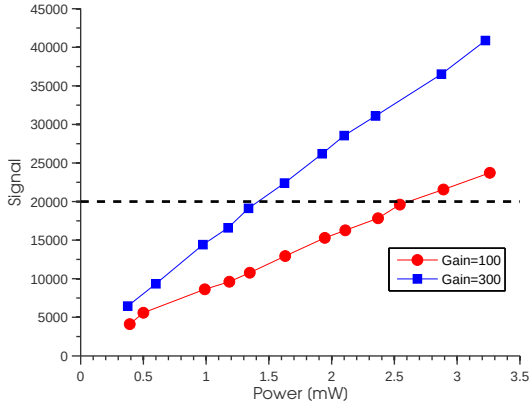

Figure 3.4: Signal returned by the EMCCD vs excitation light power at the entrance of the microscope with camera gain=100 and camera gain=300. Response has linear behavior below 20 000 counts.

$$\sigma_I = k_g \sqrt{< I - offset >} \tag{3.1}$$

as exemplified in Fig. 3.5a, for the case of a camera gain = 400 with a low intensity level, where the offset signal is 1 000 counts. The factor k_g was found to be dependent on the gain g and the intensity level. The dependence of k_g versus g is illustrated in Fig. 3.5b. The dependence of k_g upon g could be written by applying polynomial fitting method, as shown :

$$k_g = ag^2 + bg + c \tag{3.2}$$

where $a = -6.78 \times 10^{-6}$, $b = 8.81 \times 10^{-3}$, $c = 1.93$, $R^2 = 0.997$.

This noise relation differs from pure Poisson noise, which is expected since the camera signal is processed after electronic magnification thus inducing more complex noise sources. We will use the eq. 3.2 for simulations in chapter 4.

3.3 Experimental conditions for dSTORM

In the dSTORM acquisition, a strong imaging/deactivation laser (at 639 nm) illumination is applied to the sample. This illumination in addition with the STORM buffer, results in a stochastic switching of the dye between the dark and the fluorescent states [2]. The EMCCD camera acquires the images continuously

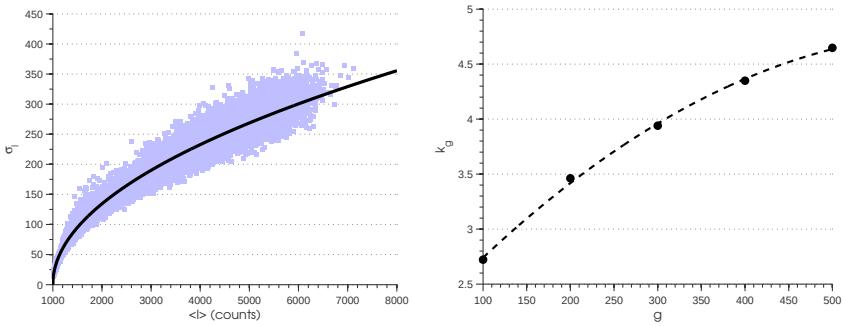

(a) (b)

Figure 3.5: Camera noise analysis. (a) Dependence between the standard deviation σ_I and the mean value of the signal measured on 500 samples $< I >$, for the case of $g = 400$. Square markers: experimental data, black line: fit using the equation $\sigma_I = k_g\sqrt{< I - 1000 >}$, $k_g = 4.3488$. (b) Relationship between the noise factor k_g and gain g. Round markers: experimental data, Dashed line: fit using a polynomial equation $k_g = ag^2 + bg + c$.

in order to obtain a "STORM movie" which will be used for super resolution reconstruction. As it was explained previously, the detection path is modified with the addition of a wollaston prism, allowing simultaneous and spatially separate acquisition of the emission images polarized in the parallel and perpendicular directions(see Fig. 3.6a).

3.3.1 Optical condition

At first, the optimization of the position and orientation of the wollaston prism is required, as well as a calibration in order to ensure to which polarization excited image corresponds each side of the projection image in the EMCCD camera. This step is important because the intensity of the $\perp$ image is adjusted by a G factor (more details in section 3.4.3), that needs to be properly measured. A check is also needed for ensuring that the excitation polarization is perfectly circular. This is performed using a rotating polarizer at the objective position (objective removed), which should give a constant intensity whatever the polarizer detection. A finer check is performed using a viscous (glycerol) fluorescent solution: the two polarized images should have intensities as similar as possible.

For dSTORM imaging, a first fluorescence image is recorded with low intensity (~ 500 W/cm^2) (below STORM blinking conditions), ensuring the identification of relevant parts of the sample (cells, ...). The intensity is then raised to 5

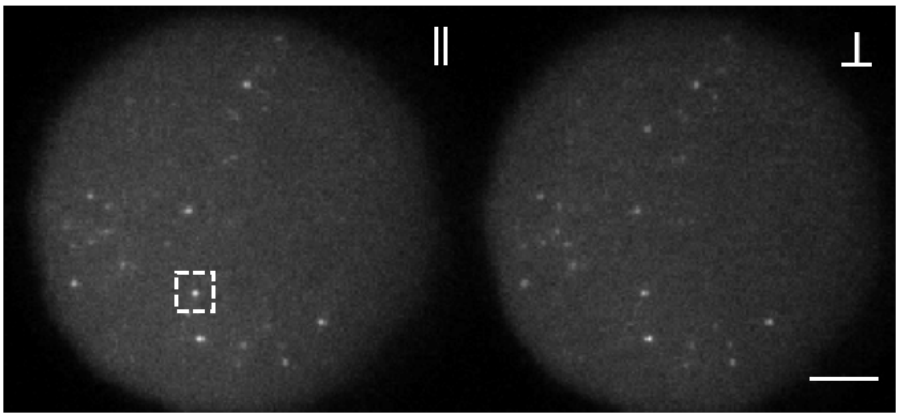

(a) Raw image

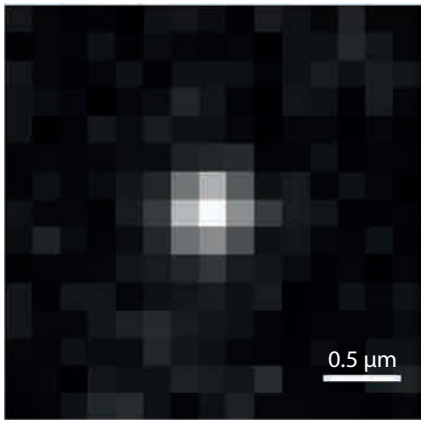

(b) PSF Image

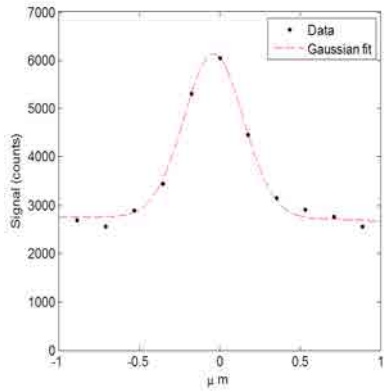

(c) PSF profile and Gaussian Fit

Figure 3.6: Raw image of tubulin labelled with Alexa 647 in a COS 7 Cell. (a) Raw data including emission images polarized along parallel and perpendicular images. Dashed area - window of analysis = 15 pixels. Scale bar: 5 μm. (b) PSF image inside window. (c) Profile of PSF and gaussian fit.

kW/cm^2, which is a typical level to provide a good compromise between signal level and blinking rate. The images are acquired at a rate of 10-30 ms/image, with a total of 4 000 - 80 000 images depending on the molecular density. The total acquisition time is therefore of about 30 min.

3.3.2 Acquisition Software

Camera control and acquisition are performed with the assistance of the software Micromanager [70], a plugin of ImageJ [71] (a Java-based image processing program). Usually, the acquisition parameters are :

1. Exposure time: 30 ms.
2. Gain (STORM images): 100-300.
3. Frames: 4 000-80 000
4. Format: TIFF (16 bits)
5. Initial record is performed in the RAM memory prior to save in the disk
6. Sequence buffer: 8 000 MB

Additionally, one image crop is performed (usually 256x512 pixels) in order to guarantee the minimum transfer delay between the camera and the computer.

Due to characteristics of the STORM technique, one computer with sufficient Random Access Memory (RAM), processor power, adequate operating system and hard drive space is important. Additionally, a STORM movie usually overpasses 5 Gb size, so a 64 bits operating system becomes necessary, as well as a high hard drive space and long-term storage. Settings are changed inside the JAVA platform in order to have the possibility to use the maximum RAM possible in ImageJ, usually 10 000 MB.

The characteristics of the computer used for the acquisition:

1. Processor : Intel® Xeon® Processor E5-1660 (3.3 GHz, 15 MB Cache)
2. Hard drive: 1 TB
3. RAM Memory: 16 GB
4. Operating system: Windows 7(64 bits)
5. Graphics card: NVIDIA Quadro 600, 1GB

Finally, data analysis in localization microscopy techniques is commonly performed off-line, for this analysis one similar computer is used. More details regarding the data analysis will be given in section 3.4 .

3.3.3 Sample preparation

In order to optimize the best experimental conditions for the polar-dSTORM imaging, different protocols have been optimized at mosaic team in Institut Fresnel (PhD work of H. Ahmed in collaboration with J. Savatier). The protocols used for the polar-dSTORM analysis will be explained in detail below, including the dSTORM medium. Buffer solution of the samples were changed with an special "dSTORM" medium (called also "switching buffer" medium) just before dSTORM acquisition. This buffer is composed mostly of MEA to achieve a final thiol concentration of 50 mM, and oxygen scavenging system to remove oxygen. The reducing thiol compound promotes a stable non-fluorescent state (dark state) [69].

DNA labelling

Coverslips were treated using Acetone-methanol-MiliQ water 5 times (5 minutes each), then sonicated in 1M KOH for 30 minutes. Then rinse thoroughly with running MiliQ water, Acetone, and again MiliQ water for 5 minutes each, then dried by blown dry. Cleaned coverslips were coated with poly-L-lysine (PLL; MW 70 000-150 000, Sigma-Aldrich) by adsorption from a filtered 0.1 g/L solution for 1 hour, carefully rinsed with water and blown dry.

Samples were prepared by mixing λ-DNA (500 μg/ml, New England Biolabs) with YOYO-1 (10 μM stock solutions in DMSO, Invitrogen) to obtain 1:20 dye/bp in total volume 150 mL with TE50 buffer (50 mM Tris-HCl, 1 mM EDTA, pH 7.5 (with KaOH)). The mixture was incubated for an hour at room temperature. DNA-YOYO-1 mixture was purified by centrifugation in MicroSpin S-400 HR Columns (GE Healthcare, Life Science). The DNA was thawed and spin-coated onto a PLL-coated cover-slip by dropping 40-80 μL, waited for 30 s then rotated at low speed. The coverslip was then rinsed with 4 mL of ddH_2O at a rotation speed of 6 000 rpm for 1 min to stretch the DNA, and to remove unbound material as an extra purification.

The coverslips with labelled DNA-YOYO-1 were then closed to a Cover-Well imaging chamber (Grace Bio Labs) that contained a switching buffer (50 mM mercaptoethylamine (MEA), Sigma-Aldrich), and an oxygen scavenging system (0.5 mg m/l glucose oxidase, 40 μg m/l catalase and 10% (w/v) glucose, Sigma-Aldrich) .

The absorption (λ_{abs}) and emission(λ_{em}) maximum wavelengths of YOYO-1 are 491 nm and 509,respectively.

Actin and Microtubules

Cell culture. All experiments were carried out on fibroblast-like COS 7 cells (African green Monkey kidney, SV40 transformed, ATCC CRL 1651). COS 7 cells were grown in an incubator at 37° and 5% CO_2 in Lab-Tek chambers (Nunc, Rochester, NY) in DMEM (Dulbecco's modified Eagle's medium) (Gibco, Saint Aubin, France), pH 7.25 plus 10% fetal calf serum (FCS), 1% sodium pyruvate, with 4 mM L-glutamine, for 12-24 h before the experiment.

Labeling actin with phalloidin-Alexa Fluor 488 in fixed cells. Cells were washed briefly with 1 mL of pre-warmed (37°C) PBS, and followed by fixation with 4% PFA in PBS for 10 minutes at room temperature (20°C). After washing the cells with PBS (3 times, 5 minutes per each), cells were permeabilized with 0.5% Triton ×100 (v/v) in PBS for 10 minutes. They were washed again with PBS twice, 5 minutes per each, and then saturated with 5% BSA (w/v) in PBS for 30-60 minutes at $4°C$. Actin filaments were labeled by adding phalloidin-Alexa Fluor 488 (Invitrogen), diluted in PBS to a final concentration of 0.5-0.7 nM. The sample was wrapped with aluminum foil to protect from light. Incubation was done overnight at 4°C. Phalloidin solution was then exchanged by 0.1% (v/v) Tween-20 in PBS in each chamber and incubated for 5 min at room temperature (20°C), two times. Samples were stored at 4°C in PBS until imaging.

The absorption (λ_{abs}) and emission(λ_{em}) maximum wavelengths of Alexa 488 are 495 nm and 519 nm ,respectively.

Labeling actin in vitro. Two protocols were used:

(1) G actin-Atto 647 (Hypermol, Bielefeld, Germany) was recycled as followed: adding of 100 μl of water to 100 μg of G actin-Atto 647, then adding 20 μl of 60 μM unlabelled G actin, and 40 μl of G buffer (5 mM of Tris Cl- high-pH 7.8, 0.2 mM of ATP, 0.1 mM of $CaCl_2$, 1 mM of DTT and 0.01% of NaN_3, kindly supplied by MF Carlier, Laboratoire d'Enzymologie et Biochimie Structurale, Gyf-sur-Yvette, France).

To start polymerization, 8 μl of KME (2 M of KCl, 20 mM of $MgCl_2$ and 4 mM of EGTA) were added to G actin for an hour at RT°. Two ultracentrifugation steps were made for recycling. First step was at 400 000 G for 30 mn, and salvage of the bottom (green color) with 150 μl of G buffer, then dialysis against 500 ml of G buffer overnight at 4°C in the dark, to recover G actin. The second centrifugation was at 400 000 G for 30 min with salvage of the supernatant (no bottom) of 20 μM of recycled G actin-Atto 647, kept on ice in the dark.

To make filamentous labeled actin, a solution with 9 μM G actin and 1 μM of G actin-Atto 647 in G buffer was made, and then addition of 5% KME for an hour at RT°. This 10 μM solution was diluted to 1 μM in F buffer (G buffer +

5% KME) and stabilized with 10 μM of Phalloidin and let overnight. An 8-well type II labtek (Nunc, Denmark) was coated with poly-L-lysine, then 200 μl of the final solution were put into a well for 30 minutes. Finally, the well was gently washed twice with F buffer to only keep filaments on the surface. For imaging, another dilution was made to 400 nM in the same buffer space.

The absorption (λ_{abs}) and emission(λ_{em}) maximum wavelengths of Atto 647 are 645 nm and 673 nm, respectively.

(2) G actin was polymerized in F actin and then labeled with Phalloidin-Atto 633 as followed: G actin (Hypermol) at 68 μM, 1.5 ml, kept on ice in G buffer was diluted in G buffer to 10 μM. Polymerisation was done by the addition of 1/20 of KME for 30 mn at RT°. The F actin was diluted 10 times in F buffer (G buffer + 1/20 of KME). 1μM Phalloidin-Atto 633 was added and incubated overnight. Two centrifuges (20 000 G for 30 min) and two washes (F buffer) were then done. F actin Phalloidin-Atto 633 solution was put into poly-L-lysine precoated 8-well type II labtek for imaging, with dSTORM buffer space.

The absorption (λ_{abs}) and emission(λ_{em}) maximum wavelengths of Atto 633 are 629 nm and 657 nm, respectively.

Labeling microtubules with two antibodies in fixed cells. Cells were washed gently with pre-warmed (37°C) PBS, and followed by fixation with 4% PFA in PBS for 10 minutes at room temperature (20°C). The fixed cells were washed in PBS (5 min, 3 times). They were permeabilized with 0.1% Triton in PBS for 10 min. They were saturated with 5% BSA in PBS (blocking buffer, 1 hour at 4°C). They were then stained with the primary antibody against tubulin (2.5 μg/mL mouse anti-β tubulin) for 60 min in blocking buffer. The sample was then rinsed with washing buffer (0.2% BSA, 0.1% Triton 100× in PBS) three times. Goat anti-mouse Alexa 647 was diluted in the same blocking buffer to 2.5 μg/mL, and was added to the sample for 60 min at 4°C. The antibody solution was changed in each chamber with 0.1% (v/v) Tween-20 in PBS for 5 min at room temperature (20°C), twice. A second fixation was done with 4% PFA in PBS for 5 min . Finally, cells were rinsed three times with PBS for 5 min and stored at 4°C in PBS until imaging.

The absorption (λ_{abs}) and emission(λ_{em}) maximum wavelengths of Alexa 647 are 650 nm and 668 nm, respectively.

Amyloid fibrils

Bovine insulin (Aβ1-40 peptide) powder, and Thioflavine-T (ThT), were purchased from Sigma. Insulin was dissolved at a concentration of 2 mg/mL in acid buffer (pH = 2, 20% acetic acid, 100 mM NaCl), then sonicated for 5 min to dissolve the aggregates. Fibrillation process was induced by heating the insulin

solution at $50°C$ during 20 h without agitation. The solution was cooled down at room temperature. Slide-A-Lyzer G2 Dialysis Cassettes (Thermo scientific) was used for removal of insulin monomers. For several experiments, insulin fibrils were further concentrated by removal of supernatant after centrifugation at 15 000 rpm for 30 min. The ThT was diluted at final concentration 1 μM. Equal volumes of ThT and insulin fibrils were mixed to get labeling ratio 1:25 (dye/monomer). The final solution was filled in 4 well type II Lab-Tek to dry, and be ready for imaging. Imaging buffer was added to Lab-Tek at the time of measurement.

The absorption (λ_{abs}) and emission(λ_{em}) maximum wavelengths of ThT are 440 and 490 nm, respectively, when ThT is added to samples containing β-sheet-rich deposits, such as amyloid fibrils [34]. Nevertheless free ThT in an aqueous medium, shows only weak fluorescence, with excitation and emission maxima at 350 and 440 nm, respectively [34].

Switching Buffer

Before imaging "switching buffer" was added. The imaging buffer includes MEA to achieve a final thiol concentration of 50 mM. MEA was stored as a solid at 4°C and prepared fresh as a 1 M stock solution in water with pH adjusted to ~8 with 1 M aqueous KOH. In order to removal oxygen, an oxygen scavenging system was applied: 0.5 mg/ml glucose oxidase, 40 μg ml/l, and catalase, 10% (w/v) glucose.

3.4 Data processing (Software)

The following section is based on a custom detection and analysis scripts written in Matlab and its equivalent Octave. The starting point of this work is a program developed by N. Bertaux (Phyti, I. Fresnel). The goal of the present implementation is to reconstruct a super resolved image of anisotropy at the nanoscale. The acquisition and camera control were realized by Micromanager Software [70].

3.4.1 polar-dSTORM image processing

After optimization of the sample preparation and data acquisition, the next step is the identification of all simple molecules in the recorded frames. The most common way of reconstruction in super resolution techniques based on localization is fitting the obtained data to a two-dimensional Gaussian function. Although the Point Spread Function (PSF) doesn't have exactly a Gaussian shape, it has been proved that is a valid approximation [72]. The program used for this purpose is based on the Multiple-target tracing algorithm (MTT) [73]. The important point addressed by this algorithm in the localization process is the ability to accurately

identify single molecules in a noisy image, which will be called in what follows the "single-molecules detection".

As it was mentioned previously, the recorded frames include the parallel and perpendicular polarized images. Assuming a translation between the two images due to their construction by the Wollaston prism, these two images are expected to be distant by a victor which is the same for all molecules of the image. The knowledge of this vector is thus required for the single molecule anisotropy calculation (see Fig. 3.7). However, since this calculation is performed on molecules which localization is required at the sub-pixel level, it is important that this vector is known at this level of precision. We chose therefore to measure this vector using the existing molecules in the image rather than with a pre-calibration which could differ in precision. However since single molecules have different signal level in the $\parallel$ and $\perp$ sides, the localization precision on both sides can very considerably from one molecule to another. We chose therefore to evaluate this vector over many single molecules to obtain an average which would represent the needed vector with a sufficient precision.

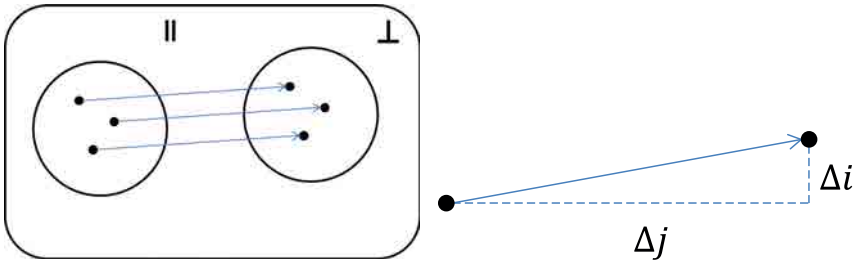

Figure 3.7: Vector determination. (a) Schematic of a recorded frame, showing single molecule spots. (b) resulting vector. The diagonal nature of the arrow is exaggerated and occurs generally only at the sub-pixel range after proper alignment of the Wollaston prism.

In the following, the polar-dSTORM algorithm is presented for the single molecule "detection" and the vector calculation. This algorithm is divided in :

1. Vector Estimation. To obtain a statistical vector estimation, we use the 100-1000 first frames, which is sufficient to acquire typically $\sim$ 50 vector estimations.

2. Pairs identification. To retrieve the molecules pairs of parallel and perpendicular emission images of the full frames (4 000 - 80 000). This will allow the calculation of anisotropy for each molecule of the dSTORM image.

At the beginning of each part, a single molecule "detection" is performed based on the MTT algorithm. This algorithm is based on several essential inputs that will be described more in the next section :

- Initial radius (r_0).
- Spatial sliding window width used for particle "detection" (w_s)
- Probability of false alarm (PFA)

And main outputs:

- Amplitude of signal (α).
- Localization coordinates (i, j).
- Final "radius" estimation (r).
- Localization precision (σ).
- Vector $(\triangle i, \triangle j)$.
- Standard deviation of the noise (σ_{noise}).

One general scheme of polar-dSTORM is presented in Fig. 3.8, including the main inputs for both sides ($\parallel$ and $\perp$). More details will be given in the following descriptions.

Adapted Multiple-target tracing algorithm (MTT)

The MTT algorithm provides efficient detection of the particles: it is able to refine the localization at sub pixel level and to optimize estimation of the PSF radius. As described previously [73], the shape of the image of individual activated fluorophores can be described as the fluorescence signal level S_{i_p,j_p} (in "counts") at the pixel coordinates (i_p, j_p), which can be expressed by [73]:

$$S_{i_p,j_p} = \alpha \times G(i_p, j_p, i, j, r) + m + N_{i_p,j_p}(\sigma^2_{noise}) \tag{3.3}$$

where α is called the amplitude of the signal, G is a bidimensional Gaussian function of the PSF with a center in (i,j) and "radius" r, m is the mean background signal and N models the noise of standard deviation σ_{noise}. The noise will be modelled as a Gaussian noise.

The Gaussian function which represents the PSF shape is expressed as (Fig. 3.9):

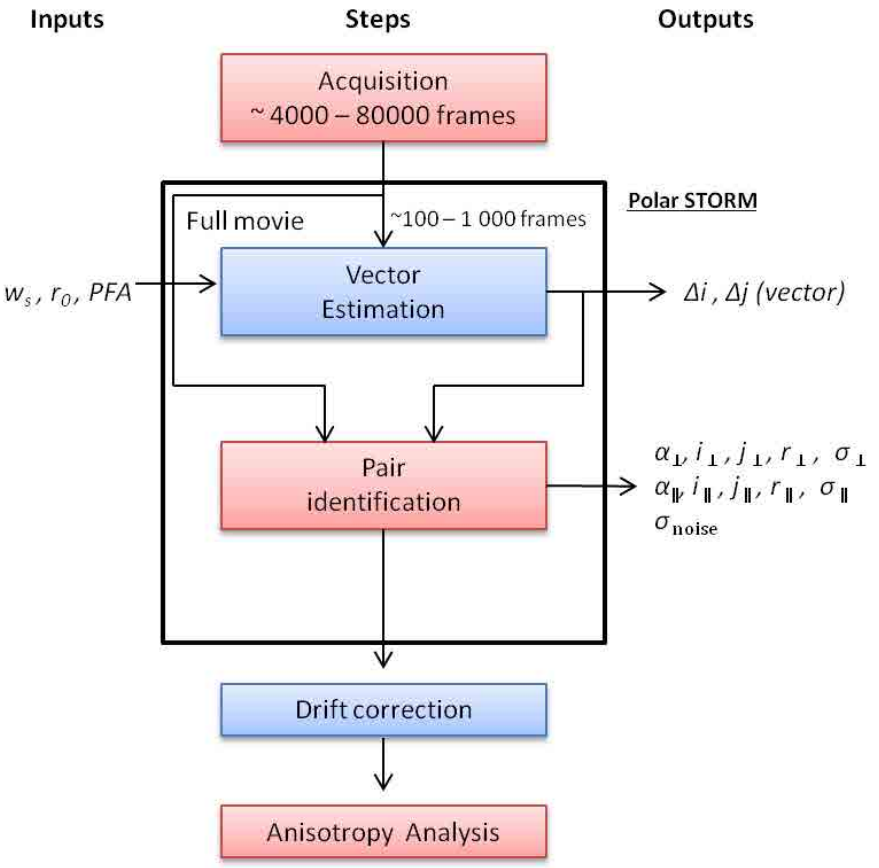

Figure 3.8: Schematic overview of the polar-dSTORM algorithm, including a detailed description of the steps performed in each frame, including main inputs and outputs.

$$G(i_p, j_p, i, j, r) = \frac{\exp^{-\frac{(i_p-i)^2+(j_p-j)^2}{2r^2}}}{\sqrt{\pi}r} \tag{3.4}$$

This function is normalized such as:

$$\int\int G^2(i_p, j_p, i, j, r) di_p dj_p = 1 \tag{3.5}$$

which therefore sets the power of the PSF function to be 1. This means

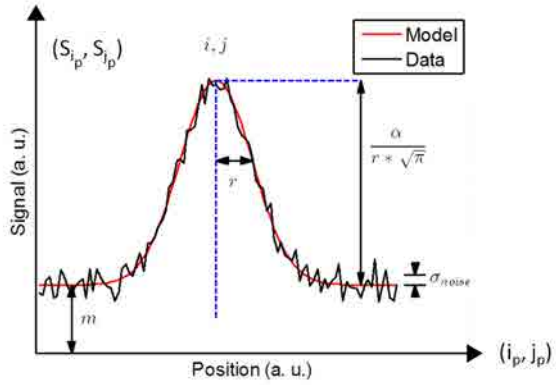

Figure 3.9: Gaussian fitting model describing the parameters used in this work.

that the power level of one molecule signal is accounting for the background substraction:

$$\int\int (S_{i_p,j_p} - m)^2 di_p dj_p = \alpha^2 \tag{3.6}$$

The signal to noise ratio (SNR) will be defined as:

$$SNR = \frac{\alpha^2}{\sigma^2_{noise}} \tag{3.7}$$

The SNR is defined as the ratio of the "signal power" to the "noise power" affecting the signal. This value allows to quantify the quality of the signal, a high ratio implies that the background is less affecting the signal and in consequence the estimation will be easier and more precise. This quantity will be considerer later for the sensitivity of the "detection".

We finally define the intensity of one molecule as the integrated signal with background removed:

$$I = \int\int \alpha G(i_p, j_p, i, j, r) di_p dj_p = 2\sqrt{\pi} r \alpha \tag{3.8}$$

The single molecule "detection" is performed in two parts:

1. "Detection" based on a Generalized likelihood ratio test. This part allows to identify the single molecule candidates for the dSTORM image.

2. Estimation based on a Gauss-Newton fit. This part allows refining the single molecule PSF parameters at the sub-pixel level.

"Detection": Generalized likelihood ratio test. For each frame, an optimal "detection" test is applied to identify the single molecules candidates, based on a generalized likelihood ratio test(GLRT). This statistical test allows making a decision between two hypotheses: particle presence (H_1) or absence (H_0)(see Fig. 3.10).

The raw image is analyzed in a sliding window (w_s) of typical size 11 $\times$ 11 pixels, comparing two different probabilities: particle presence (H_1) or absence (H_0), which are based on mathematical processing operations. This criterion is based on a fitting by a Gaussian of fixed radius $r_0 = 1.3$ (typical for our measurement) and centered on integer (i_0, j_0) pixels value. The hypothesis H_0 implies that the window contains only Gaussian noise with standard deviation σ_{noise} (Fig. 3.10a). The hypothesis H_1 implies that the window contains a PSF centered in (i_0, j_0) with a fixed constant radius r_0 and an amplitude α (Fig. 3.10a). More details regarding to the estimation of H_0 and H_1 are given in [73].

At this point, targets are not identified based by the signal, but by their H1/H0 ratio, where one high ratio indicates that the gaussian amplitude "detected" is significantly higher than the noise level. The accuracy of this decision is determined by fixing a constant false-alarm rate (CFAR), as detailed in the original MTT algorithm [73]. The role of CFAR is to define a threshold limit (calculated empirically based on Monte Carlo simulation [73]), above which any signal can be statistically considered as having a different origin than noise. To guarantee a probability of false alarm (PFA) of less than 1 pixel per image over 512 $\times$ 512 pixels, we define a value $PFA \leq 10^{-6}$. Validation of the MTT sensitivity in Monte Carlo simulated data was performed previously by Serge et al. (2008) [73], showing that the fraction of the "detected" single molecules was close to 100% ($PFA \approx 10^{-6}$) for a signal to noise ratio (SNR) higher than $\sim$ 20dB(see Fig. 3.11). This threshold was similar to the SNR observed in typical experiments of 20-35 dB. One important consideration is that this PFA is independent on the intensity and the background, and in consequence on the experimental acquisition [73].

As result of this step, one binary map including candidates "detected" single molecules is obtained (see Fig. 3.12).

"Estimation": Gauss-Newton fitting. After the candidates particles have been detected by the GLRT algorithm, the amplitude (α), radius (r) and position (i, j) need to be estimated (at subpixel scale) for each identified molecule. Optimization is performed by a Gauss-Newton method in a Maximum likelihood (ML) estimation. One multiparametric Gaussian fit on the signal intensity (see

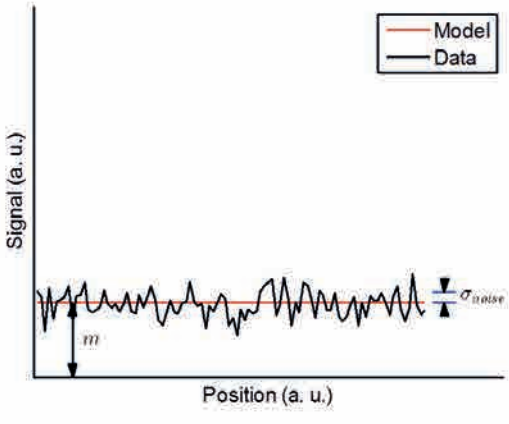

(a) H_0. No particle

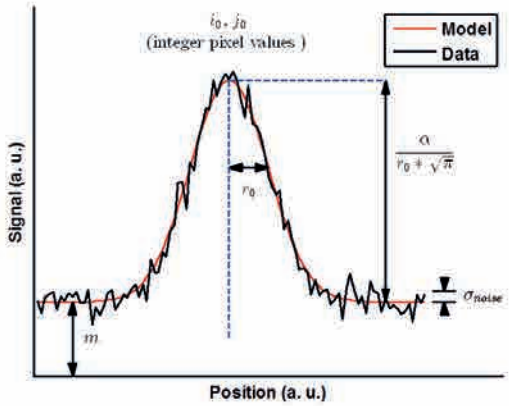

(b) H_1. Particle presence

Figure 3.10: Particle "detection" principle. A GRLT compares two hypotheses. (a) In hypothesis H_0, the window contain only Gaussian noise with standard deviation (σ_{noise}) and mean offset (m). (b) In H_1, the window contains a centered Gaussian PSF in (i_0, j_0 - Pixel Integer values) with a fixed radius r_0

eq. 3.8) is realized in order to optimize the parameters α, r, i and j in appropriate way, based on a Gauss-Newton regression. The previous parameters r_0, as well as the position (i_0 ,j_0) obtained by GRLT are considered as initial parameters of

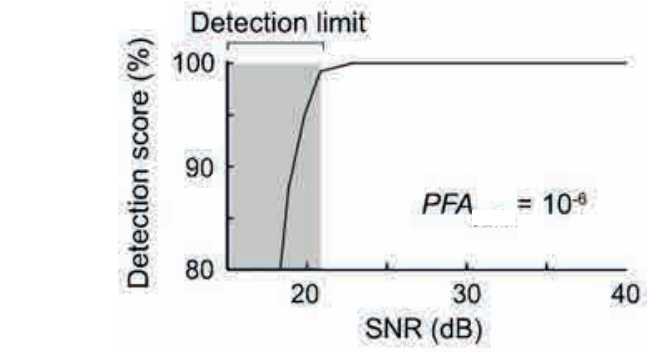

(a)

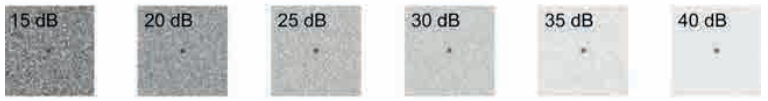

(b)

Figure 3.11: Performance of "detection" GLRT. (a) Percentage of detected peaks relative to theoretical gaussian density, according to SNR. (b) Images corresponding a Monte Carlo simulations with varying SNR (Image size= 100×100 pixels, $PFA = 10^{-6}$) [73]

the regression. Later the positions obtained will be filtered, removing aberration events (negative intensities or positions out of the sliding window).

Finally after both "detection" parts, the output will include the optimized radius (r) and the position (i, j)) at the subpixel scale, in addition to the amplitude of the signal (α). In addition, the localization accuracy (σ) is estimated.

For each parameter optimized (amplitude(α), radius(r) and position(i, j)), the Cramer-Rao bound (CRB) limit is computed following the approach developed by A. Serge et al.(2008) [73]. The CRB permits to estimate the theoretical lowest error expected for each gaussian parameter (amplitude(α), radius(r) and position(i, j)). For the case of the position parameters (i, j), this error will be referred as the positional accuracy (σ). Assuming a symmetric PSF, the values of the error will be the same for i and j positions.

The validity of the optimization performed by the Gauss-Newton fitting, as well as the reliability of the localization precision (σ) based on the CRB were analyzed based Monte Carlo simulations (Fig. 3.13) with varying SNR (10×100 pixel images, at $PFA = 10^{-6}$) by A. Serge et al. (2008) [73]. As it is shown

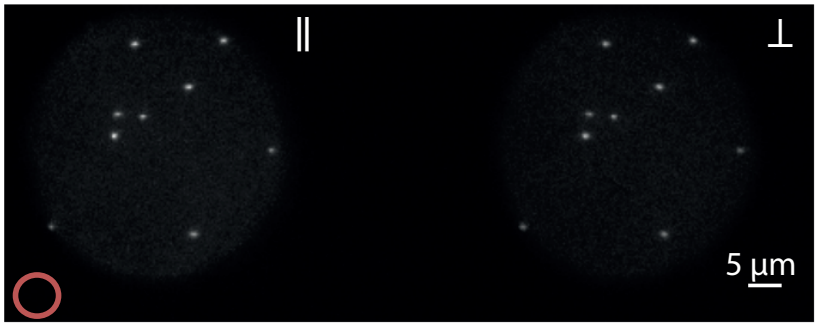

(a) Raw data

(b) Binary map after GLRT

Figure 3.12: Map result of GLRT. (a) Single frame of a dSTORM movie (Sample: fluorescent nano-beads of 20 nm on a coverslip). (b) Final binary map obtained as the result of the GLRT, pointing as circles the center of the candidates detected single molecules.

in the Fig. 3.13, the localization precision estimated (σ) is optimal for SNR higher than 20 dB, since it perfectly fits with the CRB theoretical curve. As a comparison, a three-point estimator, proposed previously to estimate single molecules localization [74], seems not appropriate for SNR lower than 30 dB. In addition, signal integration by the EMCCD pixels (not included in the model) had a small effect on location precision [75].

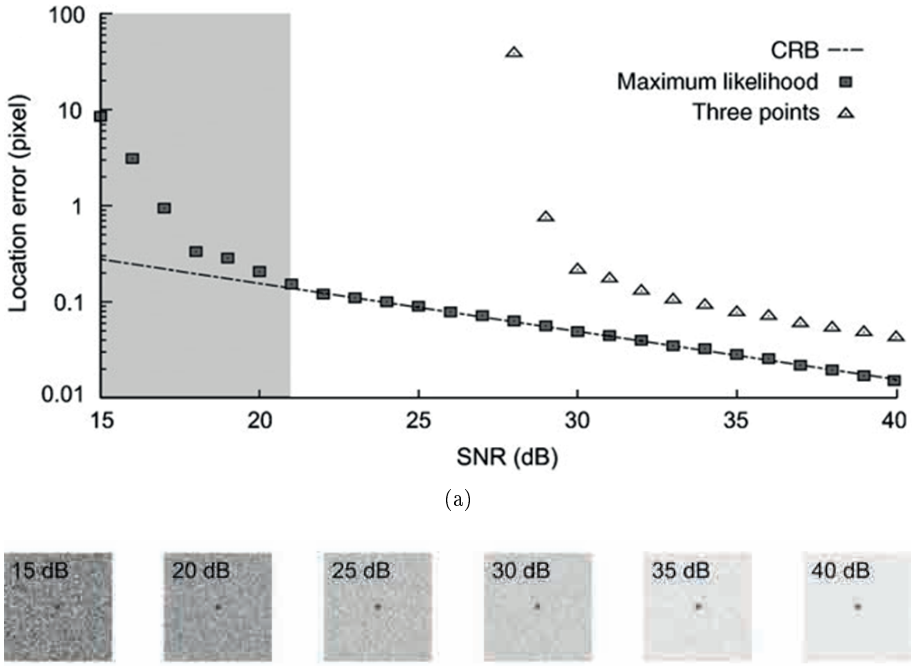

Figure 3.13: Performance of "estimation" Gauss-Newton fit in a simulated data by A. Serge et al. (2008) [73]. (a) Maximum-likelihood practical localization error for increasing SNR, as compared with the three-point estimation and the theoretical accuracy calculated based on the CRB . (b) Images corresponding a Monte Carlo simulations with varying SNR (Image size= 100×100 pixels, $PFA = 10^{-6}$)

Vector estimation

As mentioned previously, the acquired dSTORM images include the parallel and perpendicular polarized images with the assumption of a global translation between the two images. The main objective of this first part of the polar-dSTORM algorithm is to obtain a vector estimation that represents this translation between the two images (Fig. 3.14). In order to obtain this vector a statistical analysis is performed in a subset of the full frames of the STORM movie (usually 100-1000 frames).

As an initial stage of this analysis, the "detection" of single molecules using

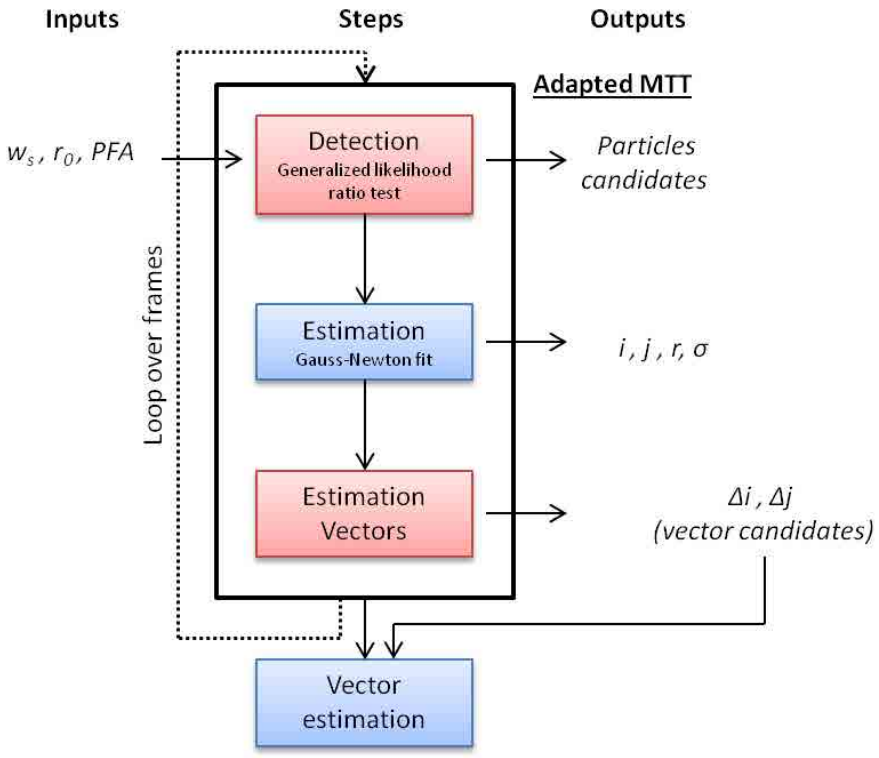

Figure 3.14: Detailed schematic overview of the adapted MTT for **vector estimation**, including inputs and outputs.

the adapted MTT algorithm described previously is realized in the first 100 or 1000 frames of the STORM movie. Then the vector estimation is performed as follows. First the distance between the right and left events are calculated for each of the frame. The events are the Gaussian centers determined by the "detection" scheme (GRLT, see above). As mentioned above, some events will be less reliable because of a low intensity level, for this reason, a statistical approach is required or pairing between two different molecules because of events proximity (see Fig. 3.15).

To obtain the best vector candidate, the algorithm will look for similar directions, assuming a problem in 2D; we consider a solution seeking for vectors of similar norms. To perform this, all the possible norms between right and left events are calculated. Then all the differences between all the norms are calculated. This leads to a statistical distribution which standard deviation is σ_{norm}.

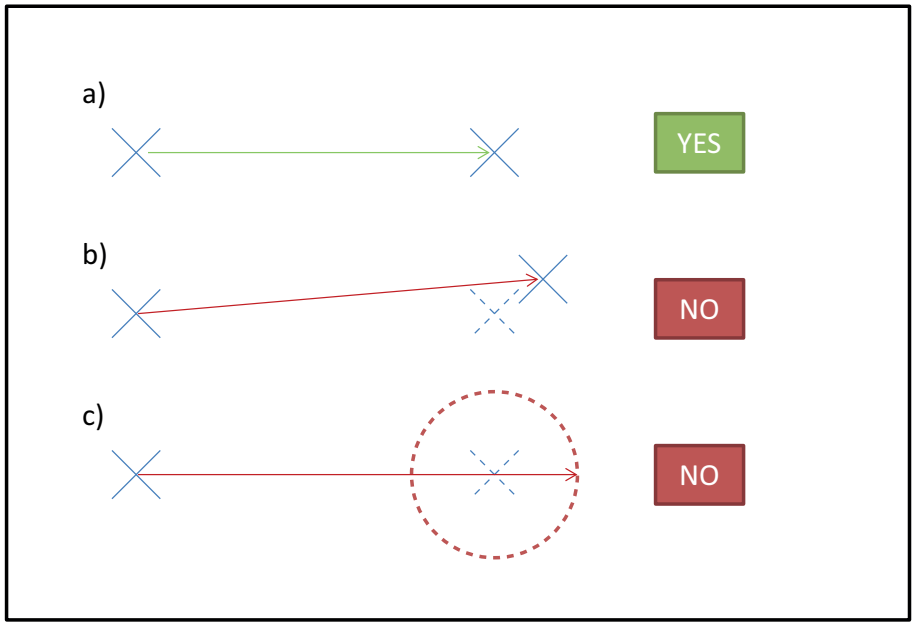

Figure 3.15: Vector estimation: possible situations. (a) Both molecules are well detected and the candidate vector is well calculated. (b) One of the intensities is too low and another close by molecule has a different intensity (different anisotropy). The vector is calculated based on the wrong couple, so this couple should be discarded. (c) One intensity is too low and in consequence the vector is not calculated due to low probability of molecule presence.

Then norms are divided in groups with similar values: each group contains only molecules pairs which vector norms are different at less than $4.2\sigma_{norm}$ (assuming that the difference between norms follows a Gaussian distribution, this value guarantees a 95% confidence level to have similar directions). Then we select the group with the maximum of similar directions (Fig. 3.16). Additionally, to guarantee a sufficient statistics ensuring a correct estimation, we consider only groups for which the minimum number of similar vectors is 3.

In order to define the final candidate vector to be used in the anisotropy estimation, the median of the vectors contained in the previously selected group is calculated in at least 100 frames. This ensures at last 30 vectors estimations. The candidate vector of a single frame is shown in Fig. 3.17.

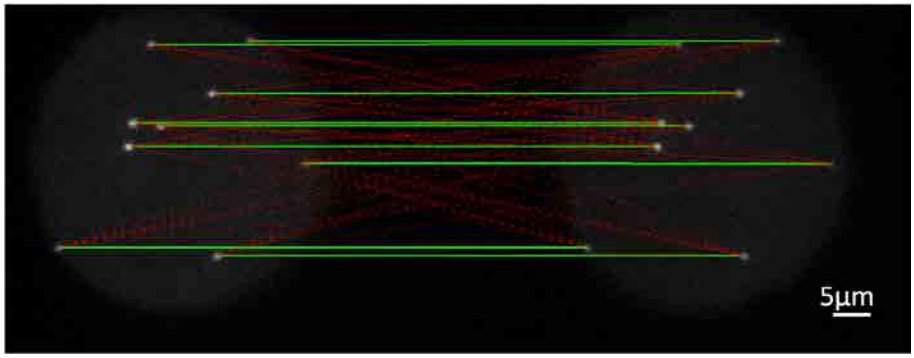

Figure 3.16: Selection of the norm candidate for a single frame. Red dashed line: all possible norm combinations. Green line: selected group of the most similar norms.

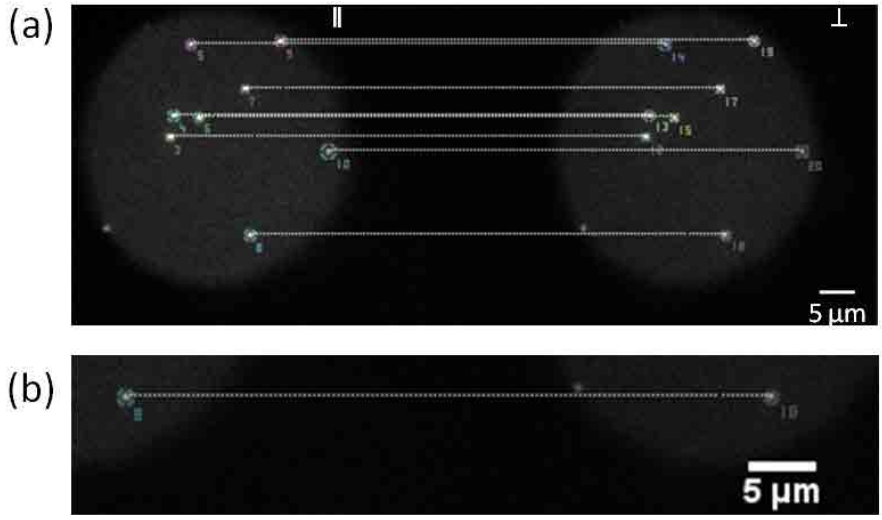

Figure 3.17: Definition of the final vector candidate. (a) One vector candidate is calculated for each frame of the STORM movie using the "Vector Estimation" part of the algorithm. The localization precision is represented as a dashed circle around the particle detected (a factor $\times 50$ is used to make it more visible). Sample: Fixed beads on coverslip. (b) Zoom on the vector candidate.

Pairs identification

After the mean vector is calculated, the next step is the final estimation of the center $(i_{\parallel}, i_{\perp})$, $(j_{\parallel}, j_{\perp})$, radius $(r_{\parallel}, r_{\perp})$, localized precision $(\sigma_{\parallel}, \sigma_{\perp})$ and ampli-

tude ($\alpha_{\parallel}$, $\alpha_{\perp}$) of each molecules pairs detected in the full STORM movie. In this part of the algorithm, the "detection" and "estimation" steps(see above) will be realized in all the acquired frames (see Fig. 3.18).

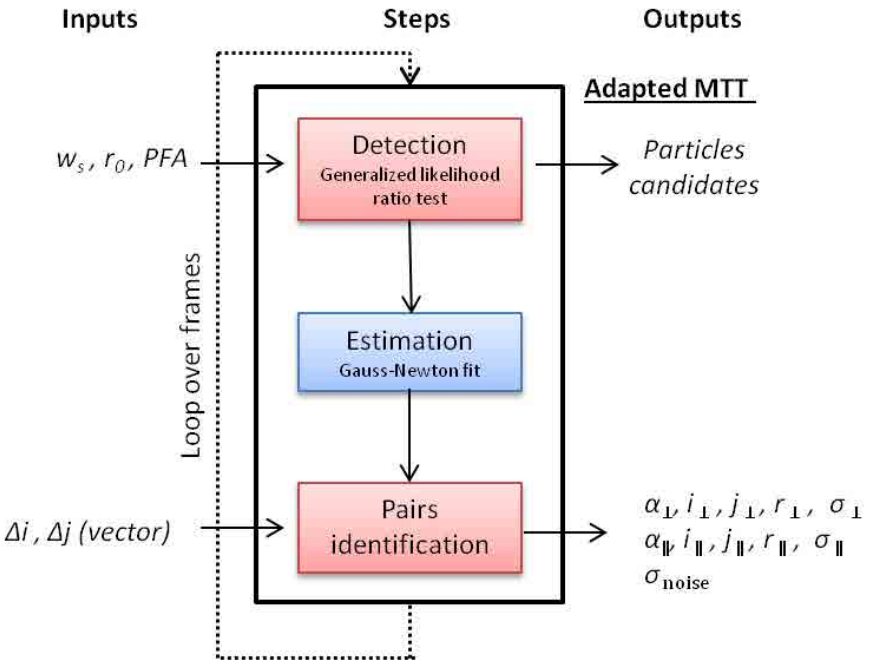

Figure 3.18: Detailed schematic overview of the adapted MTT of **pairs identification**, including inputs and outputs.

For each identified molecules on the "left" image ($\parallel$), it's "right" corresponding image ($\perp$) will be coupled by selecting the nearest neighbor to the expected position (at a vector distance from the left image). In order to ensure the validity of the pair found, the error (difference between the images distance and vector) $= [(i_{\perp} - i_{\parallel}) - \Delta i] + [(j_{\perp} - j_{\parallel}) - \Delta j]$ must be less than $2.4 \times \sqrt{\sigma_{\parallel} + \sigma_{\perp}}$ (assuming this difference as a Rayleigh distribution, this threshold value guarantees a 95% confidence level (see Fig. 3.19). A similar step is done starting from the right image molecules estimation to ensure that all couples are considered.

After this pairing step, the output will include the radius and the position of identified molecules $\parallel$ and $\perp$ images (at the subpixel scale), in addition to the amplitude of this signal (α), background variance and localization accuracy. For the purpose of anisotropy calculation, the integrated intensity I (eq. 3.8) rather than the amplitude α is required. We therefore calculate $I_{\parallel}$ and $I_{\perp}$ which depend

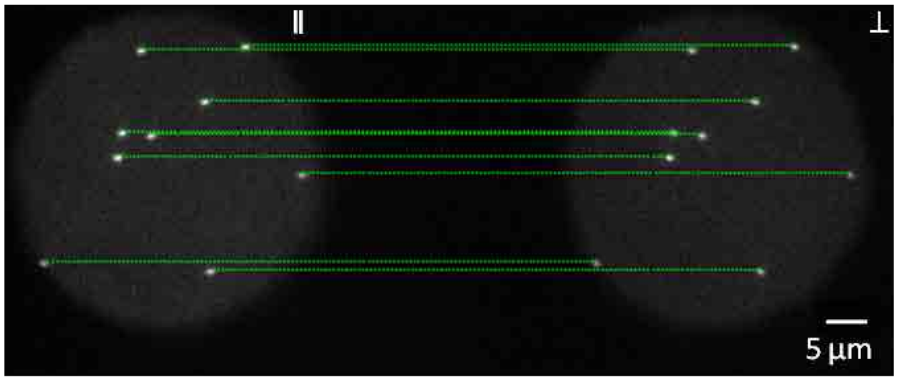

Figure 3.19: Pairs identification. Pairs of parallel and perpendicular images are identified in a single frame of a STORM Movie, based on the vector previously estimated (green line) Sample: fixed beads on coverslip.

on ($\alpha_{\parallel}$,$r_{\parallel}$) and ($\alpha_{\perp}$,$r_{\perp}$) (see Fig. 3.20).

Figure 3.20: Final output of the polar-dSTORM algorithm for an identified pair of molecules. The localization precision is represented as a dashed circle around the particle detected (a factor $\times 100$ is used to make it more visible). Sample: fixed beads on coverslip). Scale bar: 2 μm.

Comparison with previous approaches

A method called Polarization Fluorescence Photoactivation Localization Microscopy (P-FPALM) had been proposed previously to calculate the anisotropy at nanoscale [7], the method is described as follows. Acquisition in this method is performed in

similar way than polar-dSTORM: the setup includes a polarization beam splitter which allows the simulations recording of two polarized emission images, parallel ("T" image) and perpendicular ("R" image), in a single raw frame. The excitation polarization is however set to be linear which makes only sub-set of molecules (with excitation polarization detection) to be excited. The image analysis is quite different from ours. First, the P-FPALM method calculates the coordinate transformation from the left to right image (corresponding to our vector) based on a prior calibration step using cross-correlation in a nano-beads sample. Then this coordinate transformation is performed in the R image (R being changed into R') to overlap the images. This manipulation is done at the pixel level, limited by the resolution of cross correlation. Later on, the signal from both images are summed and then analyzed using standard FPALM single molecule localization routine [59], only for localization purposes. This leads to identified molecules that can be further processed for anisotropy calculation: images T and R are least-squares fitted using a two-dimensional Gaussian with center position, "fix radius", and amplitude as fitting parameters. Amplitudes α_T and α_R corresponding to the peak intensities in the T and R images, respectively, are finally used to calculate the anisotropy ratio with(See Fig. 3.21):

$$A = \frac{\alpha_T - \alpha_R G}{\alpha_T + 2\alpha_R G} \tag{3.9}$$

In comparison with this P-FPALM method, the polar-dSTORM algorithm offers an advantage regarding the coordinate transformation, since the paring is realized at molecular level for each experiment, without a precalibration experiment. In addition, the sum can be affected if we consider that the images T and R', are susceptible to different distortions, including ellipticity due to probe orientation [66]. As well due to these distortions and possible different planes between the molecules, one radius optimization is necessary in the 2D gaussian fit. In this sense, the "Intensity" as the integral of the gaussian fit, with the center position and "radius" optimization will give a more precise anisotropy calculation than a simple gaussian fit with only the center position and a fixed initial "radius" [59, 76].

3.4.2 Post-processing

Two additional refinements are included after the polar-dSTORM images are obtained: first, isolated events of localization originating from noise or non-specific localization can survive to the ditection/estimation algorithms. second, the STORM technique implies a long time of acquisition and in consequence one method to correct for the lateral drift must be implemented.

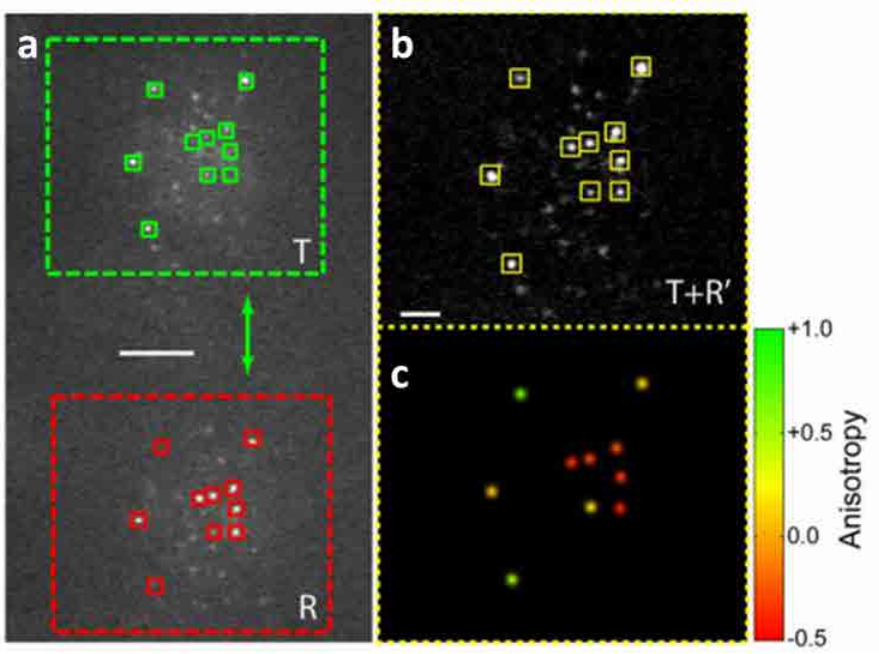

Figure 3.21: P-FPALM Example. (a) Single frame from a P-PALM image series of Dendra2-actin expressed in a fixed fibroblast including detected emission parallel (T image) and perpendicular (R image) to the incident polarization (arrow). Scale bar: 5μm. (b) Sum of the T and R' (R translated) images for localization purposes. Scale bar: 2μm (c) Localized molecules (squares in b) are plotted as Gaussian spots and the color indicates the anisotropy calculated. (Taken from [59])

Filtering of low-density events

In order to guarantee the validity of the localizations acquired, a filtering process is performed. This screening is realized identifying scattered localizations with low local molecular density, which can appear due to regions of reduced labelling densities, cellular autofluorescence and non-specifically bound proteins present in the background. These low-density localizations are filtered-out by removing them, with the criterion that "low-density" means < 3 localizations identified in a region of 50 nm $\times$ 50 nm.

Lateral drift correction

Due to the long acquisition time (20-40 min), thermal changes and mechanical perturbation of the microscope and sample holder can induce a sample lateral drift. This drift can be corrected using different methods including tracking of fiduciary markers [60], as well as using the measured structure shape itself to compensate for shape distortions [77].

Fiduciary markers are typically gold nanoparticles, quantum dots or fluorescent beads. Because they do not bleach considerably during the long acquisition time, they allow to track the drift, and to correct in real time sub-pixel size localizations. The inconvenience of this method is that it introduces extra steps of sample fabrication and artificial markers into the sample, furthermore these markers have to be located at the same depth in the sample as the investigated structures which can be cumbersome to obtain.

Since the shape of the structures imaged in the sample is not expected to change significatively during the acquisition, the structure itself can be used to determine the spacial shift between subsequent images, using cross-correlation [78].

Assuming a linear behavior of the lateral drift inside sub-stacks of images [78], the correction of this drift can be performed using the localization themselves. In this case, the data are subdivided into sections corresponding to different portions of the main stack of images (e.g. the STORM images reconstructed from frames 0-1000, 1001-2000, etc.).

Each sub-stack is processed generating a STORM image and then performing a cross-correlation of this image with the STORM image of the initial sub stack (0-1 000), resulting in a map of displacements along the X and Y axes between sub-stacks [79]. Then a "drift versus number frame" plot is deduced and interpolated for all the frames in each sub-stack. Finally, the drift estimated from the plot is subtracted for all STORM localization position along both X and Y detections. In addition, the user can select the range of frames where the cross-correlation method is expected to be more effective. The process is illustrated in the following diagram presented in the Fig. 3.22.

Fig. 3.23 illustrates the improvement of the drift correction algorithm for the case of Tubulin fibers in COS 7 Cells. The typical drift measured in our set up is about 150 nm along X and 200 nm along Y over 10 000 frames (typically 10 min).

3.4.3 Anisotropy analysis

After the polar-dSTORM analysis and refinements (explained in the previous section), the anisotropy ratio image (A) is calculated for each identified pair as the ratio described previously:

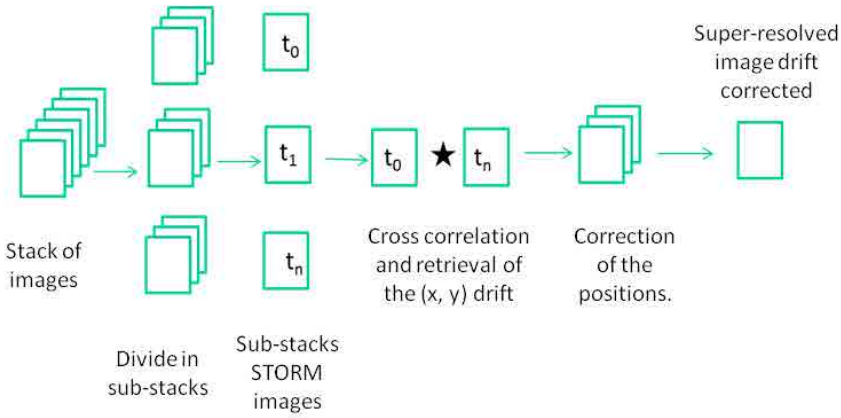

Figure 3.22: Basic scheme of the lateral drift correction

$$A = \frac{I_{\parallel} - I_{\perp}}{I_{\parallel} + I_{\perp}} \tag{3.10}$$

where $I_{\parallel}$ and $I_{\perp}$ are the intensities (signal integrated over the PSF) for both $\parallel$ and $\perp$ channels for one molecule. This equation is valid only if the detection efficiency is the same in the $\parallel$ and $\perp$ channels.

Detection calibration factor

Possible differences of detection efficiency between the parallel and perpendicular channels can be due to the diattenuation factor of the dichroic mirror, as well as the imperfection of the Wollaston prism. They are systematically detected by comparing intensities measured in a 10 μM water solution of fluorescent molecules appropriate for the used excitation wavelength, that is assumed to be isotropic, due to its fast molecular rotational dynamics. This ratio is expressed as:

$$G = \frac{I_{\parallel}}{I_{\perp}} \tag{3.11}$$

This ratio (usually between 1 to 1.6) is taken into account by rescaling the intensity of the appropriate detected image before further data processing:

$$A = \frac{I_{\parallel} - GI_{\perp}}{I_{\parallel} + GI_{\perp}} \tag{3.12}$$

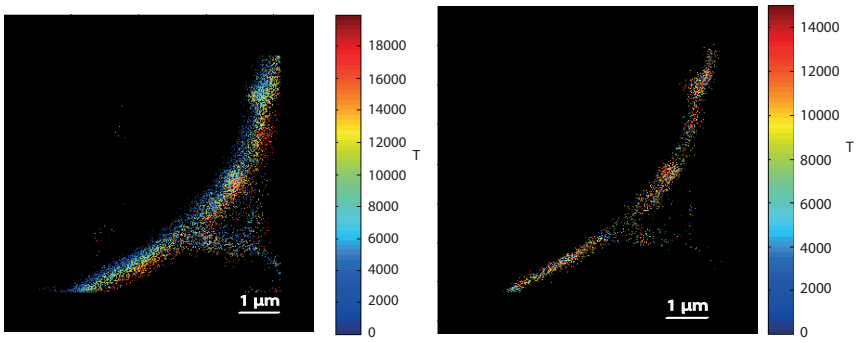

(a) (b)

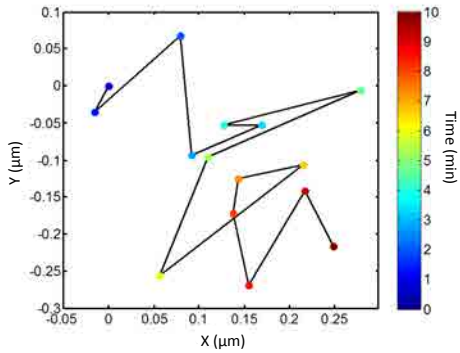

(c)

Figure 3.23: Drift correction performed in tubulin in COS 7 cell labeled with Alexa 647, (a) Reconstructed image before correction. (b) Reconstructed image after drift correction. (T=Frame number). (c) X vs Y displacement in function of time.

Events selection

At last, the precision obtained at the estimation of the anisotropy A depends on the intensity level in both $\parallel$ and $\perp$ channels, which also governs the localization precision. Depending on the precision required on A, an additional filtering will consist in rejecting molecules for which $I_{\parallel}$ and/or $I_{\perp}$ is too low, or molecules for which the localization precision is too different in the $\parallel$ and $\perp$ channels. This analysis is described in Chapter 4.

3.5 Final Display

After the sample preparation, polar-dSTORM recording and detection, the last step is the reconstruction of the final polar-dSTORM image. In order to facilitate the analysis and interpretation of the anisotropy values, two different renderings are proposed, the first one including the anisotropy from the detected events in the algorithm described above (after filtering) and the second one including all the events positions from the parallel detection image. In order to have a full spatial representation of the anisotropy values including the super resolution structural information, a combination of both of them is proposed.

3.5.1 dSTORM Image

The dSTORM detection algorithm produces two main lists of positions, the first one including all particles detected and the second one containing the couples of particles detected in the parallel and perpendicular detection images.

In order to transform this list in a high resolution image, these positions have to be rendered. The most common rendering approach is to represent localizations as Gaussian peaks with a width related with the theoretical localization precision [80]. Apart of these methods, Baddeley proposed other two optimized image rendering approaches [81], the first one based on adaptive histogram and another based on Delaunay triangulation. For this project we decided to select a simple rendering based on a pixelized representation of the detected events. A zoom permits to select the number of events to bin to produce the final rendering (typically "Zoom 5" means that a represented pixel size is 1/5 of the real size of a CCD pixel in the sample plane). The localizations are then visible in a grid which size depends on the zoom selected.

While the rendering using Gaussian blurring localization density representation, histogram equalizations, or any other enhancing filtering can significatively ease the visualization of the results, they can also hide the quantitative information of intensity level for instance, which govern the precision of the retrieved information. In this sense, the rendering can help for the interpretation of image-based microscopy and structural analysis, whereas the pure representation of localizations is more useful for quantitative approaches [82], such as the anisotropy imaging presented this work where each molecule needs to be represented with its specific anisotropy.

3.5.2 Anisotropy Image

In general, the second list contains less events than the first one, due to the restrictions mentioned above (vector selection and filtering). In order to visualize the anisotropy estimation as well as the structural information from a pure

STORM analysis, we include in the anisotropy image, a background mask of the reconstructed image containing all the points detected on the right image (see Fig. 3.24). In addition, the full super resolved image is also rendered using a gaussian blurring based on the mean localization precision of the events.

Regarding the anisotropy rendering, if there are more than one molecule per sub-pixel for specific zoom, the anisotropy reported in this pixel is the average between the molecules anisotropy inside of this pixel.

Although, the anisotropy rendering image offers a very useful tool to analyze the orientational behavior of the molecules spatially, statistical tools such as histograms can offer a good overview regarding the order behavior in one specific region or in the full sample. In the region analyzed, the histogram shape as well as the mean anisotropy $< A >$ as well as its standard deviation σ_A will be systematically given. Chapter 4 details in particular how this information can be related to the dynamical and constraint behavior of molecular orientations.

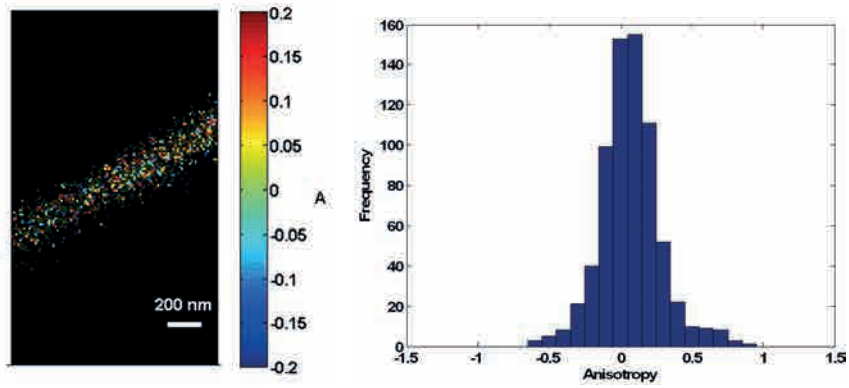

(a) (b)

Figure 3.24: Anisotropy STORM Image. (a) Super-resolved image (Sample: tubulin in a COS 7 cell labeled with Alexa 647. Color scale - the anisotropy map (events: 700). Opaque-green - Full super resolved image (events: 900)). (b) Anisotropy histogram.

3.6 Fiber morphology analysis

One of the most important application of localization microscopy techniques is the study of nanoscale morphology of filaments or fibers inside biological sample such as cells, including actin stress fibers [2], microtubules [77] and amyloid fibrils [83].

In the case of oriented media (for instance membranes or fibers), in which molecules are angularly constraint along a fiber axis (or membrane normal direction), the anisotropy depends on the orientation of the sample itself [84]. As described previously (Chapter 2), a cone distribution is used as a model for this constraint (see Fig 3.25), and the anisotropy of a single molecule will be representative of both the mean orientation of the cone (ρ) and the angular constraint (ψ) obtained by a time average over the CCD integration time (10-30 ms). The relation between A and the orientational order (ρ,ψ) will be detailed in Chapter 4.

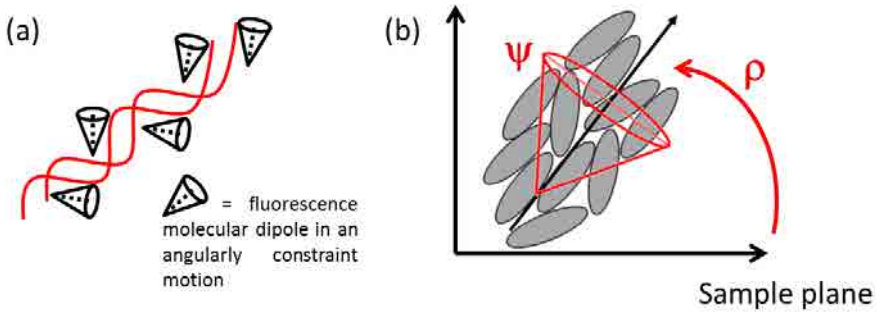

Figure 3.25: Model of molecular orientation. (a) Molecules oriented along a fiber structure resulting in a cone distribution at the sample plane. (b)Constrained distribution defined by a cone of orientation ρ relative to horizontal axis of the sample and aperture angle ψ.

In the examples studied in this work, fiber structure such as actin and tubulin are labelled with fluorophores by a linker more or less rigidly attached to the fiber. It is reasonable to suppose that if there is a cone angular constraint ρ lies along the fiber direction.

It is possible, providing that the local orientation of the fiber is known, to retrieve information on the angular disorder ψ for each measured molecule (see Chapter 4 for more detailed explanation). The first requirement is thus to be able to identify the local orientation of the fiber.

polar-dSTORM combines the possibility to study the local morphology of fiber structures (such as actin filaments, microtubules), as well as the "molecular order" at nanoscale. The fiber morphology analysis of polar-dSTORM is divided in three main parts:

1. Fiber size estimation. This permits to estimate the ultimate reachable

morphological resolution of the fibers (Full Width Half Maximum FWHM). A more refined resolution value is estimated based on the precision of the PSF fitting process.

2. Cluster Analysis. This permits to automatically identify the local orientation of fibers (ρ).

3. A versus ρ and ψ analysis. This permits to identify constraint values defined by a cone model (see Chapter 4).

3.6.1 Fiber size estimation and spatial resolution of the technique

The estimation of the fiber diameter obtained by dSTORM images uses the FWHM (full width half maximum) of pixelized data taken over a profile chosen by the user perpendicularly to the fiber (see Fig. 3.26).

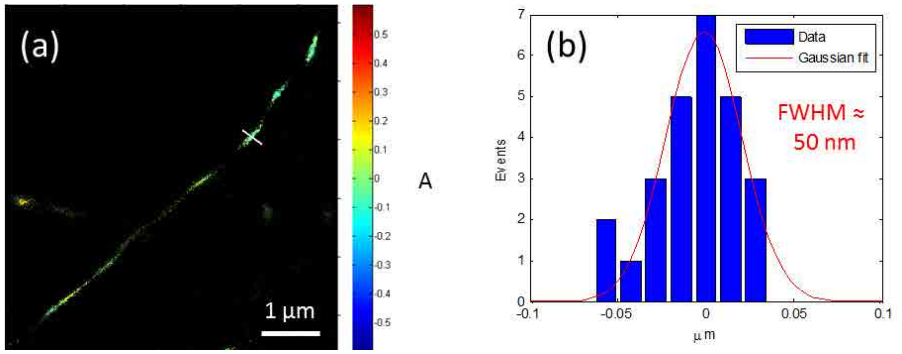

Figure 3.26: Estimation of FWHM. (a) Super-resolved image (Sample: actin fiber in a COS 7 cell labeled with Alexa 488. Color scale - the anisotropy map, opaque-green: full super resolved image, pixel size = 10.7 nm. The profile used for the FWHM estimation is indicated by a white line. (b) Pixelized profile (from white line in (a)) and Gaussian fit (red line).

The full Width Half Maximum (FWHM) has been often used as a measure of the intrinsic imaging resolution, in cluster of localizations [80] or fiber profiles [85]. To determine this resolution, the pixelized profile of the cluster or fiber diameter was fitted by a Gaussian function. The use of this approach to estimate the resolution is however very questionable for different reasons given below: we will therefore only use it as an indication of the gain in resolution obtained over the diffraction limit size.

Due to the characteristics of the STORM technique, the spatial resolution can depend of different factors including: labeling efficiency, density, size of the labeling, photo switching rate, as well as brightness of the fluorophore, and detection efficiency:

- Brightness/detection efficiency plays a very important role in the localization precision of single molecules (see Chapter 4).
- The density of molecules detected can bias the estimated resolution. To understand the importance of this aspect, we can imagine an extreme case where only a very small number of molecules label one fiber. Even with a nanometer precision, a reconstructed STORM Image will only rely on a few localizations and therefore will not be representative of the real structure, due to the limited sampling frequency [58].
- The labelling density and efficiency needs to follow the Nyquist criterion, which implies at least two measurements per resolution unit [86, 87]. For example, if one resolution of 50 nm is calculated for a STORM experiment, the molecules should have to be apart by a maximum of 25 nm, in order to satisfy the Nyquist density requirement. This is not a problem for typical densely labeled structures, however, in the case of the anisotropy measurement, low density can be achieved after the selection algorithm described above. Fig. 3.27 (from Shroff *et al* 2008 [88]) shows the main influence of the density of localized molecules versus the resolution.
- The size of the probe can affect the resolution: a small labelling unit can imply a better labeling efficiency than the bigger labels, because the fluorophore can access easily the targets in the biological environment and give a more representative picture of the labelled structure. The distance between the label and the structure should be also considered.
- The temporal resolution: because to reconstruct one STORM image takes time, there is one inherent trade-off between time and spatial resolution. In order to obtain high temporal resolution, the important factor is the photoswitching rate of the probes [58]. Consequently, the choice of probe is closely related to the desired spatial and temporal resolution.

Different methods have been proposed in order to quantify the resolution of a STORM image, including the localization accuracy and the finite label density [85]. Recently methods to measure the resolution have been proposed including a method based on Fourier ring correlation(FRC), that can be computed directly from the image [89].

Since the objective of our work is super resolution anisotropy imaging rather than detection of specific super-resolved structures, we will rather concentrate on

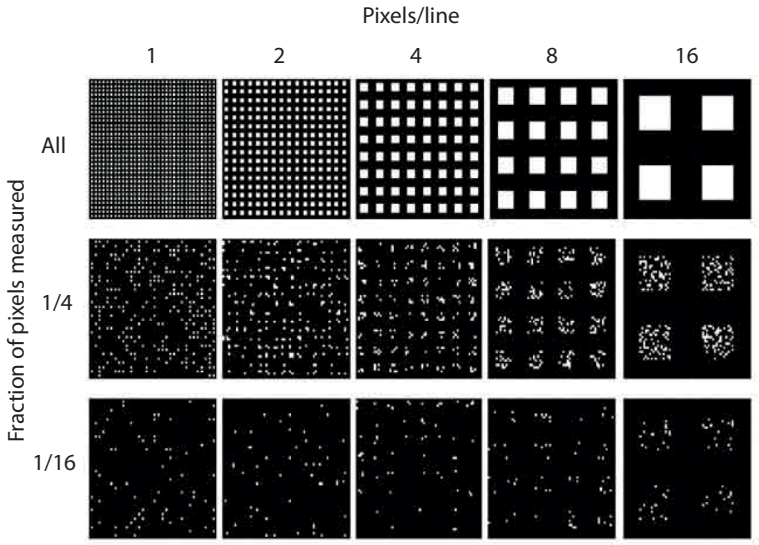

Figure 3.27: Importance of molecular density in localization microscopy. The fraction of pixels measured decreases from the top to bottom and the number of pixels per line increases from left to right. This image illustrates the Nyquist criteria, where one increment in localization precision(pixels/line) implies the need of greater sampling intervals (Taken from: [88]).

localization precision to estimate the super-resolution potentiality of our set up and give numbers of the measured FWHM of fibers when it is appropriate.

3.6.2 Cluster Approach

In order to retrieve the local orientation of fibers in a reconstructed super resolved image, an analysis based on a "cluster" of localizations is performed. Being able to identify clusters with a clear orientation (ρ angle) will allow to retrieve a molecular order information (ψ), based on the "cone" model described previously (see Chapter 4 for more details). In addition, the identification of local clusters will permit to define local regions of statistics on anisotropy (and in particular histogram analysis) to be performed.

Different methods to identify clusters are proposed:

1. Manual selection of clusters. In this case the user selects arbitrarily a region along a fiber.

2. Automatic selection of "isolated" clusters. The algorithm identifies auto-

matically different "isolated" clusters in a super-resolved image.

3. Automatic selection of clusters based on anisotropy value ranges. The algorithm identifies automatically different clusters in a super-resolved image for a given anisotropy range.

Manual selection of cluster

In this approach the selection of the region of the cluster is made directly by the user, as well as the orientation angle (ρ) which is identified by a vector using the Image Processing Toolbox® of Matlab®.

An example of this method in a tubulin fiber of a COS 7 cell is shown in the Fig. 3.28.

Automatic selection of "isolated" clusters

This analysis is performed at sub-pixel level of the super resolved image. For this purpose, one script in Matlab® was programmed, using the Image Processing Toolbox®. Assuming certain discontinuities in the super-resolved image (as in the case of isolated fibers), a cluster selection based on connectivity of sub-pixels can be performed. For the cluster selection, the super resolved image is converted into a binary image. Then the script identifies groups of connected sub-pixels and information from them is retrieved using different commands of the Image Processing Toolbox®, including orientation and the mean pixel value. The input parameters of the script are:

1. Minimum cluster size. A threshold of the number of sub-pixels used for the cluster identification is used for the analysis.

2. Connectivity. Defines the number of neighbor sub-pixels which are considered connected to the central pixel (see Fig. 3.29).

To obtain the orientation of a single cluster, one ellipse is defined surrounding the cluster region (Fig. 3.30). The angle ρ is defined as the angle between the horizontal axis "X" and the major axis of the ellipse. Fig. 3.30 shows how the axes and orientation of the ellipse are defined.

The final output of this script includes the anisotropy mean value of the clusters $< A >$ and the angle ρ. Example of identified clusters following this method in tubulin fibers in a COS 7 cell, are shown in Fig. 3.31.

Automatic selection of cluster based on anisotropy value ranges

In order to identify a cluster with a specific anisotropy value range, similar analysis as described previously is performed.

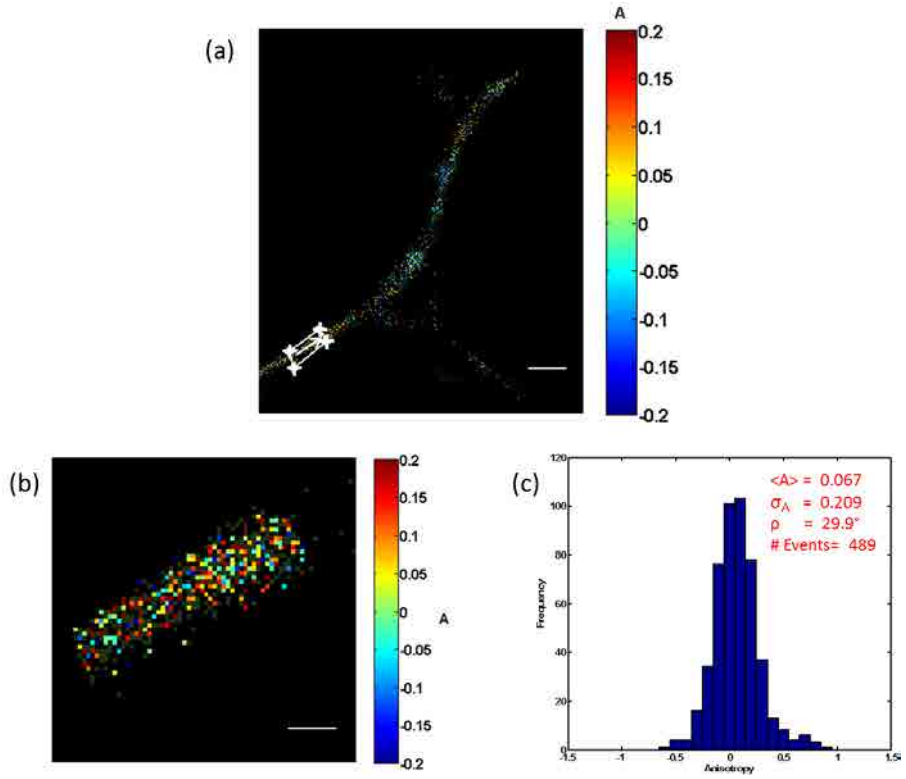

Figure 3.28: Manual selection of clusters. (a) Full super-resolved image. The cluster selected is surrounded by a white line polygon. The ρ selected by the user is represented as white arrow. Scale bar: 1 μm (Sample: tubulin in a COS 7 cell labeled with Alexa 647). (b) Cluster super-resolved image. Scale bar: 200 nm) (c) Histograms of events of selected cluster

First, the super resolved image is divided in different regions based on anisotropy. The anisotropy regions are defined as equal divisions of the full range of anisotropy values (minimum - maximum anisotropy value in the analysis image). Then one binary image is considered for each region. Later on, similar analysis as described previously, is realized in this binary image to detect clusters based on connectivity. Finally, reconnection of all the identified clusters is performed (see Fig. 3.32). The inputs for this program are:

1. Number of divisions: this number is defined by the number of sub-ranges of the anisotropy regions.

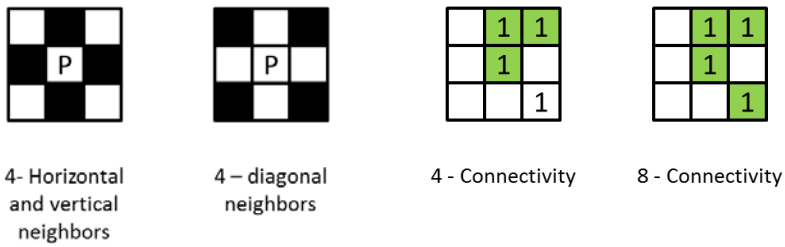

Figure 3.29: Pixel connectivity definition. (a) Pixel relationship, vertical, horizontal neighbors and diagonal neighbors (in black). (b) Example of 4-Connectivity (only considers vertical and horizontal neighbors) and 8-connectivity (considering vertical, horizontal and diagonal neighbors) in a binary image. Green filled: connected pixels.

Figure 3.30: Orientation of a cluster. Red line: defined ellipse, blue lines: axes. [Taken from documentation of Imaging Processing Toolbox of Matlab®]

2. Minimum cluster size: minimum number of pixels for a cluster that is accepted in the analysis.

3. Connectivity: defines the neighbor pixels which are considered connected to the central pixel (see Fig. 3.29).

The outputs are the same as in the previous method.

Note that in both automatic methods, one post-processing cluster selection is necessary. Some of the criteria to discard a wrong cluster are:

1. Occasionally, the orientation calculated by the Image Processing Toolbox® is not adequate, due to a bad angle estimation (Fig. 3.30).

2. Low number of events within a selected cluster.

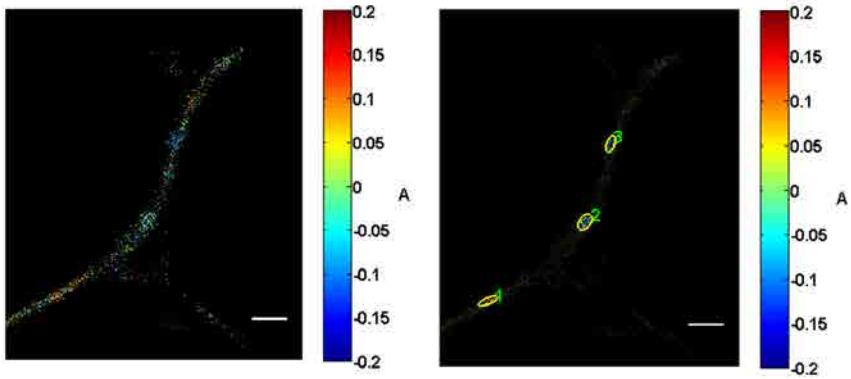

(a) (b)

Figure 3.31: Automatic cluster selection (Sample: tubulin in a COS 7 cell labeled with Alexa 647). (a) Full super-resolved image. Scale bar: 1 μ m. (b) Clusters selected from the automatic selection cluster algorithm (connectivity: 8). Regions selected are surrounded by a yellow ellipse. Scale bar: 1 μm

Histogram analysis in a single cluster

In addition to cluster identification, histogram anisotropy analysis is performed for single clusters (See Fig. 3.28c). As it will be explained in Chapter 4, the distribution shape of anisotropy histograms of single clusters depends on the dynamics, and angular constraint are therefore provide unique local information.

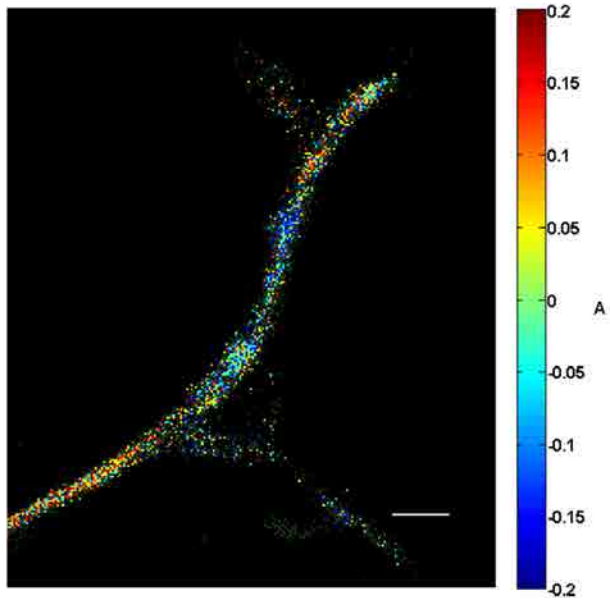

(a)

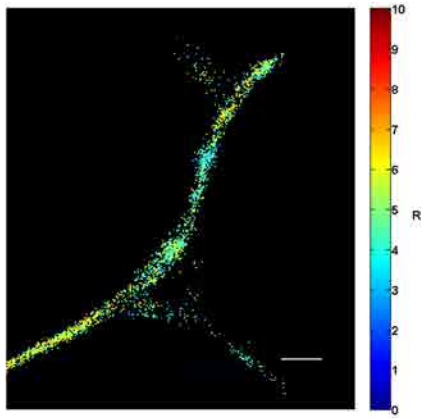

(b)

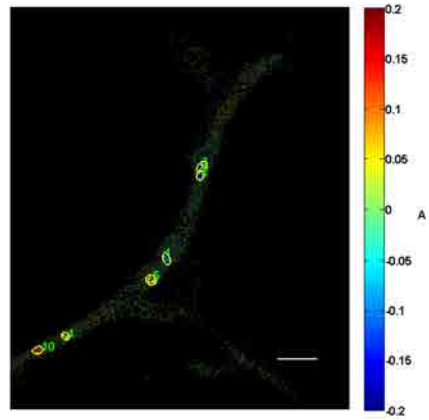

(c)

Figure 3.32: Automatic cluster selection based on anisotropy value ranges (Sample: tubulin in a COS 7 cell labeled with Alexa 647). (a) Full super-resolved image. Scale bar: 1 μm (b) Different regions based on anisotropy values (A = [-0.2,-0.18], [-0.18,-0.16],..., [0.18,0.2]). Scale bar: 1 μm. (c) Clusters selected are surrounded by a yellow ellipse . Scale bar: 1 μm

3.6.3 A versus ρ and ψ

The average anisotropy for a given "cluster" is reported as a function of ρ and ψ in Fig. 3.33 . The origin of this dependence will be detailed in Chapter 4. It shows that if ρ is known (expected in cases such as membranes or fibers, as it was explained previously), ψ can be retrieved and therefore it is possible to have access to the molecular order information. Each experimental result such as obtained in the cluster of Fig. 3.28 can be added to this graph.

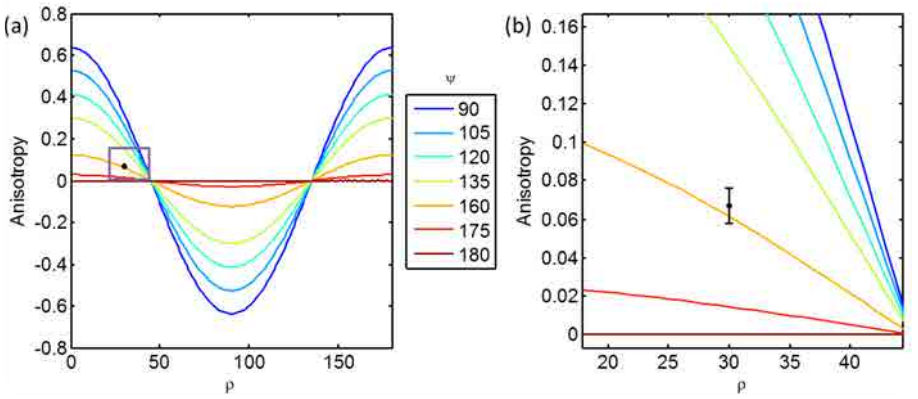

Figure 3.33: A versus ρ and ψ. (a) Theoretical anisotropy average in terms of ρ and ψ angles with experimental point shown in Fig. 3.28. (b) Zoomed region (Purple rectangle inset of (a)). Markers with bars: standard error of the mean (SEM) and simulated anisotropy (cont. lines) as a function of ρ and ψ.

The ψ value (assuming a cone model) can then be retrieved from a statistics over several measured $< A >$ and ρ values. Nonlinear Least Square method using Optimization Toolbox® of Matlab® is performed to fit the anisotropy average values for a known orientation angle (ρ), with the theoretically expected $< A > (\rho, \psi)$ dependencies developed in Chapter 4.

3.7 Conclusion

In this chapter we described the experimental set-up including: the dSTORM microscope adapted for polarized detection and the focus drift correction. In addition, the EMCCD camera calibration has been detailed. Experimental conditions for dSTORM had been described, comprising the optical part, as well as the sample preparation.

The polar-dSTORM algorithm was detailed including the "detection" and "estimation" parts. Furthermore, a post-processing analysis was described, including lateral drift correction, molecules selection and anisotropy display. Finally, a fiber morphology analysis of anisotropy was detailed.

Chapter 4

Theoretical analysis and simulations

This chapter evaluates the capacities of the polar-dSTORM technique to estimate the orientational behavior of single molecules and report super-resolution anisotropy images. Monte Carlo Simulations are conducted based on experimental scenarios, in order to define the limitations and efficiency range of the algorithm.

The first part of this chapter describes the expected behavior of the anisotropy statistics from a large collection of molecules in different situation accounting for their rotational mobility and angular constraint. The second part deals with the estimation of these anisotropies, accounting for several experimental factors such as noise and background.

Based on the results obtained from these simulations, a filtering method is proposed, relying on important factors such as intensity, PSF radius and localization precision, to guarantee a high reliability in the anisotropy estimation.

All simulations in this chapter are performed with Matlab.

4.1 Model

In what follows we develop a model that allows a preliminary understanding of the statistical results on anisotropy measured from many molecules undergoing rotational diffusion at various time scales.

4.1.1 Calculation of the anisotropy from single molecules

Stationary single molecules

The fluorescence signal from a single stationary molecule with its excitation dipole moment μ_{abs} oriented at a fixed angle $\Omega_{abs} = (\theta_{abs}, \varphi_{abs})$ and the emission dipole moment μ_{em} oriented at a fixed angle $\Omega_{em} = (\theta_{em}, \varphi_{em})$ originates from the product between the absorption probability P_{abs} and the emission probability P_{em} . Denoting E the polarization of the incident field, which propagates along the Z direction (Fig. 4.1a), the resulting fluorescence intensity polarized along the X horizontal direction in the sample plane (X, Y) can be written:

$$\begin{aligned} I_X &= P_{abs} \cdot P_{em,X} \\ I_X &\propto |\mu_{abs} \cdot E|^2 \, |\mu_{em} \cdot X|^2 \end{aligned} \tag{4.1}$$

In what follows, X will also be denoted the "parallel" or "horizontal" detection polarization ($\parallel$) and Y the "perpendicular" or "vertical" detection polarization ($\perp$) direction.

Since the emission comes from a radiating μ_{em} dipole, it is in reality collected by an objective of given numerical aperture. The emission probability has to be rewritten to account for possible mixing between polarization contributions [8]:

$$\begin{aligned} P_{em,X} &\propto \kappa_1 |\mu_{em} \cdot X|^2 + \kappa_2 |\mu_{em} \cdot Y|^2 + \kappa_3 |\mu_{em} \cdot Z|^2 \\ P_{em,Y} &\propto \kappa_2 |\mu_{em} \cdot X|^2 + \kappa_1 |\mu_{em} \cdot Y|^2 + \kappa_3 |\mu_{em} \cdot Z|^2 \end{aligned} \tag{4.2}$$

with $(\kappa_1, \kappa_2, \kappa_3)$ coefficients that account for the numerical aperture NA of the objective [8], with κ_2, κ_3 becoming non negligible for a high NA collection objective. Typically for a water immersion objective with NA = 1.2, ($\kappa_1 = 0.76, \kappa_2 = 0.01, \kappa_3 = 0.23$). For NA = 1.45 in a oil immersion medium, then ($\kappa_1 = 0.7, \kappa_2 = 0.02, \kappa_3 = 0.28$).

Defining the anisotropy A by the ratio (see Chapter 2):

$$A = \frac{I_X - I_Y}{I_X + I_Y} \tag{4.3}$$

Then the anisotropy can be simplified as a ratio depending solely on the emission dipole orientation angles, whatever the incident polarization used for the excitation:

$$A = \frac{(\kappa_1 - \kappa_2)\, \cos(2\varphi_{em})}{(\kappa_1 + \kappa_2) + 2\kappa_3 \cot^2(\theta_{em})} \tag{4.4}$$

and the total detected intensity can be written:

$$I_T = I_X + I_Y = (\kappa_1 + \kappa_2)\sin^2(\theta_{em}) + 2\kappa_3\cos^2(\theta_{em}) \tag{4.5}$$

From this equation, considering that $\kappa_1 >> \kappa_2$ and that tilted off-plane orientations ($\theta_{em} \lesssim 45°$) will be hardly detected due to their low excitation efficiency (the incident field lies in the sample plane) and their low emitted total intensity ($\kappa_1 > \kappa_3$), we can express A in the context of the detection of molecules lying in 2D in the sample plane. In this case:

$$\begin{aligned} A &\approx \cos(2\varphi_{em}) \\ I_T &\approx \sin^2(\theta_{em}) \end{aligned} \tag{4.6}$$

The assumption that out-of plane tilted angles lead to negligible contributions is a simplification, which can be explored in a first approximation. This approximation will be considered in the rest of this work because (1) the excitation efficiency of the Z component of a dipole for an incident circular polarization is about 40% times lower than the one of its in-plane components [90], (2) the collection efficiency for the Z component of a dipole is also at least 40% lower than that of the in-plane components, (3) the consequent change of the PSF from out-of plane tilted emission dipoles [66] will most probably make such molecules excluded from the analysis of single molecule localization, which is based on symmetric Gaussian spot images (see Chapter 3).

Single molecules wobbling in a cone

In cases where the molecules undergo rotation during the measurement integration time (in our case 30 ms), then the calculated intensities have to account for such rotation in an integrated form [40]:

$$I_X \propto \int_0^T \int\int \omega(\Omega_{abs}, \Omega_{em}, t)\, e^{-t/\tau_f}\, |\mu_{abs} \cdot E|^2\, |\mu_{em} \cdot X|^2 d\Omega_{abs}\, d\Omega_{em}\, dt \tag{4.7}$$

where T is the integration time of the measurement. This equation can be written similarly for I_Y. $d\Omega_{abs} = \sin\theta_{abs} d\theta_{abs} d\varphi_{abs}$ (equally for Ω_{em}) represents the integration over angles explored by both absorption and emission angles of the molecules. $\omega(\Omega_{abs}, \Omega_{em}, t)$ is the probability density of finding the absorption dipole at orientation Ω_{abs} and the emission dipole at orientation Ω_{em} at a time t later. The factor e^{-t/τ_f} is a weighting function that accounts for the fact that the emission of a photon at time t occurs with a time decay within the fluorescence lifetime τ_f (typically a few ns).

The extent of the angular integration in this equation depends on the angular aperture that the molecules explore during their rotational mobility. In this work,

we will model this rotational mobility by a constraint within an angular cone aperture ψ oriented on average with an angle ρ in the sample plane (see Fig. 4.1b). The expression of $\omega(\Omega_{abs}, \Omega_{em}, t)$ is a solution of the rotational diffusion equation subject to the boundary conditions set by the cone angle. It can be solved analytically [9, 91] and depends on the rotational diffusion time τ_{rot}, which is typically ≈ 10 ns for a protein in a solution. This time can be from much faster for a small molecule freely diffusing in a solution, to much slower for a motion in a viscous medium or in a tethered fluorophore. τ_{rot} depends globally on the local temperature, viscosity and size of the diffusing probe (see Eq. 4.7).

Two distinct situations are worth to mention. In the case of "fast" wobble (rotation within a time scale much faster than the fluorescence lifetime τ_f: $\tau_{rot} \ll \tau_f$), the molecule can rotate even before emitting its photon and therefore all the angular information of the absorption dipole (photo-selection) is lost at the emission. In the other extreme case of "slow' wobble, the molecule appears not only as totally fix in orientation between the absorption and emission events, but also within the time scale of the measurement (imaging integration time) ($\tau_{rot} \gg T \gg \tau_f$).

In this work, we will simplify the problem in a first approximation to explore the dependence of the anisotropy measured for single molecules for which the ratios τ_{rot}/τ_f and τ_{rot}/T are defined. We assume the motion taking place in 2D (reducing the variables to φ_{abs},φ_{em}) and at a regular pace such as $\varphi_{em} = \varphi_{abs} + 2\pi \cdot t/\tau_{rot}$. The angle φ_{abs} at time $t = 0$ (chosen randomly) as well as the angle φ_{em} at time t are kept within the cone aperture defined by the parameters ρ and ψ. This allows exploring the effect of both angular constraint (called molecular order in what follows) as well as dynamics of the motion within this angular limit. These parameters are illustrated in Fig. 4.2. In principle, 3D Brownian rotational motion should be considered, however at this stage the time sequence of the single molecule intensities is not the aim of the study, but rather the statistical representation of their integrated anisotropy.

Based on this model, two different situations will be described in the next sections:

1. Isotropic medium. The molecules are oriented randomly in the sample, with a given rotational diffusion time τ_{rot} which makes them either stationary (fixed molecules at random orientations) or freely diffusing, randomly in angle within $\psi = 180°$.

2. Constraint medium. The molecules are oriented in an ordered sample within a cone aperture (ρ, ψ). Stationary molecules and fast wobbling molecules will be considered.

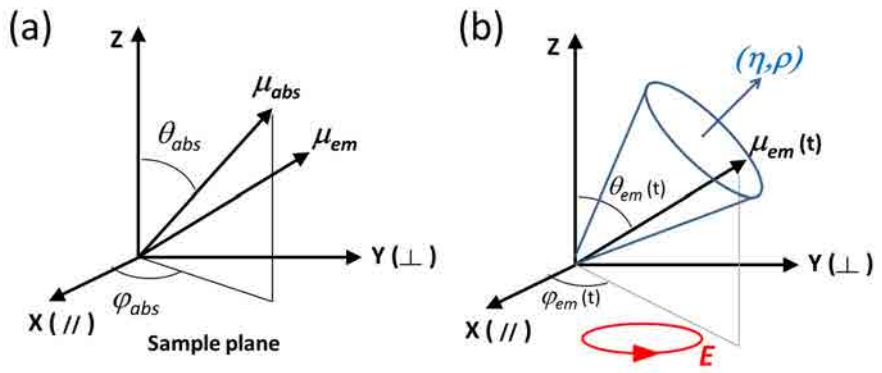

Figure 4.1: Schematic representation of (a) a stationary molecule, showing both its absorption and emission dipoles, and (b) a dynamic case where the molecule rotates within an angular constraint cone defined by the (η, ρ) orientation. In this work, the out-of plane orientation of the cone will be omitted and only the in-plane ρ orientation will be considered.

4.1.2 Isotropic sample

We first explore the case of a medium where molecules explore randomly all angles, either statically or dynamically. Historically this situation has been studied using a linear incident polarization state since this situation provides information on the ratio τ_{rot}/τ_f (see Chapter 2).

The situation of stationary single molecules $\tau_{rot} \gg \tau_f$ can be modeled analytically, considering a uniform, time independent probability $\omega(\varphi_{abs}, \varphi_{em}, t)$ for $\varphi_{abs} = \varphi_{em}$. Here we do not suppose any difference between the absorption and emission dipoles due to the molecular structure itself, which is reasonable for the fluorophores studied in this work [67]. In this case the anisotropy is simply related to the orientation of the molecule $\varphi = \varphi_{abs} = \varphi_{em}$ with the relation:

$$A = \frac{I_X - I_Y}{I_X + 2I_Y} = \frac{\cos(2\varphi)}{1 + \sin^2\varphi} \tag{4.8}$$

The result for an incident linear polarization along the X direction is shown in Fig. 4.3a. As expected, while the angle extent is uniform, there is more probability to find anisotropies around the extreme values $(-0.5, 1)$ since the $A(\varphi)$ function is of sinusoidal type with its maxima -0.5 and 1.

In order to determine the statistical behavior of single molecules' anisotropy in a given sample where the molecules are randomly oriented but undergoing

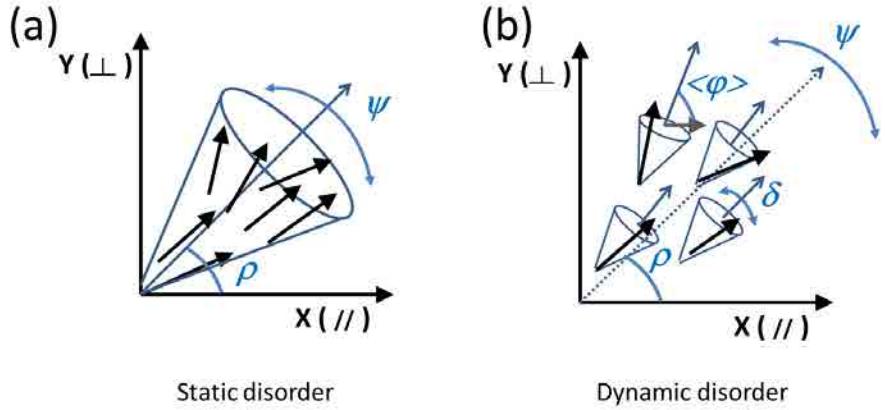

Figure 4.2: Schematic 2D representation of static versus dynamic disorder. a) In the static case, the molecules are stationary but all with different orientations, within an angular aperture ψ oriented with ρ with respect to the horizontal axis in the sample plane. b) In the dynamic case, the molecules undergo rotational mobility within the ψ aperture, with an average orientation $< \varphi >$. On average over all the molecules in space, the dipoles are pointing in a privileged direction ρ (for instance the direction of a fiber). In both cases, the averaged behavior on many molecules is a cone of aperture ψ and mean orientation ρ.

possible rotational diffusion governed by τ_{rot}, we reconstruct the anisotropy histograms of a set of 1000 molecules generated by a Monte Carlo simulation, taking φ_{abs} randomly and using the time dependence of 2D orientation given above. The resulting histograms are shown in Fig. 4.3b-d for different rotation times τ_{rot} imposed by the conditions $\tau_{rot}/\tau_f = 100$, 10 and 0.1 (motion from a "slow wobble" to a "very fast" wobble). As expected, the mean and the width of the obtained histogram depends on τ_{rot}/τ_f. The mean is affected because the rate of depolarization induced by τ_{rot} affects the A value in general, as developed in Chapter 2. Note that this is specific to cases where the incident polarization is linear, imposing a photo-selection of the excited molecules. The width of the histogram decreases with a decreasing τ_{rot}/τ_f ratio, which is obvious since when molecules rotate much faster than their fluorescence lifetime, they all undergo the same anisotropy mechanism with $A = 0$. As a general behavior, a faster rotation induces a reduction of the histogram width of observed anisotropy.

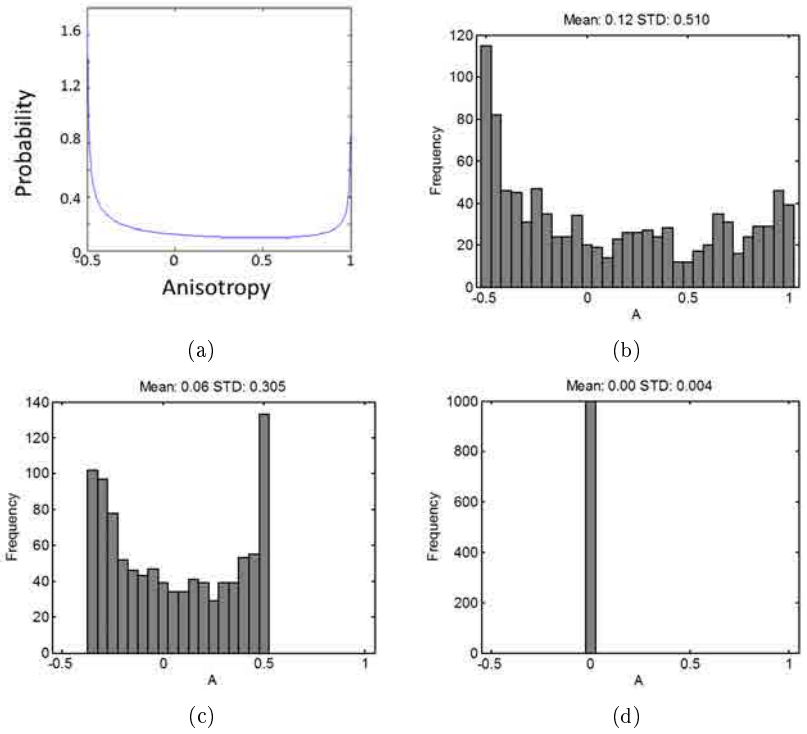

Figure 4.3: a) Anisotropy obtained by an analytical calculation for fixed molecules ($\tau_{rot} \gg T$) randomly oriented. b-d) Anisotropy histogram of single molecules in an isotropic sample based on Monte Carlo Simulation using 1000 simulated molecules: b) $\tau_{rot}/\tau_f = 100$, c) $\tau_{rot}/\tau_f = 10$ and (c) $\tau_{rot}/\tau_f = 0.1$.

4.1.3 Ordered sample

The investigation of ordered samples in a microscope sample plane (X, Y) imposes a circular incident polarization as mentioned above. The anisotropy in this case will be defined by:

$$A = \frac{I_X - I_Y}{I_X + I_Y} \tag{4.9}$$

Similarly as above, the statistical behavior of single molecules' anisotropy when constraint in angular extent is studied for different rotational time regimes. We reconstruct the anisotropy histograms of a set of 1000 molecules generated

by a Monte Carlo simulation, for two different rotational diffusion rates : τ_{rot}/τ_f = 10 000 (almost stationary), 100 (slow wobble) and 1 (fast wobble), and for different angular constraints defined by the ρ and ψ parameters. The resulting histograms are shown in Fig. 4.4 for the stationary case. The mean of the histogram $\langle A \rangle$ is seen to strongly depend on ρ, which is expected since the global pointing direction of the molecules drives their averaged anisotropy. Note that the cone aperture value ψ also has an effect on $\langle A \rangle$ in the sense that the extreme values of anisotropies that can be reached (for $\rho = 0°$ or 90°) are large (-1,1) for small ψ values and lower for large ψ values ((-0.3,0.3) for $\rho = 135°$ for instance). The other striking effect of ψ is how it affects the shape and width of the histogram. Indeed the larger the extent of angle explored by the molecules (large ψ), the wider range of available anisotropies.

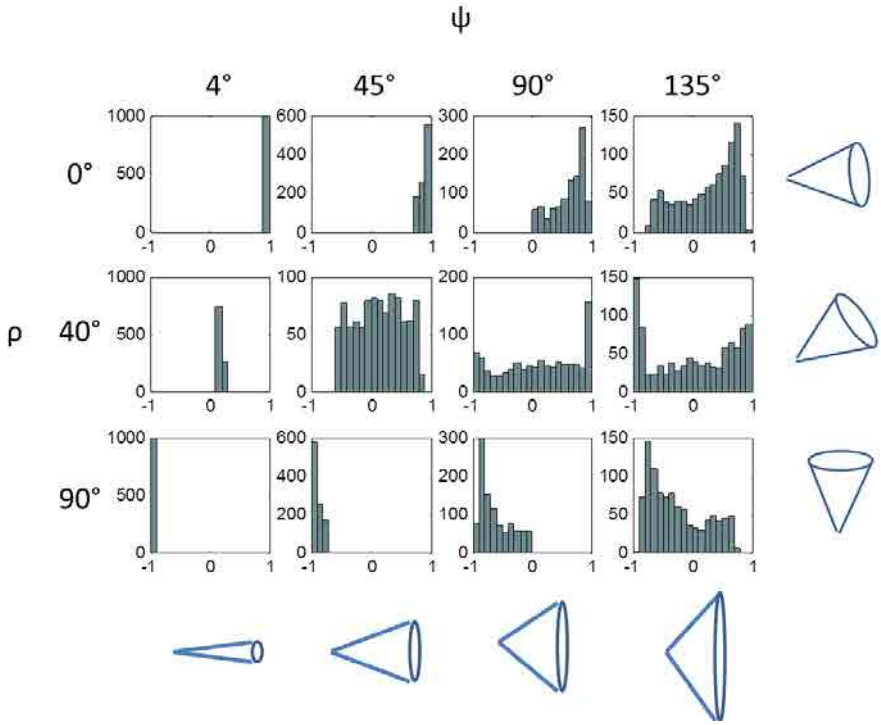

Figure 4.4: Histograms of A for stationary molecules, in different angular constraint situations varying $\rho = 0°$ (horizontal averaged orientation), 40° , 90° (vertical averaged population) and $\psi = 4$ °, 45 °, 90 °, 135 °.

In cases where the motion is not stationary, the ratio τ_{rot}/τ_f also comes into

play. We noticed that for slow wobble $\tau_{rot}/\tau_f = 100$, the obtained histograms are very similar to the ones obtained for the stationary case, which confirms that this set of experiment is not dedicated to a fine probe of the rotational diffusion time of the molecules (for a high sensitivity to τ_{rot}/τ_f , a linear incident polarization would be required). On the contrary as soon as the rotational diffusion time reaches the same order of magnitude as τ_f (fast wobbling) (Fig. 4.5), the effect is clearly distinguishable: the histogram width is now reduced and it is similar for all ρ values. Note that an even faster rotational motion ($\tau_{rot}/\tau_f = 0.1$) would lead to extremely low histogram widths. Note that there is no noise included in this model, therefore the observed behavior should be modulated by the presence of noise in real experiments, as will be developed in the next section.

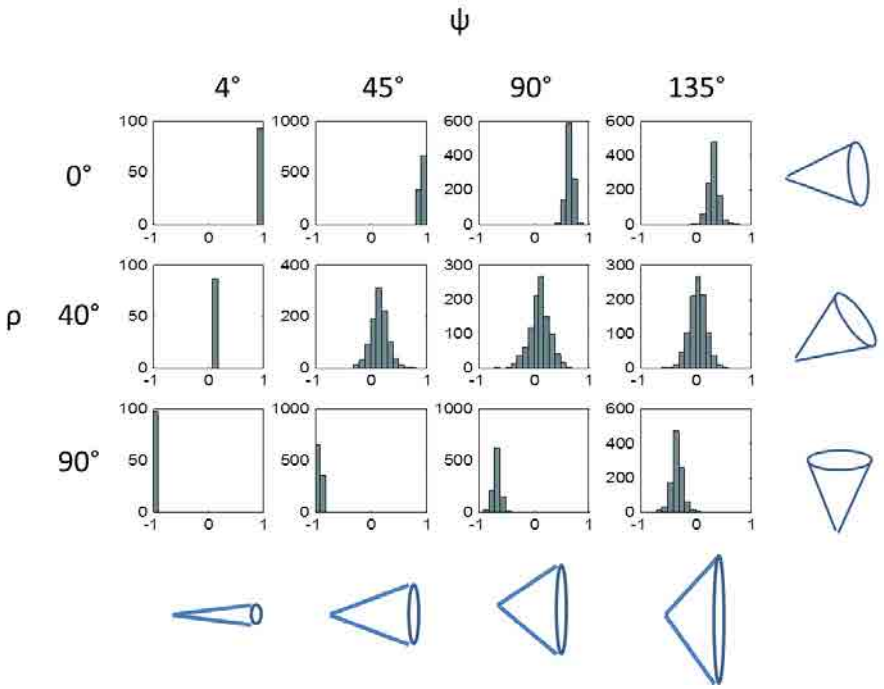

Figure 4.5: Histograms of A for fast wobbling molecules, in different angular constraint situations varying $\rho = 0°$ (horizontal averaged orientation), 40° , 90° (vertical averaged population) and $\psi = 4$ °, 45 °, 90 °, 135 °.

For all the cases presented above, there is a clear dependence of the averaged value $\langle A \rangle$ (over the molecular population) with respect to the angular constraint parameters ρ and ψ. This dependence is plotted in Fig. 4.6 for stationary

molecules. Note a similar dependence is obtained if considering molecules wobbling in a cone at any time scale, or considering the anisotropy from an ensemble of molecules statistically distributed within a cone aperture, either spatially or due to time fluctuations. In other words, this averaged information does not give any information on the time scale of the rotational diffusion, for which the analysis of the histogram width is necessary.

The function $\langle A\rangle(\rho,\psi)$ is seen to depend sinusoidally on ρ (with a contrast reducing when ψ increases), with a maximum when the molecules are globally oriented along $X = \parallel$ and a negative minimum value when the molecules point along $Y = \perp$. The most extreme case is when ψ is very small, resembling the situation of a single molecule pointing in a given direction ρ: in this case, as detailed above, $\langle A\rangle = \cos 2\rho$ with maximal values $(-1, 1)$. From this plot it is clear that if ρ is known, it is in principle possible to estimate the angular constraint ψ from the measurement of the averaged value $\langle A\rangle$ taken from many molecules. There are some other ways to access such an information as already described in the literature, using variable incident polarizations and recording the time evolution of single molecules under this excitation variation scheme [11]. This approach is however not compatible with super-resolution imaging where molecules are imaged in a very short time scale. Nevertheless the advantage of super-resolution is that many single molecules are imaged over a very small area: therefore the angular constraint information is accessible, providing that it is uniform over the spatial scale of investigation (typically from 50 nm to 200 nm).

The previous anisotropy histograms show interesting effects, however are affected in practice by other parameters such as noise. In order to analyze the effect induced by noise and by the dSTORM image processing, further simulations are necessary which account for typical experimental conditions. In the following section, simulations are presented that calculate anisotropy from single molecules in real conditions, which will allow to compare the obtained histograms with the expected ones.

4.2 Simulation of anisotropy measurements

In order to observe the effect of the experimental factors and the limitations of the polar-dSTORM detection algorithm, a simulation has been implemented to generate the raw anisotropy images. For this purpose, different theoretical scenarios have been defined:

- Fixed molecules with random orientation.
- High rotational mobility within random orientations ($\psi = 180°$).
- Fixed molecules with define orientation constraint (ψ).

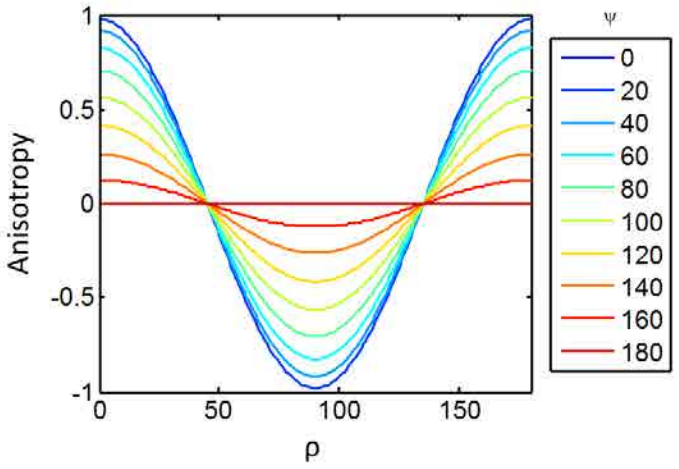

Figure 4.6: Average anisotropy value $\langle A \rangle$ as a function of the cone constraint angles ρ and ψ.

For each of these scenarios, the simulation parameters (intensity, background, PSF size) were obtained from typical experimental values, which can be visualized in the next chapter. As it was described previously, the noise model is adapted based on intensity dependent Poisson model. A detailed description of the Monte Carlo method is described in what follows.

4.2.1 Simulation method & parameters

The steps of this analysis are:

- Set initial parameters.
- Set localizations and intensity.
- Create a PSF filter.
- Blur the image with this PSF filter.
- Add background and noise.
- Run the polar-dSTORM algorithm

Initial parameters.

The initial parameters in the simulation are:

- Radius (PSF sigma). Initial radius for the "detection" algorithm. Typically it is equal to 1.7 pixels.
- Window PSF (support size of the PSF filter) and window for detection. Usually 11 x 11 pixels.
- Number of molecules per frame. Usually 4.
- Total intensity ($I_{\parallel} + I_{\perp}$) for each molecule. This value will depend on the case of study, it can be typically vary between 10 000 and 30 000.
- Offset. For the case of the Quantem 512sc camera, this value is set to 1000.
- Experimental background. Similarly as in experimental data, this value is in the range 1 500 - 3 000 counts (including offset).
- Gain of the CCD camera: 300 to 500. This value will determine the k_g value of the intensity noise model introduced in Chapter 2.
- Number of frames. For this experiment, this value is between 500 - 1 000 frames.
- Probability of false alarm (PFA) . Usually, it is set to 1×10^{-6}.
- Frame size. Usually 100 x 100 pixels.
- Initial distance vector between parallel and perpendicular image. Usually, 50 pixels.
- G factor. This value is set to 1.
- Anisotropy A per molecule. Based on A, the values of $I_{\parallel}$ and $I_{\perp}$ can be directly deduced. Indeed:

$$\begin{aligned} I_T &= I_{\parallel} + I_{\perp} \\ A &= \frac{I_{\parallel} - I_{\perp}}{I_{\parallel} + I_{\perp}} \end{aligned} \tag{4.10}$$

and therefore:

$$\begin{aligned} I_{\parallel} &= I_T \left(\frac{A+1}{2} \right) \\ I_{\perp} &= I_T - I_{\parallel} = I_T \left(\frac{1-A}{2} \right) \end{aligned} \tag{4.11}$$

Set localizations and intensity.

In this part, the positions of the emitters are selected in arbitrary way, based on the distance vector. The total intensity is selected based on the initial parameters. As a requirement of the polar-dSTORM algorithm, a minimum of 3 pairs are necessary in order to ensure the estimation of the vector coordinates as introduced in Chapter 3.

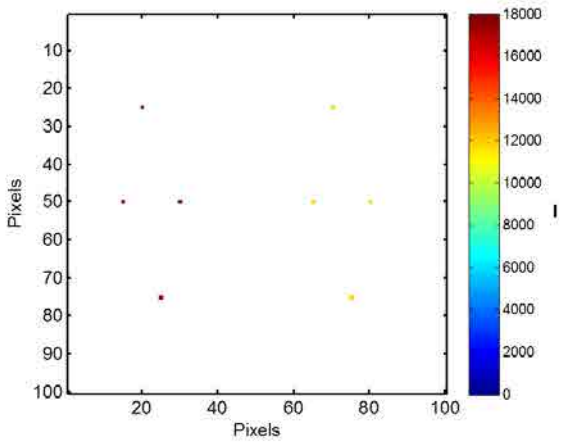

Figure 4.7: Set localizations. In this example $A = 0.2$ and $I_T = 30\ 000$ counts for all molecules of the image.

The resulting "starting situation" is illustrated in Fig. 4.7.

PSF filter.

A Gaussian (PSF) shape is defined. This Gaussian filter is created using the *fspecial* command of Matlab®, with two parameters: window size (size of the support) and PSF radius.

The generated PSF is shown in Fig. 4.8.

Blur the image with the PSF filter.

After the PSF filter is defined, the initial image containing the localizations is blurred. For this purpose, multidimensional filtering based on convolution is performed using the *imfilter* command of Matlab® (see Figure 4.9).

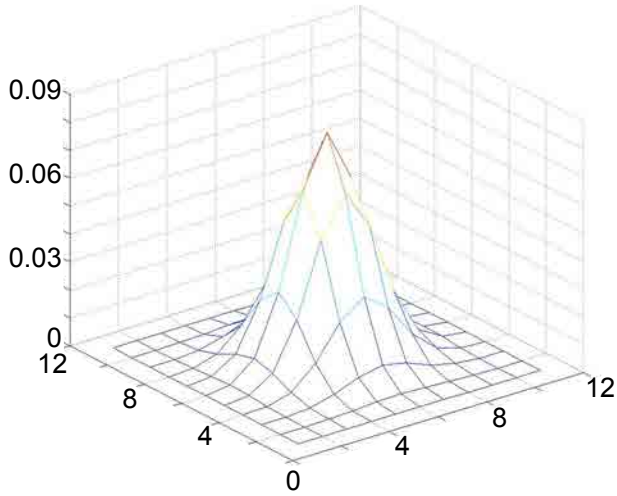

Figure 4.8: PSF generated by *fspecial* in Matlab, window size = 9 pixels and PSF radius = 1 pixel.

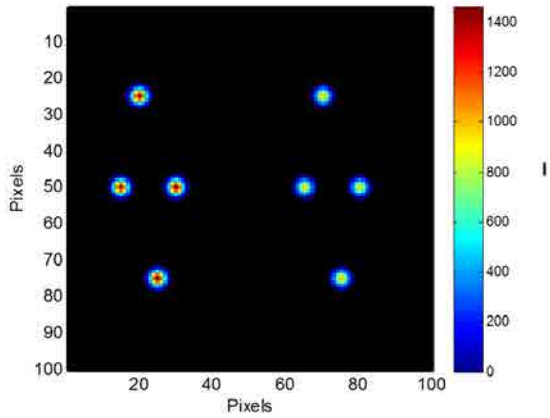

Figure 4.9: Raw simulated STORM image (window size = 11 pixels, PSF radius = 1.4 pixel). In this example A = 0.2 and I_T = 30 000 counts, for all the molecules of the image.

Add background and noise.

As it was mentioned previously, there is a clear dependence on the EMCCD gain and intensity of the noise of each pixel in the image. The noise model described

in Chapter 3 is:

$$\sigma_I = k_g \sqrt{< I - offset >} \tag{4.12}$$

with k_g a factor depending on the CCD gain, I the intensity and offset = 1 000 counts the EMCCD offset.

In this step, it is necessary to add to the image the camera offset and the background characteristic of the sample. Then the standard deviation of the noise (σ_I) is obtained for each pixel of the image. The noise is added assuming a normal distribution with mean I and standard deviation σ_I (see Fig. 4.10).

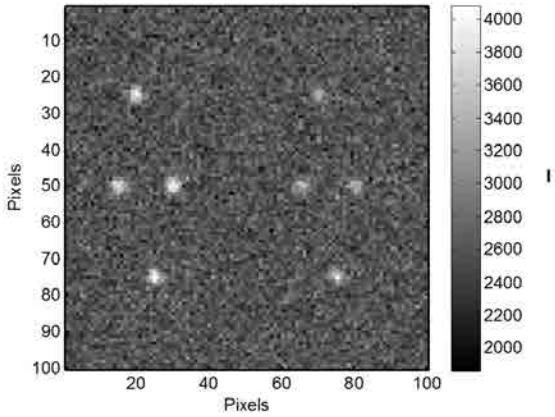

Figure 4.10: Raw simulated STORM image, including the background and noise.(window size = 11 pixels,PSF radius = 1.4 pixel). In this example A = 0.2 and I_T = 30 000 counts, Background (Bg) = 2 500 counts and camera gain = 500, for all molecules of the image.

Estimation of the anisotropy

For each "simulated" molecule, the polar-dSTORM algorithm is run based on input parameters fixed by the initially chosen values (typical values of w_s, r_0, PFA defined in Chapter 3 are given above). In order to run statistical studies, typically 100 to 1 000 molecules are measured in each considered situation. These molecules are generated in a Monte Carlo simulation starting from known values of A, $I_{\parallel}$, $I_{\perp}$, Bg (background including offset), G (gain). An example of image containing molecules of a selected anisotropy is shown in Fig. 4.10.

Results of simulation

After the simulated fluorescence image is generated, the polar-dSTORM analysis is performed: the result of the "detection" algorithm is shown in Fig. 4.11 for the molecules of Fig. 4.10.

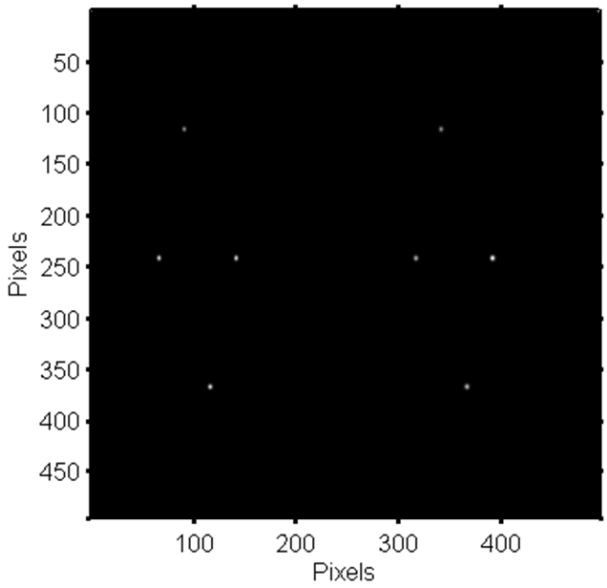

Figure 4.11: Super resolved image of the result of detection (Zoom = 5×).

Finally, an anisotropy image is generated (see Fig. 4.12) for a given representation (typically zoom 5, meaning each pixel is divided into 5 sub-pixels).

The localization precision ($\sigma_{\parallel}$ and $\sigma_{\perp}$) and fitted ($r_{\parallel}$ and $r_{\perp}$) radius histograms are then obtained for the whole population of molecules (Fig. 4.13). These histograms give an indication of the quality of the simulated molecules, which depend primarily on the intensity, background and gain conditions. In the next parts, we describe the effect of these parameters on the resulting anisotropy statistics in different situations related to dynamic and static disorder.

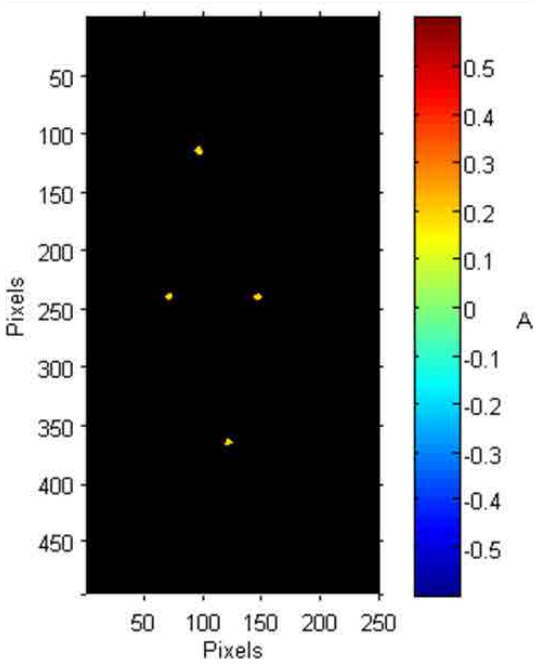

Figure 4.12: Super resolved image of Anisotropy (Zoom = 5x).

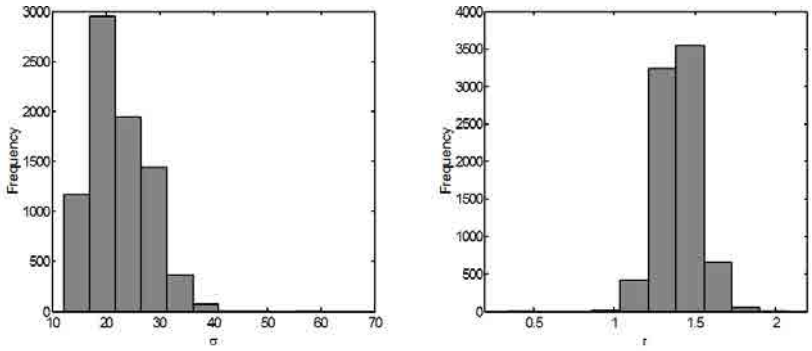

(a) (b)

Figure 4.13: Histograms of Simulation of a sample with a given anisotropy (0.2). (a) Localization precision for the simulated images (σ) in nm, assuming pixel size = 177 nm. (b) Radius histogram of the simulated images (r) in pixels (expected = 1.4 pixels).

4.2.2 Estimation precision and bias on single molecule anisotropy measurements

In order to validate the anisotropy results given by the polar-dSTORM algorithm, a statistical analysis is performed on single molecules with a well defined expected anisotropy A_{exp} (typically all molecules oriented in a single, static direction), with various intensity, background, and camera gain conditions. These experimental parameters will drive the conditions in which the localization of each molecule will be performed, and their anisotropy calculated by the polar-dSTORM algorithm. To generate enough statistics, 1000 frames with 4 pairs of single molecule spots (4 spots appearing on each $\parallel$ and $\perp$ images), leading to a total of 4000 molecules, each with an expected anisotropy $A_{exp} = 0$, were simulated for each experimental condition case.

Figure 4.14 shows different anisotropy histograms obtained for two different total intensities representative of typically low and high values obtained experimentally (I_T = 12 000 and 30 000 counts), varying as well the background (including offset) from high to low (B_g = 2500 and 1500 counts) and at a fixed camera gain of 500. The results show that while the average value $\langle A \rangle$ of the histogram seems reliable, its width (quantified by the standard deviation σ_A) is strongly affected by a decrease in intensity or an increase in background. The lowest obtained value $\sigma_A = 0.06$ corresponds to "good conditions" in terms of experimental performances (see Chapter 3), but σ_A increases up to 0.22 in more degraded conditions (still met experimentally), which can be considered as a very big standard deviation depending on the application required. This effect is due to the fact that low intensities are affected by a higher noise, which makes the evaluation of the anisotropy (which is based on intensity ratios) less reliable. The bias $\delta_{<A>} = A_{exp} - \langle A \rangle$ is only slightly increasing to 0.01 in the worst experimental conditions. Note that the use of a lower gain (300 typically) decreases slightly the observed effects, which is compatible with lower noise conditions.

From the obtained set of data it was possible to classify the molecules per total intensity and explore the dependence of both bias $\delta < A >$ and standard deviation σ_A on this intensity. Fig. 4.15 shows their dependence with respect to $I_{\parallel}$ (a similar trend is expected for I_T). In the low intensity range, representing a small portion of events (Fig. 4.15c), the bias and anisotropy error are clearly affected. It seems that for intensities above 20 000 counts, the values of obtained bias and standard deviation are more reasonable.

From these observations, it is clear that the experimental conditions will affect the robustness of anisotropy imaging. In what follows we summarize these effects for a variable single molecule anisotropy, still considering a pure stationary situation.

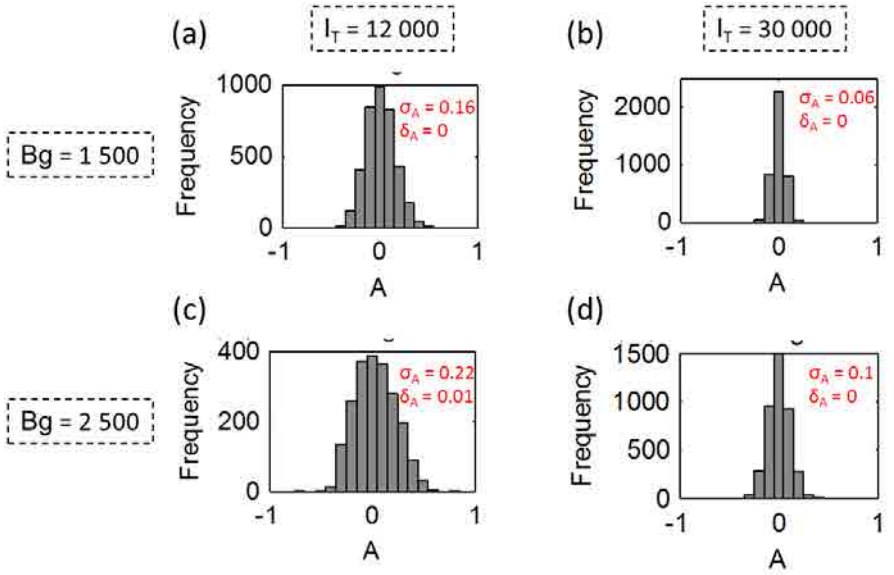

Figure 4.14: Anisotropy histograms obtained for 4000 molecules with expected anisotropy $A_{exp} = 0$, with a camera gain of 500 and experimental conditions: (a) (I_T = 12 000, B_g = 1 500 counts), (b) (I_T = 30 000, B_g = 1 500 counts), (c) (I_T = 12 000, B_g = 2 500 counts), (d) (I_T = 30 000, B_g = 2 500 counts).

Effect of the single molecule total intensity

A systematic study was done on situations similar to the one described above (4 000 simulated molecules in various experimental conditions), but varying the expected anisotropy A_{exp} in a range from -0.5 to 0.5. Figure 4.16 shows the effect of the total intensity value I_T on the standard deviation (related to the histogram width). As seen previously, σ_A increases considerably when I_T decreases, due principally to increasing noise. More strikingly, this effect is even more dramatic when the absolute value of A_{exp} increases. This is in fact expected because such high anisotropy values rely on intensities $I_{\parallel}$ and $I_{\perp}$ which become more different, one side of the image showing lower intensity and therefore higher noise.

In addition to this effect on σ_A, the anisotropy bias is also affected by the intensity conditions for all expected anisotropies (Fig. 4.17). Along the same line as above, the effect is even more pronounced for high absolute values of the anisotropy.

From this study it is clear that for a given experimental configuration, selecting the brightest molecules (in terms of I_T) leads to a more reliable determination

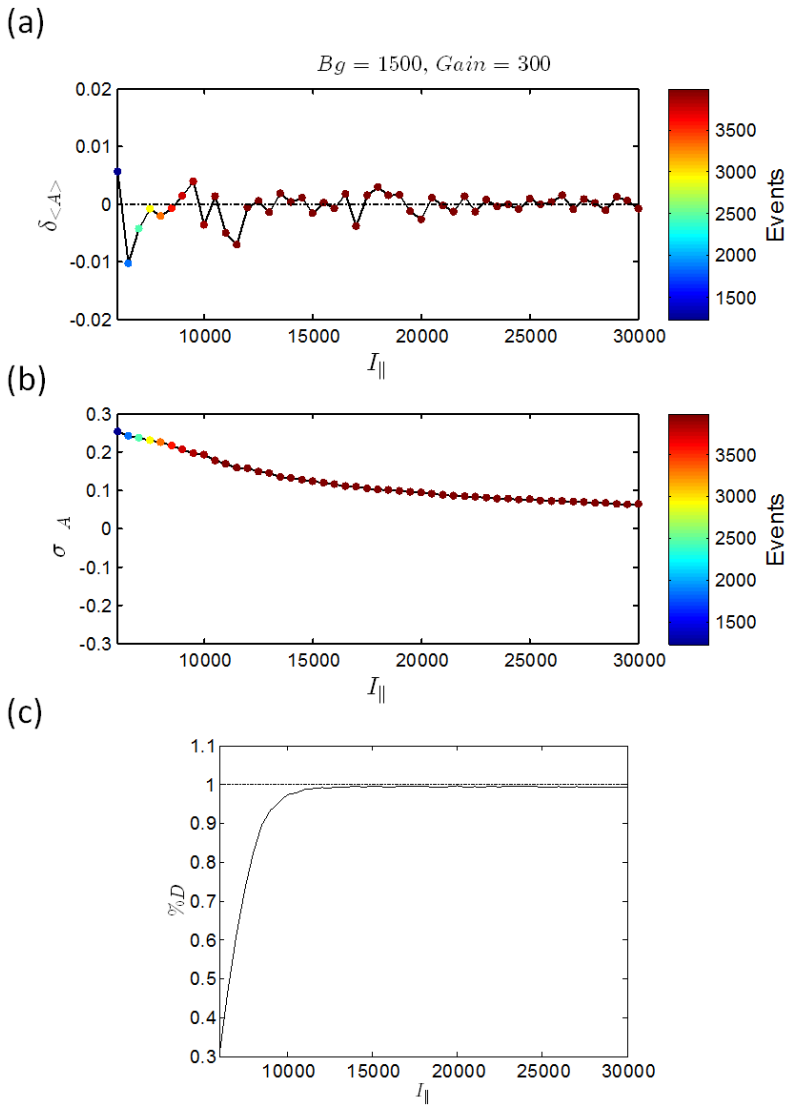

Figure 4.15: Influence of intensity ($I_{\|}$) for molecules with expected anisotropy $A_{exp} = 0$, with $B_g = 1500$ counts and Camera gain=300. (a) Bias of the average anisotropy ($\delta_{<A>}$) as a function of $I_{\|}$ collected over 4000 molecules from the simulation detailed in the text. (b) Standard deviation of the anisotropy (σ_A) as a function of $I_{\|}$. (c) Percentage of detected molecules as a function of $I_{\|}$.

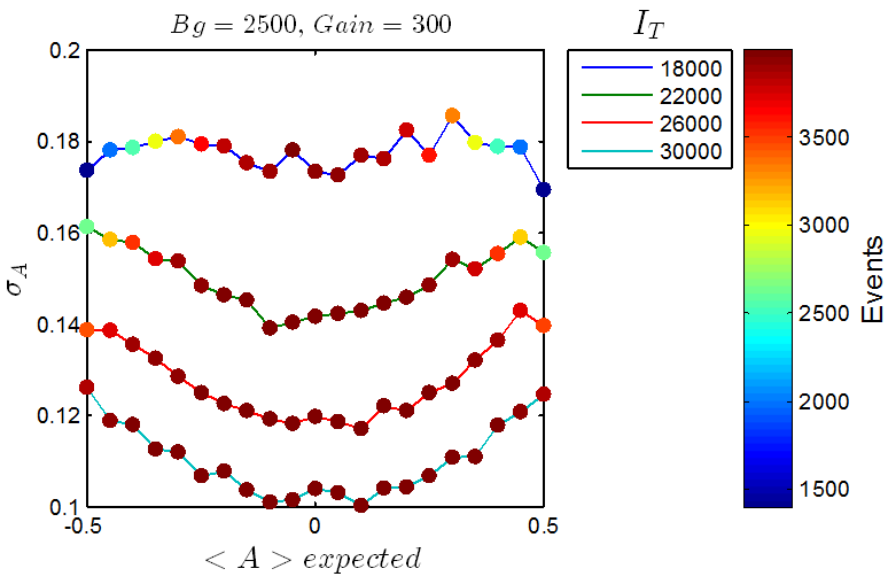

Figure 4.16: Intensity effect (I_T = 18 000, 22 000, 26 000 and 30 000 counts, B_g = 2500 counts and Camera gain=300) for different expected anisotropies A_{exp} in the range (-0.5 to 0.5).

of their anisotropy. This can be done at the expense of a loss of statistics, however it ensures that the determined anisotropies are done with a high precision. We will therefore systematically threshold the dSTORM images in terms of total intensity per molecules, keeping in mind that the lowest this threshold is, the lowest the precision on the obtained anisotropy will be.

Note that in parallel to this pure noise-induced effect (induced by low intensity and high camera gain), the background influences also strongly the observed estimation quality, by affecting the capacity of the dSTORM localization analysis to be performed with high reliability. A low background situation is therefore highly preferred for a high precision analysis.

Effect of the single molecule detection and localization

In addition to high signal to noise ratio (SNR) and low background, the anisotropy determination in the context of polar-dSTORM has to also rely on a good estimation of the localization of single molecules on the two different images ($\parallel$ and $\perp$), which can be locally affected by background and other experimental factors such

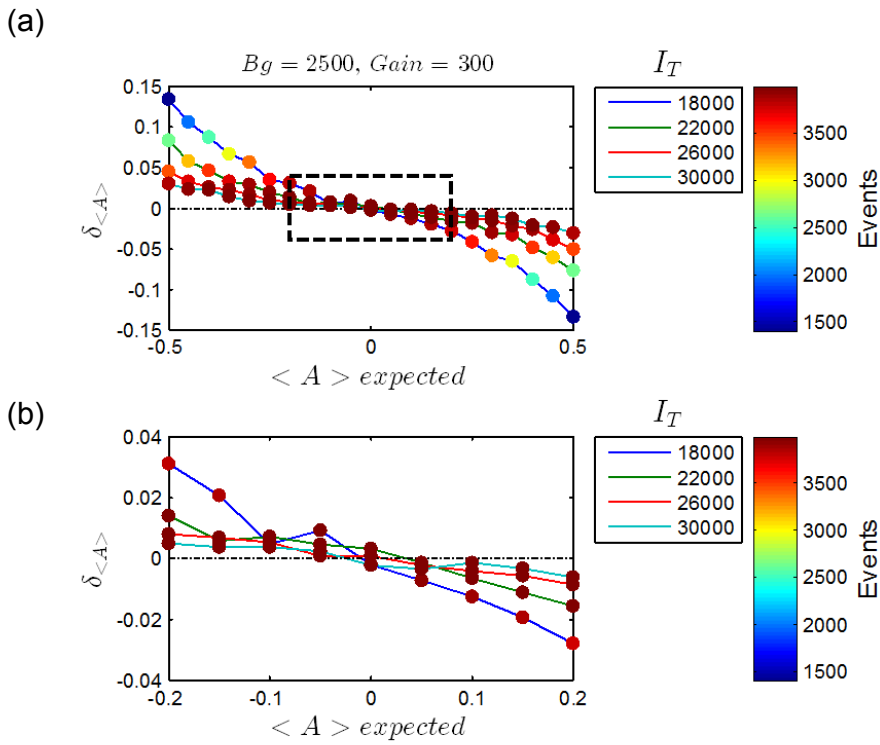

Figure 4.17: Intensity effect (I_T = 18 000, 22 000, 26 000 and 30 000 counts, B_g = 2500 counts and Camera gain=300) for different expected anisotropies A_{exp} in the range (-0.5 to 0.5).

as local environment properties which might for instance affect the photophysics of the molecules differently depending on its orientation. In order to perform a robust single molecule anisotropy estimation, we study here the possible effect of independent mechanisms which could induce different image qualities in the $\parallel$ and $\perp$ sides of the whole fluorescence image, that can affect the determined anisotropy in a non-controlled way. In our simulations, the un-balanced quality between the $\parallel$ and $\perp$ localization estimation will be induced naturally by poor experimental conditions on I_T, B_g and camera gain.

In the ideal case, we expect a similar radius r estimation in both polarized images. To quantify the effect of possible deviations from similar image qualities, we introduce a factor C_r such as the estimated radius ($r_\parallel$ and $r_\perp$) differ from 1

with an extent $C_r \in [0\ 1]$:

$$\frac{r_\perp}{r_\parallel} = 1 \pm C_r \tag{4.13}$$

C_r is equal to 0 when both estimated radius ($r_\parallel$ and $r_\perp$) are equal, and 1 when they differ by a factor of up to 2. This factor allows to classify the detected molecules by the balanced quality of their $\parallel$ and $\perp$ images, and possibly filter out molecules for which the PSF fitting quality is not guarantied enough.

Figure 4.18 represents the dependence of both $\delta_{<A>}$ and σ_A parameters on C_r, showing as well the evolution of the number of events. When C_r is small, a very strict condition is imposed on the balanced fitting quality on both polarized images, therefore very few events are considered (only those with perfectly symmetric images), and σ_A is small. When C_r increases, there is a clear increase of σ_A. $\delta_{<A>}$ is less perturbed and keeps close to its initial value. This shows that this balanced-quality criterion seems to be a determining factor for the proper evaluation precision of the anisotropy (even though the bias on A is not highly improved), especially in noisy and not highly-contrasted single molecules images.

This example shows how, in addition to intensity thresholding, an improvement on the anisotropy estimation precision can be obtained by imposing a higher filtering condition on the C_r factor. This is also visible in the obtained histograms, where a high constraint on C_r (typically < 0.1) leads to $\sigma_A \leq 0.1$, whatever the experimental conditions. This filtering should of course stay reasonable in order to keep a sufficient number of molecules in an area of investigation, which allows statistical analysis, with only changes in the limit values reached for $\delta_{<A>}$ and σ_A.

The trend represented in Fig. 4.18 is general and also observed for other total intensity, background and camera gain conditions. In general we noticed a more determining effect of the C_r filtering on the σ_A decrease for higher B_g values. It is also similar for other expected anisotropy values A_{exp}, as represented in Fig. 4.19. Note however that while playing on C_r for a higher filter in molecular selection, σ_A will always improve but $\delta_{<A>}$ stays close to its initial value.

Similarly as for the radius difference between the two images ($r_\parallel \neq r_\perp$), an imbalance in image quality can produce a difference in localization precision ($\sigma_\parallel \neq \sigma_\perp$).We investigated the possibility to filter out molecules by a similar selection factor, C_σ, characterized by a selection of molecules within a range

$$\frac{\sigma_\perp}{\sigma_\parallel} = 1 \pm C_\sigma \tag{4.14}$$

where $\sigma_\perp$ is the localization precision of the molecules in the perpendicular polarized image and $\sigma_\parallel$ in the parallel polarized image.

The results of a C_σ filtering are shown in Fig. 4.20 for an expected anisotropy $A_{exp} = 0$. Contrary to C_r, there is no strongly visible effect of the localization

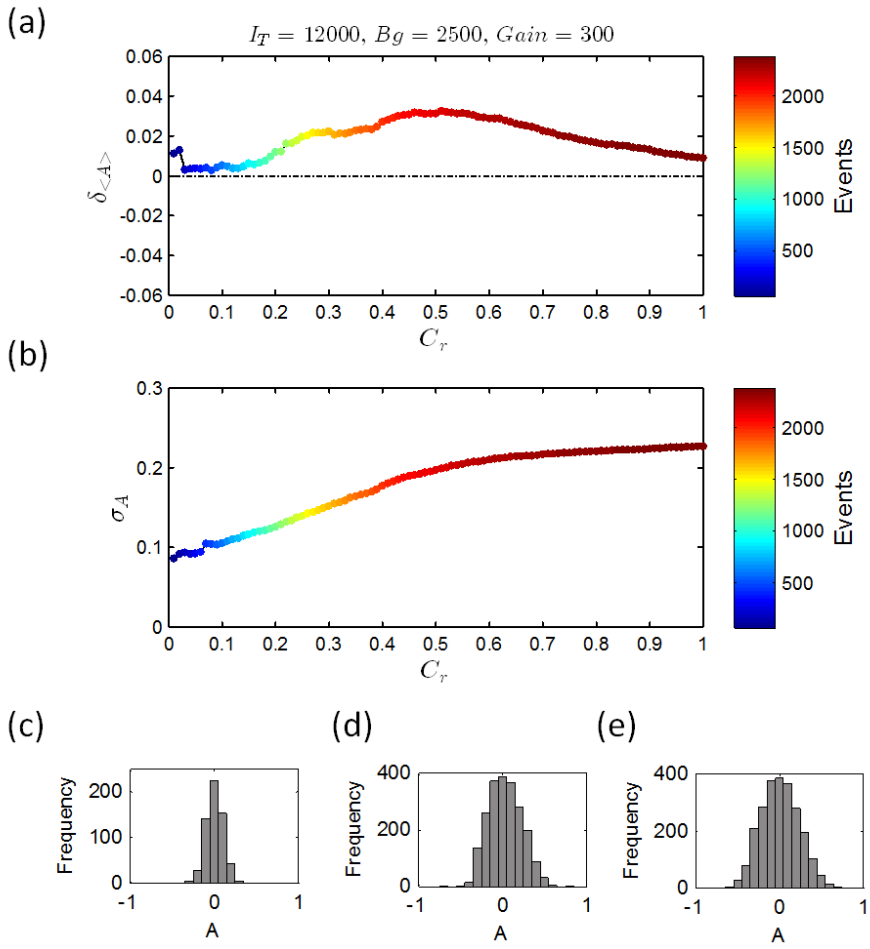

Figure 4.18: Dependence of (a) $\delta_{<A>}$ and (b) σ_A on the C_r factor defined in the text, for $A_{exp} = 0$. (c) Histogram of anisotropy for $C_r = 0.1$. (d) for $C_r = 0.5$. (e) for $C_r = 1$. Conditions: I_T = 12 000 counts, B_g =2500 counts, camera gain = 300.

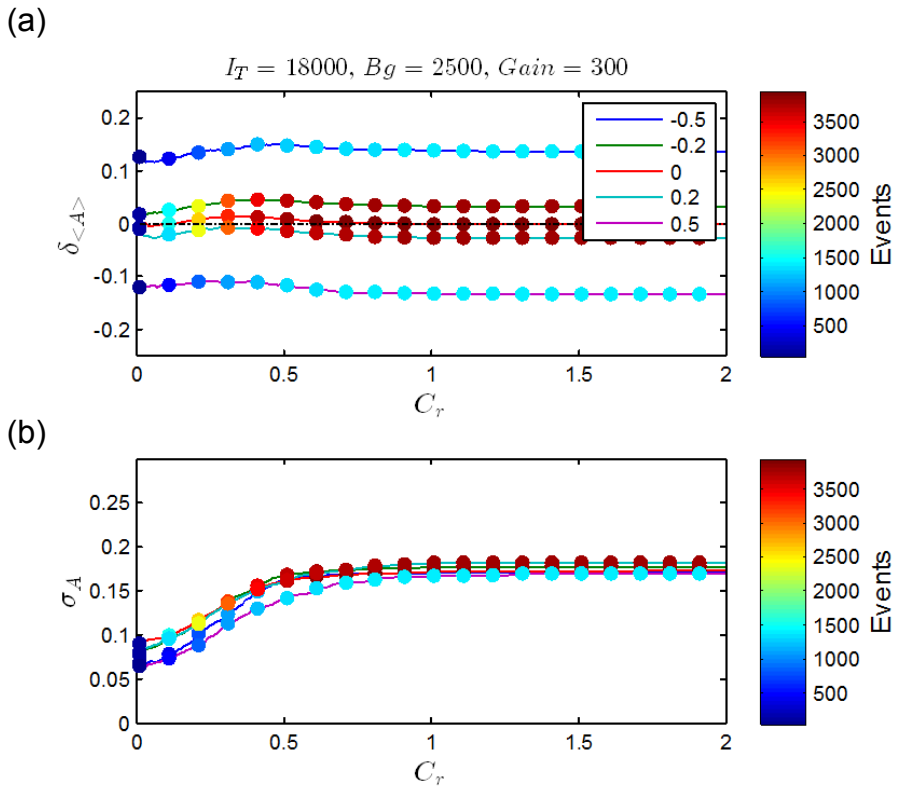

Figure 4.19: Dependence of (a) $\delta_{<A>}$ and (b) σ_A on the C_r factor defined in the text, for various A_{exp} values. Conditions: B_g =2500 counts, camera gain = 300 and I_T = 18 000 counts.

selection balance on the obtained quality of the anisotropy estimation. The reason is probably that for this anisotropy the $\parallel$ and $\perp$ images are of similar intensities, therefore we would not expect a big difference in localization precision for both images.

For more various expected anisotropies, the results depicted in Fig. 4.21 show that the effect of C_σ on the improvement of the anisotropy estimation starts occurring at quite high anisotropy values (A_{exp} = -0.5, 0.5), which is explained by the fact that for such anisotropy values, the $\parallel$ and $\perp$ images show quite different intensities, the lower intensity image being associated with a loss of localization precision. Filtering the data with such a process is furthermore delicate because it will tend to retain only molecules which have a similar localization precision

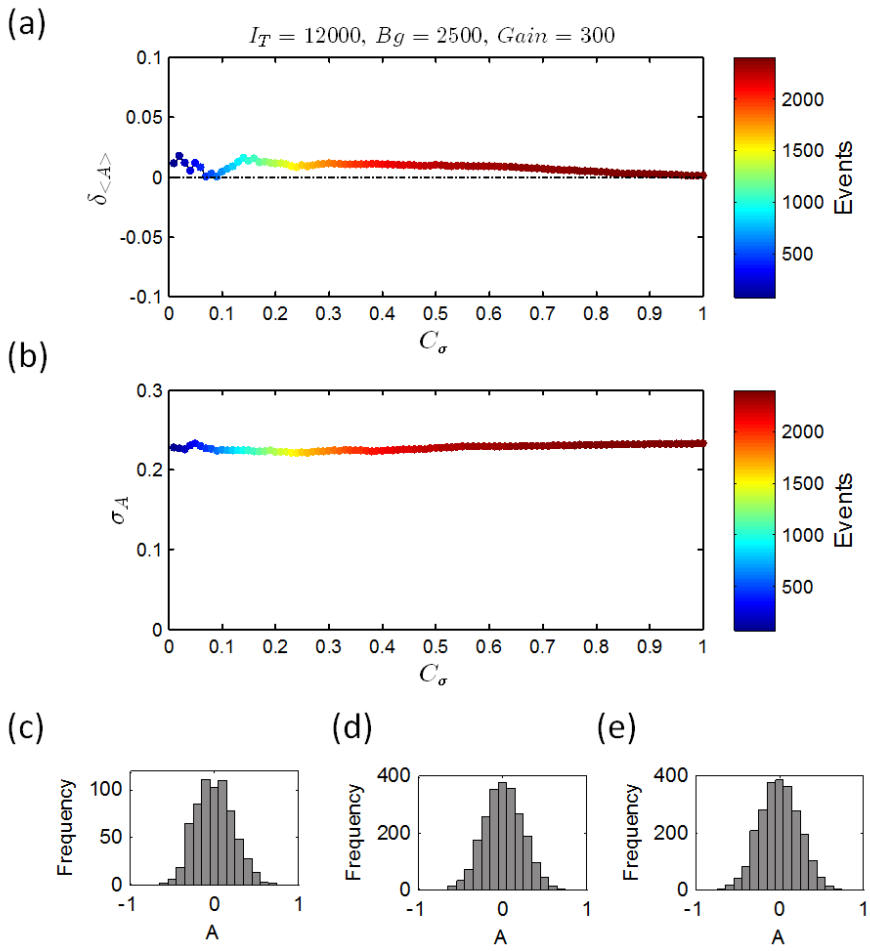

Figure 4.20: Dependence of (a) $\delta_{<A>}$ and (b) σ_A on the C_σ factor defined in the text, for $A_{exp} = 0$. (c) Histogram of anisotropy for $C_\sigma = 0.1$. (d) for $C_\sigma = 0.5$. (e) for $C_\sigma = 1$. Conditions: I_T = 12 000 counts, B_g =2500 counts, camera gain = 300.

on both sides of the polarized image, which is associated to molecules of certain anisotropy values which are not too big. This introduces therefore an artificial bias.

Overall in this analysis it has been shown that two kinds of filtering on the data can be useful when trying to improve the anisotropy determination and

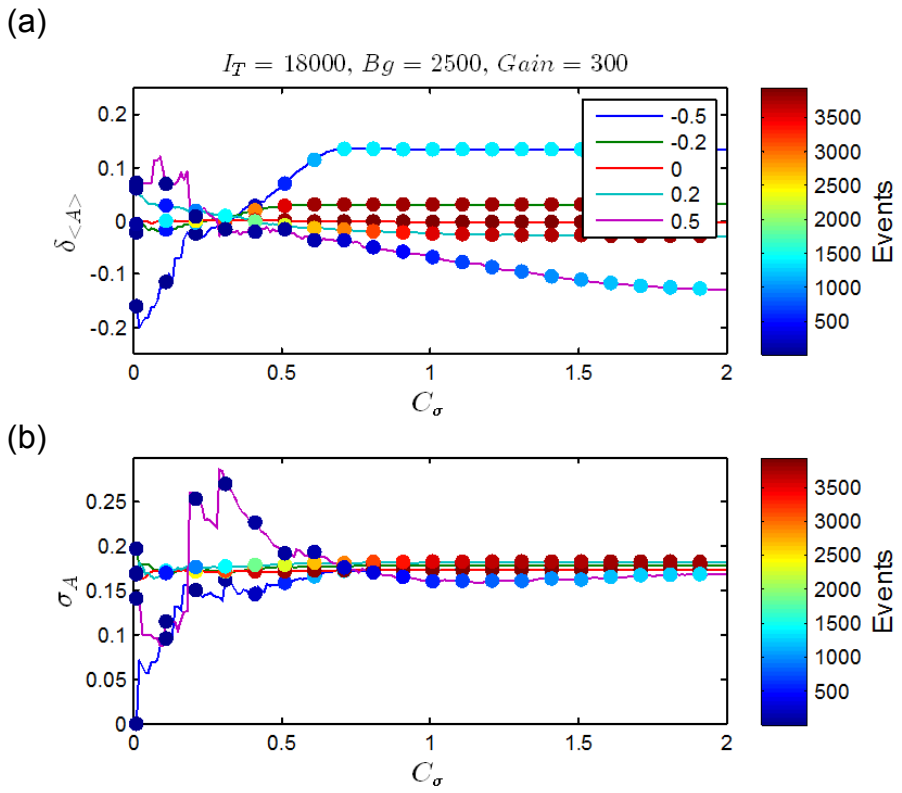

Figure 4.21: Dependence of (a) $\delta_{<A>}$ and (b) σ_A on the C_σ factor defined in the text, for various A_{exp} values. Conditions: B_g =2500 counts, camera gain = 300 and I_T = 18 000 counts

precision: the total intensity and the balance between Gaussian fit radius.

4.2.3 Result of data processing on a sample with randomly oriented, stationary molecules

The examples described above treat the problem of determination of a single molecule. In what follows, we consider an ensemble of molecules which possess random values of anisotropies due to their stationary angular position. This example is a good illustration of what happens on an anisotropy histogram when bias and loss of precision occur. For this simulation, 90 dSTORM images were simulated, each of them includes 41 pairs of molecules with different anisotropies ranging from -1 to 1. The frame size is 512x512 pixels in order to contain all the considered molecules at sufficient inter-distance. For this situation, the expected mean anisotropy is $\langle A \rangle = 0$ and the anisotropy histogram should resemble the one of Fig. 4.3a (with limits [-1 1]).

Figure 4.22 presents a typical raw simulated fluorescence image for a sample in this case.

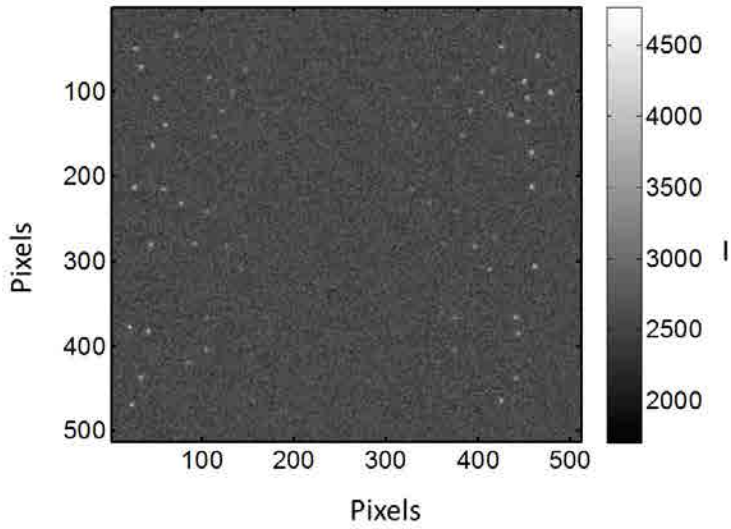

Figure 4.22: Raw simulated fluorescence image of fixed molecules with random, fixed orientations. Conditions: I_T 30 000 counts, window size = 11 pixels and PSF radius = 1.7 pixel.

The result of the "detection" algorithm of the polar-dSTORM analysis is shown in Fig. 4.23.

The final anisotropy image is shown in Fig. 4.24, showing a large variety of values as expected.

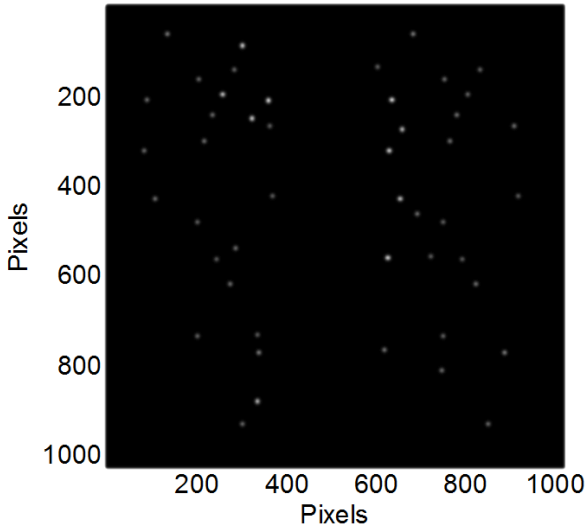

Figure 4.23: Super resolved image of the simulated data (zoom = 2 ×, meaning a pixel size reduced by a factor 2 with respect to the initial image).

The localization precision and radius histograms are represented for the ∥ image in Fig. 4.25). As expected, a wide range of radius and localization precision values are obtained, due to the wide range of intensities involved to generate a large range of anisotropy values.

Histograms of anisotropy obtained for various values of the total intensities are shown in Fig. 4.26. Clearly these histograms do not resemble Fig. 4.3a, the main reason being the ineffective molecular localization on the ∥ or ⊥ image when the anisotropy value is extreme (indeed for A = -1,1, there is a maximum intensity on one side and a weak or not measurable intensity on the other polarization). This is due to the fact that the polar-dSTORM algorithm is based on single molecule detection in both polarization channels for an accurate determination of the anisotropy, the drawback being this blindness to molecules purely oriented along the ∥ or ⊥ axes. Since most of our studies are performed in fibrillar structures with a careful analysis at different fibers orientation, this limitation is not determining in our study and the fiber orientation can be chosen accordingly.

We observe nevertheless that in the best conditions (high-I_T, low-camera gain and low-B_g), the obtained histogram is still large with only A absolute values above 0.6 poorly represented. This become worse for more degraded experimental conditions, the total intensity being a determining factor.

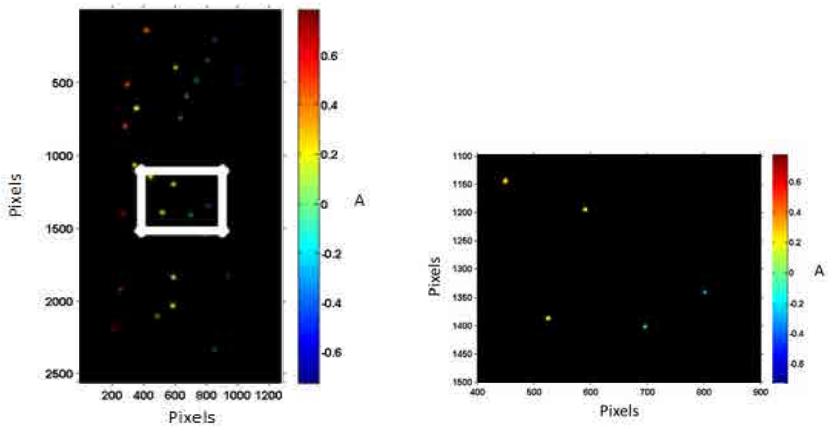

(a) (b)

Figure 4.24: Super resolved anisotropy image obtained from the polar-dSTORM algorithm run on the images as shown in the previous figures (Zoom = 5 ×).

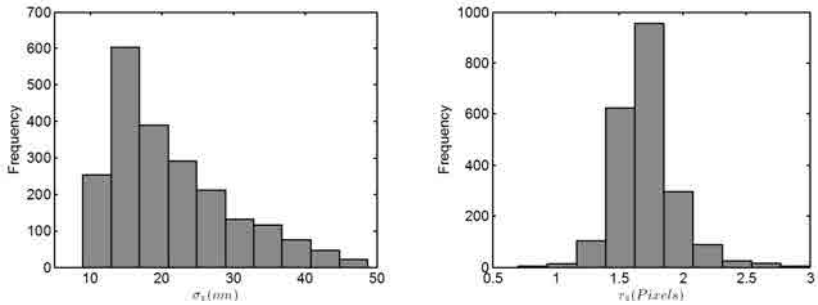

(a) (b)

Figure 4.25: Histograms obtained from the polar-dSTORM analysis on simulated data for a sample containing a wide range of anisotropies: (a) Localization precision for the ∥ image (assuming pixel size = 107 nm) (b) Radius histogram obtained in the ∥ image (expected value = 1.7 pixels).

In order to visualize if statistical analysis of an ensemble of fixed molecules can be improved under the filtering conditions introduced in the previous section, we performed a C_r and C_σ filtering as described above. This study was performed for a various set of intensities, background and camera gain, only one being

represented here. Figure 4.27 shows the variation of the anisotropy bias $\delta_{<A>}$ and histogram-width (represented by σ_A) for a low intensity case, as a function of the C_r factor of filtering imposed on the single molecules analysis.

Figure 4.27 is representative of low I_T values conditions. It shows first that $\delta_{<A>}$ varies only slightly with C_r but in a way that is not controlled (there is no clear trend, even though high filtering (low C_r) permits to obtain low bias). The histogram width does not vary considerably however the histogram shape does. Indeed the expected histogram shape (as flat as possible) is obtained only for high filtering conditions ($C_r < 0.1$). This is even more true in high background conditions, which tend to bias a lot the anisotropy determination. Similarly as discussed above, a filtering in radius is therefore a good solution to exclude molecules for which the anisotropy error can be induced by a imbalance between the images quality. Note that for high I_T there is however not much gain in performing such filtering: indeed a low C_r value will disregard the very different intensity level cases, which are also relevant molecules in this situation.

The results in terms of C_σ filtering are shown in Fig. 4.28. Similarly as for C_r there is no striking variation of $\delta_{<A>}$ and σ_A, and the statistical results seem rather to be more affected by the filtering than without. There is even no specific gain in terms of histogram shape, which stays quite constant whatever the C_σ filtering conditions. The more important feature in this study is the strong decrease in the number of molecules investigated, following the same trend that in cases where all the anisotropy values might be present, a too strong filtering is a risk to exclude molecules which exhibit specifically very different intensity in both polarized images.

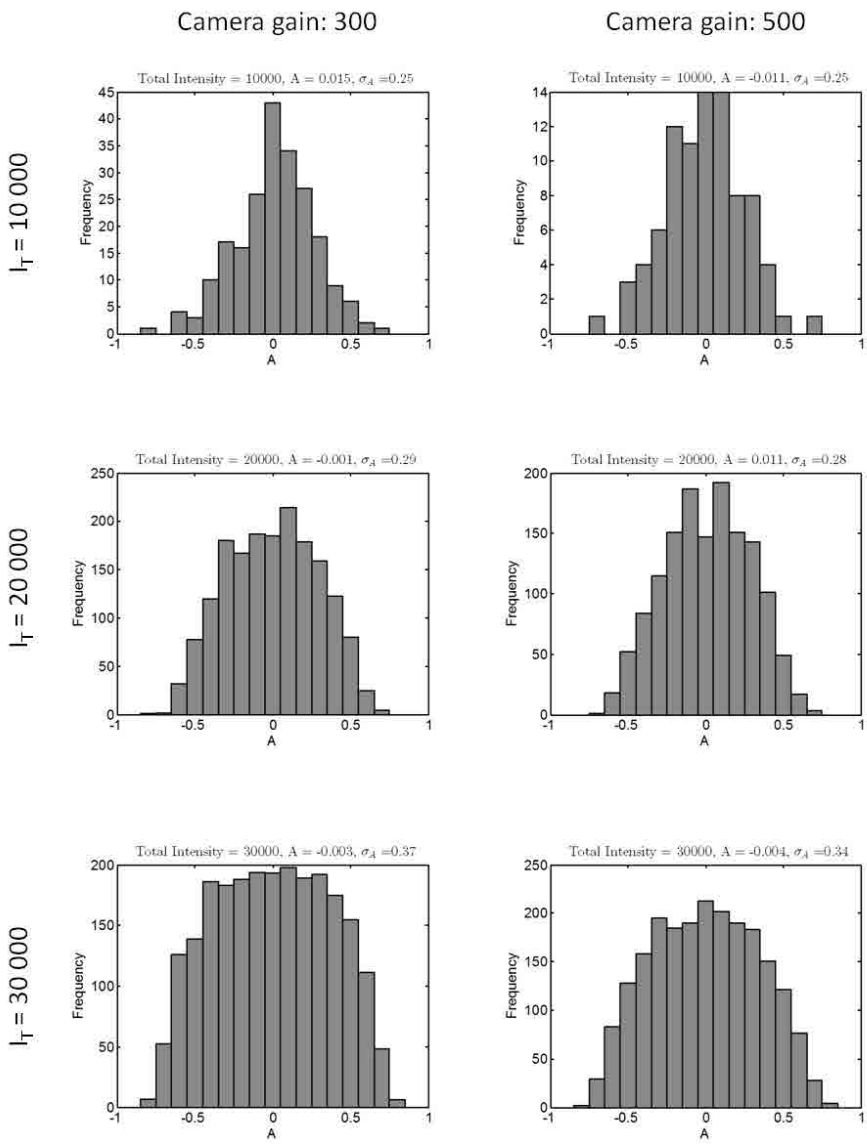

Figure 4.26: Anisotropy histograms obtained from the polar-dSTORM analysis on simulated data for a sample containing a wide range of anisotropies. I_T = 10 000, 20 000, 30 000 counts, B_g = 1500 counts, camera gain = 300, 500.

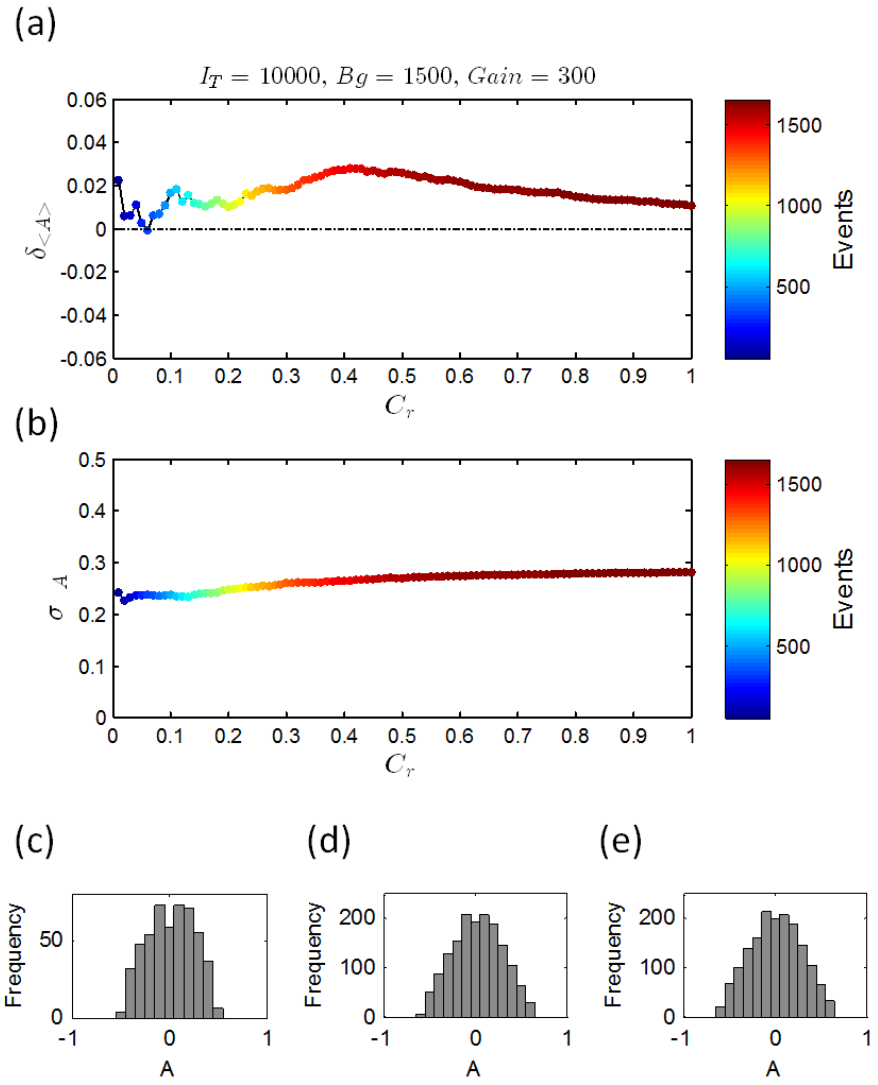

Figure 4.27: Filtering based on the radius criterion (C_r factor) in a situation with randomly oriented, stationary molecules. Dependence of (a) $\delta_{<A>}$ and (b) σ_A on C_r, for $A_{exp} = 0$. (c) Histogram of anisotropy for $C_r = 0.1$. (d) for $C_r = 0.5$. (e) for $C_r = 1$. Conditions: I_T = 10 000 counts, B_g =1500 counts, camera gain = 300.

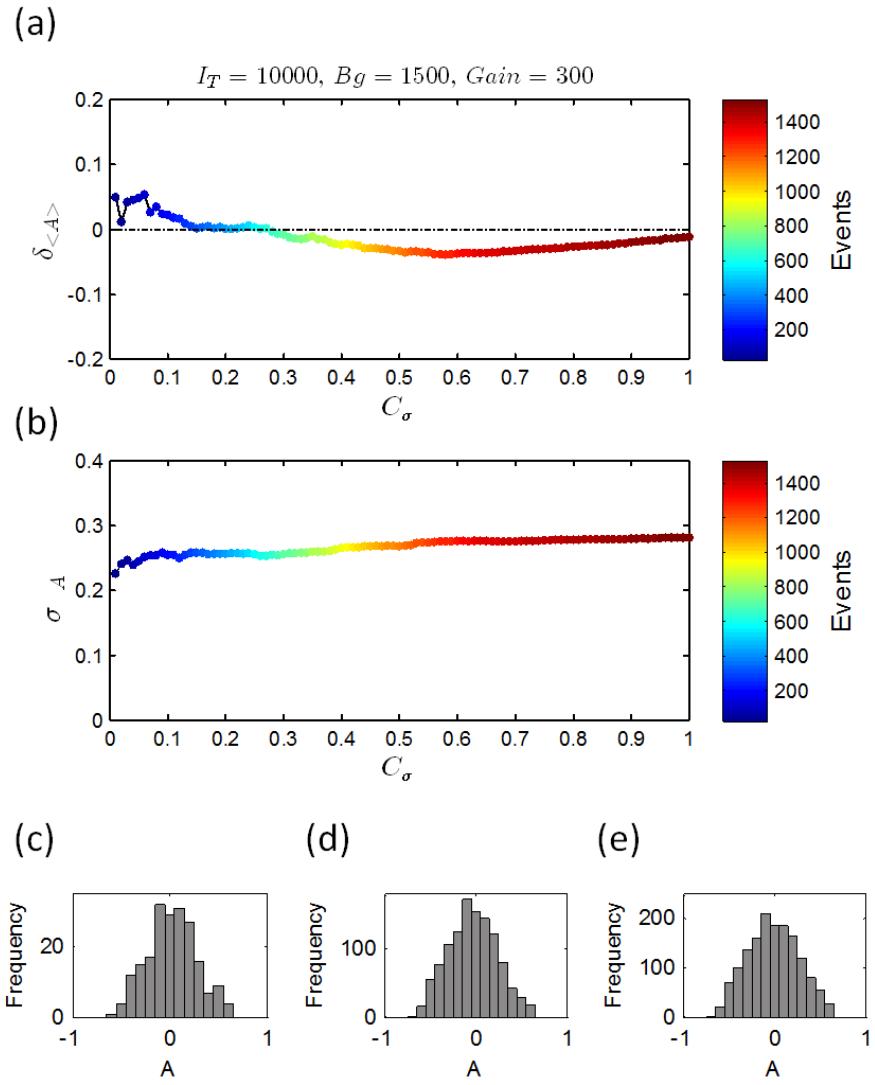

Figure 4.28: Filtering based on the radius criterion (C_r factor) in a situation with randomly oriented, stationary molecules. Dependence of (a) $\delta_{<A>}$ and (b) σ_A on C_r, for $A_{exp} = 0$. (c) Histogram of anisotropy for $C_\sigma = 0.1$. (d) for $C_\sigma = 0.5$. (e) for $C_\sigma = 1$. Conditions: I_T = 10 000 counts, B_g =1500 counts, camera gain = 300.

4.3 Conclusion

In this Chapter, a theoretical approach was presented, to validate the correct anisotropy estimation by the polar-dSTORM algorithm. First, a simple model was implemented in order to predict the rough behavior of anisotropy statistical results in a few key cases, involving stationary versus non-stationary molecules, and constraint versus non-constraint orientational order. Even though this model is based on simplified situations (2D, non Brownian motion), it is adapted to study the relevant observations in the frame of this work. The results are systematically presented in anisotropy histograms, which serve as a basis for understanding the observed behaviors in the future experiments.

In order to account for experimental factors (total intensity, background, camera gain) in the expected anisotropy histograms, we performed a complete polar-dSTORM analysis on simulated images, taken from Monte Carlo simulations which include the noise parameters defined in the experimental Chapter. This simulation allowed us defining possible determining parameters in the anisotropy estimation, in particular its bias relative to an expected value, and its precision given by the standard deviation.

Generally it was noticed that the total intensity is a determining factor for both the bias and estimation precision of the anisotropy, as can be naturally understood from noise. This effect however depends on the anisotropy absolute value, which is related to the fact that high-anisotropy corresponds to low-intensity on one side of the polarized image. We gave in this Chapter an estimation of the bias and error expected from typical situations met in the experimental data, which will serve as a basis for understanding the obtained statistics.

We finally implemented a tentative filtering criterion to improve bias and errors, based on radius and localization precision analysis when fitting single molecules by Gaussian functions. These criteria (in particular the radius balance analysis) might be useful in populations where the anisotropy range is not very large, which might require a preliminary knowledge or check of the anisotropy statistics. The filters introduced in this Chapter will therefore be systematically tried on situations where they are expected to improve the obtained statistics.

Chapter 5

Application of polar-dSTORM in biological samples

This chapter describes the application of the polar-dSTORM in biological samples. First, the method is validated on known nano-objects made of bright, zero-anisotropy emitters (fluorescent nano-beads), and the limits related to signal to noise level are illustrated. Second, the method is applied to different samples corresponding to specific situations in terms of signal to noise, background, anisotropy distributions, which require each an application of the methodology developed in the previous chapter. Results and interpretation are presented for: randomly oriented molecules attached to poly-L-lysine, labelled tubulin and actin in fixed cells, as well as, labelled actin, amyloid peptide fibrils and DNA fibers immobilized on a surface in vitro. Finally, a study on freely diffusing single molecules is described in order to evaluate the feasibility of the technique on mobile emitters freely rotating in a viscous medium.

5.1 Anisotropy of fluorescent nano-beads

In order to simulate experimentally an "ideal" case in terms of noise, background and intensity, an analysis on very bright emitters of known anisotropy (nano-beads) is presented. For this experiment, blue nano-beads (Fluospheres diameter 20nm, 625-645 nm, Invitrogen ®) were used. The anisotropy is expected to be zero, due to the complete depolarization of the signal (the reason is the strong fluorescence resonant energy transfer between randomly oriented in the nano-beads). Widefield image of the beads is presented in Fig. 5.1.

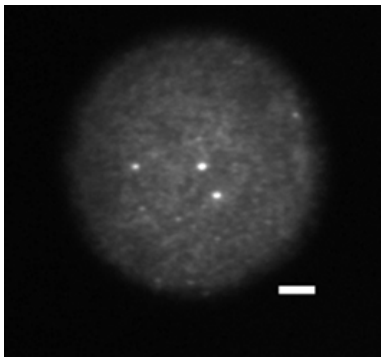

Figure 5.1: Widefield image of nano-beads directly attached to the coverslide. Scale bar: 5 μm.

5.1.1 Fixed nano-beads

The first experiment was performed on fixed beads attached to cover glass, the beads concentration was adapted to visualize only few of them ($\sim$ 4 to 30 beads in the field of view). A 20 μL droplet of $\sim$ 10 nM of 20 nm fluorescence beads was placed on a glass coverslip and allowed to evaporate slowly. Then the sample was washed two times with milli-Q water in order to remove non-fixed beads. The sample was illuminated with 639 nm wavelength at an excitation power of 0.5 mW/cm^2. The experimental conditions are: background signal = 1 500 counts, camera gain: 1. The dSTORM stack for this sample was $\sim$ 6 000 frames. Localization precision obtained from polar-dSTORM analysis: $\sim$ 35 nm.

Figure 5.2a shows a polar-dSTORM image of the fluorescent nano-beads, as well as its corresponding anisotropy histogram. The number of events participating to this histogram is quite high since the nano-beads constantly emit during the dSTORM stack, with a progressive bleaching. As expected, the anisotropy histogram is centered on $<$A$>$ = 0, however the distribution is quite large and the retrieved standard deviation $\sigma_A = 0.13$ shows that there is an influence of less precisely localized beads which affects the final variation of anisotropy.

Due to the widefield illumination used in polar-dSTORM and the strong brightness of the observed nano-beads, it is possible to detect a few nano-objects which are out of focus. In order to avoid these out of focus events and to visualize only the anisotropy from the most reliable events, we perform a filtering of intensity, radius and localization precision, as described in the previous chapter, getting a lower anisotropy variation of $\sigma_A \sim 0.05$.

It is important to note that the level of counts reported in Fig. 5.2 and the associated noise cannot be directly related to the results obtained in the

previous chapter, due to the low camera gain, which implies a lower intrinsic noise variation. Based on the intensity dependent Poisson model described in the previous chapter, the standard deviation of the noise for a camera gain of 300 is approximately two times higher than the standard deviation of the noise for a camera gain of 1.

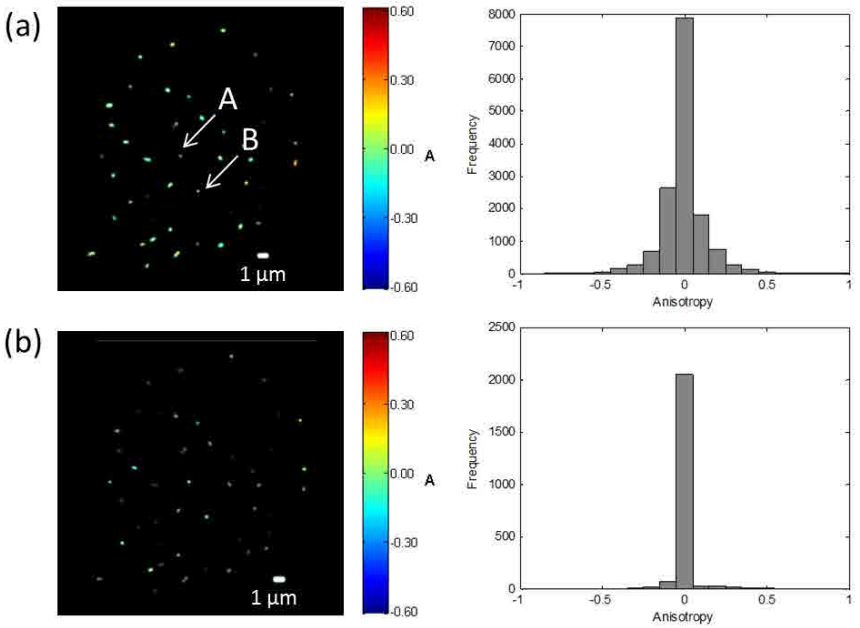

Figure 5.2: polar-dSTORM anisotropy analysis image of fixed nano-beads. Pixel size = 53 nm, size of blurring Gaussian = 30 nm. (a) No intensity restriction. Anisotropy variation: $\sigma_A = 0.13$ and (b) Restriction: $I_T > 8000$ counts, C_r=0.5 and C_σ=0.5 (see Chapter 4). Anisotropy variation: $\sigma_A = 0.06$. [Right side: anisotropy histogram. Left: polar-dSTORM image.]

In order to reach on optimal signal to noise condition, we selected two particular beads (Fig. 5.3) which intensity is quite constant (low bleaching) and high ($I_T > 20\ 000$ counts). As a consequence, the variation of anisotropy obtained is small ($\sigma_A \sim 0.005$), corresponding to a localization precision of 10 nm. This value can be considered to be the lowest possible anisotropy variation for a sample analyzed with polar-dSTORM, in a sample with fixed emitters.

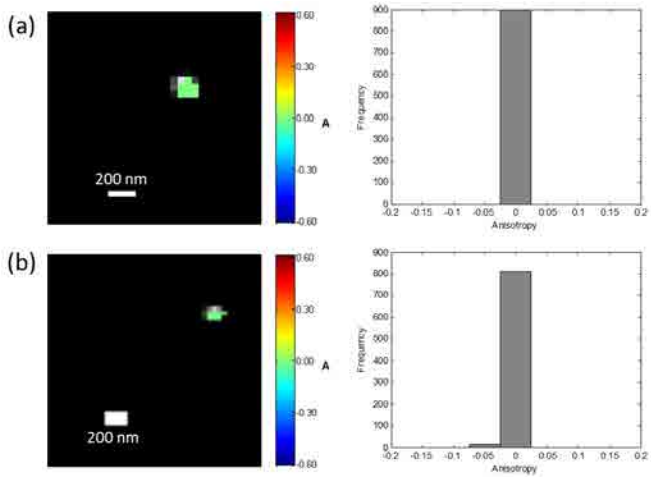

Figure 5.3: Single fixed nano-beads of bright intensity. The anisotropy image is super-imposed with the dSTORM image (grey). Pixel size = 53 nm, blur = 30nm. (a) Bead A in Fig. 5.2a, $\sigma_A = 0.005$ and $I_T = 26\ 000$ counts. (b) Bead B in Fig. 5.2a, $\sigma_A = 0.006$ and $I_T = 22\ 000$ counts. [Right side: anisotropy histogram. Left: polar-dSTORM image.]

5.1.2 Moving nano-beads

In a second validation test, fluorescent nano-beads freely diffusing in Glycerol 80 %(w/w) were analyzed. Anisotropy analysis of single nano-objects diffusing in a medium, allows simulating more difficult conditions (for instance involving PSF deformation due to motion) with the idea of later studying properties from the environment at nanometric scale, such as viscosity and temperature (see section 5.6).

Widefield image of moving beads are show in Fig. 5.4.

As the case of fixed beads, the anisotropy histograms are expected to be narrow. Nevertheless due to bad estimated events, which are out of focus but also slightly deformed, σ_A is higher than 0.1 (Fig. 5.5a). If we apply similar filtering as above in terms of total intensity, radius and localization precision, then the anisotropy variation lowers down to 0.1 (Fig. 5.5b). Moreover, if we apply a more strict restriction in terms of localization precision and radius, we are able to obtain $\sigma_A = 0.06$ (Fig. 5.5c).

This study shows that the estimation of the anisotropy in polar-dSTORM is extremely sensitive to the quality of the localization of the detected events, with an obvious loss of precision in the case of PSF deformation due to defocus or

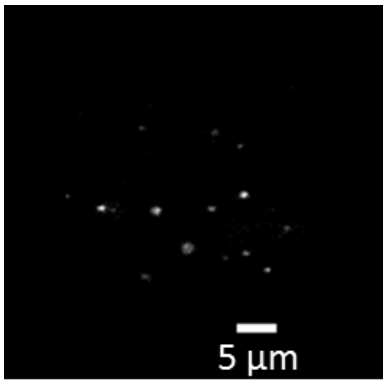

Figure 5.4: Widefield image of nano-beads (Fluospheres 20 nm, 625-645 nm, Invitrogen ®) freely diffusing in Glycerol 80 % (w/w).

emitter motion. It shows nevertheless that in the ideal case of very bright emitters over negligible background, an estimate precision of $\sigma_A \sim 0.005$ is reachable with our experimental set-up, which validates its use for further analysis in biological samples.

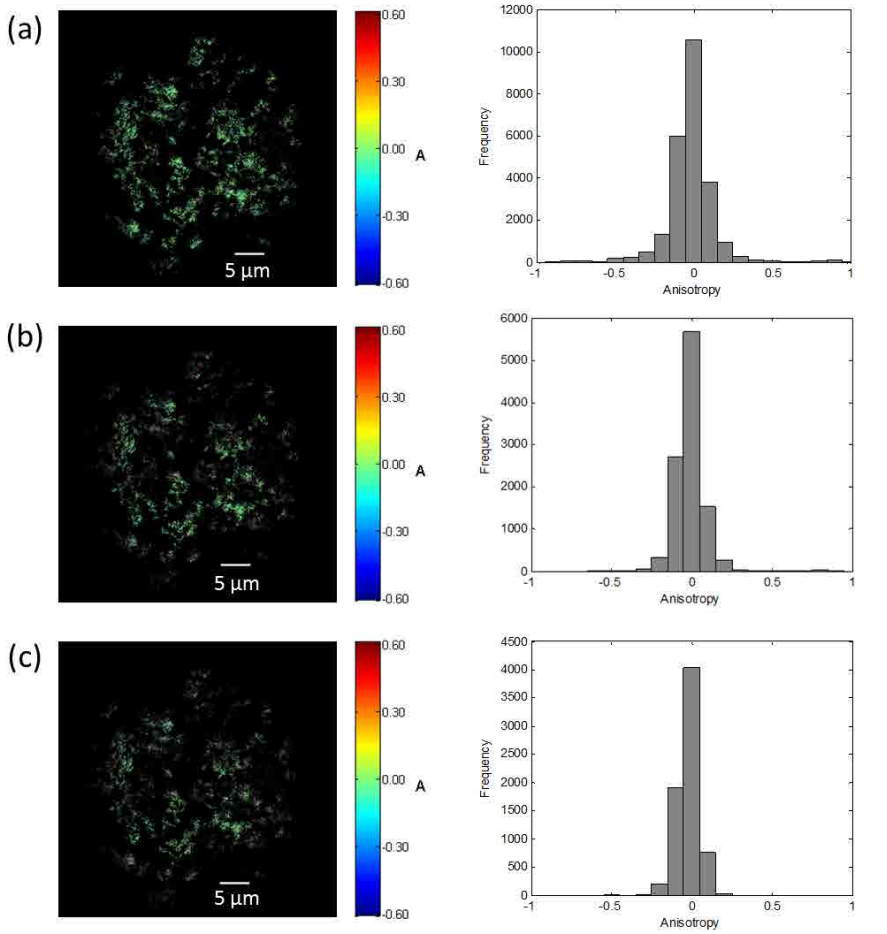

Figure 5.5: polar-dSTORM anisotropy analysis of nano-beads freely diffusing in Glycerol 80 % (w/w). Pixel size = 53 nm and gaussian blur = 30nm. (a) No intensity restriction, $\sigma_A = 0.17$. (b) Restriction: $I_T > 8000$ counts, C_r=0.5 and C_σ=0.5, $\sigma_A = 0.1$. (c) Restriction: $I_T > 8000$ counts, C_r=0.2 and C_σ=0.2 , $\sigma_A = 0.06$ [Right side: anisotropy histogram. Left: polar-dSTORM image (grey), super-imposed with anisotropy image (color).]

5.2 polar-dSTORM anisotropy imaging of randomly fixed single molecules

As mentioned in the theoretical analysis in the previous chapter, for fixed molecules attached to the sample surface with random orientations, we expect an anisotropy histogram with a wide range of value which extent depends on the signal conditions.

To model this case experimentally, molecules of Atto 633 attached to a Poly-L-lysine coated slide were analyzed give experimental conditions. The polar-dSTORM anisotropy image is presented in Fig. 5.6a. The obtained single molecule localization is about 25 nm on average.

The anisotropy results in a shape which resembles a narrow peak centered on an average anisotropy of 0 (Fig. 5.6b). This shape is far from being realistic since one would expect a large collection of random anisotropy from molecules fixed in both angles and positions.

For this image, the average of the total intensity retrieved is 17 000 counts (Fig. 5.7) and the anisotropy standard deviation (σ_A) is 0.289, similar to the value expected from the simulation analysis ($\sigma_A = 0.29$ for total intensity = 20 000 counts) (see Chapter 4).

As mentioned in the previous chapter, the anisotropy estimation is mostly governed by the total intensity level. Although many molecules were detected, the histogram is clearly deformed due to photon noise. When a further filtering is performed based on the total intensity, much less molecules are measured (Fig. 5.8a) and the consequent histogram shape is significantly changed (Fig. 5.8b). The resulting shape has been obtained using a filtering of $I_T > 30\ 000$ counts, which should lead to a standard deviation of anisotropy of about 0.1 (for A = 0) to 0.14 for more extreme anisotropies values (A = 0.8). As we can observe from the image the number of molecules selected decreases but the precision increased in the anisotropy estimation. The new anisotropy histogram width for this sample is 0.4, similar to what is expected from our simulation (0.37), for a camera gain= 300 and a total intensity = 30 000 (see Chapter 4).

Note that the measured histogram does not reach maximal values A = (-1, 1) since in those cases one side of the image does not contain any detectable events due to almost vanishing intensities. As a consequence there is an intrinsic bias in the detected histogram that has to be accounted for in the data interpretation. This is why we systematically compare an experimental results with simulations which effectively account for these anisotropy values in the initial parameters.

Finally based on this simple experiment, one can deduce a few important properties of single molecules anisotropy imaging : (1) the precision and bias of anisotropy determination depend majorly on the detected total intensity; (2) this can have important consequences on the interpretation of the statistical analysis

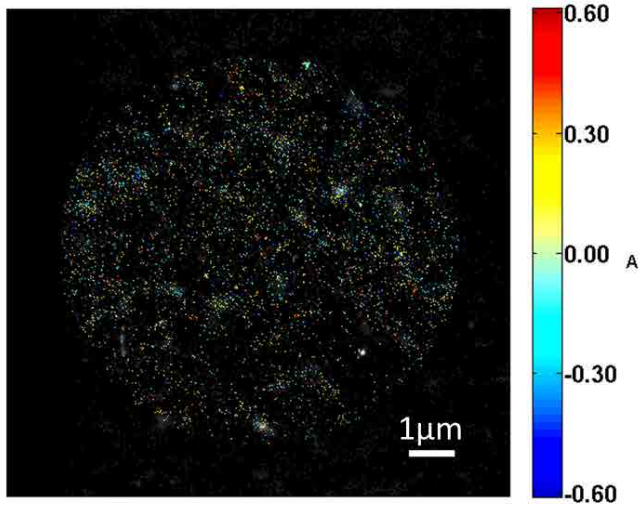

(a)

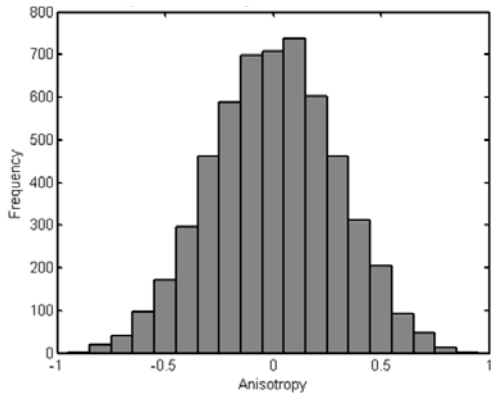

(b)

Figure 5.6: polar-dSTORM anisotropy analysis of Atto 633 attached to a Poly-L-lysine coated coverslide. (a) polar-dSTORM anisotropy image (color), superimposed to the dSTORM image (grey). (Pixel size = 21.4 nm) (b) Anisotropy histogram.

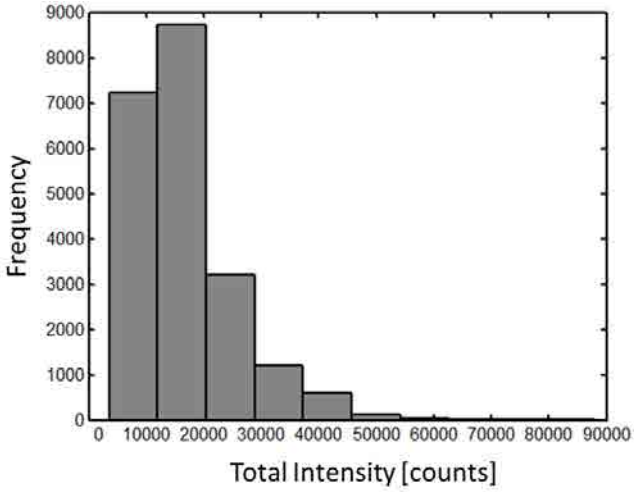

Figure 5.7: Total intensity histogram obtained from Fig. 5.6 for Atto 633 attached to a Poly-L-lysine coated coverslide.

on single molecules which should be known and accounted for; (3) this will also have important consequences on anisotropy super-resolution imaging, since the intensity conditions ensuring proper anisotropy estimation are intrinsically correlated with the localization precision: as long as the total intensity values are above a certain limit (which should be kept ideally above 20 000 for reasonable estimation conditions), anisotropy imaging can be combined with super resolution and provide reliable structural imaging. This will be however at the expense of a loss of a high number of molecules which could be used for pure dSTORM imaging.

5.3 polar-dSTORM anisotropy imaging in fibers structures in fixed cells

Microtubules

Tubulin labeled with Alexa 647 was imaged using polar-dSTORM in fixed COS 7 cells, and rendered as a super-resolution anisotropy (see Fig. 5.9a). In order to guarantee the right estimation of anisotropy still with a reasonable amount of molecules, only events with total intensity higher than 10 000 were selected. Regarding resolution, the localization precision average obtained from the anisotropy

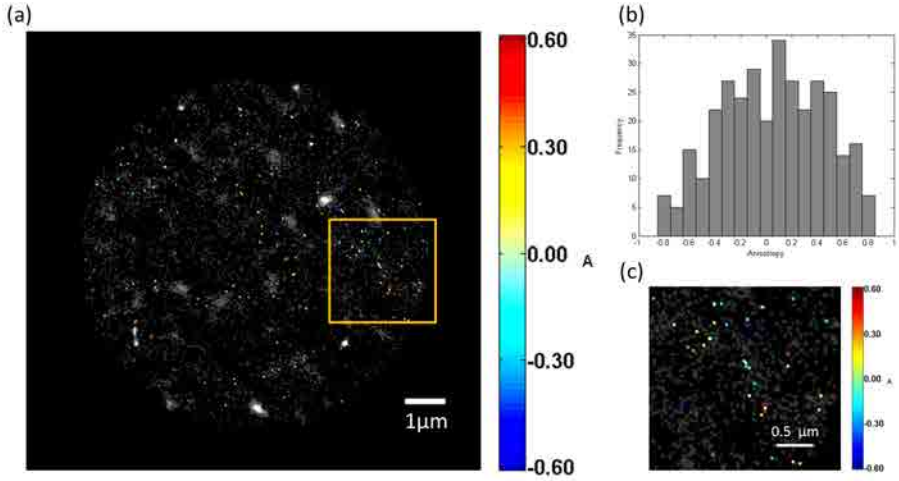

Figure 5.8: polar-dSTORM analysis of Atto 633 molecules attached to a Poly-L-lysine coated coverslide with a total intensity minimum of 30 000 counts. (a) polar-dSTORM anisotropy image (pixel size = 21.4 nm). (b) Anisotropy histogram. (c) Zoom in selected area (orange square).

events is 18 nm.

More careful analysis of isolated fibers shows that the experimental conditions impose a resolution of the order of 60 nm (Fig. 5.9b). A zoom on single molecules belonging to tubulin fibers shows that the anisotropy values are essentially centered on 0 (Fig. 5.10, 5.11). The anisotropy histogram obtained from isolated fibers does not seem to depend on the fiber orientation (Fig. 5.11), resembling the situations investigated theoretically for $\psi > 170°$ (see Chapter 4).

Following the analysis described in the polar-dSTORM methodology (see Chapter 4), more information can be gained from the investigation of anisotropy averages obtained from fibers of different orientations (Fig. 5.11). Indeed comparing the obtained value of fibers of known orientations ρ (see Chapter 3 for a direct evaluation of ρ) to the theoretical plot A (ρ,ψ) obtained from a statistical cone model, it is possible to retrieve a numerical value for the orientational constraint ψ undergone by the molecules (Figure 5.11). As can be observed in Fig. 5.10, the retrieved ψ value for different ρ orientations is equal to 180° which represents a totally disordered behavior. This higher disorder is most probably due to the flexible linker between the tubulin fibers and the probe dye Alexa 647, due to the presence of the two antibodies. As detailed in Chapter 4, more information can be gained from the shape of the A histogram obtained from isolated

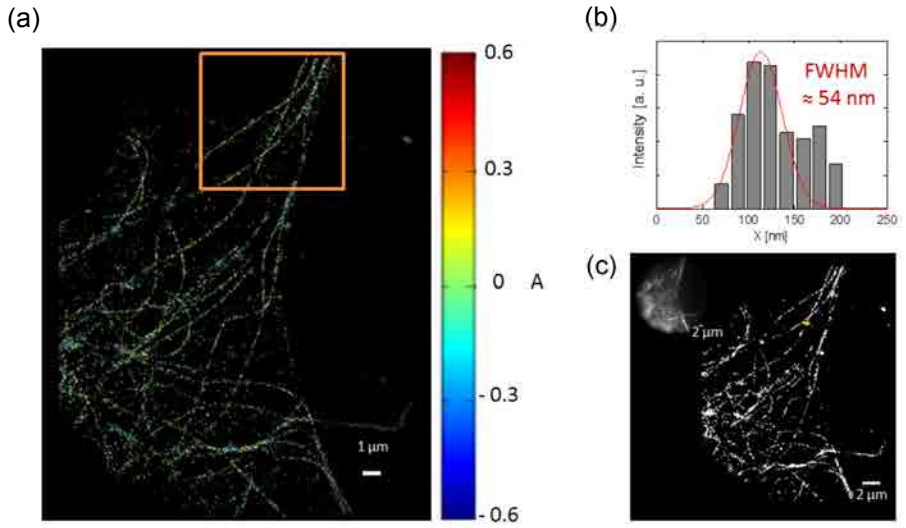

Figure 5.9: polar-dSTORM analysis of tubulin in COS 7 cells labeled with Alexa 647. (a) polar-dSTORM image, pixel size = 17nm. (b) Full Width Half Maximum (FWHM). (c) Super resolved image, pixel size = 17 nm and Gaussian blur: 25 nm. Inset: widefield image.

portions of fibers. The obtained standard deviation from one experimental data is of the order of $\sigma_A = 0.2$, which seems large but is still corresponding to the noise limit expected from the experimental conditions (see Chapter 4).

Indeed for this analysis, the minimum total intensity was set to 10 000 counts, that will imply a σ_A higher than 0.18 (which is the value we obtained theoretically for $I_T = 18\ 000$ counts. In order to test the improvement in precision in the anisotropy estimation with the signal level, one selected fiber is analysed with a higher threshold of a total intensity I_T of 15 000 counts (Fig. 5.12). This restriction implies a decrease of σ_A from 0.17 to 0.15, of course concomitant with a decrease of the number of selected events from 274 to 72. It is worth to notice that the obtained σ_A is smaller than the case shown in the simulation results for $I_T = 15\ 000$ counts, which can be due to a slightly different background value (here Bg $< 2\ 500$ counts).

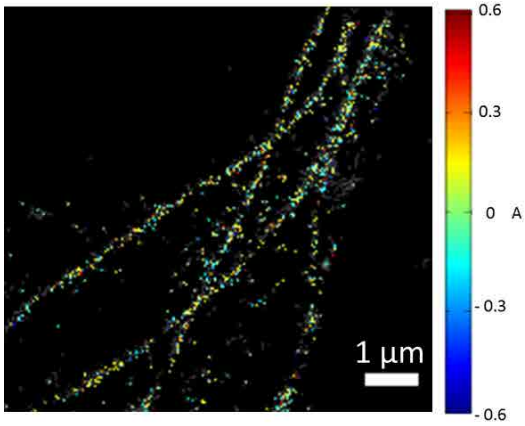

(a)

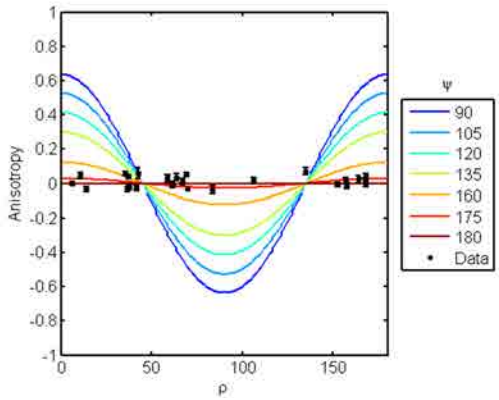

(b)

Figure 5.10: polar-dSTORM analysis of tubulin fibers in COS 7 cells labeled with Alexa 647. Left: zoomed region of anisotropy image, $I_T > 10\,000$ counts, pixel size = 17 nm and Gaussian blur: 25 nm. (Orange square inset of Fig. 5.9a). Right: anisotropy average measured on isolated tubulin fibers (markers with bars: standard error of the mean (SEM)) and simulated anisotropy (cont. lines) as a function of ρ and ψ).

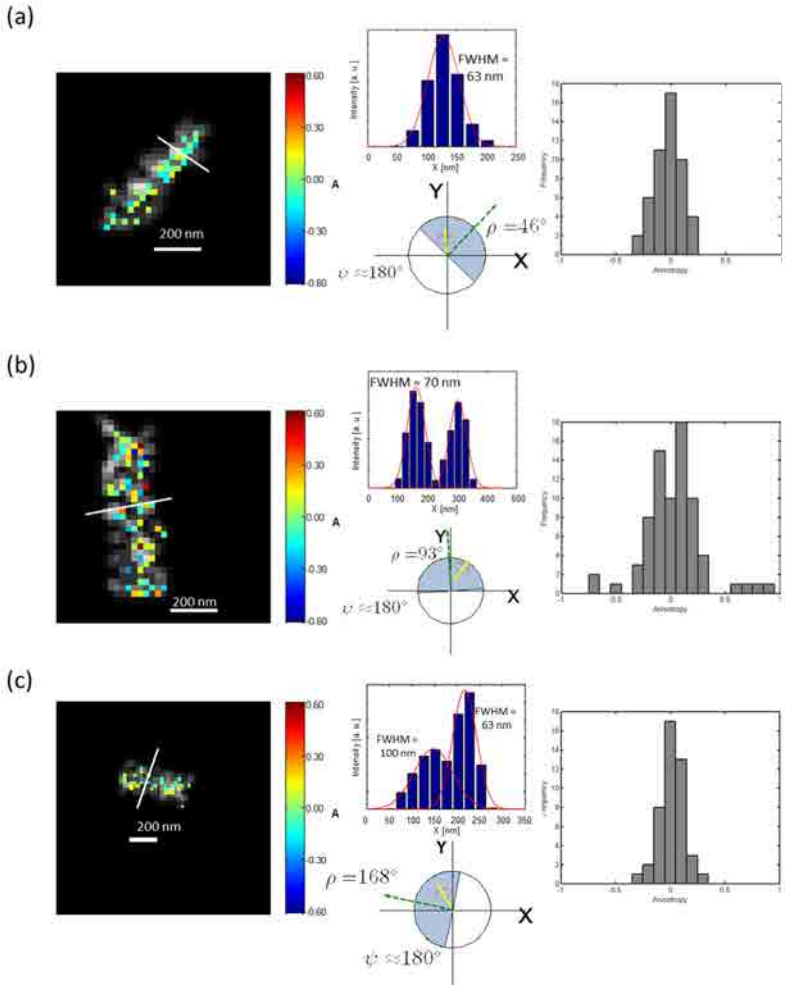

Figure 5.11: polar-dSTORM anisotropy analysis isolated tubulin fibers in COS 7 cells, labelled with Alexa 647 for different ρ angles (color: anisotropy image; grey: dSTORM image). Total Intensity $>$ 10 000 counts, pixel size = 25 nm and localization precision for depicted molecules used as a value for Gaussian (blur): 30nm. Orientation measured by cluster analysis (see Chapter 3) (a) $\rho = 46°$. (b) $\rho = 93°$. (c) $\rho = 168°$. [Left: polar-dSTORM anisotropy image, center-up: FWHM, center-low: schematic molecule distribution based on the obtained cone model and right: anisotropy histogram.] The dashed line points the ρ direction while the yellow line shows a single molecule fluctuating in orientation.

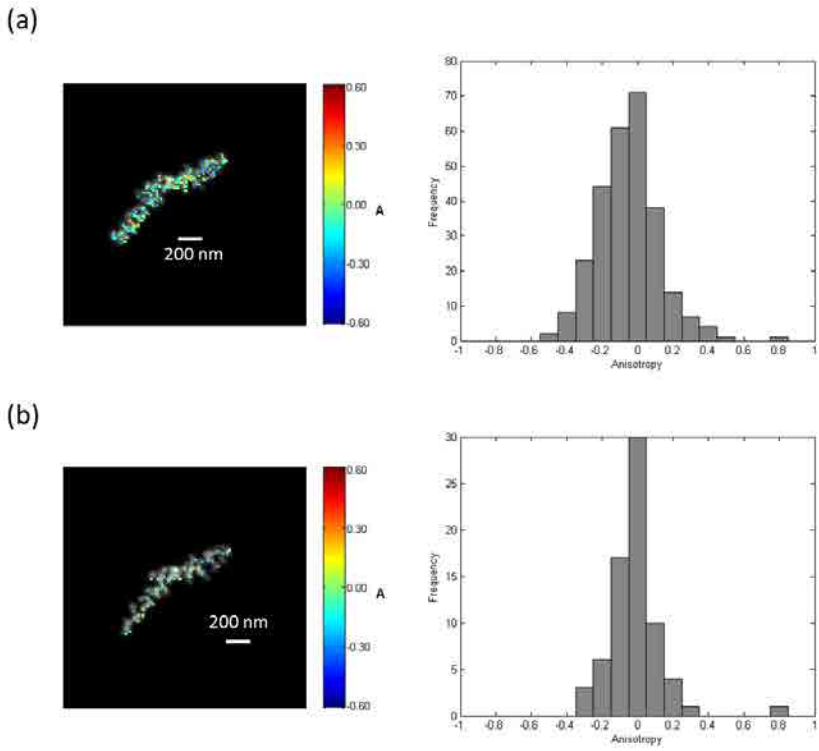

Figure 5.12: Intensity influence on the anisotropy estimation. Sample: isolated tubulin fiber in COS 7 cells, labelled with Alexa 647. (a) No restriction of intensity, $\sigma_A = 0.17$. (b) $I_T > 15\,000$ counts, $\sigma_A = 0.15$. [Left: polar-dSTORM Image.(Pixel size: 17 nm, Gaussian blur of STORM image (gray): 30 nm) Right: Anisotropy histogram]

Finally we can conclude that the obtained histogram width is clearly limited by our experimental condition (I_T, B_g in particular). This proves that the observed orientational behavior is highly dynamic and furthermore isotropically oriented. The Alexa 647 dye attachment to the tubulin fibers obviously leaves a high degree of flexibility with fluctuations faster than the CCD integration time (30 ms), which can be understood from the non-rigid linker and the presence of water in the cells even through they are fixed.

Actin

Experiments were performed on oriented actin stress fibers in fixed cells. Order in actin fibers labelled with phalloidin in vitro [13] and in cells [12, 43] has been probed previously by fluorescence microscopy as described in the introduction, using ensemble measurements.

Experiments were performed on oriented actin directly labeled by phalloidin-Alexa 488 in COS 7 cells.

Figure 5.13 depicts dSTORM anisotropy imaging (Fig. 5.13a), Contrary to the results obtained previously on tubulin, the anisotropy undergoes changes of value depending on the fiber orientation, which is a signature of the presence of order. Note that we mostly see here fiber bundles which form a more complex meshwork [92]. This effect is even observed within a single fiber bundle which locally changes its orientation (Fig 5.14). In zoomed parts (Fig. 5.15), fiber bundles exhibition anisotropy which varies with the orientation of the fibers in a way which is a signature for orientational constraint of the dyes along the fiber. This orientational constraint is known to exist in such systems and has been previously reported using ensemble imaging techniques combined with linear dichroism approaches [43].

In such measurement, it has been found that the label undergoes a statistical (spatial and/or temporal) orientational disorder within an aperture angle of about 130° - 140°. However, these measurements cannot decipher the dynamic nature of the orientational behavior. In order to guarantee the right estimation of anisotropy and reliably interpret our data, only events with total intensity higher than 20 000 counts were selected. Localization precision average for the anisotropy events is 27 nm (minimum: 7 nm), and Full Width Half Maximum in a selected thin fiber is 17 nm (Fig. 5.13b), which proves the functionality of super-resolution for our technique.

In the present observations, a further insight on the orientational behavior is brought by the observation of anisotropy histograms from individual portions of actin fibers (Fig. 5.15). The anisotropy histograms are shown to be quite narrow with a width limited by instrumental noise ($\sigma_A = 0.13$), while their average is varying when the fiber orientation is tuned. First, the extent of this variation of A can tell us about the dynamic motion of the label attached to phalloidin. Indeed if the label was totally static it could explore a wide range of A values, which we estimate to be about [-0.8, 0.8] due to the bias, induced by the experimental signal and background conditions (ideally, A $\in$ [-1, 1]). This is clearly not the case here: even for horizontal fibers the maximum reachable A value is about 0.6. This tells us that each molecule undergoes some dynamic motion (at time scale $<$ 30ms) around a mean orientation value. To know the angular extent of this dynamic motion, we analyse the dependence of the $<$A$>$ mean values obtained for different fibers orientation (Fig. 5.14). The experimental points ($<$A$>$ be-

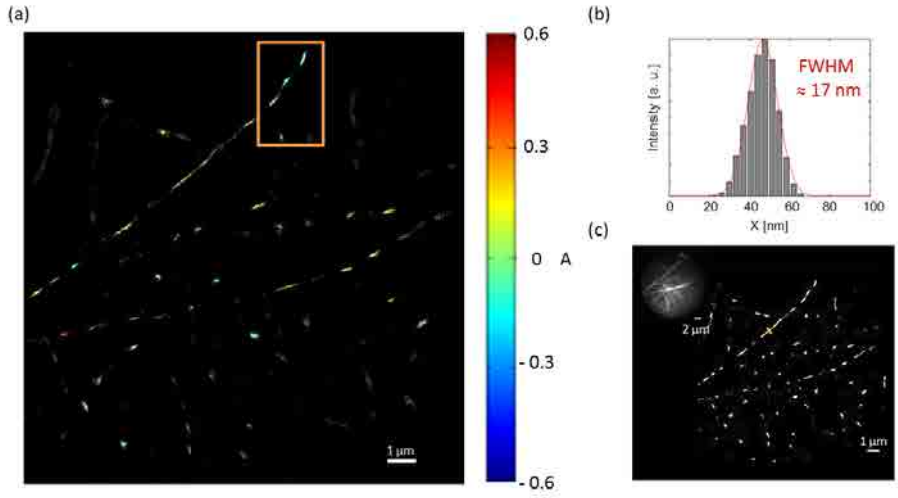

Figure 5.13: polar-STORM analysis of actin fibers in COS 7 cells directly labeled with phalloidin-Alexa 488. (a) polar-dSTORM anisotropy image, pixel size=10.7 nm, blur = 25 nm. (b) Full Width Half Maximum (FWHM). (c) Super resolved image, pixel size=3.6 nm and gaussian blur: 15 nm. Inset: widefield image.

ing in the range [-0.35, 0.35]) follow well a theoretical model where the molecules would be dynamically ($\tau_{rot} < 30$ ms) rotating within a total angular constraint of $\psi \sim 130°$, oriented on average (ρ) along the fiber itself. A closer look at individual histograms in Fig. 5.15 can give us more information on the angular behavior of this motion. Some models (based on F-actin labelling) have indeed speculated that the molecule could undergo rapid motion within a smaller angular range ($\delta \sim 40 - 80°$) within a cone which itself tilted azimuthally around the fiber [11]. If it was the case, then the molecules would be able to reach very high anisotropy values (about [-0.8, 0.8]) in particular for vertical or horizontal fibers. This is clearly not observed here. The histogram widths are rather limited by our experimental conditions (noise, background) which shows that for each fiber orientation ρ, all molecules behave with the same orientational behavior. In order to confirm the contribution of experimental conditions to the histogram width observed, we performed further filtering procedures to the data such as introduced in Chapter 4. Finally the explored range of <A> values tend to confirm a dynamical motion within the whole angular aperture $\psi \sim 130°$ for all molecules. This value is also consistent with order previously measured in phalloidin-labelled in intestinal microvilli cells, $\psi \approx 104°$ in [12], obtained previously by fluorescence microscopy (the data were measured only on horizontal fibers). Recently, $\psi \approx 137°$ has been

retrieved by polarization-resolved fluorescence microscopy for phalloidin-stained actin stress fibers in COS 7 cells [43].

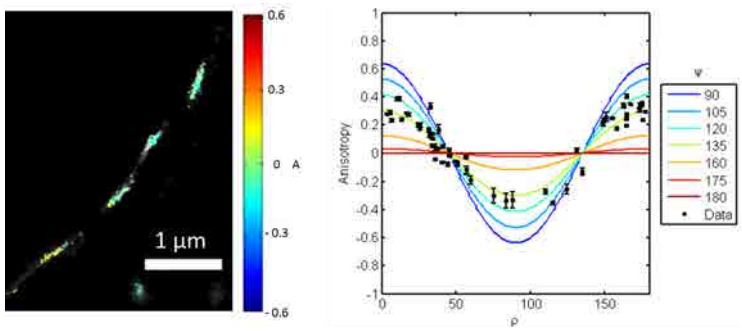

(a) (b)

Figure 5.14: polar-dSTORM analysis of actin fibers in COS 7 cells directly labeled with phalloidin-Alexa 488. Right: zoomed region of anisotropy image, $I_T > 20$ 000 counts, Bg $\sim$ 1 800, pixel size=10.7 nm and blur = 25 nm. (Orange rectangle inset of Fig. 5.13a). Left: anisotropy average measured on isolated single actin fibers (markers with bars: standard error of the mean (SEM)) and simulated anisotropy (cont. lines) as a function of ρ and ψ).

However, these measurements were performed on ensemble averaging: the single molecule approach used here proves that this motion is highly dynamic within the time scale of the CCD integration time. This is probably governed by the fixation procedure which leaves a large degree of freedom to small molecules for rotational diffusion. Nevertheless in the phalloidin binding mechanism [22], a remaining orientational constraint is imposed which is experienced by the fluorescent molecule. The super-resolution images coded in anisotropy cannot however report at this stage the precise structural information on actin (twisted regions) because of the high degree of mobility left.

Using a filtering on the "radius" of the PSF, which imposes r to be fitted on both $\parallel$ and $\perp$ images with high and identical precision, we introduced a constraint on the parameter C_r in a specific actin label phalloidin-Alexa 488 fiber. This filter shows that for $<A> = 0$ it is in principle possible to further increase the precision in the anisotropy estimation (σ_A) from 0.15 to 0.07 (see Chapter 4). We observe experimentally an decrease of (σ_A) from 0.15 to 0.075 ($C_r = 0.1$) down to 0.06 ($C_r = 0.05$) (although in this case the number of events decrease from 152 to 30, making the (σ_A) value less reliable). Nevertheless this sensitivity of σ_A to C_r tends to confirm that the observed histogram width is indeed related to noise and experimental factors.

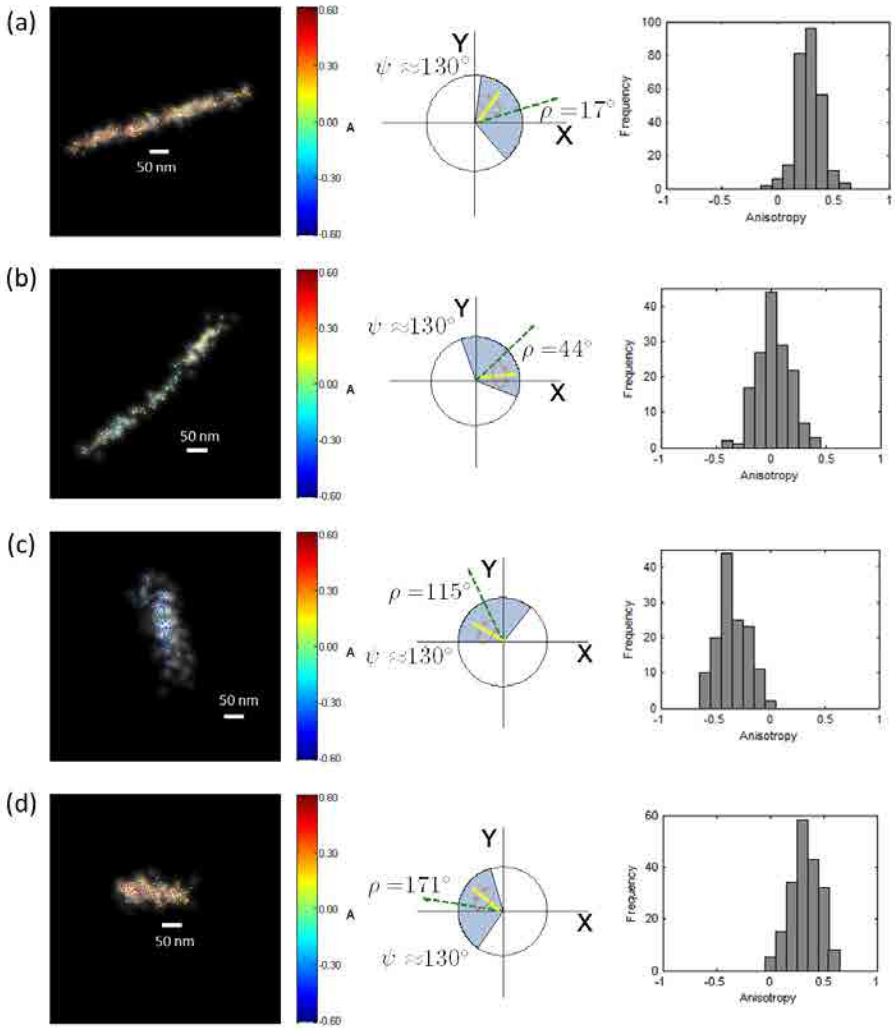

Figure 5.15: polar-dSTORM anisotropy analysis of isolated Actin fibers in COS 7 cells, labelled with phalloidin-Alexa 488 for different fiber orientation angles (the ρ and ψ values here are given based on a dynamic model ($\tau_{rot} < 30$ ms) within a cone aperture ψ along the ψ angle which corresponds to the fiber orientation). $I_T > 20\,000$ counts, pixel size = 3.6 nm and localization precision for depicted molecules(blur): 15 nm. (a) $\rho = 17°$. (b) $\rho = 44°$. (c) $\rho = 115°$. (d) $\rho = 171°$. Left: polar-dSTORM image, center: molecule distribution based on cone model and right: anisotropy histogram. The dashed line points the ρ direction while the yellow line shows a single molecule fluctuating in orientation.

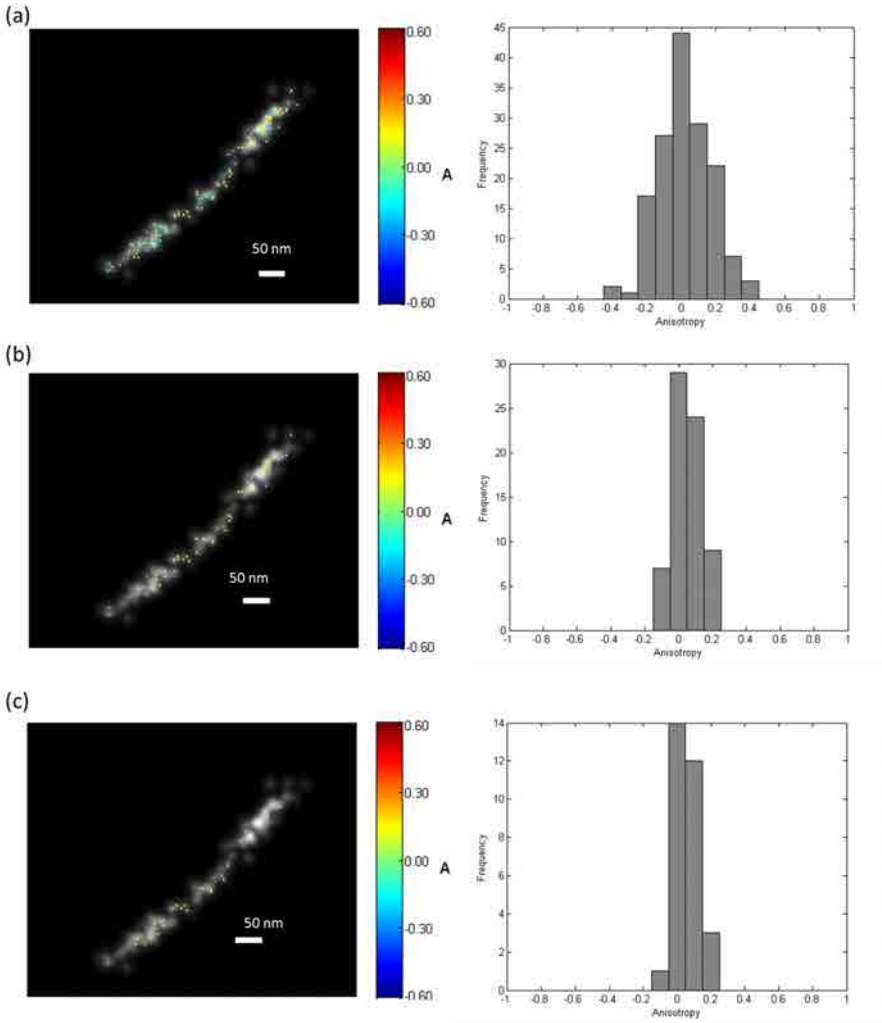

Figure 5.16: Radius influence in isolated actin fiber labelled with phalloidin-Alexa 488 in cells. (a) Without C_r restriction ($< A >$: 0.02, σ_A: 0.15 and events: 152). (b) $C_r = 0.1$ ($< A >$: 0.05, σ_A: 0.075 and events: 69). (c) $C_r = 0.05$ ($< A >$: 0.05, σ_A: 0.06 and Events: 30).

5.4 polar-dSTORM anisotropy imaging in "in vitro" fiber structures

In vitro actin. Actin in vitro fibers labeled with phalloidin-Atto 633 were analyzed with the polar-dSTORM algorithm. Figure 5.17 shows the results obtained on a single fiber. In this case the actin is supposed to be deposited as isolated fibrils, which makes the image analysis much more difficult since the labelling density is probably smaller than in stress fiber bundles in cells. The measured signal per molecule was also slightly smaller. polar-dSTORM imaging (Fig. 5.17a) and in particular zoomed fibers (Fig. 5.18a) show the anisotropy changes with the orientation of the fibers, which is a clear sign for orientational constraint of the dyes along the fiber.

In order to guarantee the right estimation of anisotropy, only events with total intensity higher than 20 000 counts were selected. Localization precision average for the anisotropy events is 65 nm, and Full Width Half Maximum in a selected fiber is 84 nm (Fig. 5.17b), this profile shows that the global resolution is probably not ideal due to low SNR and more delicate drift correction due to sparse structuring.

A further insight on the orientational behavior of the label on F-actin in vitro can be retrieved by the observation of histograms from individual regions of fibers (Fig. 5.19). The anisotropy histograms are shown to be quite large (width $0.3 > \sigma_A > 0.2$), while their average is varying when the fiber rotates. Note that this relatively large width does not necessarily means that the molecular angles are static in time: such situation would lead to histograms covering the whole [-0.8, 0.8] accessible anisotropy range, which is not the case here. Supposing a totally dynamic motion ($\tau_{rot} < 30$ms), the dependence of $<$A$>$ relative to the fiber orientation ρ would lead to a cone aperture of about 135° (Fig. 5.18b). However, contrary to the previous observation on actin stress fiber bundles in fixed cells, we observe here, with the same intensity filtering, much larger histograms. The observation of the shape of these histograms for known fibers orientations (e.g. $90°, 45°$ in Fig. 5.19) tends towards a model in which the molecular dynamics angle would be more constraint ($\delta \sim 90°$) but with an average orientation tilted relative to the fiber orientation ($\beta \sim 30°$) such as the whole exploration of angles would be an effective cone of aperture $\psi \sim 135°$. The angle $\delta \sim 90°$ suggested here for the angular constraint is based on maximum reachable anisotropy value, which do not surpass [-0.6, 0.6] even for horizontal or vertical fibers (note that even with an experimental bias (see Fig. 4.26), values up to [-0.8, 0.8] should be reachable). A deeper analysis of this effect is presented in section 5.5 . Moreover, we do not see any histogram shape change when applying the same filtering as in Fig. 5.16. This model is finally very close to a model developed previously for directly labeled F-actin fiber deposited on myosin (with $\delta \sim 40° - 80°$ and a tilt

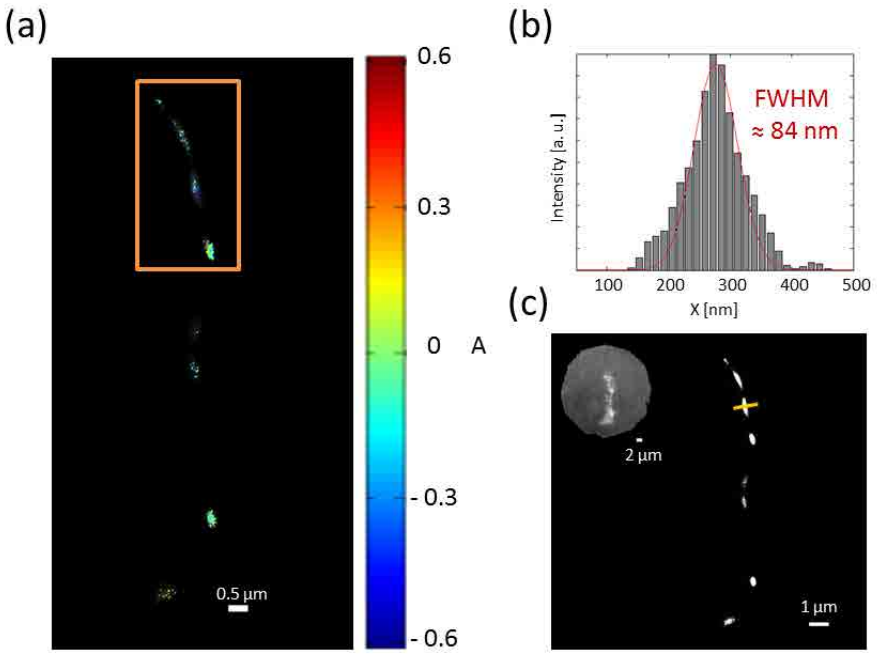

Figure 5.17: polar-dSTORM analysis of actin in vitro labeled with phalloidin-Atto 633. (a) polar-dSTORM anisotropy image, pixel size=13 nm. (b) Full Width Half Maximum (FWHM). (c) Super resolved image, pixel size=13 nm and Gaussian blur: 25 nm. Inset: widefield image.

angle $\beta \sim 50°$ relative to the fiber axis) [11]. The measurement that were required to retrieve this information was based on isolated single molecules observed by more than two polarization settings, during observation times of tens of seconds. Here, even through we do not observe single molecules for a long time, their spatial information helps us to retrieve similar information with the additional capacity to reconstruct super-resolved information.

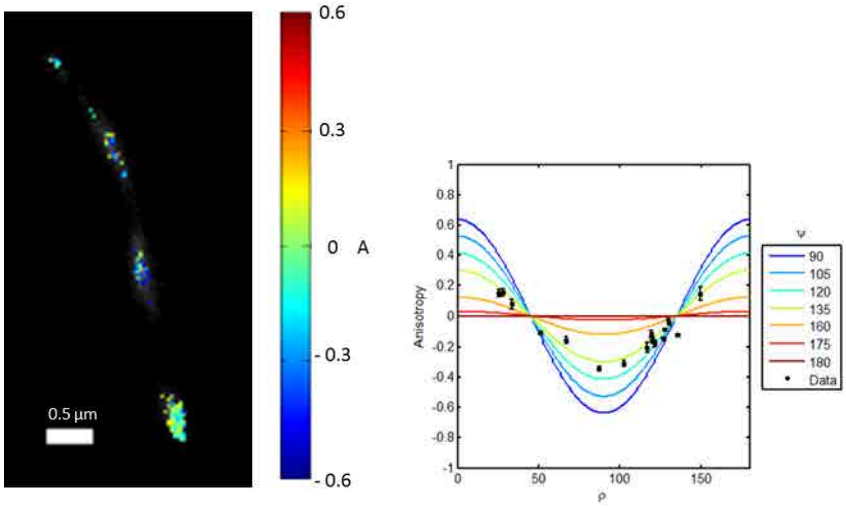

(a) (b)

Figure 5.18: polar-dSTORM analysis of Actin fibers in vitro directly labeled with phalloidin-Atto 633. Right: zoomed region of anisotropy image of actin fiber, I_T > 20 000 counts, Bg > 8 000 counts, pixel size = 13 nm and Gaussian blur: 25 nm. (Orange rectangle inset of Fig. 5.17a). Left: anisotropy average measured on isolated single actin in vitro fibers (markers with bars: standard error of the mean (SEM)) and simulated (cont. lines) as a function of ρ and ψ).

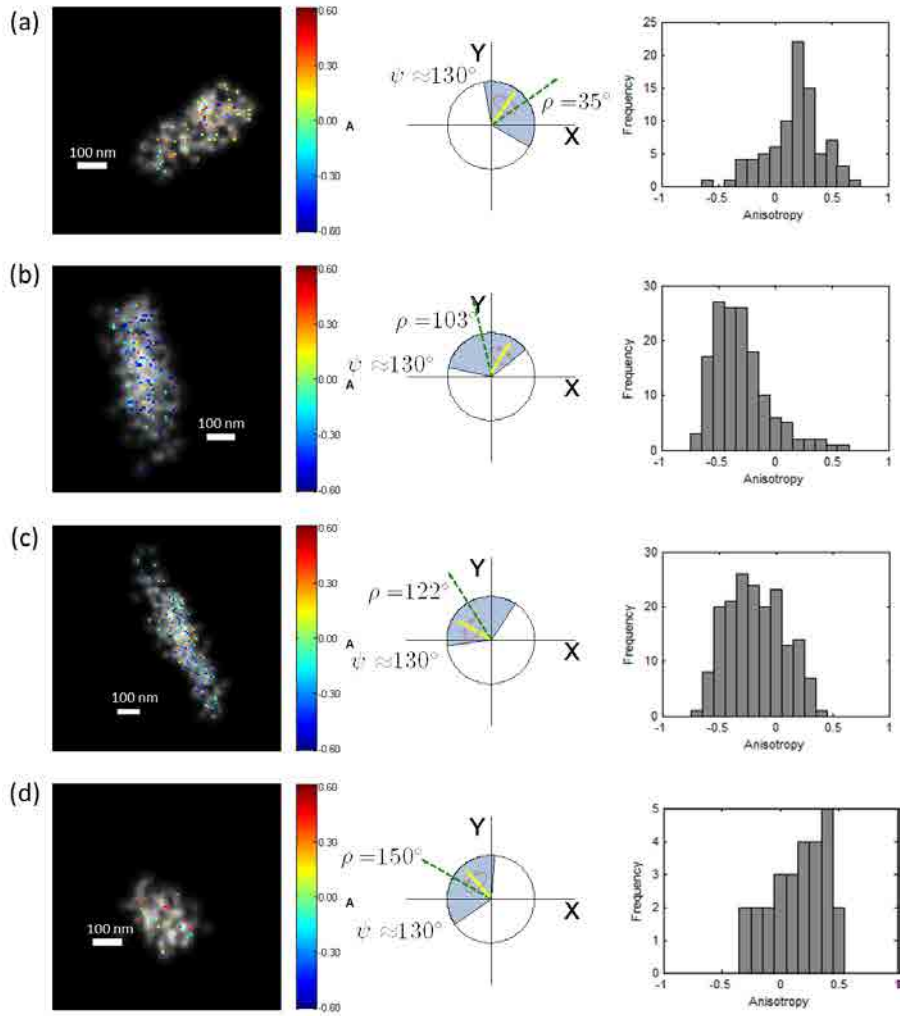

Figure 5.19: polar-dSTORM anisotropy analysis of isolated Actin fibers in vitro, with different fiber orientations given by the ρ angles. $I_T > 20\,000$ counts, pixel size = 8.9 nm and localization precision for depicted molecules(blur): 25 nm. (a) $\rho = 35°$. (b) $\rho = 103°$. (c) $\rho = 122°$ (d) $\rho = 150°$. Left: polar-dSTORM Image, center: molecule distribution based on a full dynamic cone model and right: anisotropy histogram. The dashed line points the ρ direction while the yellow line shows a single molecule fluctuating in orientation.

Amyloid (ThT)

Amyloid fibrils labelled with thioflavine-T (ThT) were analyzed with the polar-dSTORM method. In this sample we could observed by eye striking differences in the retrieved dSTORM images from the $I_{\parallel}$ and $I_{\perp}$ intensities. Due to the high orientation constraint, the parallel (Fig. 5.20c) and the perpendicular (Fig. 5.20a) dSTORM images show respectively majorly vertical and horizontal fibrils only. For this reason we show both reconstruction in addition to the anisotropy image (Fig. 5.21).

Actually, this difference between intensities has to be taken into account, because it induces a different localization precision for both polarization images. In addition, it has been published the effect of the polarization excitation, as well as the molecular orientation, for the position accuracy of fluorophore localization [66, 93, 94].

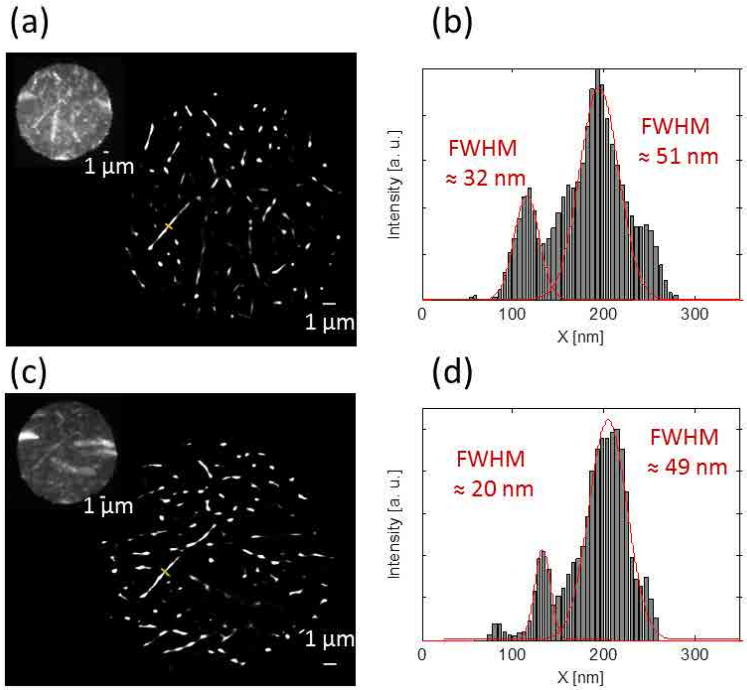

Figure 5.20: dSTORM images of Amyloid fibrils in vitro directly labeled with ThT. Left: Super resolved images: $I_{\parallel}$ (c) and $I_{\perp}$ (a), pixel size=5 nm and Gaussian blur: 15 nm. Inset: widefield image. Right: FWHM.

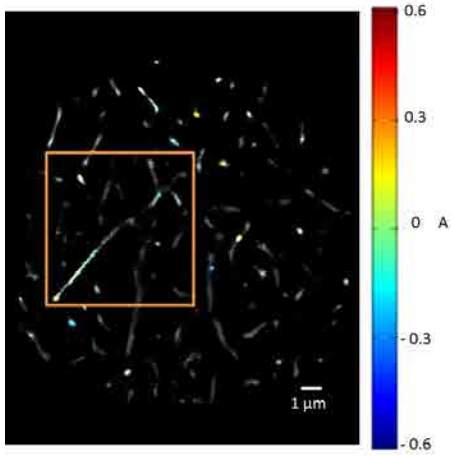

Figure 5.21: polar-dSTORM image of Amyloid fibrils in vitro directly labeled with ThT. $I_T > 20\ 000$ counts, Bg $\sim$ 2 000 counts, pixel size = 5 nm and Gaussian blur = 15 nm.

polar-dSTORM imaging in amyloid fibrils (Fig. 5.21) and in particular zoomed fibrils (Fig. 5.22a) shows that the anisotropy varies strongly with the orientation of the fibrils, which is a clear signature for orientational constraint of the dyes along the amyloid fibril. An orientational constraint of about $\psi \sim 80° - 110°$ has been reported previously in ensemble measurements, in similar samples, implementing polarization resolved fluorescence microscopy [44].

In order to guarantee the right estimation of anisotropy, only events with total intensity higher than 20 000 counts were selected. Localization precision of the anisotropy events is around 20 nm, and Full Width Half Maximum in a selected fiber is $\sim$ 30 nm (Fig. 5.20b and d), with profile showing the co-existence of several parallel fibers in the image.

The analysis of averaged value <A> as functions of the fibrils orientation shows an average angular constraint of $\psi \sim 95°$, which is consistent with previously found values [44].

A further insight on the orientational behavior is obtained by the observation of histograms from individual regions of amyloid fibrils (Fig. 5.23). If the orientational order was quite static, the obtained orientational constraint $\psi \sim 95°$ would lead to broad histograms, especially for $\rho \sim 45°$. The anisotropy histograms are shown to be still quite narrow with a width ($\sigma_A = 0.17$) just slightly above instrumentation noise. This seems to indicate a quite dynamic behavior within time scale below 30 ms. Also the histogram shape (narrower than in the

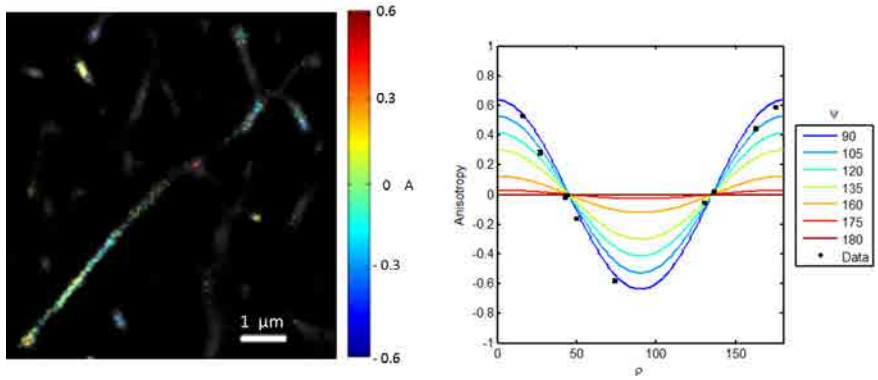

(a) (b)

Figure 5.22: polar-dSTORM analysis of amyloid fibrils in vitro labeled with ThT. Right: zoomed region of anisotropy image of amyloid fibrils, $I_T > 20\,000$ counts, Bg $\sim 2\,000$ counts, pixel size = 5 nm and Gaussian blur: 15 nm. Orange rectangle inset of Fig. 5.21. Left: anisotropy average measured on isolated single amyloid in vitro fibrils (markers with bars: standard error of the mean (SEM)) and simulated (cont. lines) as a function of ρ and ψ)

previous case of actin in vitro) does not favor more refined models such as the "tilted" cone inferred previously. Here, the dynamical motion extents over the whole angular range $\psi \sim 95°$ around the direction ρ along the fibril axis. This is probably governed by the labelling procedure which leaves a remaining degree of freedom to small molecules for rotational diffusion. Nevertheless in the ThT binding mechanism to the β-sheet of the amyloid, a high orientational constraint is imposed which is reported by the fluorescent molecule.

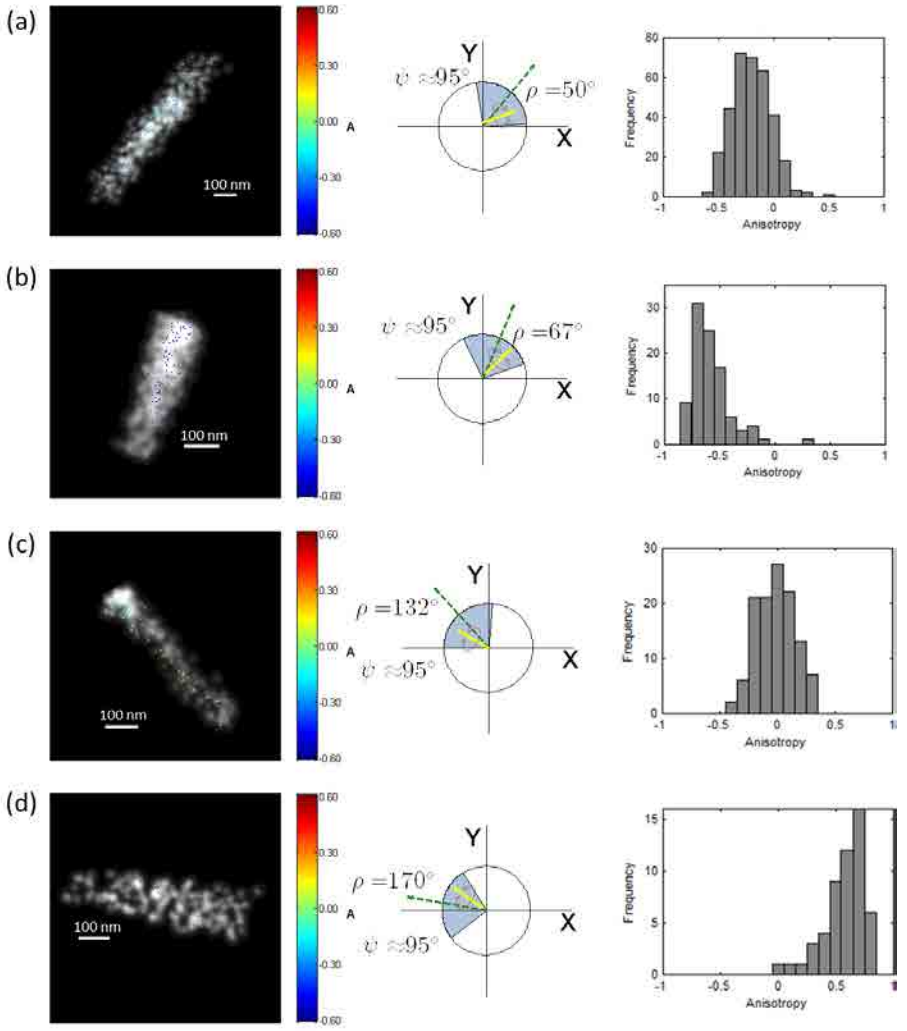

Figure 5.23: polar-dSTORM anisotropy analysis of isolated amyloid fibrils in vitro, labelled with ThT with different fibril orientation given by the ρ angles. $I_T > 20\,000$ counts, pixel size = 3.56 nm and localization precision for depicted molecules (blur): 20 nm. (a)$\rho = 50°$. (b) $\rho = 67°$. (c) $\rho = 132°$ (d) $\rho = 170°$. Left: polar-dSTORM Image, center: molecule distribution based on cone model and right: anisotropy histogram. The dashed line points the ρ direction while the yellow line shows a single molecule fluctuating in orientation.

DNA

DNA labelled with YOYO-1 has been analyzed with the polar-dSTORM method. The orientation behavior of YOYO-1 as an intercalant has been thoroughly studied but lead to some controversy.

Previous works have reported various interpretation of polarized data in YOYO-1 DNA systems. The most used model is a global orientation of the dyes within a cone aperture with $\psi \sim 0°$ and a mean orientation of 75° to 90° relative to the DNA fiber axis [14, 49–51]. This model has been recently refined using more polarization states of excitation [14]. A fast wobbling of $\psi \sim 50°$ has been found and a mean orientation of 90° relative to the fiber axis, in dsDNA fibers immobilized between optical tweezers. Note that in principle optimal SNR condition should be able to decipher the contribution from local structural changes occurring on the DNA immobilized structure, including the possible presence of non-intercalated dye (which has been pointed out in literature [48]). The bis-intercalation characteristic of YOYO dye [48] has been indeed proved based on linear dichroism analysis performed on polarized light spectroscopy. This implies two different intercalation behaviors: either intercalating or electrostatic binding to the fiber. Overall this angle is due to the depolarization caused by the relatively slow DNA fluctuations ("slow wobble") [14], in addition to the rapid, intrinsic dynamics on the nanosecond timescales between fluorescence excitation and emission [95].

polar-dSTORM imaging of DNA (Fig. 5.24a) immobilized on a coverslip and in particular zoomed regions (Fig. 5.25a) shows the anisotropy changes with the orientation of the fibers, which is a clear signature for orientational constraint of the YOYO dye along DNA .

At last, the mixing ratio of YOYO retrieved to DNA has been shown to influence the intercalating behavior. For mixing ratio (dye: DNA base) below 0.125 for YOYO, the long axis in the chromophore is nearly perpendicular to the DNA helix axis (orientation consistent with intercalation) and for a higher mixing ratio, the dye will be aligned to the pitch of the grooves of the DNA [48]. For the analysis described in this section, we used a labeling ration 1:20 dye/bp, in consequence we expect a majority of intercalation binding.

In order to guarantee the right estimation of anisotropy, only events with total intensity higher than 8 000 counts were selected. This value is different than the other experiments presented previously, because under this criteria only few molecules were selected. One of the main challenges of the super-resolved DNA imaging is indeed the low intensity retrieved from the YOYO-1 dyes, especially under the high power illumination conditions necessary for the localization microscopy methods (STORM, PALM, dSTORM, etc.). Nevertheless, the total intensity criteria of 8 000 counts is enough for evaluating the orientational constraint in the DNA, still with lower precision than in the previous samples. Localization precision of the anisotropy events is around 30 nm (minimum: 10

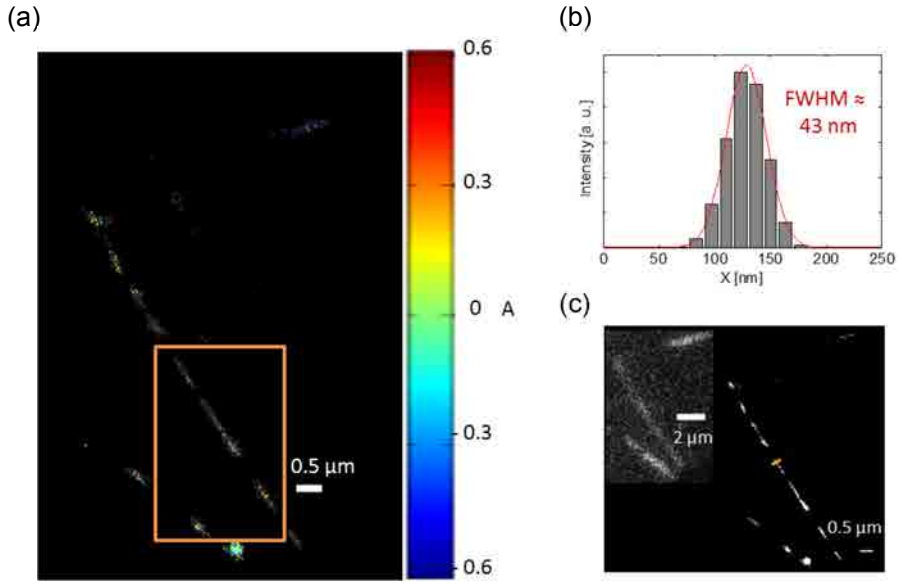

Figure 5.24: polar-dSTORM analysis of isolated DNA labelled with YOYO-1. (a) polar-dSTORM Image, pixel size=21 nm and gaussian blur: 30 nm. (b) Full Width Half Maximum (FWHM). (c) Super resolved image, pixel size=13 nm and gaussian blur: 30 nm. Inset: widefield image.

nm), and Full Width Half Maximum in a selected fiber is ~ 40 nm (Fig. 5.24b).

A further insight on the orientational behavior is gained by the observation of histograms from individual regions of DNA (Fig. 5.26). The anisotropy histograms are shown to be narrow with a width ($\sigma_A \sim 0.15$ to 0.2) limited by instrumental noise, while their average is varying according to a law resembling a cone aperture of about $\psi \sim 90°$ (Fig. 5.25b). Note that in the averaged $<A>$ value reporting on the $A(\rho, \psi)$ curve the ρ values are shifted by 90° to be consistent with an observation of average orientation perpendicular to the DNA fiber axis. This value is consistent with order constraint previously measured for DNA labelled with YOYO even if immobilized on a surface [14], confirming also that this motion is highly dynamic within the time scale of the CCD integration time. This has been explained by the labelling procedure which leaves a relatively large degree of freedom to small molecules for rotational diffusion within the binding pockets formed between the base pairs of the DNA fibers.

Overall, our technique confirms the fast dynamic wobbling within a cone aperture of about 90° perpendicularly to the DNA fibers.

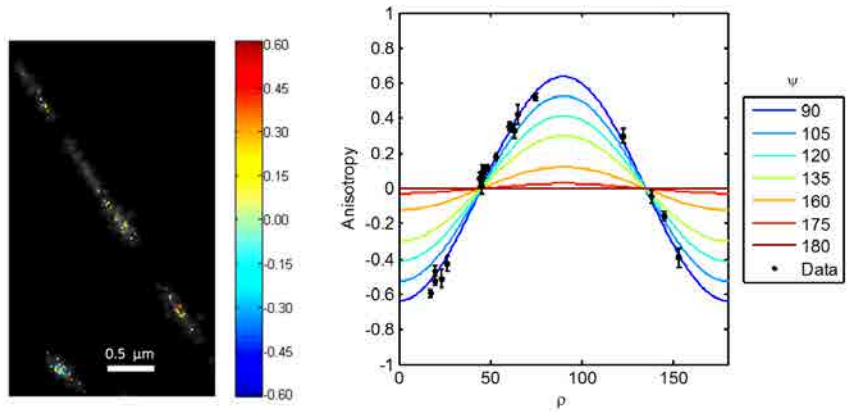

(a) (b)

Figure 5.25: polar-dSTORM analysis of isolated DNA labelled with YOYO-1. Right: zoomed region of polar-dSTORM image of DNA ,$I_T > 8\ 000$, Bg $\sim 1\ 200$, pixel size=21 nm and gaussian blur: 30 nm. (Orange rectangle inset of Fig. 5.24a). Left: anisotropy average measured on isolated DNA (markers with bars: standard error of the mean (SEM)) and simulated (cont. lines) as a function of ρ and ψ).

5.5 Molecule orientation representation.

The anisotropy super resolved images combined with anisotropy give information on the orientation and dynamics of the dye within a sample.

In this section, we aim at giving a more usual representation of the orientational behavior of single molecules attached to a sub-resolved biological structure.

2D representation.

The orientation of the molecule can be expressed in terms of its emission dipole angles: φ and θ (Fig. 5.27a). We first suppose the molecules to be stationary (fix orientation in time). With the simplification of neglecting the Z longitudinal contribution of the excited dipole in the high NA collection (see Chapter 4), the intensity of the fluorophore can be expressed as:

$$\begin{aligned} I_{\parallel}(\theta,\varphi) &= \sin^2(\theta)\cos^2(\varphi) \\ I_{\perp}(\theta,\varphi) &= \sin^2(\theta)\sin^2(\varphi) \\ I_T(\theta) &= \sin^2(\theta) \end{aligned} \tag{5.1}$$

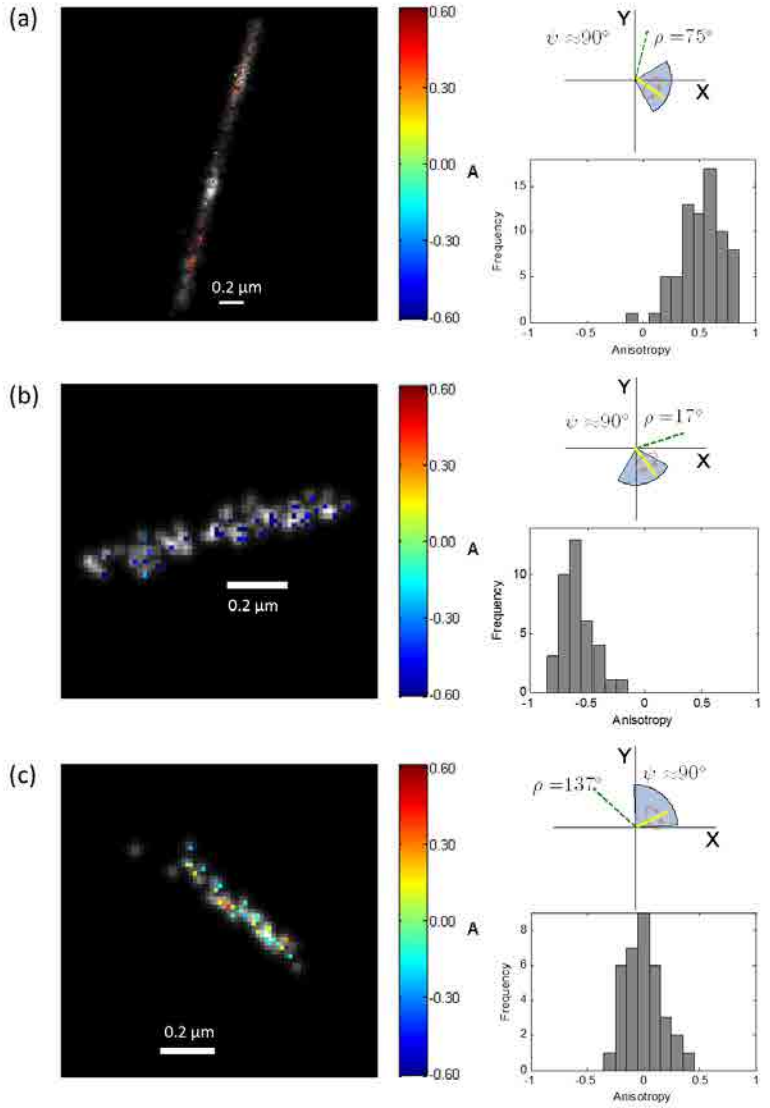

Figure 5.26: polar-dSTORM anisotropy analysis of isolated DNA labelled with YOYO-1 with different fiber orientations given by the ρ angles. Pixel size = 15 nm and localization precision for depicted molecules(blur): 30 nm. (a) $\rho = 75°$ ($I_T > 8\,000$ counts). (b) $\rho = 17°$ ($I_T > 8\,000$ counts). (c) $\rho = 137°$ ($I_T > 4\,500$ counts). Left: polar-dSTORM image, right up: molecule distribution based on cone model and right down: anisotropy histogram. The dashed line points the ρ direction while the yellow line shows a single molecule fluctuating in orientation.

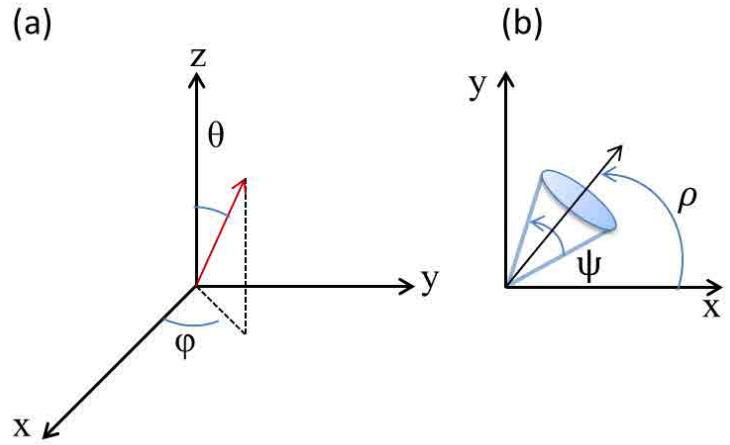

Figure 5.27: (a) Representation of the single molecule emission dipole (red arrow) orientation in terms of φ and θ. (X, Y) is the sample plane and Z is the optical axis direction. (b) Constrain distribution defined by a cone of orientation ρ relative to X and aperture angle ψ.

The single molecule anisotropy is defined as:

$$A(\varphi) = \frac{I_{\parallel} - I_{\perp}}{I_{\parallel} + I_{\perp}} = \cos^2(\varphi) - \sin^2(\varphi) = cos(2\varphi) \tag{5.2}$$

Based on the equation 5.2, the φ angle can in principle be obtained directly from the anisotropy:

$$\varphi = \frac{1}{2}\arccos(A) \tag{5.3}$$

Each event analyzed in the polar-dSTORM algorithm is represented as a stick with the estimated φ angle and with the correspondent anisotropy color. Note that in principle two solutions are possible for φ, namely φ as defined above and $180° - \varphi$. This indetermination can be waved using more excitation/detection polarization states, which is not required for most of the samples studied in this work due to the need of high signal to noise ratios. We therefore chose here to concentrate on fiber orientation which are as close as possible to horizontal and vertical, situations which correspond to expected averaged molecular directions along which the ambiguity is less a problem. In what follows, we chose to show only one stick orientation corresponding to the most probable orientation from

what is known in the literature, for instance along the fiber and not perpendicularly to it for actin and amyloid. In addition to the stick representation, the super resolved image is added as a background in grey scale. Examples of this representation in an isolated actin fiber in COS 7 cell, actin fiber in vitro, DNA and amyloid fibril are shown in Fig. 5.28.

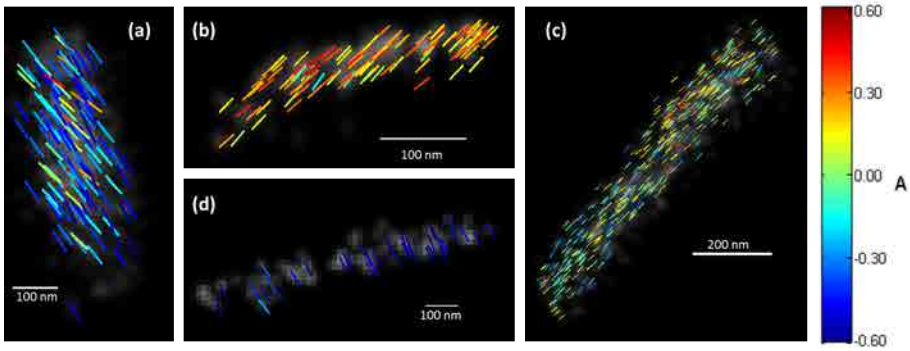

Figure 5.28: Single molecule 2D orientation representation, each event is represented as stick with φ angle and anisotropy color. (a) Isolated actin in vitro fiber. Pixel size: 8.9 nm and blur: 25 nm. (b) Isolated actin fiber in COS 7 cells. Pixel size: 4 nm and blur: 15 nm. (c) Isolated amyloid fibril in vitro labeled with ThT. Pixel size: 4 nm and blur: 20 nm. (d) DNA labelled with YOYO-1. Pixel size: 15 nm and blur: 30 nm.

Obviously in the actin case (both in vitro and in fixed cells), the single static molecule model does not lead to a physical picture since the average direction of the collection of molecules does not point in the fiber direction, which we would expect from a purely statistical reason. We therefore need to introduce the possibility of dynamic motion within a cone constraint, as already known from the separate inspection of the dependence of $\langle A \rangle$ with respect to the fibers orientations (see previous sections).

Introducing now the possibility of angular motion within the 30 ms time scale of the CCD integration, inside an angular aperture defined by the cone $(< \varphi >, \delta)$ (see Fig. 5.27b), the obtained anisotropy becomes an integrated form:

$$A(< \varphi >, \delta) = \frac{1}{\delta} \int_{<\varphi> - \frac{\delta}{2}}^{<\varphi> + \frac{\delta}{2}} \cos(2\varphi) d\varphi \tag{5.4}$$

Therefore

$$A = \frac{1}{2\delta}[\sin(2 < \varphi > -\delta) - \sin(2 < \varphi > +\delta)] = \frac{1}{\delta} \cos(2 < \varphi >) \sin\delta \tag{5.5}$$

Supposing that the individual molecular wobbling angle δ is known, the effective mean orientation of this molecular cone can thus be deduced from the measurement of A using :

$$< \rho >= \arccos\left[A\frac{\delta}{\sin\delta}\right] \cdot \frac{1}{2} \tag{5.6}$$

It is therefore possible to represent for each molecule, involving a dynamic disorder, its average pointing direction in order to localize structural information in sub-resolved image, for instance. The dependence $< \varphi >$ as a function of A is shown in Fig. 5.29 for several values of δ. We can see that the higher δ is, the smaller range of possible A values can be expected.

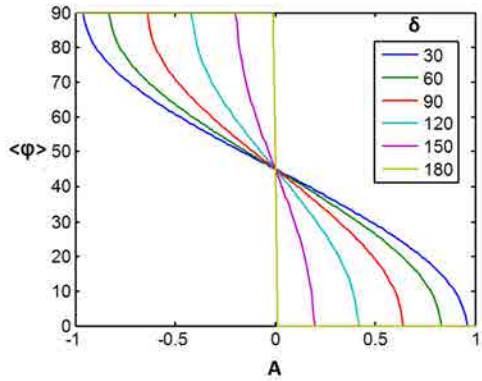

Figure 5.29: Dependence $< \varphi >$ as a function of A for several values of δ.

Fig. 5.30 shows the same samples as studied above, representing $< \varphi >$ plots as sticks and accounting for an angular disorder per molecule of δ which seems the most reasonable in terms of behavior of the whole molecular population. For instance for the example shown in the individual fiber of actin in vitro, the anisotropy range reached is about [-0.6, 0.6], which limits the angular wobbling angle of single molecules to about $\delta = 100°$ (Fig. 5.29). Note that this δ value can be compared to the published values of wobbling angle in F-actin labeling, obtained from the long-time polarized observation of individual molecules [11] ($\delta 4 \approx 40 - 80°$).

The wobbling angle per molecule obtained in the other cases (actin cells, DNA, amyloid) are very similar to the averaged values (over many molecules) ψ obtained previously. This indicates that the orientational behavior of the molecules in this case is not a tilted wobbling cone but rather a cone oriented in the fiber direction

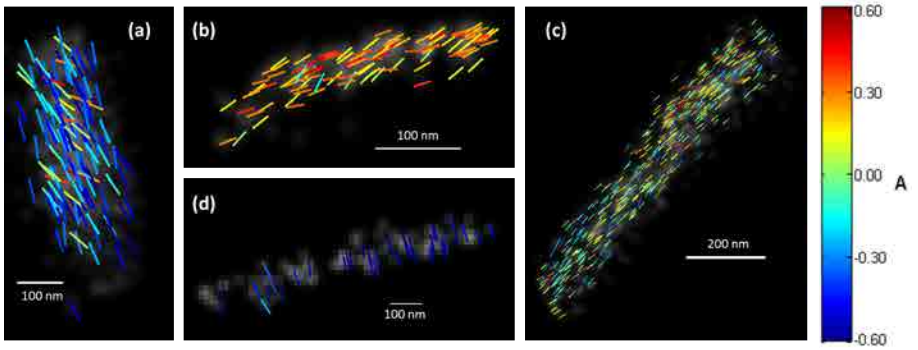

Figure 5.30: Single molecule 2Dd orientation representation, each event is represented as stick with $< \varphi >$ angle and anisotropy color. (a) Isolated actin in vitro fiber. Pixel size: 8.9 nm, blur: 25 nm and $\delta = 100°$. (b) Isolated actin fiber in COS 7 cells. Pixel size: 4 nm, blur: 15 nm and $\delta = 130°$. (c) Isolated amyloid fibril in vitro labeled with ThT. Pixel size: 4 nm, blur: 20 nm and $\psi = 95°$. (d) DNA labelled with YOYO-1. Pixel size: 15 nm, blur: 30 nm and $\psi = 90°$.

(or perpendicular, in the DNA case). This is also visible in the representation of Fig. 5.30 which shows more parallel sticks in these cases. This representation also allows pointing some specific behaviors such as a variability of orientational behavior along the fiber length, as seen in the case of the amyloid fibril.

Finally, this representation is not dedicated to decipher in great detail the orientational behavior of the molecules in fibrillar structures, but can nevertheless point specific dynamical behavior that are not accessible by other methods. This visualization offers therefore an interesting tool to analyze local orientation changes in fibers at the nanoscale.

3D representation.

In our previous treatment, the out of plane information is left aside by the normalization by the total intensity. An approximation of the θ angle can however be obtained using a statistical information on the total intensity. Indeed supposing that in the whole collection of recorded molecules, some of them are lying in the plane, then those should give a maximum reachable intensity. Since $I_T = I_{\parallel} + I_{\perp} = \sin^2\theta \cdot I_0$, θ could then be retrieved from the measurement of I_T, from which I_0 is estimated to be the highest reachable intensity. This leads to:

$$\theta = \arcsin\left(\sqrt{\frac{I_T}{I_0}}\right) \tag{5.7}$$

This approach is not a rigorous quantitative measure of θ but permits to estimate out of plane behavior in one image.

After the angles: θ and φ are calculated then they can be used for a 3D representation of the orientation. Each event is represented as 3D stick with the orientation of θ and φ, as described in Fig. 5.27. In a similar way as the 2D representation, the color is defined by the anisotropy value. Furthermore, the dSTORM image is added as background. Interestingly this representation shows same possible variation of the 3D orientation along a given fiber in actin, DNA and amyloid (Fig. 5.31).

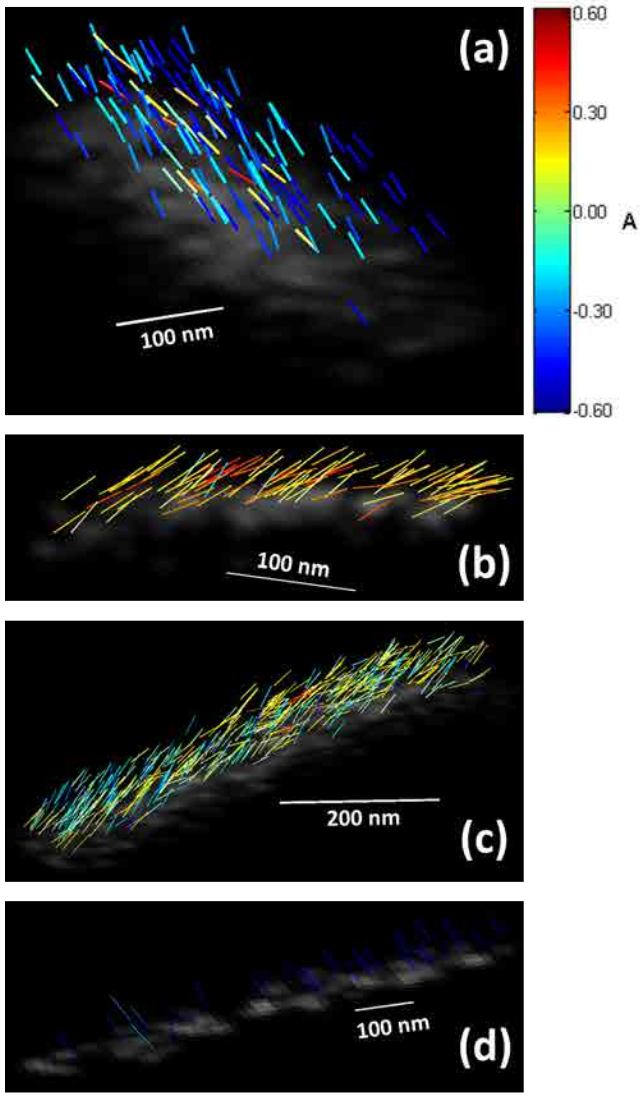

Figure 5.31: Single molecule 3D orientation representation, each event is represented as 3D stick with $< \varphi >$, θ angles and anisotropy color. (a) Isolated actin in vitro fiber. Pixel size: 8.9 nm and blur: 25 nm. (b) Isolated actin fiber in COS 7 cells. Pixel size: 4 nm and blur: 15 nm. (c) Isolated amyloid fibril in vitro labeled with ThT. Pixel size: 4 nm and blur: 20 nm. (d) DNA labelled with YOYO-1. Pixel size: 15 nm and blur: 30 nm.

5.6 Anisotropy imaging of freely diffusion single molecules

In this last section, we investigated the potential of our technique to probe local viscosity/temperature behavior based on anisotropy of single molecules freely rotating in a viscous solution.

The fluorescence anisotropy from dispersed fluorophores in a liquid medium denoted r is closely related to their Brownian rotational dynamics according to Perrin's equation [38]:

$$\frac{1}{r} = \frac{1}{r_0}\left(1 + \frac{\tau_f}{\tau_{rot}}\right) \tag{5.8}$$

where r is the anisotropy measured in an ensemble of molecules if they would not rotate (fixed), τ_{rot} is their rotational correlation time and τ_f their fluorescence lifetime. The anisotropy r is measured under linear polarization of excitation and is defined as:

$$r = \frac{I_{\parallel} - I_{\perp}}{I_{\parallel} + 2I_{\perp}} \tag{5.9}$$

This equation implies that the molecular rotation during the lifetime of the molecule induces a fluorescence depolarization (lower value of r). It is known that one increment in temperature contributes to a decrease of r, due to the faster rotation of the molecules. This has been recently measured at the nanoscale close to heated metal nanoparticles [96]. This can be explained by the Debye-Stokes-Einstein equation [38]:

$$\tau_{rot} = \frac{V\eta(T)}{k_B T} \tag{5.10}$$

where T is the local temperature, $\eta(T)$ the dynamic viscosity of the embedding medium, V the hydrodynamic molecular volume and k_B the Boltzmann constant.

The variation of r, as a function of temperature, based on a theoretical analysis of fluorescein in 4:1 glycerol-water mixture is depicted in Fig. 5.32 [96].

Experiments were performed on our set-up in order to measure the viscosity effect on r. Atto 633 molecules freely diffusing in solution with two different glycerol concentrations were analyzed. We observed one increment of the mean anisotropy from 0.2 to 0.29 for 72% Glycerol w/w and 85% Glycerol w/w, (expected anisotropy 0.205 and 0.303) as shown in the histograms of Fig. 5.33. This test shows the reliability of the measurement even in conditions where the histogram width is quite large due to limits in the experimental conditions, indeed it is known from the section 5.1.2, that diffusing objects tend to deform their

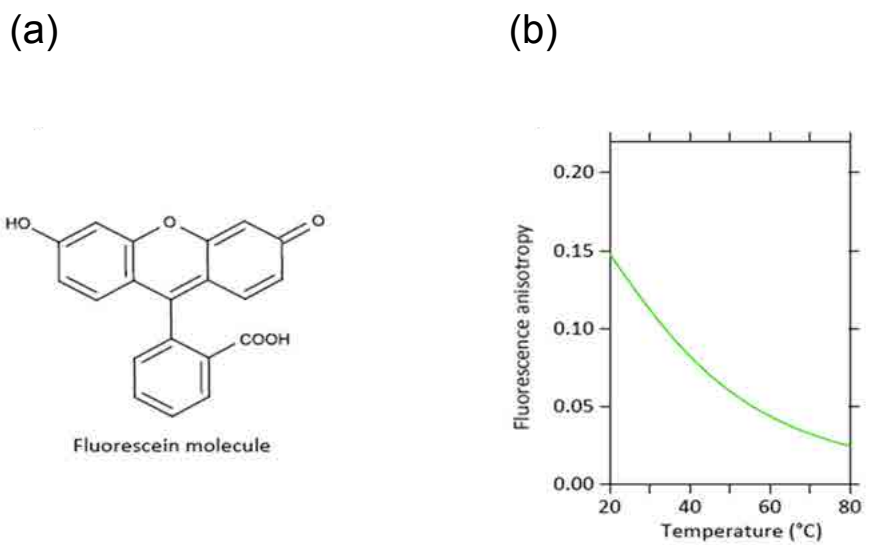

Figure 5.32: Fluorescence polarization anisotropy calibration. (a) The chemical structure of fluorescein. (b) Theoretical curve of fluorescence anisotropy r as a function of the temperature for fluorescein dissolved in a glycerol - water (4:1) mixture.

PSF and lead to a lower quality of estimation in the intensity, localization, and therefore anisotropy.

Following this analysis, we have measured the anisotropy variation of Atto 633 molecules freely diffusing in Glycerol 87 % (w/w) over a lithographic structure of regularly spaced nanospheres of gold, illuminated at their plasmonic wavelength, an ideal source of heat which size is governed by the illumination area (Fig. 5.34b).

We observed a displacement of the average anisotropy of 0.32 for the heated sample in the presence of a green laser excitation (532nm) at 0.05 W, in comparison with a mean anisotropy of 0.28 of the sample without the presence of the green laser (Fig. 5.35). This indicates an effect of heating however with low precision ($\sigma_A \sim 0.2$).

Following the methodology described in Chapter 4, a filtering is performed in terms of total intensity, radius and localization precision, allowing to reduce the standard deviation to ~ 0.05. This filtering, even through the number of used events is lowered, permits to point with much better precision the shift of anisotropy due to local heating. From our measurement, we estimate the generated increase of temperature to about 40°C. Note however that to obtain a

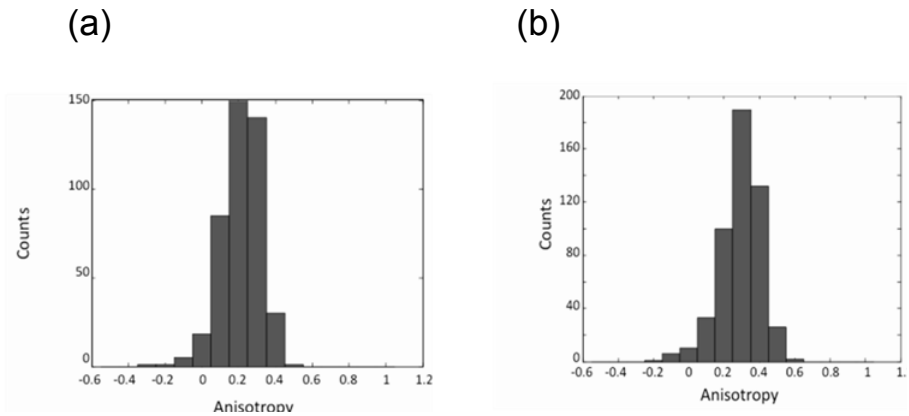

Figure 5.33: Anisotropy histogram of Atto 633 molecules freely diffusing in (a) Glycerol 72 % (w/w) and (b) Glycerol 85 % (w/w).

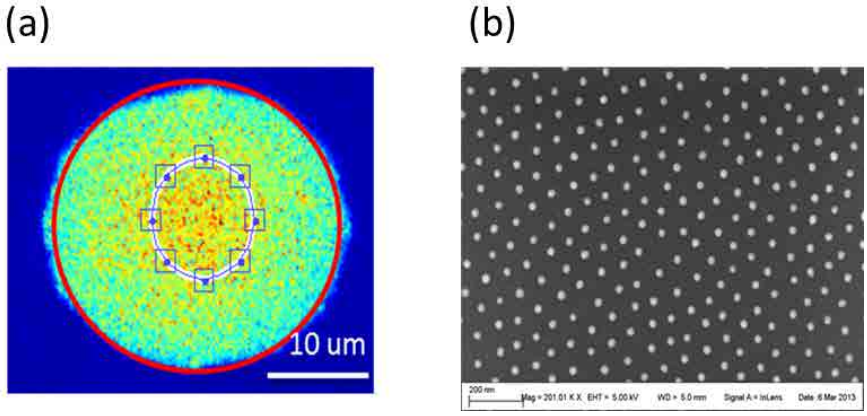

Figure 5.34: Heating scheme. a) Illumination scheme, red circle= excitation area of the 639 nm laser, blue inside circle = excitation area of the 532 nm laser. b) Image of lithographic gold nanospheres of size around $\sim$ 20 nm. This structure was fabricated at Max Planck Institute of Biochemistry in collaboration with G. Baffou (mosaic, I. Fresnel).

precision of $\Delta T = 1°C$ in our measurement, a σ_A in anisotropy of ~ 0.005 would be required. This experiment, initially designed to observe small elevations of temperature at the nanoscale, was not continued for this reason, freely diffusing molecules do not permit indeed to reach this precision (Fig. 5.36).

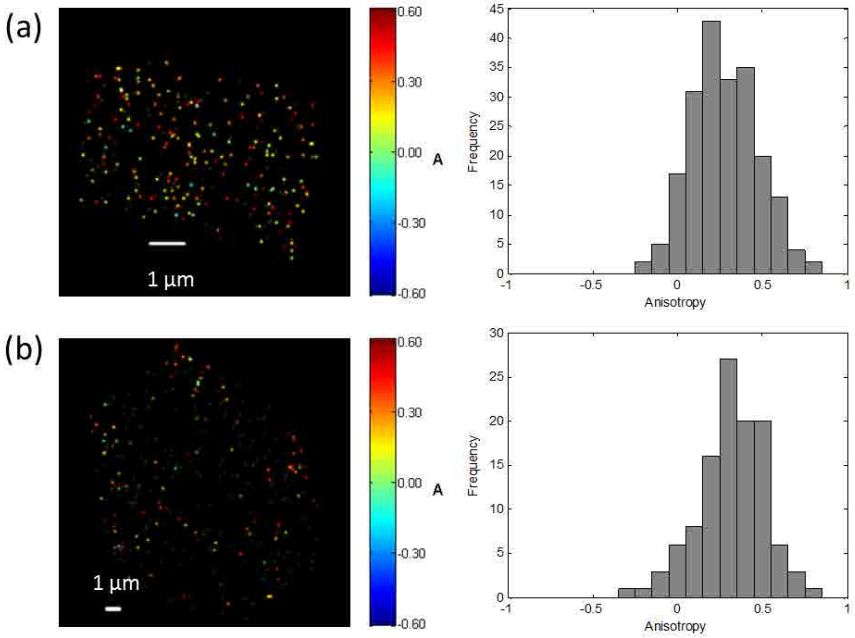

Figure 5.35: Anisotropy analysis of Atto 633 molecules freely diffusing in Glycerol 87 % (w/w) over a lithographic nanospheres of gold, illuminated at their plasmonic wavelength. (a) Heated sample A=0.28, σ_A=0.195, events= 205 and pixel size=53 nm. (b) Non-heated sample A=0.32, σ_A=0.197, events= 112 and pixel size=89 nm. [Left: anisotropy image, right: anisotropy histogram, anisotropy events (color) and dSTORM events (dark green)].

5.7 Conclusion

In this chapter, we have shown the possibility to report with high precision orientational behavior spatially in structured bio-molecular media including: actin fibers, tubulin, DNA and amyloid fibrils.

In addition, we have shown that polar-dSTORM can reveal information on the dynamics of the orientational mechanisms imaged in ordered samples, making possible super-resolution structural imaging where both spatial and rotational properties of molecules can be reported in one single image.

Experiments on fluorescent nano-beads were realized in order to identify the limitations of the polar-dSTORM technique in the "best" experimental conditions. Additionally preliminary studies on anisotropy analysis in diffusing single molecules were presented, with the goal to observe anisotropy changes due to vis-

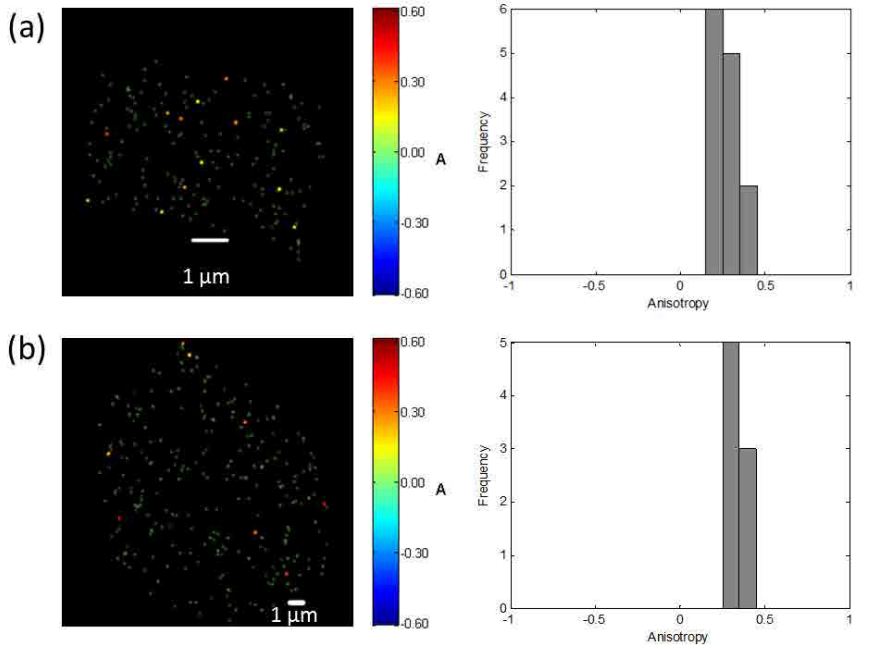

Figure 5.36: Anisotropy analysis of Atto 633 molecules freely diffusing in Glycerol 87 % (w/w) over a lithographic nanospheres of gold, illuminated at their plasmonic wavelength. Filtering was performed in order to reduce the width of the anisotropy histogram: $I_T > 5000$, $C_r = 0.1$ and C_σ=0.1. (a) Heated sample A=0.27, σ_A=0.06, events= 13 and pixel size=53 nm. (b) Non-heated sample A=0.36, σ_A=0.05, events= 8 and pixel size=89 nm. [Left: anisotropy image, right: anisotropy histogram, anisotropy events (color) and dSTORM events (dark green)].

cosity and temperature increment in freely diffusing molecules at subdiffraction scale.

These studies show overall that particular case much be taken when analyzing orientational behavior from single molecules, in particular when this is related to sub-resolution spatial information for structural imaging. Nevertheless we show that when careful analysis is performed, even through at the expense of a loss of events for statistical analysis, robust spatial information can be derived.

Chapter 6

Polarized Super-resolution Optical Fluctuation Imaging (polar-SOFI)

The most established developments in super resolution microscopy described previously in the Introduction are based on fluorescence localization techniques. There is however an alternative technique which becomes increasingly popular, based on fluorescence time fluctuations: Super-resolution Optical Fluctuation Imaging (SOFI) [15].

3D diffraction-unlimited resolution can be in principle obtained by statistical analysis of the temporal fluorescence fluctuations based on fluorophore exhibiting characteristic time dynamics of emission relative to unspecific signal such as background [15]. This statistical analysis relies on the calculation of so-called "cumulant" which contain cross-correlation information of time fluctuation between close-by pixels. Besides the resolution improvement, the cumulant analysis also reduces significantly the image background and in consequence the image contrast is improved.

Unlike fluorescence localization microscopy techniques, SOFI analyzes the full image sequence in parallel, and does not depend on the spatial-temporal isolation of individual fluorophores [97]. Therefore, blinking and signal-to-noise ratio (SNR) are as not crucial as the localization microscopy techniques (STORM, PALM, etc.). Besides, the SOFI technique can be implemented on common widefield microscopes and can be implemented using similar fluorophores as used for dSTORM [98].

In this chapter, we propose an adapted SOFI method, able to image molecular

orientation behaviors in static and dynamic environments (polar - SOFI). This technique is based on the balanced SOFI algorithm (bSOFI) developed previously by Geissbüehler et all [99]. First, a brief introduction to the SOFI technique will be given. Then the methodology of polarized SOFI (polar-SOFI) will be described. A first validation will be given based on Monte Carlo simulation implemented on molecules undergoing rotational diffusion while in an angular constraint. These simulations have required including time fluctuations for the molecules emission. Then, a brief discussion will concern the comparison between polar-dSTORM and polar-SOFI. Finally, one conclusion based on the possible application and limitations of the polar-SOFI technique will be developed.

6.1 Introduction

Super-resolution optical fluctuation imaging (SOFI) was introduced recently by Dertinger et al. [15, 100], who developed a super- resolution method based on statistical analysis of temporal fluorescence fluctuations of molecules, with the goal of surpassing the limits of existing super-resolution techniques in terms of acquisition rate, 3D capabilities, background rejection, in a set-up compatible with wide field illumination. SOFI is based on the stochastic fluctuation of emitters and does not required specific reactivation or synchronization processes in the fluorophores excitation schemes. Based on simulations and experiments on model systems, they have proved a considerable gain in resolution by computing temporal n-th order cumulants (a quantity expressed below that resembles a n-th order correlation function, in time and possibly space) or spatio-temporal n-th order cross-cumulants. SOFI is now applied to real-time studies in live multicolor bio-imaging [98].

The principle of SOFI is based on fluorophores that exhibit at least two different "on" and "off" emission states, emitting in a stochastic way, recorded using a pixel size below the diffraction spot size. The calculation of the n-th order cumulant of the pixel signal will keep only the highly correlated fluctuations of fluorophores present in each pixel, rejecting uncorrelated background signals. Increasing n-th order will lead to a nonlinear increase of the decorrelation to noise and neighbor pixels, leading to an increase in resolution. Simulations and practical implementations show a resolution improvement of a factor $\sqrt{n}$ using temporal cumulants [15], the resolution being still limited by the pixel size of the detector [15]. Higher resolution improvements can be reached using spatio-temporal cross-cumulant on over-sampled SOFI images using an effectively reduced pixel size [100]. An improvement factor of n has even been proven by employing additional image processing which includes re-weighting of SOFI cross-cumulant images in the Fourier domain [100], which has been proven successful experimentally up to the fourth cumulant order [101]. In principle "unlimited" improvement

of resolution below the diffraction limit can be reached in ideal cases where all the molecules have identical brightness) [15].

The initial implementation of SOFI is described in the Fig. 6.1.

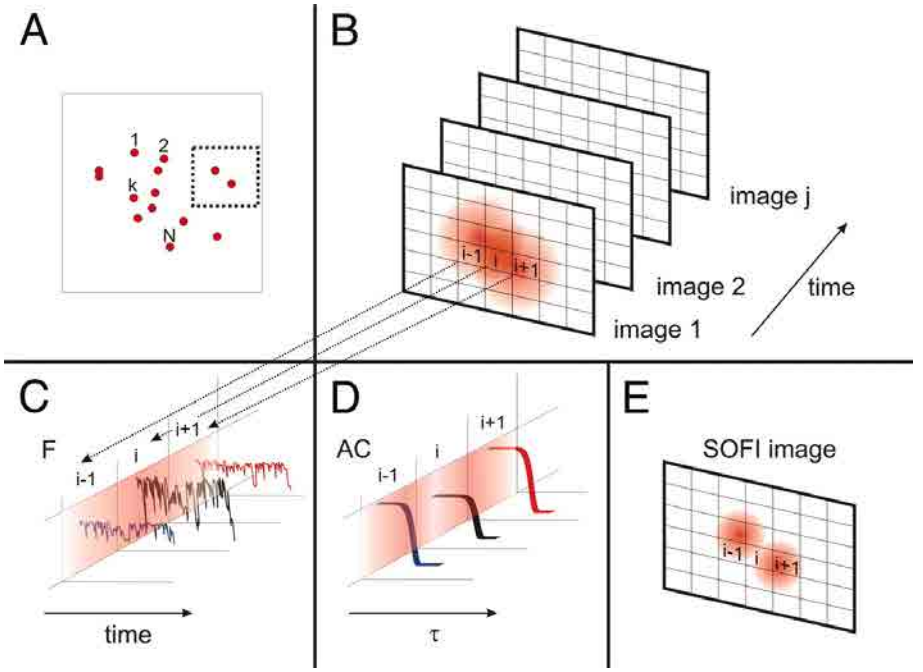

Figure 6.1: SOFI principle. (A) Emitter distribution in the sample plane. (B) Magnified region of the dotted box in A. In this case, the two neighboring emitters cannot be distinguished because of the optical diffraction limit. The fluctuations are recorded in a movie stack. (C) Each pixel contains a time trace, which is composed of the sum of individual emitter signals, whose PSFs are overlapping the pixel of interest. (D) The second-order correlation function is calculated from the fluctuations time trace of each pixel. (E) The SOFI signal value assigned for each pixel is given by the integral over the second-order correlation function (Imaged obtained from [15]).

A SOFI image finally reports on the temporal/spatial degree of correlation as well as molecular brightness [15]. Contrary to STORM, single molecules can be detected even in low SNR conditions, without the need of long molecular dark states [102]. Since the computed cumulant depends of the blinking characteristics of the analyzed molecules, by comparing several cumulant orders, it is possible to extract parameters like molecular brightness, density and blinking characteristics

in addition to benefiting from the increment in resolution and contrast. This extraction (named balanced-SOFI: bSOFI), which requires additional operations that involve spatial deconvolution of cumulants and ratios between cumulants, also permits to correct for the strong nonlinearity of the SOFI efficiency with respect to molecular brightness [99].

This capacities of the SOFI method allow to monitor the microenvironment of fluorescent molecules, as well as the blinking statistics, in a similar functional imaging as for Fluorescence Correlation Spectroscopy (FCS) [103, 104], but in combination with a sub-diffraction resolution [102]. Other applications of SOFI emerge today. For example, a version of the SOFI method is called antibunching microscopy [105]. For this SOFI version, the authors considered the generic property of the fluorescence emitters to emit photons one by one, using time-correlated single photon counting instrumentation [105]. In addition, SOFI has been probed with quantum dots [15, 100], reversibly photostatting fluorescence protein ("photocromic stochastic optical fluctuation pcSOFI" [98]), blinking organic fluorophores [99,101,106] and fluctuations based on diffusion-assisted Förster resonance energy transfer [107].

6.1.1 SOFI principle

Cumulants

Since the understanding of cumulant is one of the main points of SOFI microscopy, we will introduce the basics of the cumulant calculation and its properties. The SOFI principle described here, including its balanced-SOFI version, are based on several references [15, 97, 99–102], as well as on the theoretical studies performed in [108, 109].

Assuming a fixed sample (an image pixel) labeled with N independently fluctuating sources (fluorophores, labeled k), we can define the intensity detected for the given fixed position (r) of the pixel in an image temporal sequence as:

$$I(r,t) = \sum_{k=1}^{N} \varepsilon_k U(r - r_k) s_k(t) + b(r) + noise(r,t) \tag{6.1}$$

where r_k are the emitters positions within the image pixel, ε_k is their intensity amplitude (brightness) and $s_k(t) \in [0,1]$ is their normalized temporal fluctuations. b is the time-constant background from autofluorescence or residual back scattered illumination, and *noise* the space and time noise function which is expected to have a zero mean. $U(r - r_k)$ is the PSF of the optical system centered on each emitters' position, with:

$$U(r) = exp\left(-\frac{x^2}{2\sigma_x^2} - \frac{y^2}{2\sigma_y^2} - \frac{z^2}{2\sigma_z^2}\right) \tag{6.2}$$

We assume that the emission of different emitters r_k are not correlated in time, so that all time cross-correlated terms between different emitters will vanish. In SOFI, the n-th (auto-)cumulant of the detected signal fluctuations $\delta I(r,t) = I(r,t) - \langle I(r,t)\rangle_t$ is calculated for each pixel and depicted in an image. The calculation of n-th order cumulants are based on the n-th order correlation terms:

$$G_n(r,\tau_1,...\tau_n) = \langle \delta I(r,t)\delta I(r,t+\tau_1)...\delta I(r,t+\tau_n)\rangle_t \tag{6.3}$$

The calculation of G_n permits to obtain quantities that are dependent on the n-th power of the PSF and to reject time fluctuating functions that are not cross-correlated in time (such as noise and background). For instance:

$$G_2(r,\tau) = \sum_{k=1}^{N} U^2(r-r_k)\ \varepsilon_k^2\ \langle \delta s_k(t)\delta s_k(t+\tau)\rangle_t \tag{6.4}$$

The n-th power of the PSF $U^n(r)$ results in a "new" PSF reduced by a factor $\sqrt{n}$, thus increasing the spatial resolution in 3D:

$$U^n(r) = exp\left(-n\frac{x^2}{2\sigma_x^2} - n\frac{y^2}{2\sigma_y^2} - n\frac{z^2}{2\sigma_z^2}\right) = exp\left(-\frac{x^2}{2(\frac{\sigma_x}{\sqrt{n}})^2} - \frac{y^2}{2(\frac{\sigma_y}{\sqrt{n}})^2} - \frac{z^2}{2(\frac{\sigma_z}{\sqrt{n}})^2}\right) \tag{6.5}$$

This is the main reason of the resolution improvement in SOFI technique. Note that if we only raise the PSF of multiple molecules with a power n, then there is no resolution improvement, as we can observe in Fig. 6.2. On the contrary, assuming independently and stochastically blinking, one emitter only correlates with itself, so the time correlation operation allows to extract additionally individual molecules selection.

Raising n thus allows benefiting from an improved resolution. The drawback of pure time correlation in achieving super-resolution capabilities is that high order ($n > 3$) correlation functions contain products from lower order correlations. The calculation of derived n-th order cumulant $C_n(r,\tau_1,...\tau_n)$ permits to eliminate these lower-order quantities. In our work we will extensively use the second and fourth cumulants which are detailed as [109]:

$$\begin{aligned} C_2(r,\tau_1) &= G_2(r,\tau_1) \\ C_4(r,\tau_1,\tau_2,\tau_3) &= G_4(r,\tau_1,\tau_2,\tau_3) - G_2(r,\tau_1)G_2(r,\tau_3) \\ &- G_2(r,\tau_1+\tau_2)G_2(r,\tau_2+\tau_3) - G_2(r,\tau_1+\tau_2+\tau_3)G_2(r,\tau_2) \end{aligned} \tag{6.6}$$

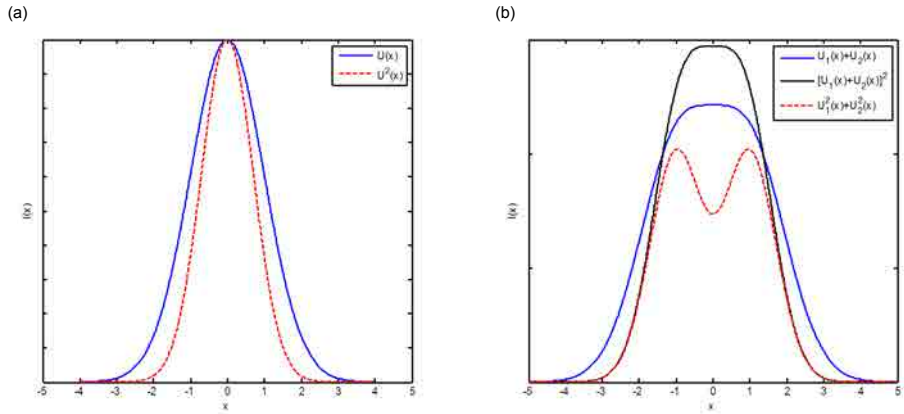

Figure 6.2: PSF squaring. The PSF is approximated with a Gaussian: $U(x) = \exp(-x^2/(2\sigma^2))$ and $U_{1,2}(x) = U(x \pm \sigma)$ (a)The PSF is narrowed by $\sqrt{2}$, by squaring. (b) Two spots are separated by 2σ, in this case only the two gaussian can be defined by the individual squaring.

Using the mathematical properties of cumulant, these new quantities can be generalized as:

$$C_n(r, \tau_1, ...\tau_n) = \sum_{k=1}^{N} U^n(r - r_k)\, \varepsilon_k^n\, w_{n,k}(\tau_1, ...\tau_n) \tag{6.7}$$

where $w_{n,k}(\tau_1, ...\tau_n)$ is a weighting function that depend on the time fluctuation properties of individual emitters (this function is more detailed below). The factor ε_k^n indicates that the resulting cumulant SOFI image exhibits a nonlinear dependence with respect to the molecular brightness, giving a much brighter appearance (to the power n) to molecules which are initially brighter within a given pixel of analysis. This therefore leads to an artificially-high dynamic range for high order cumulants.

In principle the cumulant calculation is feasible over all time delays accessible in the SOFI image stack, and a strong reduction of noise is observed when averaging over several time lags [15]. This however enlarges considerably the computation time for high order cumulants. Computing only the zero time lag value $\tau_1 = ... = \tau_n = 0$ allows circumventing this problem and benefiting from high SOFI signals [15], however it does not eliminate noise in the image and it is therefore not appropriate for low SNR data. Another solution has been found using spatial cross-cumulants, as described below [100].

Spatio-temporal cross-cumulants

Generalizing the SOFI principles in both time and space domain permits to access a finer sampling grid in the final cumulant images and potentially treating low SNR cases. The computation consists in calculating spatio-temporal cross-cumulants between different positions r_i within a single detector pixel. At the order n =2 it becomes:

$$\begin{aligned} XC_2(r_1, r_2, \tau) &= \sum_{k=1}^{N} U(r_k - r_1)U(r_k - r_2)\, \varepsilon_k^2\, \langle \delta s_k(t)\delta s_k(t+\tau)\rangle_t \\ &= U(\frac{r_1 - r_2}{\sqrt{2}}) \sum_{k=1}^{N} U^2(r_k - \frac{r_1 + r_2}{2})\, \varepsilon_k^2\, \langle \delta s_k(t)\delta s_k(t+\tau)\rangle_t \end{aligned} \quad (6.8)$$

This expression shows that a cross-cumulant depends on the cross-correlation position, at the geometric center between r_1 and r_2, and is weighted by a PSF factor which depends on the distance $r_1 - r_2$, called in what follows "distance factor" [100]. This factor is significant only when r_1 and r_2 are in close distance smaller than the PSF size, which is permitted using an over-sampled grid on the initial image. The uncorrelated nature of the noise in neighboring sub-pixels in the calculation of cross-cumulants finally reduces the noise in a SOFI image. This idea can be generalized at the order n:

$$XC_n(r_1, ..., r_n, \tau_1, ..., \tau_n) = d_n(r_1, r_2, ..., r_n) \sum_{k=1}^{N} U^n(r_k - r)\varepsilon_k^n w_{n,k}(\tau_1, ...\tau_n) \quad (6.9)$$

where $d_n(r_1, r_2, ..., r_n) = \prod_{i<j}^{n} U\left(\frac{r_i - r_j}{\sqrt{n}}\right)$ is a generalized distance factor and, $r = \frac{\sum_{i=1}^{n} r_i}{n}$ represents the geometrical mean of the considered positions.

The computation of the spatio-temporal cross-cumulants of each pixel with (n-1) of its neighboring pixels finally results in a n-fold finer sample grid in the final image. An example of the computation of a finer grid is shown in Fig. 6.3 for the fourth order cumulant, which shows two possible schemes of calculations based on allowing or not the pixel repetitions (auto-cumulants) in the cumulant combinations. Finally in practice, the calculation of cross-cumulants is based on Eq. 6.9 for a zero time lag ($\tau_1 = ... = \tau_n = 0$), without pixels repetitions in order to increase the pixel grid density and reduce any bias coming from noise contributions in auto-cumulants. In addition, the combination with the shortest sum of distances with respect to the considered pixel ($r = \frac{\sum_{i=1}^{n} r_i}{n}$) is selected [99]. Finally after obtaining the intermediary pixels created by the finer sampling

grid, it is also important to compensate for their spatial decrease of correlation represented by the distance factor. This decrease is compensated by an additional normalization by this distance factor, assuming a Gaussian PSF [100, 101]. Note that this step of the algorithm can also be used to estimate the PSF $U(r)$. For this, the correction factor is iteratively optimized (using a 2D Laplacian cost function on an initial Gaussian PSF) until all pixels have similar weights [101]. This estimation is useful for further quantification analysis, as detailed below.

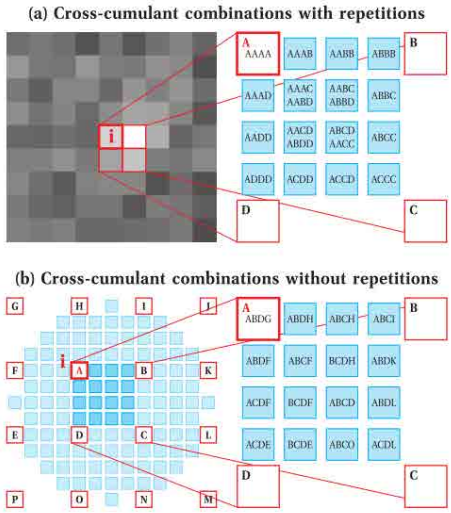

Figure 6.3: 2D fourth order cross-cumulant combinations for pixel i with and without repetitions. Different combinations inside a neighborhood matrix of I is used to generate 15 intermediary pixels in between the original pixel matrix (ABCD). In this case, combinations leading to the same intermediary pixels can be averaged in order to remove more noise. (a) For the repetition approach, all the n-combinations inside a 2×2 neighborhood are considering. (b) For this approach, a 4x4 neighborhood of pixel i is selected to generate the intermediary pixels. In order to simplify the procedure, only combinations with the shortest sum of distance with respect the output pixel are considered.

Finally for a final representation of the cross-cumulant images, a deconvolution can be performed assuming a Gaussian cumulant PSF. Note that it has been pointed out that cumulant images, which are free of background, are appropriate for high quality deconvolution operations, which is a big advantage especially in noisy, low SNR conditions [100].

Improving further the resolution by Fourier-reweighting

The spatial resolution in n-th cumulant SOFI images is improved by a factor $\sqrt{n}$ with respect to the wide field image. It has been proved however that additional image processing could improve even further this resolution. This scheme, called Fourier reweighting [100], consists in calculating the Fourier transform of the $U^n(r)$ appearing in the cumulant images, multiplying it by a Fourier-reweighted function $\frac{\widetilde{U}(nk)}{\widetilde{U^n}(k)}$ (where $\widetilde{U}(k)$ denotes the Fourier transform of $U(r)$ at the spatial frequency k), and recalculating the inverse Fourier transform of this new image. This operation used in the end a reduced-size PSF ($U(nr)$), chosen because the support of the optical transfer function (OTF) of a cumulant image is n times larger that the support of the system's OTF. This scheme has been demonstrated using for $U(r)$ a Gaussian PSF, or a PSF estimated from the distance factor measurement in cross-cumulants (see above) [100].

The complete scheme illustrating the steps of the SOFI algorithm including Fourier-reweighting is summarized in Fig. 6.4 [101].

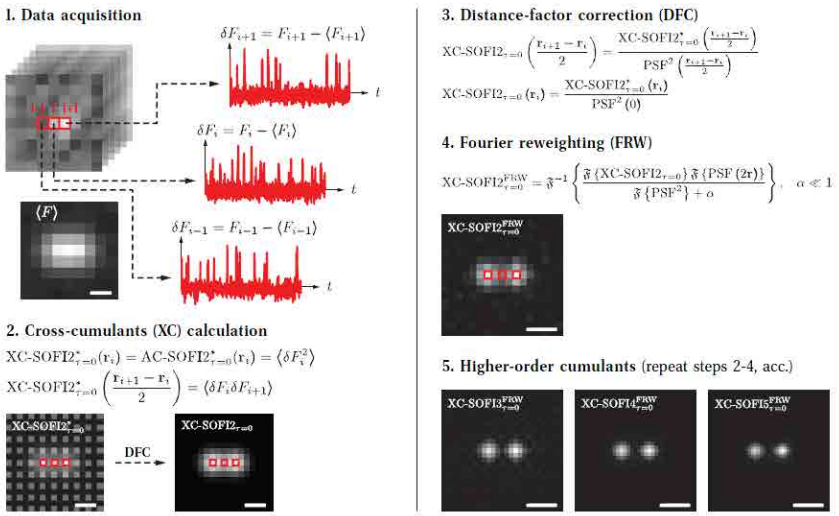

Figure 6.4: Different steps of calculating cross-cumulant SOFI with Fourier reweighting, illustrated for the second order. (Image obtained from [101]). 1. Data acquisition. 2. Cross-cumulants (XC) calculation. 3. Distance factor correction. 4. Fourier reweighting. 5. Higher-order cumulants.

This procedure has shown an improvement of a factor n in the resolution of n-th order cumulant images [100]. Note however that if noise contributions

become strong, Fourier-reweighting starts to fail at higher orders [101]. Recently this procedure has been replaced by a simpler one using first a linearization of the $U^n(r)$ function (see below) and a pure reconvolution by $U(nr)$ [99].

6.1.2 Balanced SOFI (bSOFI)

Linearization

Finally, an additional implementation has been recently performed to circumvent the nonlinear response of (cross-)cumulants with respect to molecular brightness, called linearization. One of the important limitations of the SOFI technique for quantitative analysis is the nonlinear response in molecular brightness and blinking statistics, which contribute with a power n in the (cross-)cumulant images (see Eq. 6.9). This limits the use of high order (cross-)cumulants (n>3) since images appear with a strong, artificial dynamic range, hiding structural details within an apparent background. Recently, an adaptation of the original SOFI procedure has been proposed to circumvent this issue, called balanced SOFI (bSOFI) [99]. This algorithm allows balancing the image contrast in order to correct the nonlinear brightness and blinking response of the original SOFI. Since a linear (cross-)cumulant image is obtained with respect to molecular quantities (brightness per molecule, density, fluctuation statistics), it has been also used to obtain quantitative estimation of these quantities, which were not accessible from a pure SOFI image.

First, we consider cross-cumulant images already corrected by the distance factor (see Eq. 6.9). Assuming that the molecular properties (brightness, density, fluctuation statistics) are constant locally (over the sub-pixel window of analysis), then the cross-cumulants can be approximated as [99]:

$$\kappa_n(r) = \epsilon^n(r)\,\omega_n(r)\,\sum_{k=1}^{N} U^n(r - r_k) \tag{6.10}$$

It appears from this equation that taking the n-th root of this function linearizes the brightness dependence without compromising the resolution improvement of the cross-cumulant.

In practice, the cross-cumulant images are then first deconvolved by the cumulant PSF estimated from the distance factor correction (see above), then n-th rooted. The deconvolution is performed using a Lucy-Richardson algorithm, which is an iterative deconvolution without regularization that computes the most likely image representation knowing the PSF and assuming Poisson noise [99]. An extra step of reconvolution by $U(nr)$ is performed to retrieve an expected resolution of PSF reduced by a factor n.

Estimation of molecular parameters

Equation 6.9 contains parameters that can be estimated from the cross-cumulant images. Assuming a uniform spatial distribution of molecules inside a detection volume V centered on r, we can estimate $\sum_{k=1}^{N} U^n(r-r_k) \approx N(r)\zeta_V(U^n)$, from the expectation value of $U^n(r)$ within the detection volume V $\zeta_V(U^n) = 1/V \int_V U^n(x)dx$. This leads to [99]:

$$\kappa_n(r) = \epsilon^n(r)\ \omega_n(r)\ N(r)\ \zeta_V(U^n) \tag{6.11}$$

From this equation, the cross-cumulant $\kappa_n(r)$ term is directly related to the molecular brightness $\epsilon(r)$ and the molecular time fluctuation statistics $\omega_n(r)$. Indeed $\zeta_V\{U^n\}$ is known from the PSF shape, for instance for a 3D Gaussian [99]:

$$\zeta_V(U^n_{3D}) = \frac{c(\sigma_{x,y}, \sigma_z)}{n^{3/2}}, \tag{6.12}$$

where $c(\sigma_{x,y}, \sigma z)$ is a constant depending on the PSF size.

Then $\omega_{n,k}(r)$ can be related to the photo-physics of individual emitters, in particular its *on* and off rates of emission. Assuming the simple case where the molecules fluctuates between two states (a bright S_{on} and a dark S_{off}), their relative durations τ_{on} and τ_{off} and can be related to the *on* and off rates:

$$\begin{aligned} \rho_{on} &= \frac{\tau_{on}}{\tau_{on} + \tau_{off}} \\ \rho_{off} &= 1 - \rho_{on} \end{aligned} \tag{6.13}$$

The signal of the emitters is modeled as 1 for S_{on} and as ξ for S_{off} with $\xi \in [0, 1)$. Based on a Bernoulli distribution with rates probabilities $\rho_{on,k}$, the factors $\omega_{n,k}$ are defined as [99]:

$$\begin{aligned} \omega_{1,k} &= (1-\xi_k)\rho_{on,k} \\ \omega_{2,k} &= (1-\xi_k)^2\rho_{on,k}(1-\rho_{on,k}) \\ \omega_{3,k} &= (1-\xi_k)^3\rho_{on,k}(1-\rho_{on,k})(1-2\rho_{on,k}) \\ \omega_{4,k} &= (1-\xi_k)^4\rho_{on,k}(1-\rho_{on,k})(1-6\rho_{on,k}+6\rho^2_{on,k}) \\ &\vdots \\ \omega_{n,k} &= (1-\xi_k)^n f_n(\rho_{on,k}), \end{aligned} \tag{6.14}$$

where $f_n(\rho_{on,k}) = \rho_{on,k}(1-\rho_{on,k})\frac{\partial f_{n-1}}{\partial \rho_{on,k}}$ is the n-th order cumulant of a Bernoulli distribution with probability $\rho_{on,k}$. Then the cross-cumulant can be approximated by:

$$\kappa_n(r) \approx \epsilon^n(r)\ f_n(\rho_{on}; r)\ N(r)\ \zeta_V(U^n) \tag{6.15}$$

From Eq.6.15 it is possible to pixel-wise estimate N, ϵ and $\rho_{on,off}$ by solving an equation system, or using a fitting procedure. In the publication introducing the bSOFI technique, the authors use the second and fourth cumulant orders to build the ratios:

$$\begin{aligned} K_1(r) &= \frac{\zeta_V(U^2)\kappa_3}{\zeta_V(U^3)\kappa_2}(r) = \epsilon(r)(1-2\rho_{on}(r)) \\ K_2(r) &= \frac{\zeta_V(U^2)\kappa_4}{\zeta_V(U^4)\kappa_2}(r) = \epsilon^2(r)(1-6\rho_{on}(r)+6\rho_{on}^2(r)) \end{aligned} \tag{6.16}$$

This leads to an estimation of the molecular brightness:

$$\epsilon(r) = \sqrt{3K_1^2(r) - 2K_2(r)} \tag{6.17}$$

, of the on-time ratio :

$$\rho_{on}(r) = \frac{1}{2} - \frac{K_1(r)}{2\epsilon(r)} \tag{6.18}$$

and finally of the molecular density:

$$N(r) = \frac{\kappa_2(r)}{\epsilon^2(r)\rho_{on}(r)(1-\rho_{on}(r))} \tag{6.19}$$

The spatial resolution of this estimation is set by the lowest order cumulant, in this case the second order. The balanced SOFI flowchart is described in Fig. 6.5. As described above, it involves deconvolution followed by linearization (resulting in the so-called balanced cumulant called $\kappa_{B,n}(r)$. The extracted molecular parameters are represented using $\kappa_{B,n}(r)$ as a transparency mask. They can finally provide information on fluorescence blinking, which is sensitive to the chemical micro-environment (the on time ratio is indeed related to the concentration of the triplet state quenchers such as oxygen), but can also be used to deduce some other local properties such as temperature and pH. Note however that the brightness estimation has been proved to loose its robustness when molecules of very different brightness are present in the sample [99]. This might lead to remaining heterogeneities, which limits its use to only qualitative analysis.

In the next section, we describe an implementation of bSOFI adapted for the polar-SOFI technique, based on the bSOFI algorithm previously developed [99]. It is essentially similar to the procedure explained in Fig. 6.5, using deconvolution, linearization (which is a key point for the quantitative use of the cumulant), and

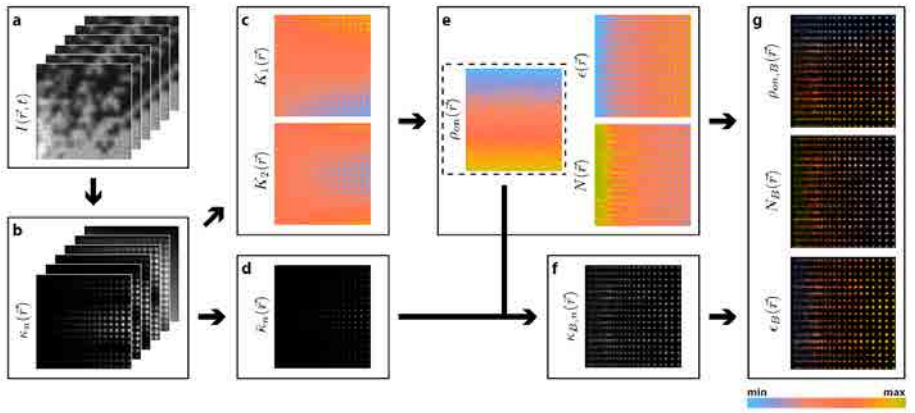

Figure 6.5: bSOFI flowchart. (a) Raw data. (b) Cross-cumulant computation up to order n. (c) Cumulant ratios K_1 and K_2. (d) Deconvolved cumulant of order n. (e) Molecular brightness ($\epsilon(\vec{r})$), on-time ratio ($\rho_{on}(\vec{r})$) and molecular density estimation ($N(\vec{r})$). (f) Balanced cumulant order n based on calculation explained in the text. (g) Color-coded molecular parameter maps overlaid with balanced cumulant as a transparency mask (Image obtained from [99]).

reconvolution. In addition, an attempt to use the molecular brightness estimation for polar-SOFI images is presented.

Note that in all the rest of this chapter, the estimated cumulant quantities $\kappa_{B,n}$ will be denoted C_n to simplify the notations.

6.2 Methodology

In this section we described the experimental setup, as well as the experimental conditions for polar-SOFI. In addition, the software used for cross-cumulant estimation based on the balanced SOFI Matlab Toolbox [99] is described.

Finally, the anisotropy analysis is detailed.

6.2.1 Experimental Setup

Due to the versatility of SOFI microscopy, we performed polar-SOFI in a conventional widefield microscope, initially adapted for polar-dSTORM microscopy, as described previously in the Chapter 3. Similarly as for polar-dSTORM, this setup is adapted to retrieve the perpendicular (called " $\perp$ " in what follows, corresponding to the vertical axis of the sample plane) and parallel (" $\parallel$ ", cor-

responding to the horizontal axis of the sample plane) polarization states of the fluorescence images.

6.2.2 Experimental conditions for polar-SOFI

In the polar-SOFI acquisition, a laser illumination at 639 nm or 488 nm is applied to the sample. This illumination in addition with the buffer described in the Chapter 3 results in a stochastic fluctuation of the dye between dark and fluorescent states. The EMCCD camera acquires the images continuously, in order to obtain a "SOFI image stack", which will be used for the cumulants calculation.

As in the case of polar-dSTORM, the detection path is modified with the addition of a Wollaston Prism, allowing simultaneous and spatially separate acquisition of the emission images polarized with parallel and perpendicular directions.

Acquisition Software

The camera control and acquisition are performed with the assistance of the Micromanager Software [70], a plugin of ImageJ [71] in similar way than polar-dSTORM. Typical acquisition parameters are:

1. Exposure time: 30 ms.
2. Gain: 100-300.
3. Frames: 100 - 2 000. 2 000 is used for piecewise polar-SOFI analysis. In the piecewise analysis, each stack division is usually 50-300 images long.
4. Format: TIFF (16 bits)

In this case, the memory is not a limiting resource as in the case of the STORM imaging since only a reduced number of frames are required.

The characteristics of the computer used for the acquisition are the same as in the case of polar-dSTORM (see Chapter 5).

Experimental condition and sample preparation

The experimental conditions and sample preparation protocols are similar to the ones used in the polar-dSTORM experiment. Similar concentration of buffers as polar-dSTORM experiment was used, being composed mostly of MEA to achieve a final thiol concentration of 100 mM. Small changes as a function of incident laser power have been necessarily do to adjust reversible photostatting of organic dyes to a suitable level for SOFI. Since it is not necessary to have isolated molecules as dSTORM, we increases the incident laser power until we start to see the dye to

blink, usually 80% of the incident power necessary for dSTORM . In this work, the samples studied for polar-SOFI are the same as described for polar-dSTORM since the goal was essentially to evaluate the feasibility of both techniques.

6.2.3 Data processing (Software)

The following section is based on an open-source Matlab toolbox for balanced SOFI (bSOFI) [99] and custom anisotropy analysis script, both written in Matlab. The goal is to reconstruct a super resolved image of anisotropy based on the SOFI technique [70].

The detailed schematic overview of the polar-SOFI algorithm is presented in Fig. 6.6. Description of each step is given in what follows.

Occasionally, due to the dye photo-bleaching during the acquisition, some artifacts in the cumulant calculation can appear. One method to circumvent this problem, is to acquire a big stack (1000 to 2000 images) and analyse piecewise in blocks of frames [106]. In consequence, the changes in the mean signal within the sub-stacks are negligible. Later on, the resulting cumulant images of each substack are summed together before any further analysis. In what follows, the cumulant analysis will be described based only on the substacks images or in short stacks ($<$ 300 frames).

polar-SOFI image processing

The first step of the polar-SOFI algorithm is to retrieve bSOFI images both on the $\perp$ and $\parallel$ detection channels. An overview of the adapted bSOFI algorithm is presented in Fig. 6.7.

After the acquisition of a stack of 50-300 frames, cross-cumulants are calculated assuming a zero time lag for each pixel for the whole image containing both $\parallel$ and $\perp$ channels. The computation of a cross-cumulant image is performed for each pixel with its n-1 (n: cumulant order) neighboring pixels, allowing an oversampling (n-times) in the final image, as described in Section 6.1.1. A cumulant SOFI image is created, the value of each pixel being the estimated cross-cumulant. Then several steps are then performed using the bSOFI program to retrieve a final cumulant image (see Section 6.1.1 for details):

1. a distance factor is applied to avoid heterogeneities between the inter-pixels generated by cross-cumulants
2. the cross-cumulant image is deconvolved using a Lucy-Richardson deconvolution method (deconvlucy, The Mathworks, Inc.)
3. the pixel's values are n-th rooted, in order to linearize the cross-cumulant signal with respect to the emitted intensity

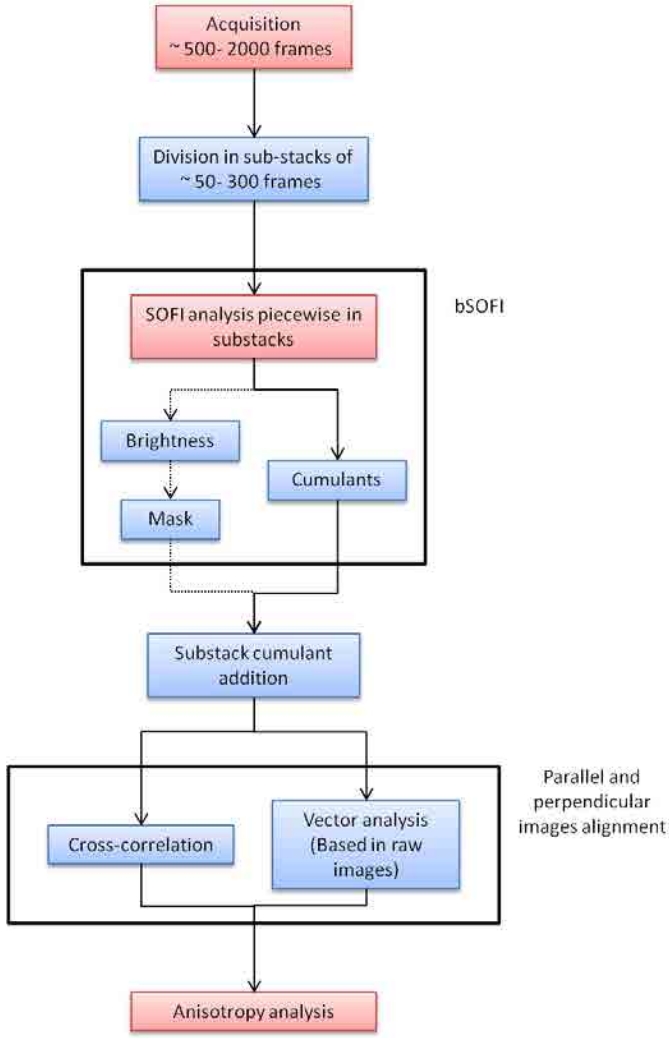

Figure 6.6: Detailed schematic overview of the polar-SOFI algorithm.

4. small pixel's values (1% - 5% of the maximum) are removed from the cross-cumulant image in order to eliminate deconvolution artifacts

5. a reconvolution step with a PSF size divided by n is performed

The resulting SOFI image for the n-th order cross-cumulant (called "cumu-

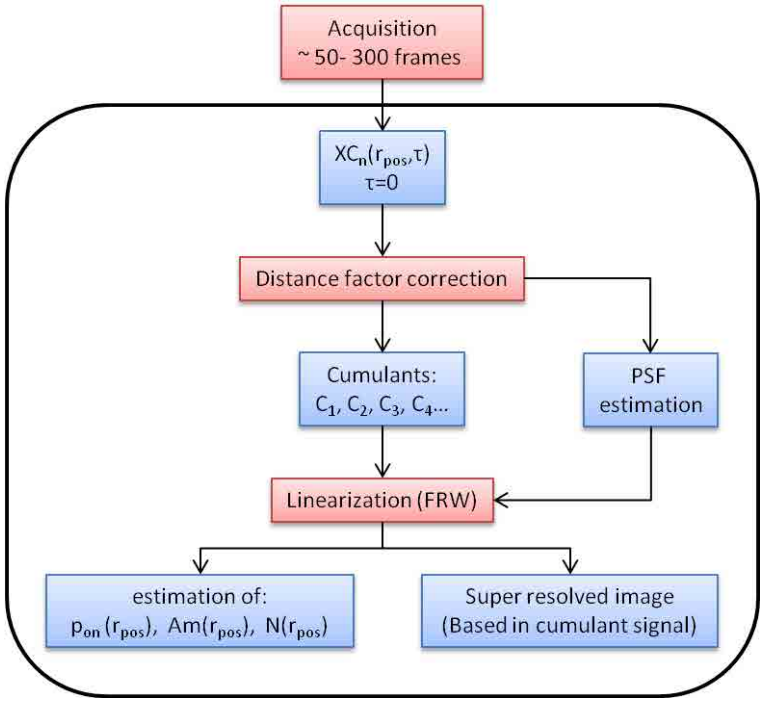

Figure 6.7: Scheme of the Balanced SOFI (bSOFI) implementation [99] adapted for polar-SOFI.

lant" for simplification) is denoted C_n.

Post-processing

After the cumulant images are obtained from the bSOFI algorithm, as described above, the next step is the calculation of an anisotropy super-resolution image based on these cumulants:

$$A = \frac{C_{n\parallel} - C_{n\perp}}{C_{n\parallel} + C_{n\perp}} \tag{6.20}$$

Where C_n is the cumulant image of order "n", with an index indicating the $\parallel$ and $\perp$ images cumulants.

For the anisotropy calculation, a direct operation on the $\parallel$ and $\perp$ side of the whole image is necessary since the information is now a pixelated image and not any more single molecules positions and intensities such as for polar-dSTORM.

The identification and alignment of the parallel (||) and perpendicular ($\perp$) images is therefore necessary (Fig. 6.8). Due to the importance of keeping the resolution information, the correct alignment at subpixel level is a crucial step. In addition, an error in the alignment can imply a bad estimation of anisotropy since each pixel contains its proper anisotropy information.

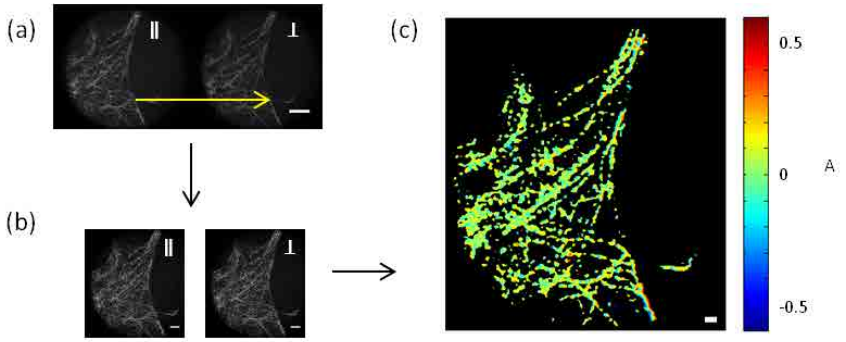

Figure 6.8: Overview scheme of the parallel and perpendicular C_2 images alignment in Tubulin in COS 7 cells, labelled with Alexa 647. (a) C_2 image. (Scale bar: $5\mu m$), translation vector in yellow. (b) Separated images of $C_{2\parallel}$ and $C_{2\perp}$ obtained after processing (Scale bar: $2\mu m$). (c) Polar-SOFI image based on the 2^{nd} cumulant images (Scale bar: $1\mu m$).

For this purpose two methods are proposed, depending on the molecular density and type of image:

1. Alignment based on a registration algorithm.
2. Vector estimation.

In the first method, assuming that the $\parallel$ and $\perp$ images have similar image features, a registration method is used for the alignment. For this purpose, we use StackReg [110], a plugin of ImageJ [71]. Prior to use the plugin we split the image into 2 images. (Fig. 6.9).

The main function of the StackReg plugin is to operate mathematical functions on the 2 images (such as cross-correlations) in order to align these images. In this plugin, four types of transformation are available: translation, rigid body (a combination of translation and rotation) , scaled rotation and affine transformation (dilatation).

In our case, we only consider the translation option since there is no other transformation a prior expected from the image formation by the wollaston prism.

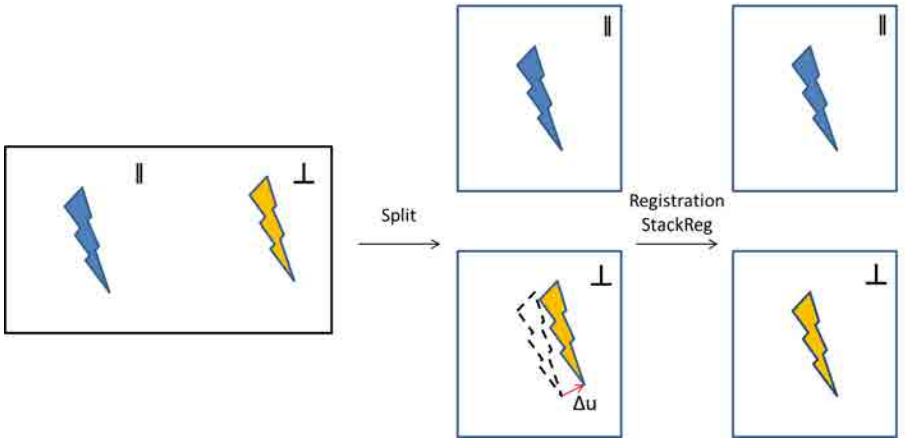

Figure 6.9: Overview scheme of the registration based on the StackReg [110] plugin. Δu is the translation value applied to the $\perp$ image to align both $\parallel$ and $\perp$ images in the same reference frame.

This method is robust for cases in which the intensity in parallel and perpendicular images is high enough. This approach is therefore weaker when the molecules are oriented along the $\parallel$ and $\perp$ directions since in this case the intensity on the other channel is very weak. In highly ordered samples, it is common to have such cases, therefore in this situation an intensity based registration is not adequate, and a method based on images features will be more appropriate.

The second method proposed is based on the vector estimation described in the Chapter 3. This method requires to detect in part of the images single molecules which can be localized with sufficient precision ($\sim$ less than the expected resolution). The raw SOFI images does not have necessity purely isolated molecules as for the localization microscopy methods (STORM, PALM, etc.), however, in some situations, it is possible to "detect" some isolated molecules and to identify the translation vector between their $\parallel$ and $\perp$ images. After the vector is estimated based on the SOFI movie analysis, one region is selected manually in the parallel image and the corresponding perpendicular image is retrieved based on the vector estimation (Fig. 6.10).

Anisotropy analysis

Prior to any further analysis, one threshold is applied to the cumulant image, in order to reduce the heterogeneities occurring during the cumulant calculation. The anisotropy ratio image (A) is calculated as eq. 6.20.

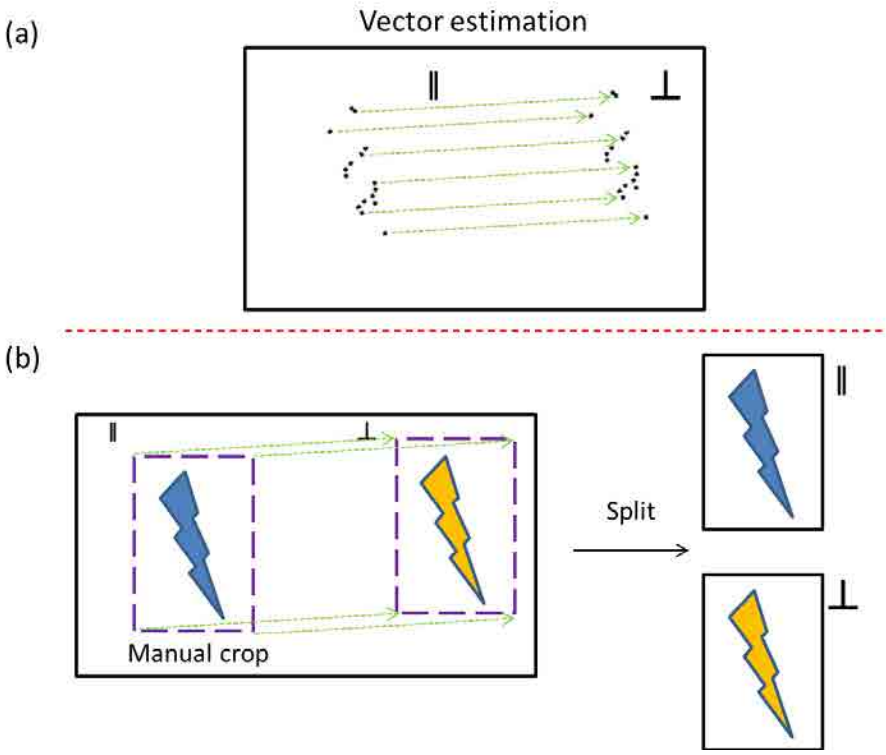

Figure 6.10: Overview scheme of the alignment based on the vector estimation. (a) Vector estimation on the "SOFI" movie. (b) Image alignment.

In comparison with the polar-dSTORM technique, the polar-SOFI anisotropy is reported per pixel, while in polar-dSTORM it is given per event of localization. In terms of complexity, the polar-SOFI algorithm requests less computational effort than polar-dSTORM, for treatment and for final rendering. Nevertheless it is important to remember that polar-dSTORM offers a single molecule anisotropy value, whereas polar-SOFI estimates anisotropy in a pixel region, that does not necessarily contain a single molecule but rather several molecules. The obtained information is therefore rather an ensemble anisotropy value.

For a correct measurement of A, possible differences of the efficiency between the parallel and perpendicular channels are systematically detected similarly as in polar-dSTORM by comparing intensities measured in a 10 μM water solution of Atto 633 or Alexa 488, that is assumed to be isotropic, due to its fast molecular rotational dynamics. A correction factor is expressed as:

$$G = \frac{I_{\parallel}}{I_{\perp}} \tag{6.21}$$

With $I_{\parallel}$ and $I_{\perp}$, the intensities measured with $\parallel$ and $\perp$ channels. This ratio (usually in the range 1-1.8) is taken into account by rescaling the cumulant signal of the appropriate detected image before further data processing:

$$A = \frac{C_{n\parallel} - G \cdot C_{n\perp}}{C_{n\parallel} + G \cdot C_{n\perp}} \tag{6.22}$$

The anisotropy image is then directly reconstructed based on this operation on the cumulant images. Contrary to polar-dSTORM, no further rendering is necessary for polar-SOFI, since the anisotropy is obtained directly from the ratio between the pixels' value of the parallel and perpendicular images (Fig. 6.8c).

Although, the anisotropy rendering image offers an useful tool to analyze the orientational behavior in one region, statistical tools such as histograms can offer a better overview regarding the order or disorder behavior in one region or in the full sample (Fig. 6.11). Polar-SOFI combines the possibility to study the morphology of fiber structures (such as actin filaments, microtubules and DNA), as well as the "molecular order" at a sub-diffraction limit scale. The fiber structure analysis of polar-SOFI is divided in three main parts:

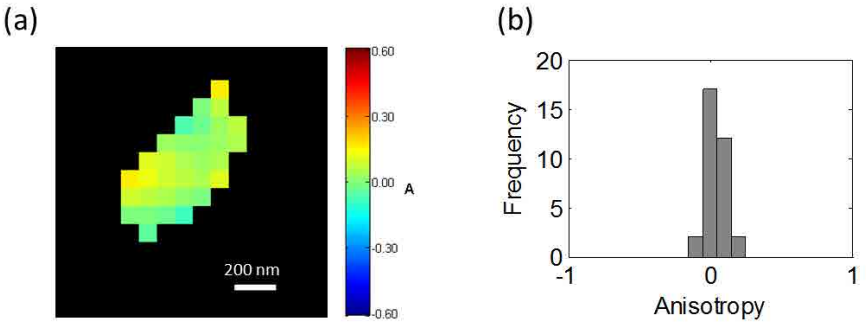

Figure 6.11: Anisotropy SOFI Image of a single fiber structure. (a) C_2 image (Sample: tubulin in a COS 7 cell). (b) Anisotropy histogram of the selected structure.

1. Fiber size (resolution). The maximum morphological resolution of the fibers (Full Width Half Maximum FWHM) can be estimated based on the cumulant image, as well as the expected resolution based on prior theoretical calculations developed for SOFI microscopy [100].

2. Cluster Analysis. Similarly as for polar-dSTORM, this permits to define the local orientation in fibers.

3. Anisotropy analysis to retrieve ρ vs ψ. Using the approach developed for polar-dSTORM, the use of the A (ρ, ψ) curve (see Fig. 6.14) permits to identify constraint distribution defined by a cone orientation.

Fiber size (Resolution) Assuming the PSF as approximately Gaussian, the n-th order cumulant increases the resolution of $\sqrt{n}$ [15](Fig. 6.12). Nevertheless, it has been demonstrated the possibility to obtain a resolution improvement of almost n-fold compared to the diffraction limited image, based on a Fourier reweighting [100].

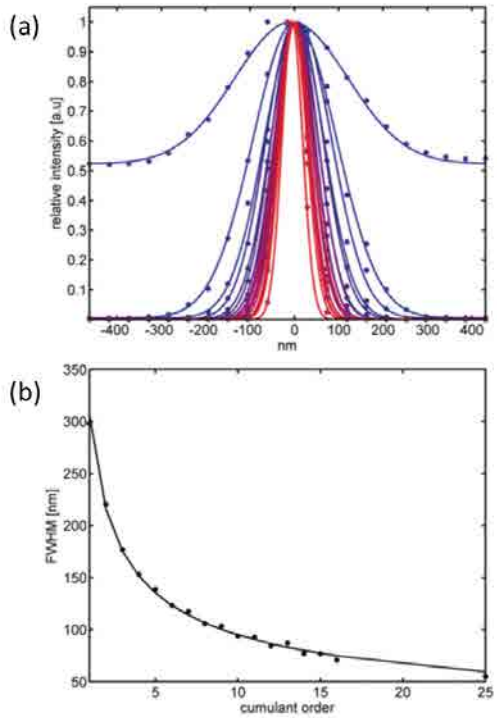

Figure 6.12: Resolution enhancement of SOFI. (a) Gaussian fits of cross-section SOFI images of QDs deposited on a coverslip for normalized cumulants order 2-25. (b) Fitted Full Width Half Maximum (FWHM) as a function of the cumulant order (Fig. obtained from [15]).

Even though SOFI microscopy seems to have unlimited resolution capability [15, 100], there are different factors, which limit the possible resolution improvement, especially the signal to noise ratio (SNR) and blinking rate. In experimental conditions, a 4 times resolution improvement has been demonstrated [101], using fourth order cumulant and the Fourier reweighting principle. Although this modest enhancement in resolution is smaller than what can be obtained by the localized microscopy techniques ($\sim 10\times$), there are still advantages as a function of relaxed SNR requirements and acquisition time. In this sense, SOFI microscopy could be more adequate for short acquisition times (therefore giving access to more dynamical processes), high labeling density or low SNR. It has been proven that SOFI can work with five times lower SNR as compared with dSTORM [101].

In our implementation of polar-SOFI, the resolution improvement is close to $\sqrt{n}$. No specific gain was observed using the Fourier reweighting. This could be due to the low intensities, obtained due to the separation into the $\parallel$ and $\perp$ channels, but also to the high background presented in some of the samples (low SNR).

As in polar-dSTORM, the Full Width Half Maximum (FWHM) in fiber structure is used as a measure of the fiber profiles as well as an estimation of our resolution. To determine the FWHM, the profile of a cluster or fiber was fit with a Gaussian function.

Fiber orientation measurement (Cluster Approach) In a similar way as described for polar-dSTORM, in order to retrieve the local orientation in a reconstructed super resolved image of fibers, an analysis based on the identification of "clusters" of pixels is performed.

In this approach the selection of the region of the cluster is made directly by the user (Fig. 6.13a). The orientation angle (ρ) of this cluster is determined using the Image Processing Toolbox® of Matlab®. In addition, it is possible to perform statistical analysis (anisotropy histogram, mean and standard deviation) in the selected region and use it for further data interpretation (identification of the probe dynamic behavior for instance). An example of this approach in tubulin fibers in a COS 7 cell is shown in Fig. 6.13.

As in the case of polar-dSTORM, the average anisotropy for a given "cluster" is reported in the reference graph of $A(\rho, \psi)$ shown as in Fig.6.14. Contrary to polar-dSTORM, the reported anisotropy value may be already averaged values over an ensemble of molecules.

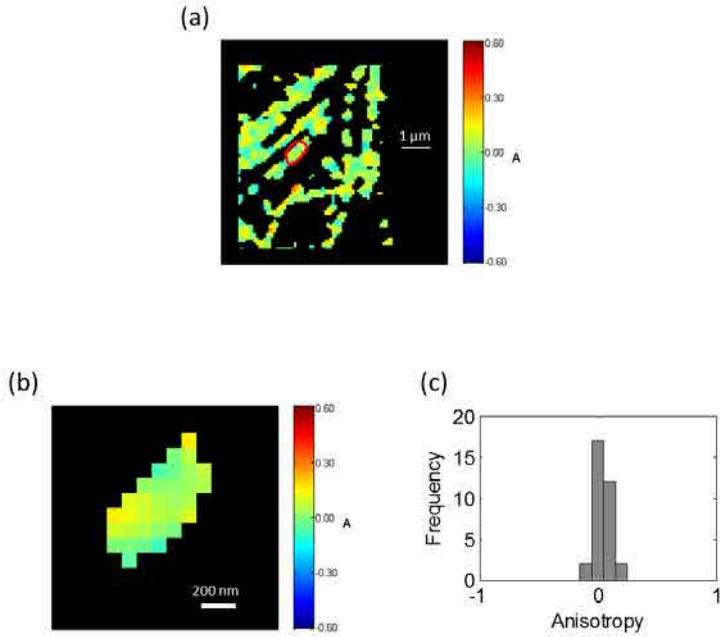

Figure 6.13: Manual selection of clusters. (a) SOFI super resolved image of the anisotropy obtained from the second order cumulant. A cluster is selected in the region surrounded by a red line (Sample: tubulin in a COS 7 cell). (b) Cluster super resolved image of anisotropy. (c) Histogram of anisotropy pixels of the selected cluster.

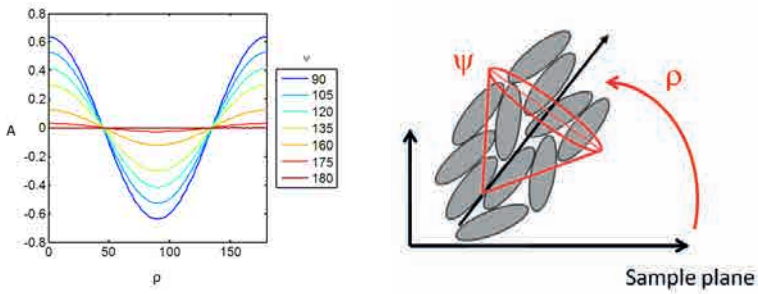

(a) (b)

Figure 6.14: (a) Theoretical anisotropy average as a function of ρ and ψ angles as defined in (b).

6.3 Theoretical analysis

In this section, we validate the application of the polar-SOFI algorithm through a Monte Carlo Simulation based on signals conditions obtained typically in our biological samples. The limitations and detection conditions of the algorithm are analyzed, in particular the effect of noise and cumulant order on the precision of the anisotropy estimation.

6.3.1 Model

A similar 2D Model, to that described previously in Chapter 4, is proposed to represent the rotational behavior of single molecules. This model assumes that the molecule absorption and emission dipoles are parallel and rotating in the sample plane at a rate $1/\tau_{rot}$ with $\tau_{rot} < \tau_f$ (τ_f being the fluorescence lifetime of the molecule). This rotation is constraint in a core of aperture ψ and direction ρ (in the sample plane) relative to the $\parallel$ direction.

6.3.2 Simulation

In order to observe the effect of the noise and the limitations of the polar-SOFI approach, a simulation has been implemented to generate a typical signal which fluctuation occurs with a characteristic "blinking" time-scale. For each of these scenarios, the 2^{nd} and 4^{th} cumulant images are calculated. As it was described previously in the Chapter 3, the noise model was adapted based on an intensity dependent Poisson model. A detailed description of the Monte Carlo method is described in what follows.

Simulation Method & parameters

The steps of the analysis are described in what follows.

Set initial parameters. The initial parameters in the simulation are:

- Radius ("r"): initial radius for the "detection" algorithm (see Chapter 4 for polar-dSTORM).
- PSF window (usually 11×11 pixels): area within which the spatial analysis (Gaussian fit, integrated intensity) is performed.
- Number of molecules per frame.
- Intensity. This value will depend of the case of study. When the molecule is "off", zero intensity will be assigned for parallel and perpendicular images.

- Offset. For the case of the Quantem 512sc camera, this value is set to 1 000.
- Experimental background. For this simulation, background is 1 500 or 2 500 counts.
- Number of stacks. Cumulant images will be obtained per stack.
- Number of frames per stack. For these experiments, this value is around 1 000.
- Transition statistics for the blinking behavior (see Fig. 6.15).
- k_g. Noise constant, as defined previously (see Chapter 3). This constant is dependent on the gain of the camera (typically gain 300 and 500 are chosen).
- Frame size (typically 50 $\times$ 100 pixels).
- Distance vector between pairs (typically 50 pixels).
- G factor. This value is set to 1.
- Distance between molecules. This parameter is used to evaluate the minimum distance in which we are able to identify two different molecules.

Defining the blinking behavior of molecules. SOFI microscopy is based on fluctuating molecules. The blinking behavior per molecule is simulated as a hidden time-continuous Markov model (a Markov process is a stochastic model in which a random system changes state depending on probabilities that depend on its current state) between on and off states (Fig. 6.15) inspired from [101]. This model allows to vary the time scale of the blinking behavior and generate random time traces following the same time scale behaviors, as required for our Monte Carlo simulations. First, a fluctuation time trace (Fig. 6.16) is generated by the hmmgenerate function of the Statistical Toolbox of Matlab ®for a given pixel considered as containing a single emitter. The amplitude reached during this time trace is either 0 or 1 (two states).

Two different transitions scenarios were considered: "slow" and "fast" blinking. The corresponding statistics between the emissive and nonemissive states are ($P_{00} = 0.85$, $P_{11} = 0.15$, $P_{01} = 0.15$, $P_{10} = 0.85$) for the "slow" blinking, and ($P_{00} = 0.5$, $P_{11} = 0.5$, $P_{01} = 0.5$, $P_{10} = 0.5$) for the "fast" blinking. Typical fluctuation time traces for these two scenarios are represented in fig. 6.16. Second, this signal will be scaled with a given total intensity then blurred with a given PSF (as done in Chapter 4) and background, and then artificially affected

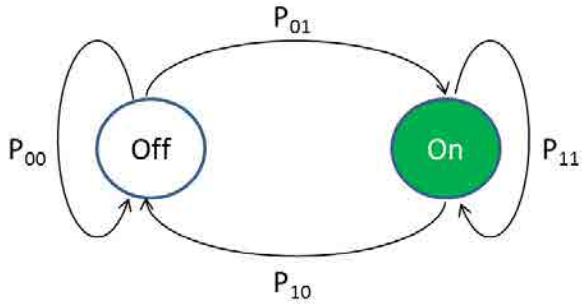

Figure 6.15: Scheme of 2-states (on, off) hidden Markov model used for the blinking behavior, including the probabilities $P_{00}, P_{10}, P_{01}, P_{11}$ transition.

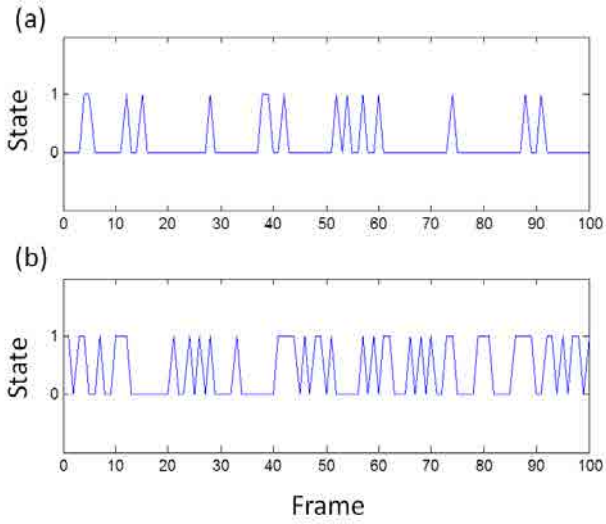

Figure 6.16: Blinking time trace. Example of blinking trace for a given molecule based on the Markov model described in the text. (a) Slow blinking. (b) Fast blinking.

by noise (using the model described in Chapter 3). This gives rise to an image of a fluctuating single molecule which can be analysed using SOFI.

Set localizations and intensity. In this part, the positions and intensity of the emitters are defined as show in Fig. 6.17a) based on the initial parameters. The intensity of each considered pixel will be multiplied to the blinking time trace of each molecule. When the blinking trace has a value of zero for a given frame, the intensity of the molecule for parallel and perpendicular image will be zero.

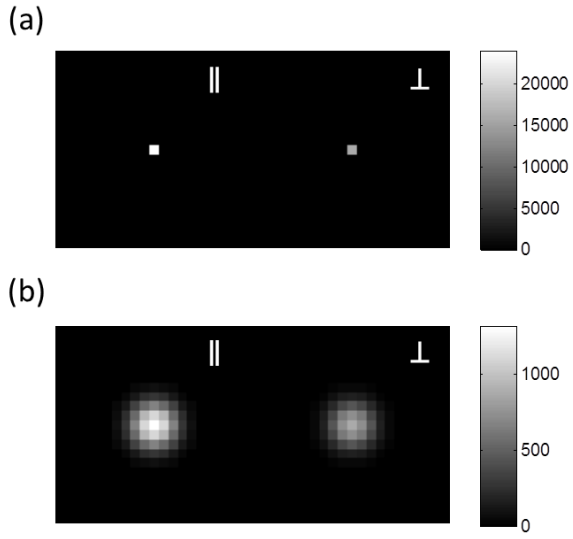

Figure 6.17: Set localizations and image blurring. (a) Center of PSF. (b) Blurring (PSF radius = 1.7 pixels, filter window 11 pixels). Here the chosen anisotropy is 0.2 and the total intensity is 40 000 counts

PSF filter. Prior to the Gaussian blurring, a Gaussian (PSF) filter is defined. This filter is created using fspecial command of Matlab®, with the parameters of the window size and PSF radius (Fig. 6.18).

Blur the image with the PSF filter. After the PSF filter is defined, the initial image with the localizations is blurred (Fig. 6.17b).

Add background and noise. The camera offset and the background characteristic of the sample are added, and the noise based on the previous intensity dependent Poisson model (see Chapter 3) is included (Fig. 6.19).

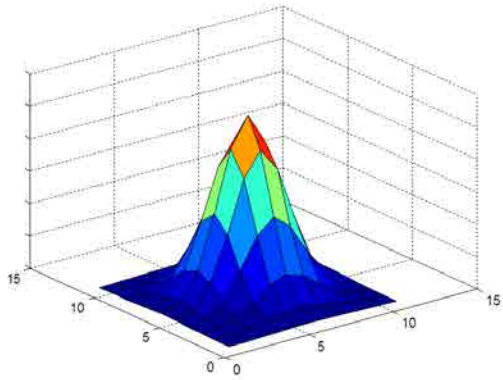

Figure 6.18: PSF generated by the fspecial function in Matlab, window size = 11 pixels and PSF radius = 1.7 pixel (in order to mimic experimental conditions).

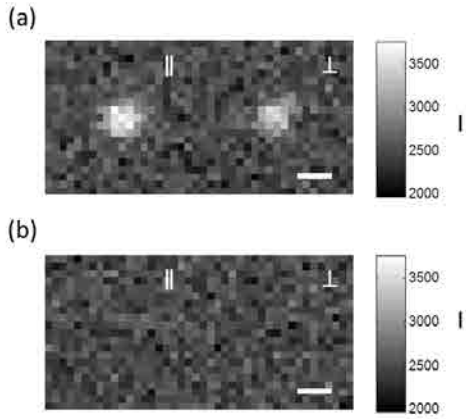

Figure 6.19: Raw simulated SOFI single frame, including the background and noise (Window size = 11 pixels, PSF radius = 1.7 pixel). (a) "On" state. (b) "Off" state. Here the background is 2 500 counts

SOFI implementation.

The raw "SOFI" movie stacks are then generated accounting for the simulated blinking traces based on the chosen fluctuation statistics. They are analyzed with the bSOFI Matlab Toolbox [99]. Example of images obtained for the second, fourth cumulant and brightness estimation are shown in Fig.6.20.

We generally perform a thresholding using a mask for C_2, C_4 and ε images, to remove image artifacts which appear due to deconvolution operations, as usually done in the literature [99].

The resolution improvement brought by the SOFI processing is visible in these images, as shown by the FWHM estimation.

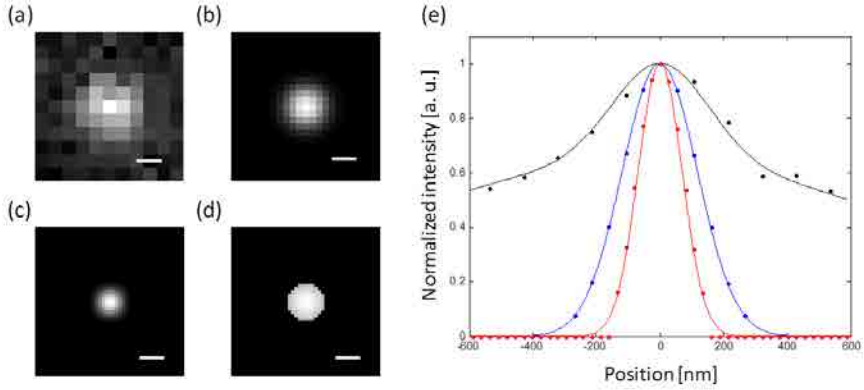

Figure 6.20: SOFI Simulation and resolution estimation. Simulated results from a single fluctuating emitter with the initial parameters: initial intensity = 30 000 counts, radius = 1.7 pixels, background signal = 2500 counts, camera gain = 300 over 1000 frames. (a) Widefield image of a selected frame (pixel size = 107 nm). (b) Second cumulant image (pixel size = 53.5 nm). (c) Fourth cumulant image (pixel size = 26.75 nm). (d) Brightness estimation calculated by bSOFI (Mask thresholding for the fourth cumulant was used to avoid heterogeneities). Scale bar = 200 nm. (e) Intensity and cumulant signal profiles. Black points: widefield (FWHM = 351 nm), blue points: second cumulant (FWHM = 278 nm) and red points: fourth cumulant (FWHM = 163 nm). Gaussian fit (lines).

The simulated SOFI image stacks were used for several tests that seemed to be important to check before performing any experimental analysis. We summarize here the relevant points which were considered:

- Verification of the linear proportionality between cumulant signal and intensity. Since the anisotropy in polar-SOFI is based on cumulant signals, they

should verify a linear dependence with respect to fluorescence intensity.

- Bias and precision of anisotropy calculated from cumulant images. These parameters have to be analyzed for different anisotropy values and different signal levels.

- Anisotropy imaging and artifacts from close-by molecules. Since the anisotropy is estimated per pixel, overlap between molecular signals might lead to artifacts in their anisotropy estimation.

Blinking behavior influence At the beginning of the simulation description, two types of blinking trajectories ("fast" and "slow" blinking) were defined.

In the simulation, we have observed that the variation in the SNR due to the on-time ratio is not very significant. It has been published that the SOFI technique is less affected by the photo-switching kinetics than STORM microscopy [101]. Since the purpose of this section is to evaluate the polar-SOFI estimation in the most realistic scenario, we use in the follow analysis the "fast" blinking behavior.

Cumulant signal linearity

One important characteristic for the use of cumulants for the anisotropy calculation and interpretation is the proportionality between the cumulant signal and the initial intensity (I_T) set as a known parameter.

Indeed our calculation of intensity is now based on a ratio of cumulants calculated in the $\parallel$ and $\perp$ channels, therefore requiring a linear response of their cumulant with respect to the signal in the respective $\parallel$ and $\perp$ channels.

Based on the simulation described previously, we analyzed 100 simulated PSF fluctuating traces, where each trace has 1000 frames with a given background (2500 counts), camera gain (300), radius (1.7 pixels), PSF window (11 pixels $\times$ 11 pixels) and initial intensity (5 000 to 30 000) with the balanced SOFI toolbox. The window size for analysis is defined as $5\times$ radius $\times\sqrt{n}$, and we select the closer odd number to define a workable window size, in order to define the center of the gaussian in a given pixel. In addition, one thresholding mask is applied to the brightness estimation based on the 4^{th} cumulant (threshold of 100).

After the cumulant images are obtained, we need to calculate for each molecule the $C_{n\parallel}$ and $C_{n\perp}$ values necessary to evaluate its anisotropy. The required cumulant signal can be either retrieved per pixel (to form an image) or integrated over a window of analysis, which is appropriate for the single molecules' simulations. To quantify this cumulant signal, first we define a window box with center in the Gaussian maximum of 13 pixels $\times$ 13 pixels for C_2 cumulant and 17 pixels $\times$ 17 pixels for C_4 cumulant and brightness estimation (note that the pixel size is

different for C_2 and (C_4, ε), due to their different sub-pixel definition). Then we integrate the pixel signals inside this window to get an cumulant average signal and subtract the background based on the average signal of the contour pixels.

In Fig. 6.21, we observe a clear linearity between the 2^{nd} cumulant signal and the expected total intensity (I_T). For the 4^{th} cumulant, there is a linearity for the high intensity levels ($I_T > 10\ 000$) however the dependence becomes non-linear for lower I_T signals. It means that for low intensities the quantification of the anisotropy based on this cumulant can be biased.

Finally in the case of the brightness estimation, we observe a strongly non-linear behavior, in consequence this parameter can only be used for qualitative analysis. Previously in the literature, it was indeed mentioned that the brightness estimation should be used for qualitative purposes [99].

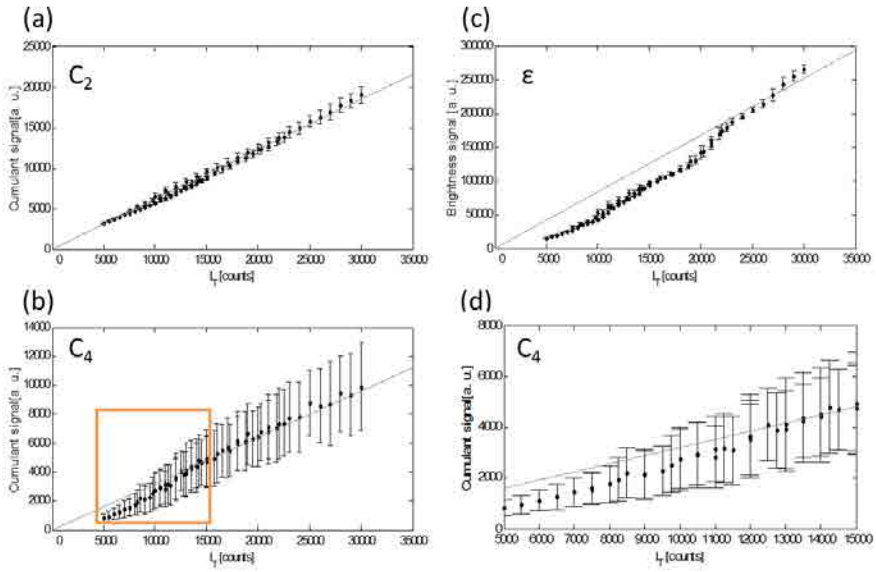

Figure 6.21: Cumulant signal linearity. (a) Simulated Intensity vs Second cumulant signal. (b) Simulated Intensity vs Fourth cumulant signal. (c) Simulated total Intensity vs Brightness estimation. (d) Zoom from orange rectangle. Continuous line: interpolation by a linear curve.

Bias and precision of the estimated anisotropy from cumulant images

In order to validate the quality of estimation of anisotropy obtained by the polar-SOFI method, a Monte Carlo simulation is performed. For this simulation, 100 SOFI image stacks were simulated with 1000 frames each. Each SOFI stack contains one fluctuating molecule (1 pair of PSF) with a given anisotropy. This analysis was performed for different anisotropies from -0.5 to 0.5. The frame size is 21 $\times$ 42 pixels.

Contrary to the polar-dSTORM method proposed previously, where the anisotropy estimation is evaluated per molecule (event), for polar-SOFI the estimation is performed per pixel. Possible bias in the anisotropy can appear in one image due to low levels of intensity, therefore the quality of the anisotropy estimation is not necessarily homogeneous over an image. This is illustrated in Fig. 6.22: in the central pixel the cumulant signal is high and there is no bias in anisotropy, on the border of the spot, the cumulant signal decrease by a factor of 2 leads already to a bias of 0.012. Due to additional noise effect in the low signal pixels, the pattern of the bias $\delta_{<A>}$ is not necessarily centered on the PSF image. Even though the effect shown here does not exhibit a strong bias, it nevertheless illustrates the potential artifacts that can affect a polar-SOFI anisotropy image due to strong variation in the signal levels.

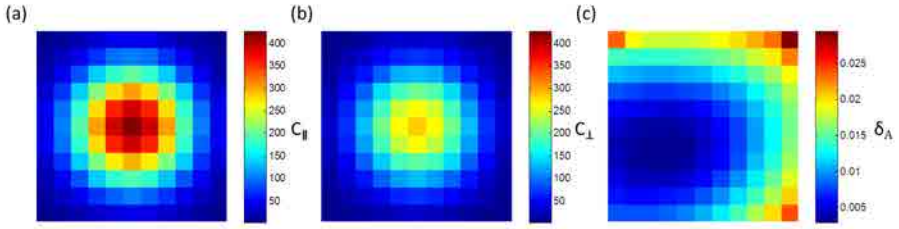

Figure 6.22: Bias of anisotropy estimation (δ_A) in a single molecule polar-SOFI image. Parameters of simulation: A=0.2, I_T = 40 000 and Bg = 2 500 (a) $\parallel$ second cumulant image. (b) $\perp$ second cumulant image. (c) Bias ($\delta_A = A_{estimated} - A$) for second cumulant image.

In order to quantify the precision and bias of the estimated anisotropy in a more general way, we analyzed the anisotropy based on the center pixel of parallel and perpendicular images for different anisotropies values (Fig. 6.23).

Similarly to the case of polar-dSTORM, we observe a more pronounced anisotropy bias for the high absolute values of anisotropy, especially for low cumulant signals, in both the second and fourth cumulants. A similar behavior is observed in the anisotropy precision σ_A (Fig. 6.23a and 6.23b), the effect for the fourth

cumulant being slightly higher than for the second cumulant, in particular at low intensities. For the representation of σ_A and $\delta_{<A>}$ for different A values, we use similar graphs as for polar-dSTORM except that now the signal level refers to the cumulant signal and not to an intensity. Nevertheless it is possible to calculate the total intensity from the initial parameters used for the simulation. We therefore use this number and evaluate the intensity from an integration over the simulated Gaussian PSF image before any SOFI process. This permits to compare to previous dSTORM results.

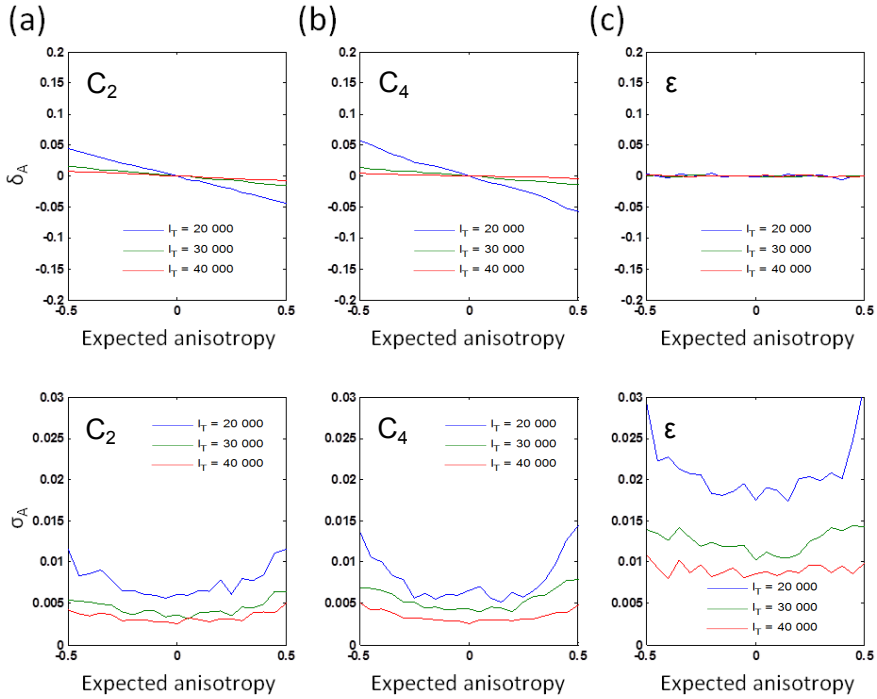

Figure 6.23: Anisotropy analysis at the center of the simulated PSF for cumulant and brightness estimations. (a) C_2. (b) C_4. (c) Brightness estimation (ε) by bSOFI. Up: anisotropy bias as a function of the expected anisotropy (δ_A). Down: standard deviation of anisotropy estimated (σ_A). Total simulated initial intensity : 20 000 counts (red line), 30 000 counts (green line) and 40 000 counts (red line).

Although we pointed out previously the non-linear response of the brightness estimation as a function of the effective intensity, we quantify as well the

anisotropy bias and variation based on the brightness value ε per pixel in both $\parallel$ and $\perp$ channels, given by:

$$A = \frac{\varepsilon_{n\parallel} - \varepsilon_{n\perp}}{\varepsilon_{n\parallel} + \varepsilon_{n\perp}} \tag{6.23}$$

The brightness image seems to guaranty a good anisotropy estimation at the center of the PSF, whatever the expected anisotropy. This might be due to the fact that the nonlinearity occurs at intensities lower than 20 000. Nevertheless, the precision on A (σ_A) is lower using the brightness as a signal. In addition, since the brightness estimation in the bSOFI algorithm is based on a ratio between cumulants, all the bias and loss of precision related to the cumulant estimation can affect the anisotropy estimation when the signal is low.

The estimation analysis was performed so far in the central pixel of the single molecule in Fig. 6.22a b. It is visible from Fig. 6.22c that some estimation problems also occur in the border of the spot, due to the loss of signal.

In order to visualize the statistics of the bias per pixel for a given anisotropy, an additional analysis was performed. In this study, a window of 11×11 pixels was selected arbitrarily for the second and fourth cumulant (the center of this window is aligned on the center of the simulated PSF), and the bias $\delta_{<A>}$ was estimated for all pixels belonging to the window, for which the cumulant signal is known. Figure 6.24 shows the resulting statistics for $A = 0$ and $A = 0.2$.

The cumulant signal is normalized to its maximum in the graphs of Fig. 6.24, since the idea here is to see the statistical behavior of $\delta_{<A>}$ and not its dependence on I_T or cumulant signal, which is reported in Fig. 6.23. Figure 6.24 shows that the more the cumulant signal decreases, the more the diversity of δ_A values appears, due to noise explaining the image variations in Fig. 6.22c. In addition, C_4 appears clearly more sensitive than C_2 to a loss of signal with a stronger bias.

Figure 6.25 shows the effect of cumulant signal thresholding on the resulting anisotropy precision σ_A. Clearly, thresholding the C_2 and C_4 signals above $\sim$ 30% of their maximum values already provides a reliable estimation of A.

Anisotropy imaging and artifacts from close-by molecules. In order to evaluate the limitation of the polar-SOFI technique in its imaging mode, we simulated a pair of molecules with different blinking traces. The molecules were separated by 1 to 5 pixels (Fig. 6.26) covering distances well below and well above the diffraction limit (the PSF radius is 1.7 pixels). Each SOFI image stack is made of 1000 frames. The frame size was 140 × 100 pixels in order to cover all considered inter-molecular distances in a single treatment.

The simulation parameters were similar to the previous test: PSF radius = 1.7 pixels, camera gain = 300 and background signal is 1 500 or 2 500 counts.

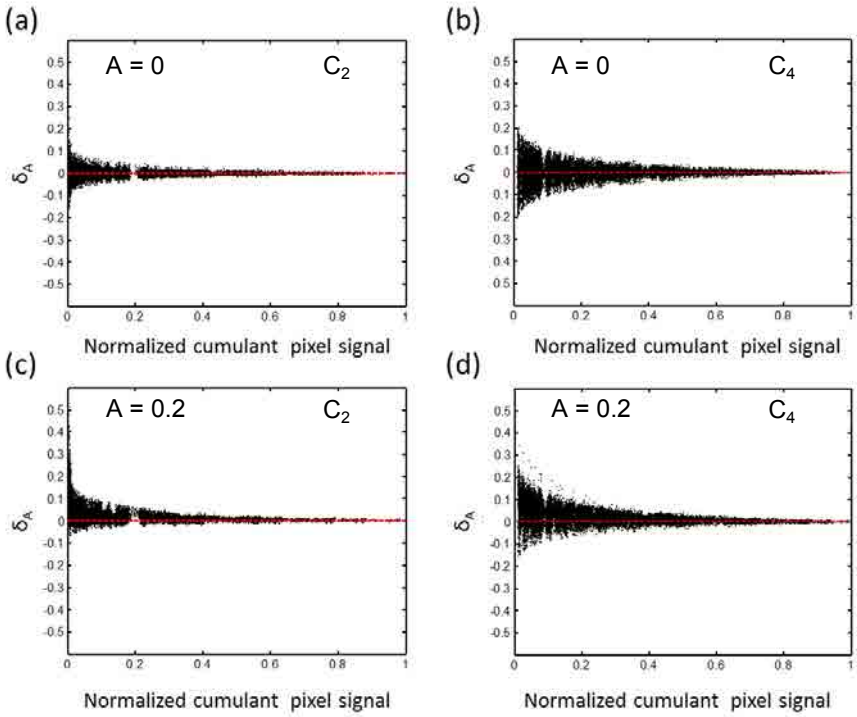

Figure 6.24: Anisotropy bias (δ_A) as a function of the (normalized) cumulant signal per pixel for a given anisotropy. Second cumulant: (a) A = 0 and (c) A=0.2. Fourth cumulant: (b) A = 0 and (d) A=0.2.

After the raw SOFI movie stack was obtained, it was analyzed with the "adapted" bSOFI matlab toolbox [99]. A threshold was applied to the estimated cumulant images to remove the artifacts generated after the cumulant calculation.

Case where the two molecules have the same anisotropy We first analyzed two molecules with $A = 0.2$, for the second and fourth cumulant, with total intensities of 40 000 counts (Fig. 6.27a and b) and 20 000 counts (Fig. 6.27c and d). The distances between the molecule are chosen to represent cases easily resolvable using C_4 but with more difficulty using C_2. As expected, we can observe a better anisotropy estimation for high initial intensity than for low initial intensity, for both C_2 and C_4, with more variation of A over the cumulant images. When the molecules are in close proximity, the inter-molecules region

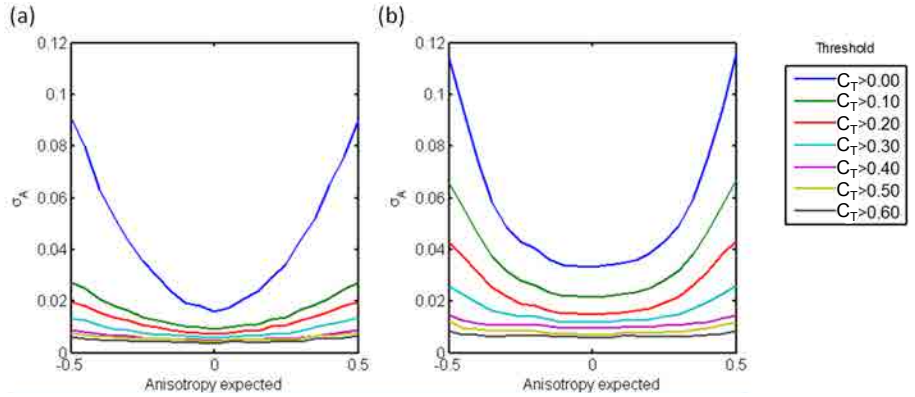

Figure 6.25: Standard deviation of Anisotropy (σ_A) as a function of the expected anisotropy (same conditions as in Fig. 6.23) and for a given total cumulant signal($C_{n\parallel} + C_{n\perp}$) threshold ($C_T$) relative to its maximum value. (a) C_2. (b) C_4.

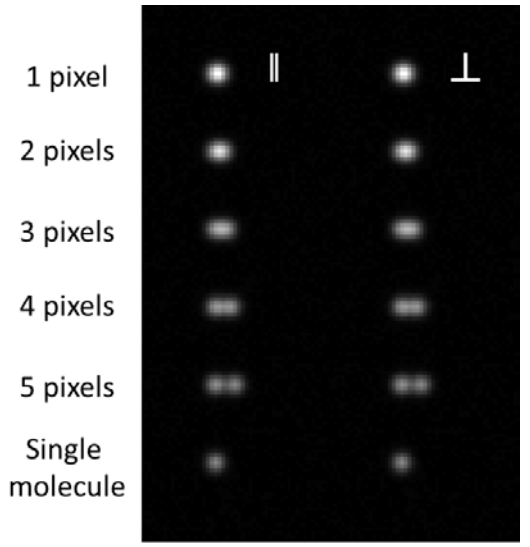

Figure 6.26: Simulated widefield image for the anisotropy imaging test with 2 molecules distant by the indicated pixel numbers.

is also more strongly affected by anisotropy variations for low intensities. Note that the fourth cumulant requires a higher threshold than the second cumulant in order to avoid the heterogeneities of the cumulant estimation due to the low

signal to noise ratio. This test shows overall that for high intensities ($\sim$ 40 000 counts) the anisotropy image of two identical molecules is quite robust and the molecules can be easily resolved using C_2 at a 4 pixels interdistance. In lower intensity conditions (20 000 counts), they are less easily resolved (C_4 only is able to differentiate them) and A varies in their edge and inter-molecule region. Consequently low signal conditions may lead to visible anisotropy artifacts in the final A image with a decrease of precision (Fig. 6.28).

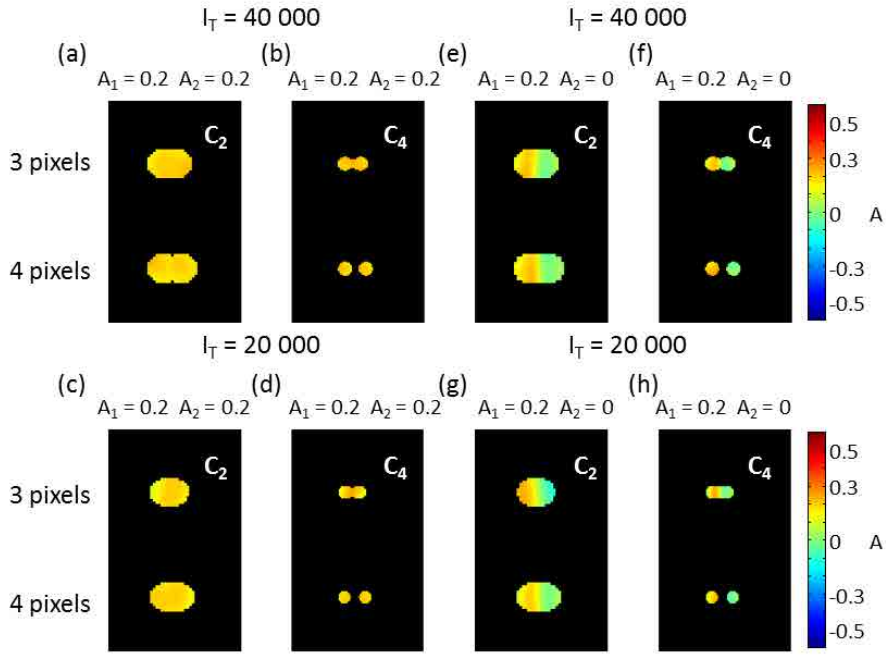

Figure 6.27: Simulation of two molecules (of anisotropies A1 and A2) separated by 3 and 4 pixels. C_2 and C_4 images are shown for different parameters indicated in the images. Simulation parameters: camera gain = 300, PSF radius= 1.7 pixels and background= 2500. (a-d) A1 = A2 = 0.2, (e-h) A1 = 0.2, A2 = 0; (a,b) and (e,f): I_T = 40 000; (c,d) and (g,h): I_T = 20 000; Threshold condition: (a) $C_{2,T} = 0.03$, (b) $C_{4,T} = 0.11$, (c) $C_{2,T} = 0.11$, (d) $C_{4,T} = 0.25$, (e) $C_{2,T} = 0.03$, (f) $C_{4,T} = 0.11$, (g) $C_{2,T} = 0.12$ and (h) $C_{4,T} = 0.25$.

Histograms of C_2 and C_4 for molecules separated by 3 pixels show the intensity dependence of σ_A, as well as the anisotropy bias due to the proximity of the molecules (see Fig. 6.28). For high intensities, C_2 seems quite robust as a function of anisotropy estimation and variation (the histogram of A for the two molecules is

the same as for a single molecule). For low intensities on another hand, anisotropy estimation in C_2 can have some bias due to the proximity of the molecules. Regarding C_4 for low intensities, C_4 anisotropy histograms of a single molecule show higher σ_A than the pair of molecules, however the anisotropy bias is smaller for the single molecule. This anisotropy variation in the single molecule case in C_4 is due to the influence of the SNR in the cumulant estimation. For high intensities on the other hand, C_4 shows a clear effect in the anisotropy estimation and variation due to the proximity of the molecules.

We also simulated the results obtained from the brightness (ε) estimation. The images look similar to the C_4 images, showing relatively good results. This is mainly because the imposed thresholding is performed with I_T high enough so that nonlinearity problems do not appear.

We finally checked the effects of the background and camera gain. When background increases and the gain increases, heterogeneities in the anisotropy image increase and distinguishing the two molecules gets more difficult. In this situation it will be necessary to set a higher signal threshold.

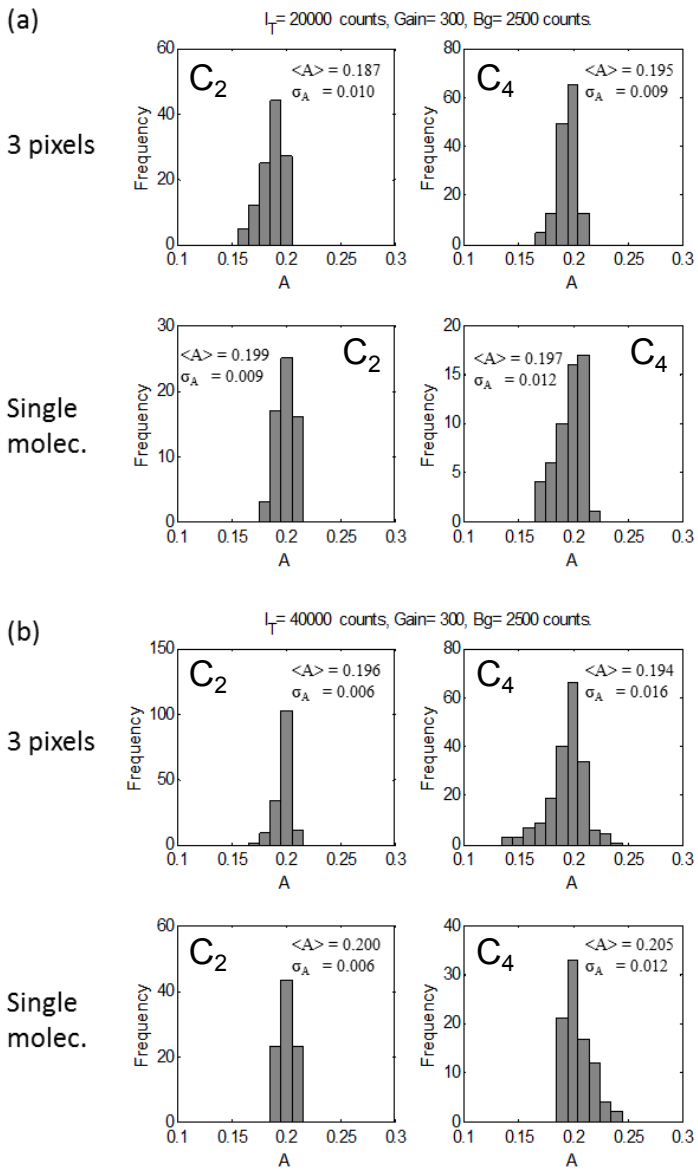

Figure 6.28: Anisotropy histograms for C_2 and C_4 for simulated single molecule and two molecules at close inter-distance of 3 pixels based on Fig. 6.27. (a) I_T = 20 000 counts. (b) I_T = 40 000 counts. Both molecules have an anisotropy A = 0.2.

Case where the two molecules have different anisotropies In order to evaluate the robustness of the anisotropy image when two molecules with different anisotropies are at close inter-distance, we performed a similar simulation as described previously. The two molecules have the same total intensity but there anisotropies are different.

Results for molecules with anisotropies 0.2 and 0 are presented for two different initial intensities 40 000 counts (Fig. 6.27e and f) and 20 000 counts (Fig. 6.27g and h). In this case for high intensities we observe more homogeneity in the anisotropy estimation in both C_2 and C_4 images. The intermediate region between the molecules takes intermediate A values but there is no apparent distortion of the final A image. For low intensities on the other hand, the expected anisotropy values appear distorted spatially, resulting, similarly as above, in anisotropy image artifacts.

In order to evaluate the effect of background, the results for molecules with anisotropies 0.5 and 0 are presented for two different backgrounds: 1 500 (Fig. 6.29a) and 2 500 (Fig. 6.29b), with initial intensity 20 000 counts. A higher background leads to: a lower resolution for C_2, and a higher degree of A artifacts with strong heterogeneities appearing at the edge of the molecules' images and in the inter-distance. C_4 is overall more sensitive to a loss of signal due to stronger bias and loss of precision (see Fig. 6.29). The heterogeneities at the edge of the molecules' images and in the inter-distance in C_2 and C_4 are observed more in detail in the Fig. 6.30.

Figure 6.31 shows the histogram of anisotropies for molecules with expected anisotropies 0.5 and 0. We observe the increment of heterogeneities for molecules close by less than 3 pixels. In C_4 at high background and 2 pixels inter-distance, we observe a high number of heterogeneities (A = 1), and the anisotropy of the second molecule (A = 0.5) seems totally vanish.

Comparing both results of pairs of anisotropies, the anisotropy estimation is more affected for the couple (A1=0.5, A2 = 0) than (A1=0.2, A2=0) when the two molecules are close (<4 pixels). It is because the difference between the intensities of the close molecules can bias the right cumulant estimation. For the fourth cumulant image with molecules separated by 3 pixels, we observe a good anisotropy estimation for A1=0.2 and A2=0, but for the other couple (A1=0.5 and A2=0) at this distance we observe a strong heterogeneities in the anisotropy estimation.

Although we observed a good estimation of anisotropy based on brightness when the molecules are separated by more than 3 pixels and with one high threshold, still the nonlinearity should be taking to account. In addition, the number of heterogeneities in experimental conditions of the brightness estimation is high.

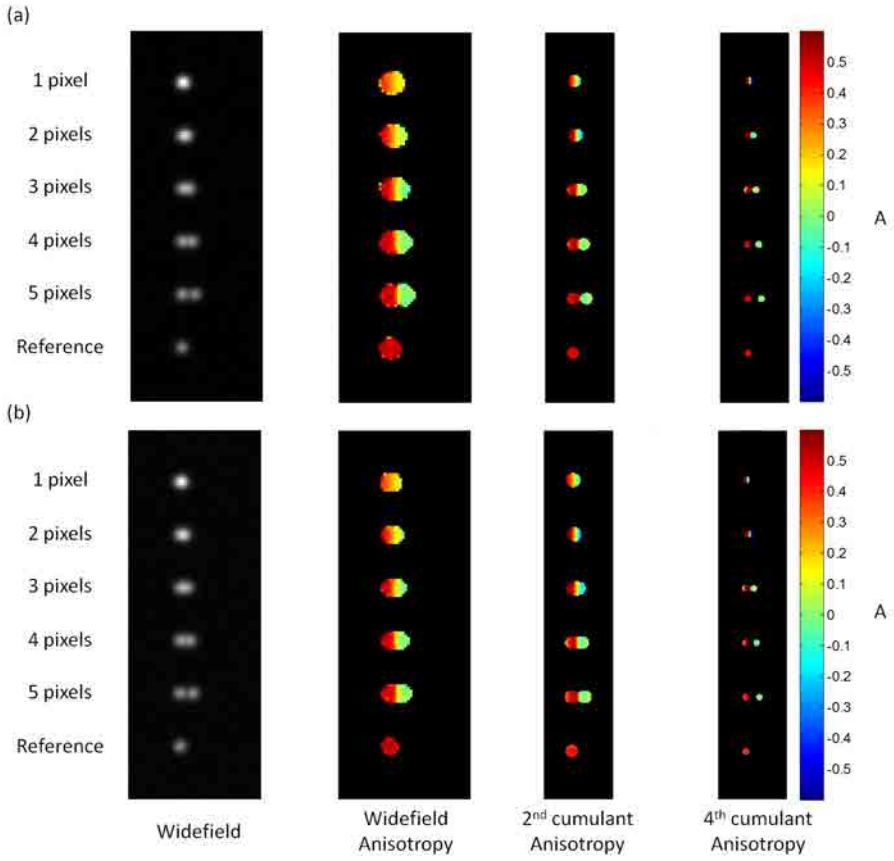

Figure 6.29: Simulation of two molecules with different anisotropy (0 and 0.5) and a given distance between them (1 to 5 pixels). Simulation parameters: I_T = 20 000, camera gain = 300 and PSF radius = 1.7 pixels. (a) Background= 1 500 counts. (Normalized cumulant signal threshold: $C_{2,T}$ = 0.12 and $C_{4,T}$ = 0.15) (b) Background=2 500 counts. (Normalized cumulant signal threshold: $C_{2,T}$ = 0.12 and $C_{4,T}$ = 0.26)

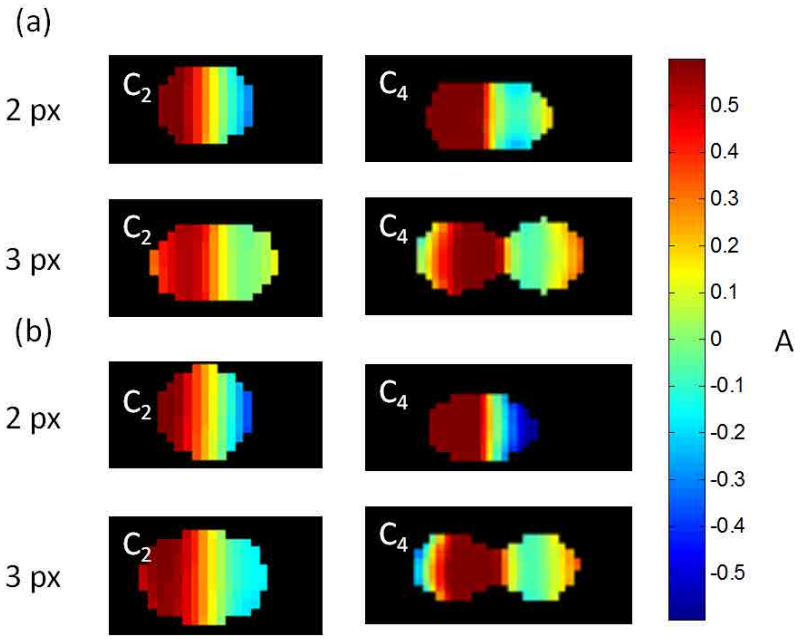

Figure 6.30: Zoom from Fig. 6.29 based on simulation of two molecules with different anisotropy (0 and 0.5) and a given distance between them (2 and 3 pixels). Simulation parameters: I_T = 20 000, camera gain = 300 and PSF radius = 1.7 pixels. (a) Bg = 1 500 counts. (Normalized cumulant signal threshold: $C_{2,T}$ = 0.12 and $C_{4,T}$ = 0.15) (b) Background=2 500 counts. (Normalized cumulant signal threshold: $C_{2,T}$ = 0.12 and $C_{4,T}$ = 0.26)

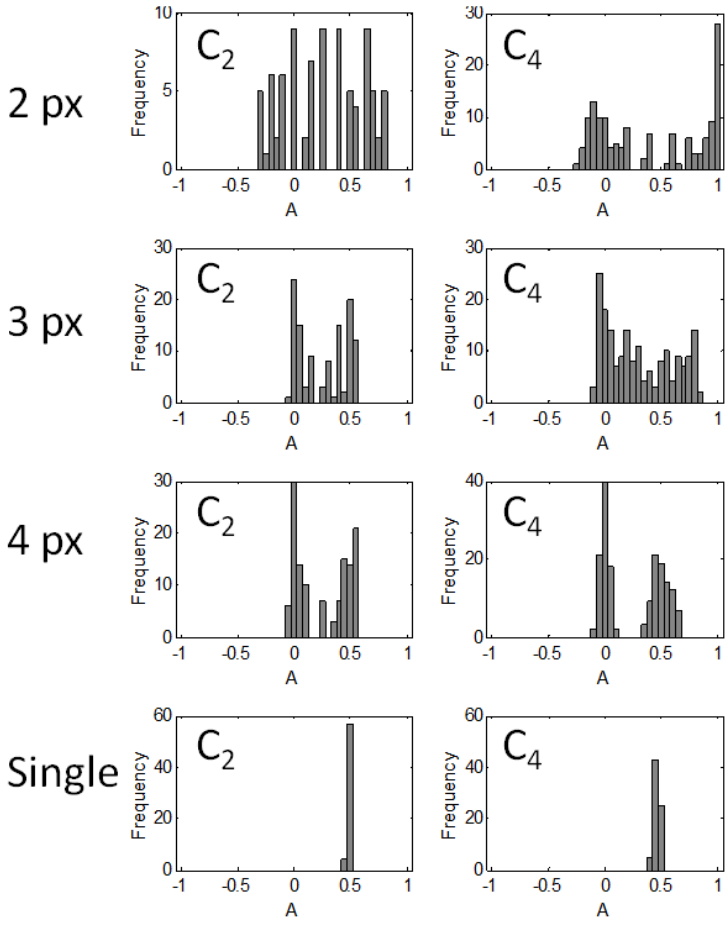

Figure 6.31: Anisotropy histograms of simulation of two molecules with different anisotropy (0 and 0.5) and a given distance between them (1 to 4 pixels). Simulation parameters: I_T = 20 000, camera gain = 300, PSF radius = 1.7 pixels, Bg= 1 500 counts. (Normalized cumulant signal threshold: $C_{2,T}$ = 0.12 and $C_{4,T}$ = 0.15)

6.4 polar-SOFI experimental results

This section describes the application of the polar-SOFI technique in biological samples similar to the one presented in Chapter 4. In addition, it presents a methodology to quantify the molecular orientational order at sub-diffraction limit. Furthermore, a comparison with the polar-dSTORM algorithm is realized. We chose often to discuss similar images in both dSTORM and SOFI in order to compare to reference anisotropy value measured in dSTORM. The SOFI images are recorded under similar intensity conditions as in dSTORM but in situations were single molecules do not necessarily isolate from each-other. Typically this occurs in the beginning of a dSTORM stack recording, which is not used for dSTORM analysis but usable for SOFI.

The only sample which we could not analyze in polar-SOFI was the actin-based sample, due to low signal to noise ratio (SNR). Although, we observed right anisotropy estimation, the low SNR in this particular experiment limits the final resolution improvement to the diffraction limit.

6.4.1 Molecules attached to Poly-L-lysine

We analyzed with the polar-SOFI algorithm the isotropic sample of Atto 633 molecules attached to a Poly-L-lysine coated slides. In this case, the SOFI movie stack was 200 frames long, with a camera gain of 300.

The polar-SOFI images for C_2 and C_4 are presented in Fig. 6.32. As expected the mean anisotropy is around 0 (C_2), and the range of anisotropy detected is big with a histogram shape close to the expected one in similar intensity level conditions (see Chapter 4). In the C_4 anisotropy image, a deformation of the histogram is observed, probably due to the higher sensitivity of C_4 to bias and loss of precision when the intensity get small (see Fig. 6.23).

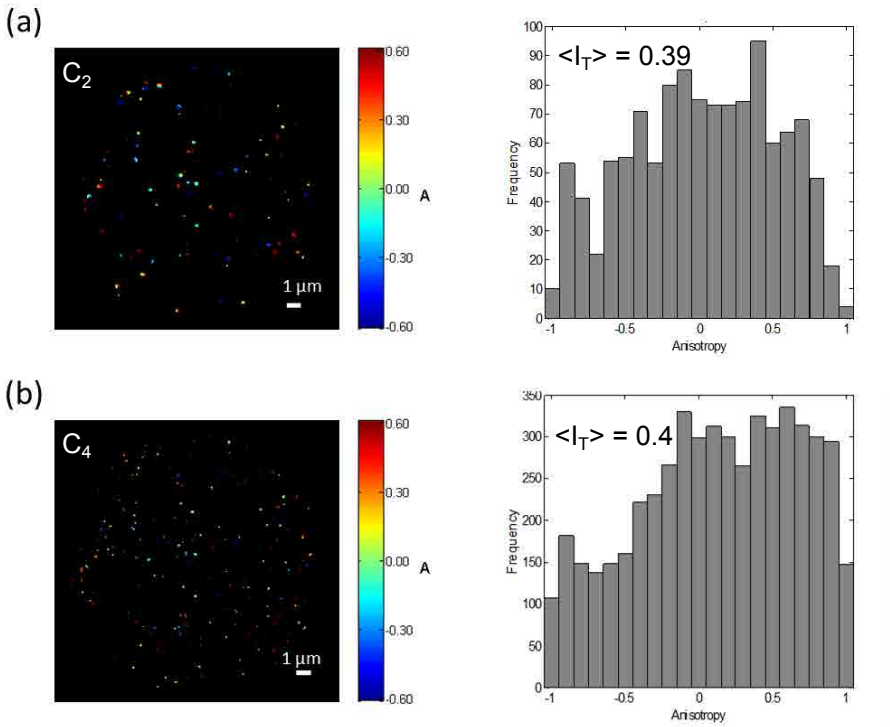

Figure 6.32: polar-SOFI Analysis of Atto 633 molecules attached to Poly-L-lysine. (a) Anisotropy image from C_2. Left: polar-SOFI Image (pixel size = 54 nm). Right: anisotropy histogram. (b) Anisotropy for C_4. Left: polar-SOFI Image (pixel size = 27 nm). Right: anisotropy histogram. The $<I_T>$ threshold is given in normalized units with respect to the maximum I_T.

6.4.2 Tubulin in COS 7 Cells

In Fig. 6.33, we present the results of tubulin fibers labeled with Alexa 647 in COS 7 cells for the second cumulant. We use for this sample exactly the same cell region as in polar-dSTORM, in order to have a comparative situation. Other regions and cells gave very similar results. In this image, the intensity level was on average $I_T \sim 15\ 000$ and the Bg $\sim 2\ 500$ counts. There is a clear improvement as a function of background rejection due to the SOFI processing, that allows to observe some structures that are not very well defined in the widefield image (Fig. 6.35). With the purpose of reducing the number of heterogeneities occurring from the SOFI process artifacts due to noise; a threshold based on the total cumulant signal ($C_{n\perp} + C_{n\parallel}$) is used. By analyzing a profile on an isolated fiber, we find a FWHM of 278 nm on the C_2 image. The expected theoretical resolution is 198 nm (diffraction limit: 280 nm) for C_2 ($\lambda_{em} = 665$ nm). Nevertheless in the next section, we propose a small change in the polar-SOFI algorithm in order to get closer to this expected resolution.

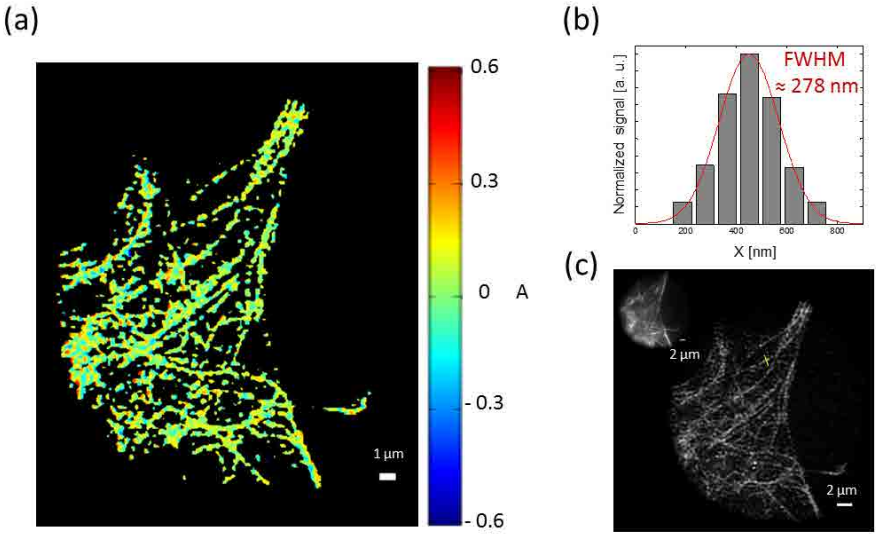

Figure 6.33: polar-SOFI Analysis (C_2) of Tubulin in COS 7 cells labeled with Alexa 647. (a) polar-SOFI anisotropy image (C_2), pixel size = 89 nm. (b) Full Width Half Maximum (FWHM) of an isolated fiber. (c) C_2 image, pixel size = 89 nm. Inset: widefield image.

For the C_4, the resolution improves down to 175 nm, however, the number of heterogeneities increases for this cumulant image, as well as for the anisotropy

image. Clearly, the anisotropy estimation is more affected by the fourth order cumulant calculated with visible regions of high anisotropy values, which was predicted in our simulations. C_4 is indeed more sensitive to noise, background an proximity between molecules. This effect is visible in zoomed regions in Fig. 6.35.

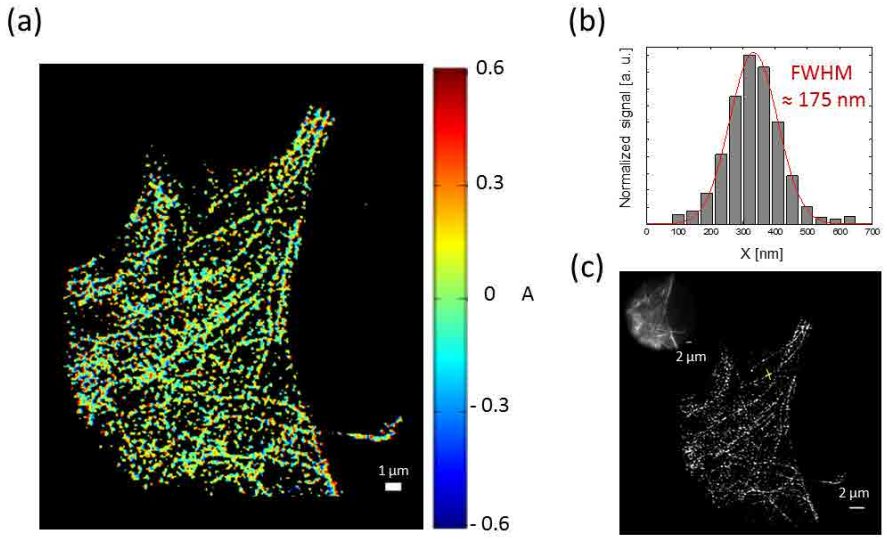

Figure 6.34: polar-SOFI Analysis (C_4) of Tubulin in COS 7 cells labeled with Alexa 647. (a) polar-SOFI anisotropy image (C_4), pixel size = 44 nm. (b) Full Width Half Maximum (FWHM) of an isolated fiber. (c) C_4 image, pixel size = 44 nm. Inset: widefield image.

Figure 6.36 shows the increment of heterogeneities in C_4 for bundles, due to the proximity of molecules as explained in section 6.3.2.

Based on the retrieved anisotropy images, an analysis on individual fibers was performed in both C_2 and C_4 cases. The corresponding orientation ρ and average anisotropy <A> are reported in Fig. 6.37. From the plot of ρ vs anisotropy superimposed to the theoretical curves introduced in Chapter 4, we are able to retrieve information on the presence of the order/disorder in the sample. In the case of our tubulin sample, an isotropic behavior ($\psi = 180°$) is observed, similarly to the value obtained by polar-dSTORM (Fig. 6.37). As it was discussed before, this isotropic behavior is due to the double antibody labelling used for this sample.

Isolated fibers were selected from the second (Fig. 6.38) and fourth (Fig. 6.39) cumulant images to investigate the statistical behavior of the retrieved

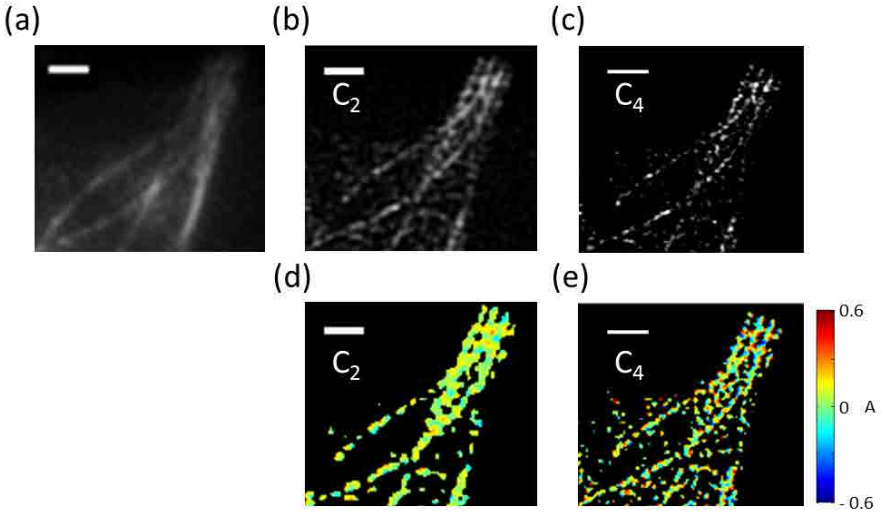

Figure 6.35: Zoom of Tubulin in COS 7 cells, labelled with Alexa 647 (a) Wide-field image. (b) C_2 image. (c) C_4 image. (d-e) Corresponding anisotropy images (Scale bar: 2 μm).

anisotropies. Note that in these figures a thresholding in cumulants signal is performed based on our simulation criteria (see Fig. 6.25) in order to ensure reasonable estimation precision and bias conditions for A. The isotropic behavior is confirmed, observing the same value of anisotropy (A=0) for all ρ angles. In terms of anisotropy variation σ_A, we observe a standard deviation of 0.05 for C_2 and 0.1 for C_4. The increment in the width of the anisotropy histograms for C_4 is consistent with our simulations which show that C_4 is more sensitive to noise. The obtained experimental σ_A values appear to be about 2x the value expected from noise (Fig. 6.25), however these simulations were performed on isolated molecules, from our theoretical studies in close-by molecules we know that anisotropy heterogeneities appear (Fig. 6.27). Simulations of molecules with similar signal conditions lead to σ_A values close to what is seen here experimentally, showing that the observed histogram width originates from noise and proximity of fluctuating molecules. Note that the obtained σ_A is also smaller than in polar-dSTORM (Fig. 5.11). This is explained by the higher intensity I_T of SOFI signals, which contain a larger number of molecules.

Finally overall, the changes on the anisotropy color observed in Fig. 6.38 and 6.39 are due to instrumental conditions and not real changes of the orientational behavior of the molecules attached to tubulin. To avoid these heterogeneities,

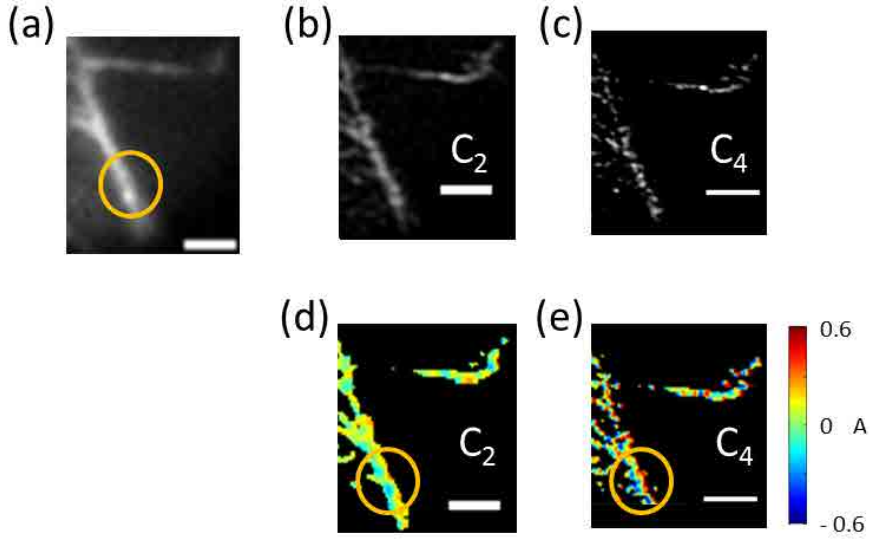

Figure 6.36: Heterogeneities in anisotropy estimation of a tubulin bundle in COS 7 cells, labelled with Alexa 647 (a) Widefield image. (b) C_2 image. (c) C_4 image. (d-e) Corresponding anisotropy images (Scale bar: 2 μm).

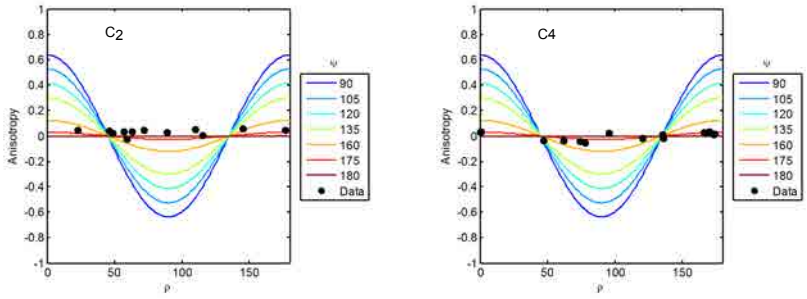

(a) (b)

Figure 6.37: Anisotropy average measured on tubulin fibers based on polar-SOFI images (a) C_2. (b)C_4 (markers with bars: standard error of the mean (SEM)) and simulated (cont. lines) as a function of ρ and ψ)

care will have to be taken specially on the level of the cumulant signals.

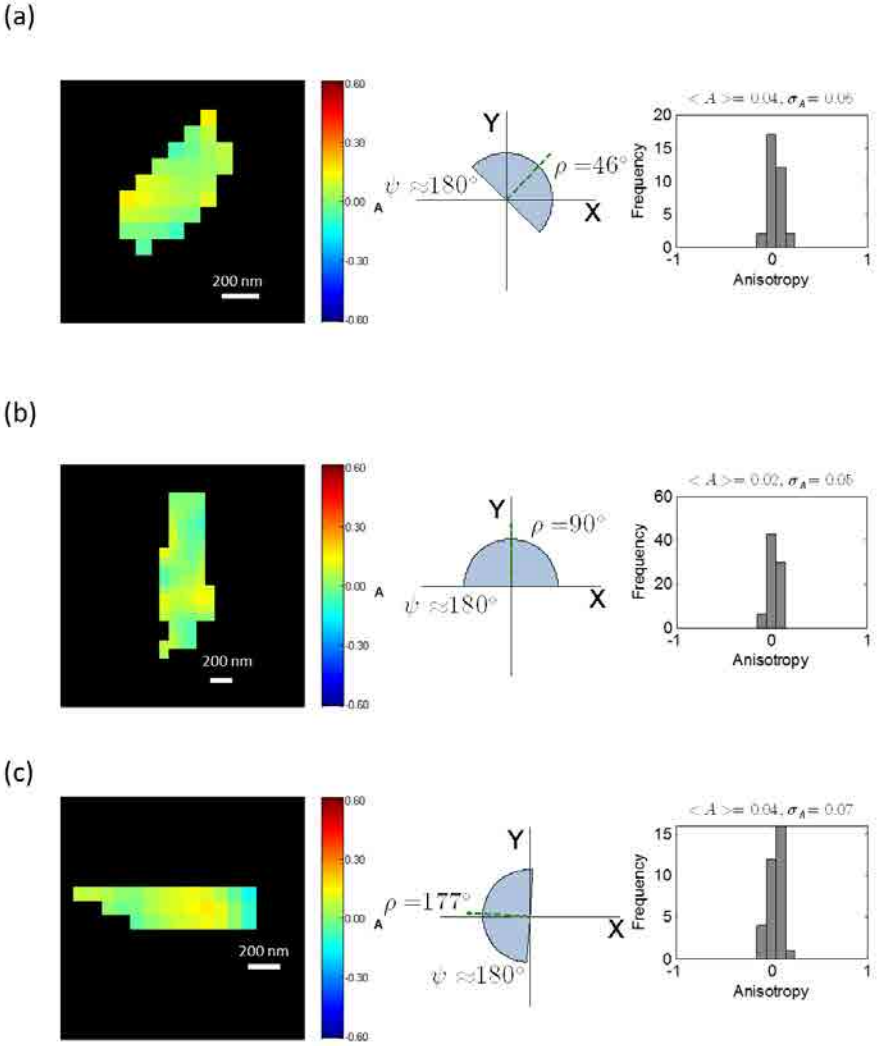

Figure 6.38: Isolated Tubulin in COS 7 cells, labelled with Alexa 647 for different ρ angles. Pixel size = 89 nm. Left: polar-SOFI Image (C_2). Center: molecule distribution based on a cone model. Right: anisotropy histogram.

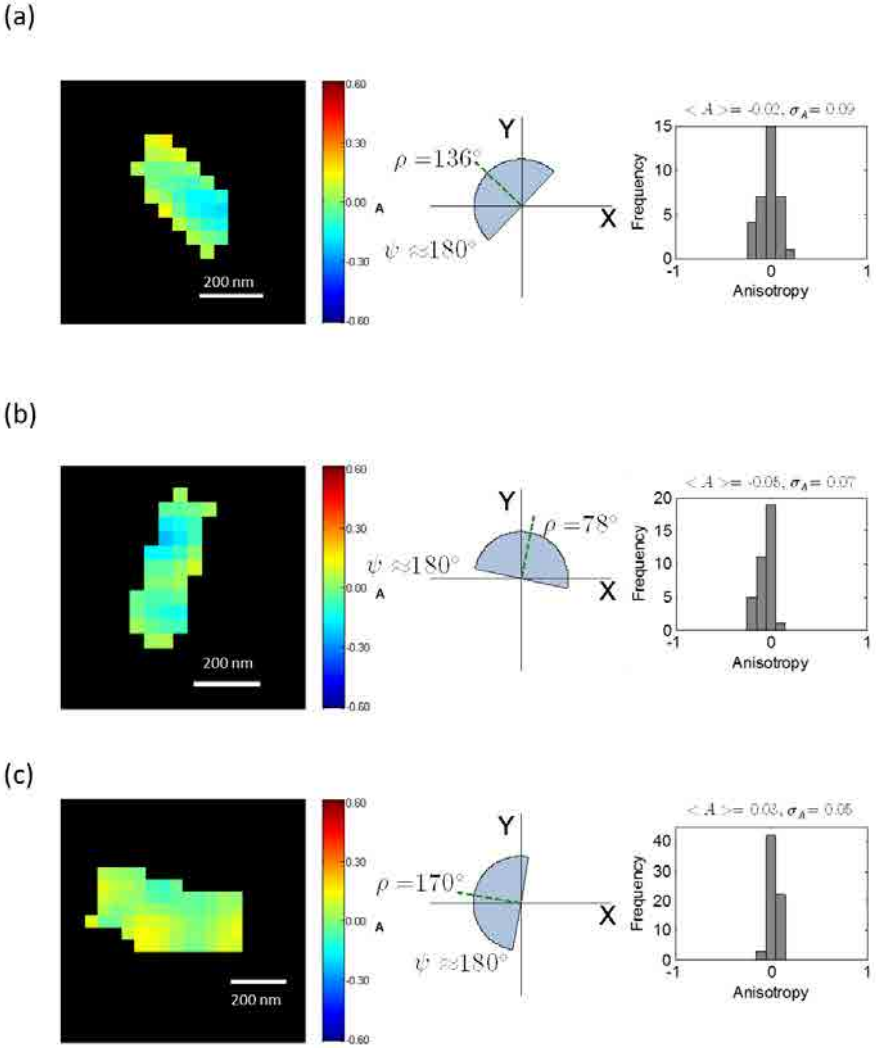

Figure 6.39: Isolated Tubulin in COS 7 cells, labelled with Alexa 647 for different ρ angles. Pixel size = 44 nm. Left: polar-SOFI Image (C_4). Center: molecule distribution based on a cone model. Right: anisotropy histogram.

6.4.3 Amyloid fibrils labeled with ThT in vitro

In Fig. 6.40, we present the results of amyloid fibrils labeled with ThT in vitro for the second cumulant. In this image, the signal is typically $I_T \sim 20\,000$ counts on the fiber and the background $\sim 2\,000$ counts. There is a large diversity of fibers diameters and lengths , due to the aggregation process which is polydisperse in size. We studied nevertheless the thinner structure by polar-SOFI. The clear improvement as a function of background removing allows to observe some isolated structures that are not clearly defined in the widefield image (Fig. 6.42). In this case, the expected theoretical resolution is 142 nm for C_2 ($\lambda_{em} = 490$ nm). The smallest structures we could see give a FWHM of 252 nm.

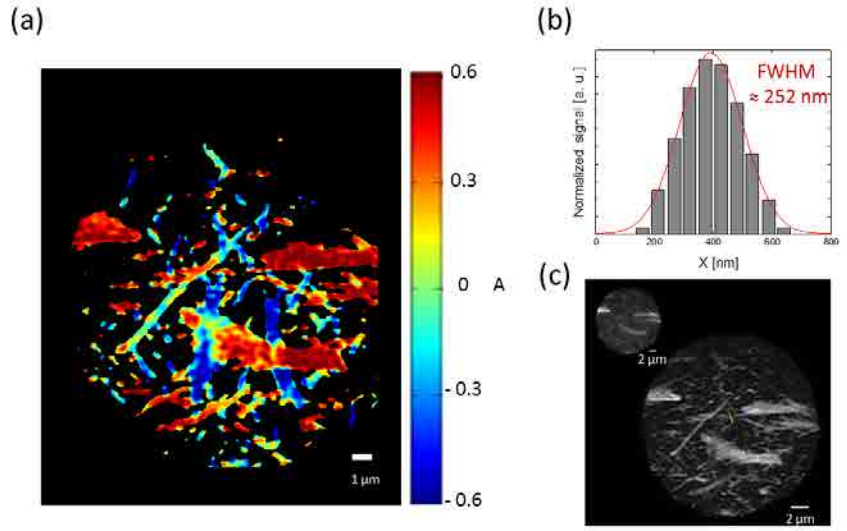

Figure 6.40: polar-SOFI Analysis (C_2) of amyloid fibrils in vitro directly labeled with ThT. (a) polar-SOFI image (C_2), pixel size = 54 nm. (b) Full Width Half Maximum (FWHM) of an isolated fiber. (c) C_2 image, pixel size = 54 nm. Inset: sum of widefield images stack.

For the C_4 cumulant, the resolution improves to 160 nm. However, as in the tubulin sample, heterogeneities might appear artificially in the C_4 signal and anisotropy estimation.

These effects are also more easily seen in zoomed regions as shown in Fig. 6.42.

An analysis of the anisotropy for several fibers of known orientations permits to retrieve a value for the angular constraint of the ThT inside amyloid fibrils

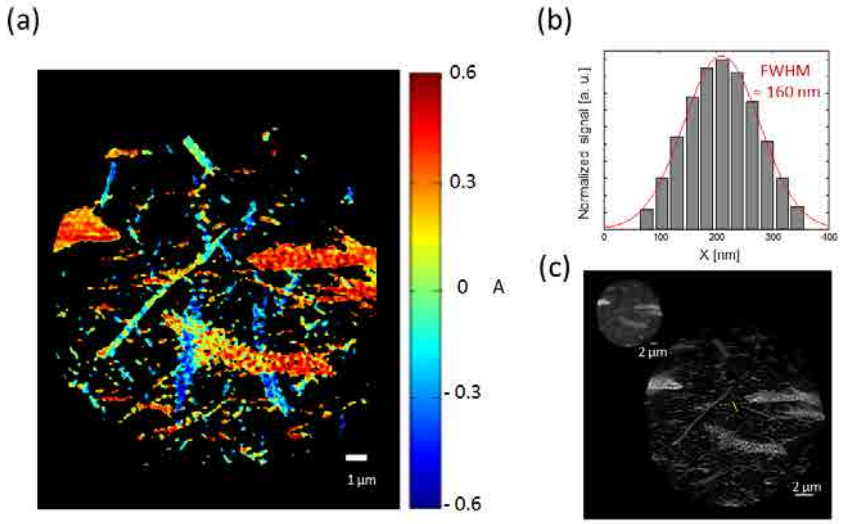

Figure 6.41: polar-SOFI Analysis (C_4) of amyloid fibrils in vitro directly labeled with ThT. (a) polar-SOFI Image (C_4), pixel size = 27 nm. (b) Full Width Half Maximum (FWHM). (c) C_4 cumulant image, pixel size = 27 nm. Inset: sum of widefield images stack.

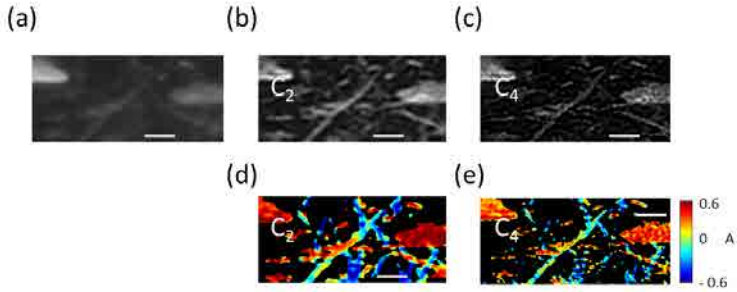

Figure 6.42: Zoom of amyloid fibrils in vitro directly labeled with ThT. (a) Sum of widefield images stack. (b) C_2 image. (c) C_4 image. (d-e) Corresponding anisotropy images (Scale bar: 2 μm).

($\psi \sim 95$ °) (Fig. 6.43), which is similar to the value obtained by polar-dSTORM (see Chapter 5). The A (ρ, ψ) dependence obtained experimentally from C_2 follows a more smooth variation along the curve $\rho \sim 95$ °, while for C_4 there

are more fluctuations specially at the high A values close to 0.5 or -0.5. It is indeed expected that for these ranges of values, the C_4 polar-SOFI analysis leads to more bias than C_2 and lead therefore to possible biased measurements in ψ. The best way to avoid such bias is to ensure a high SNR and low background. In our measurement, the expected bias in A using the C_4 analysis when $A \sim 0.5$ is about $\delta_{<A>} = 0.1$, which is close to the observed fluctuations in Fig. 6.43.

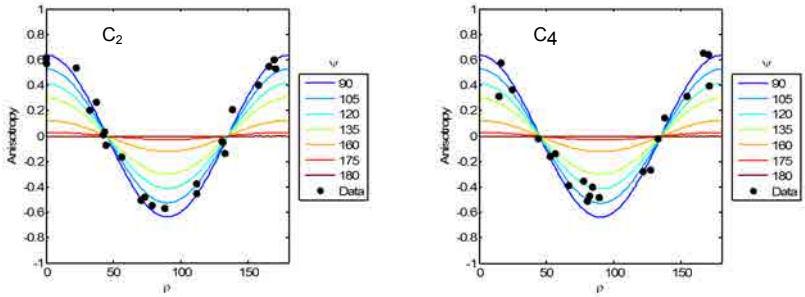

(a) (b)

Figure 6.43: Anisotropy average measured on amyloid fibrils based on polar-SOFI images (a) C_2. (b) C_4 (markers with bars: standard error of the mean (SEM)) and simulated (cont. lines) as a function of ρ and ψ)

Isolated fibers were selected from the second (Fig. 6.44) and fourth (Fig. 6.45) cumulant images. Similar to the tubulin measurements, we observe a standard deviation(σ_A) increases from 0.05 to 0.1 when using C_2 and C_4, which is expected from noise (except in Fig. 6.45a, which is probably a more heterogeneous distribution). Nevertheless, the present conditions allow to identify the homogeneity of the ψ values within a small region of amyloid fibril.

This complements the information that was obtained in polar-dSTORM: while at nanometric/molecular scale, there is probably a structural disorder within the fibrils, the larger scale shows homogeneous behaviors. Exceptions arise in a few cases like fig. 6.45a, where A varies with large changes over small distances within the same fibril. This precise case can only be explained by a local change of ρ, similarly as a different "crystallization" direction taken during the aggregation process), which was also visible in dSTORM. Overall, this example shows that polar-SOFI anisotropy images are able to probe orientational behavior homogeneities at the sub-diffraction scales. Note that to get a complete picture of the (ρ, ψ) values without any assumption on the local fiber orientation, more polarization states directions are required for the excitation or detection [10, 63].

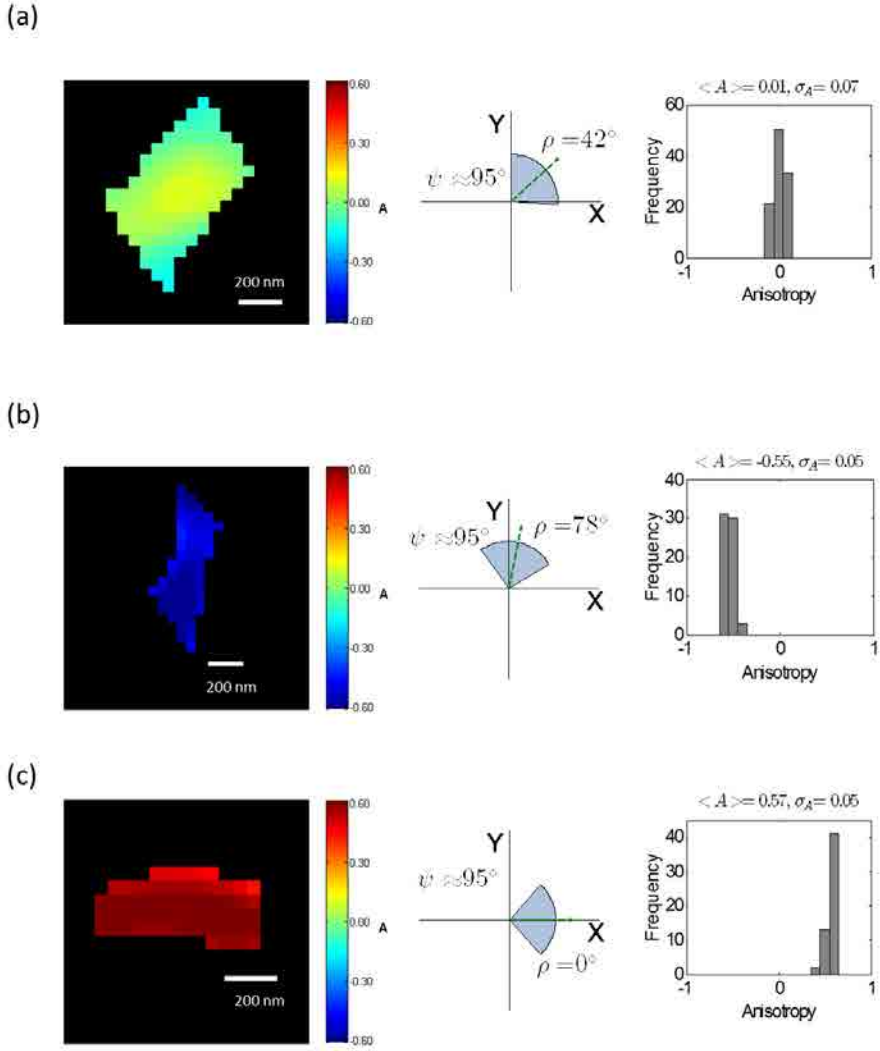

Figure 6.44: Isolated amyloid fibrils in vitro directly labeled with ThT for different ρ angles. Pixel size = 54 nm. Left: polar-SOFI Image (C_2), center: molecule distribution based on a cone model. Right: anisotropy histogram.

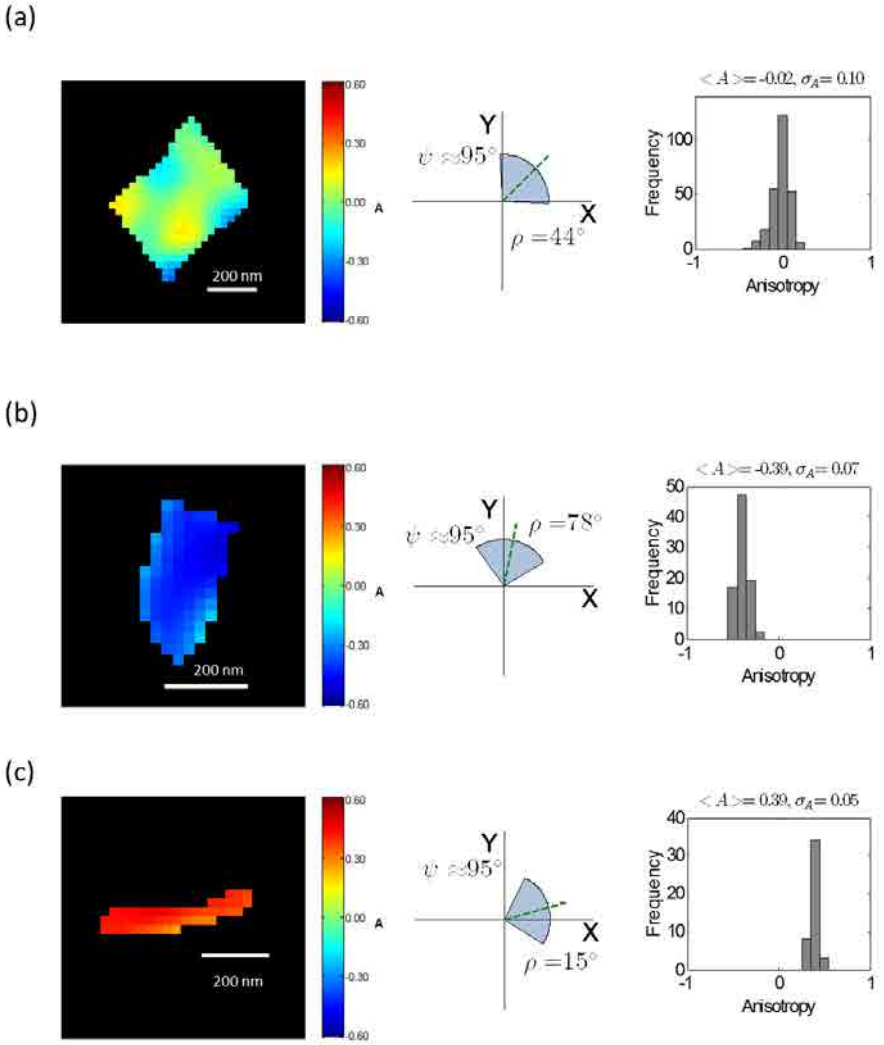

Figure 6.45: Isolated amyloid fibrils in vitro directly labeled with ThT for different ρ angles. Pixel size = 27 nm. Left: polar-SOFI Image (C_4), center: molecule distribution based on a cone model. Right: anisotropy histogram.

6.4.4 DNA

Due to the experimental characteristics of the measurements we performed on DNA fibers (see Chapter 5), such as short acquisition time (due to bleaching of the YOYO-1 label), low SNR and low blinking rate, DNA is a good candidate to be analyzed by the SOFI technique.

In what follows, we present the results of DNA labeled with the intercalating dye YOYO-1 (Fig. 6.46 and 6.47). In this case, the expected theoretical resolution is 147 nm for the second cumulant (λ_{em} = 509 nm), but we obtained a 285 nm on a typical isolated fiber(see Fig. 6.46). Similarly as presented for tubulin and amyloid fibrils, the background and low SNR might be responsible for the discrepancy and extra processing involving re-convoluting with a PSF of adequate size can improve this resolution(see section 6.4.5).

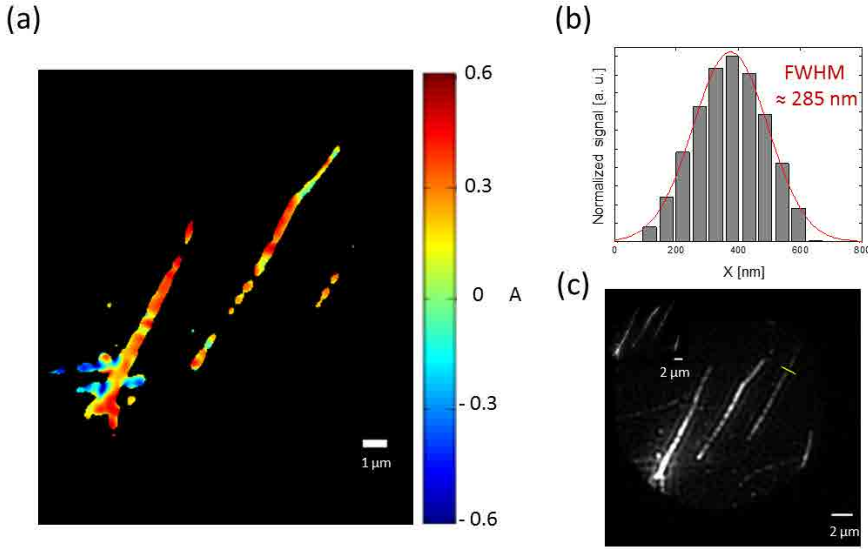

Figure 6.46: polar-SOFI anisotropy analysis of isolated DNA fibers labelled with YOYO-1 . (a) polar-SOFI anisotropy image (C_2), pixel size = 54 nm. (b) Full Width Half Maximum (FWHM). (c) C_2 image, pixel size = 54 nm. Inset: sum of widefield images stack.

For the C_4, the resolution improves down to 170 nm, which is below to the diffraction limit expected for this experiment (208 nm, Fig. 6.47).

In order to compare the improvement as a function of background removing and possible apparition of heterogeneities, we show a zoomed area of the widefield,

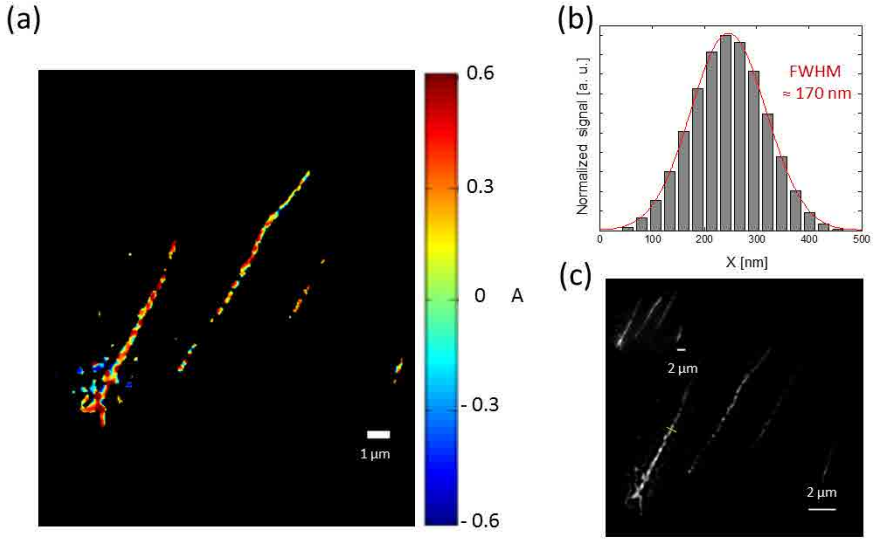

Figure 6.47: polar-SOFI anisotropy analysis of isolated DNA fibers labelled with YOYO-1. (a) polar-SOFI anisotropy image (C_4), pixel size = 27 nm. (b) Full Width Half Maximum (FWHM). (c) C_4 image, pixel size = 27 nm. Inset: sum of widefield images stack.

C_2 and C_4. There is visible reduction of background in both cumulants. However, the number of heterogeneities increases for the C_4 image, and as a consequence the anisotropy values are affected (see Fig.6.48).

Based on the comparison of the obtained A values from isolated fibers to the theoretical A (ρ, ψ) dependence, we are able to retrieve a mean value of $\psi \sim 107°$ (Fig. 6.49a) for C_2, which is somewhat higher than the value obtained by polar-dSTORM ($\psi \sim 85°$). This variation can be due to the low SNR that maybe does not biases slightly the obtained anisotropy when it reaches its extreme value. It can also be due to the fact that we average over several single molecules within a single cumulant pixel, which can change the anisotropy average if the order is close to static. Note that similarly to the A value obtained from polar-dSTORM, the sign of the obtained anisotropies for fiber oriented close to vertical or horizontal direction show that the YOYO-1 dye is globally oriented perpendicularly to the DNA fibers.

Concerning the fourth cumulant (see Fig. 6.49b), the SNR and number of

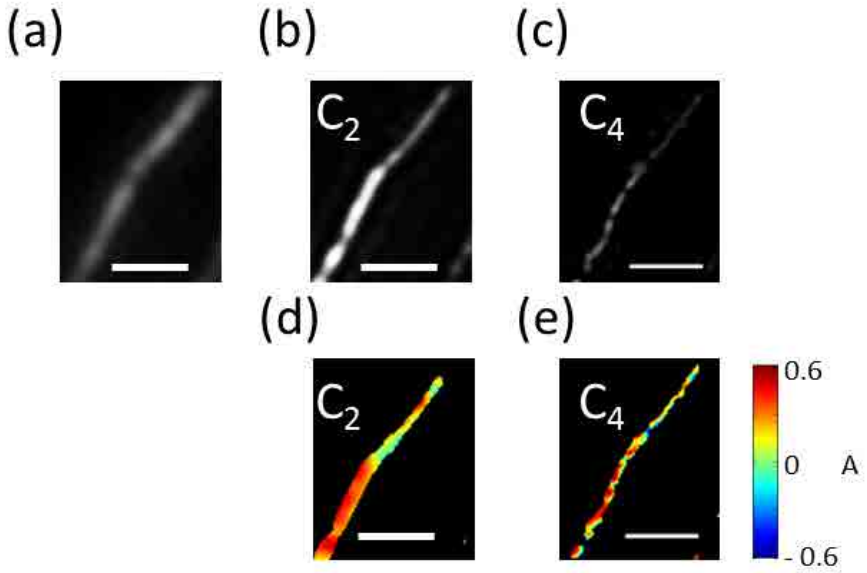

Figure 6.48: Zoom of an isolated DNA fiber labelled with YOYO-1 . (a) Sum of widefield images stack. (b) C_2 image. (c) C_4 image. (d-e) Corresponding anisotropy images (Scale bar: 2 μm).

heterogeneities influence the ψ angle estimation, obtaining a ψ angle of about 119° (Fig. 6.49b). In this case, there is a clear deviation from the single molecule value obtained by polar-dSTORM, which confirms the possibility of a bias due to an average over close to static disorder. Nevertheless, polar-SOFI offers a clear visualization of the angular constraint of intercalants in DNA [48].

Isolated fibers were selected from the second (Fig. 6.50) and fourth (Fig. 6.51) cumulant images. In terms of anisotropy variation, we can observe a standard deviation of 0.03-0.05 for the second cumulant and 0.04 to 0.1 for the fourth cumulant. We observe an increment in the width of the anisotropy histograms calculated from the fourth cumulant, as expected from our simulations in the previous section.

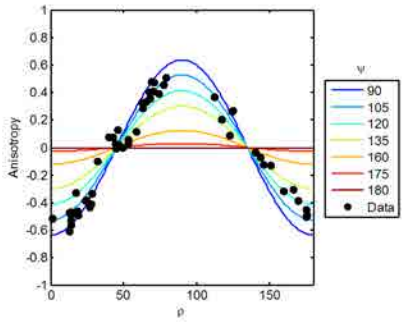

(a)

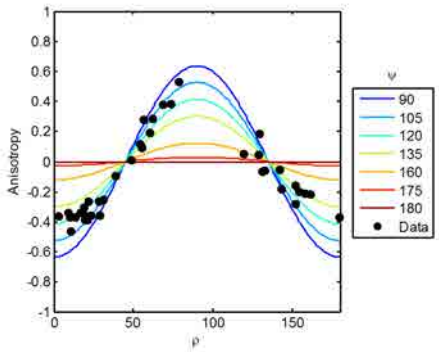

(b)

Figure 6.49: Anisotropy average measured on isolated DNA fibers labelled with YOYO-1 based on polar-SOFI images (a) C_2. (b) C_4. (markers with bars: standard error of the mean (SEM)) and simulated (cont. lines) as a function of ρ and ψ)

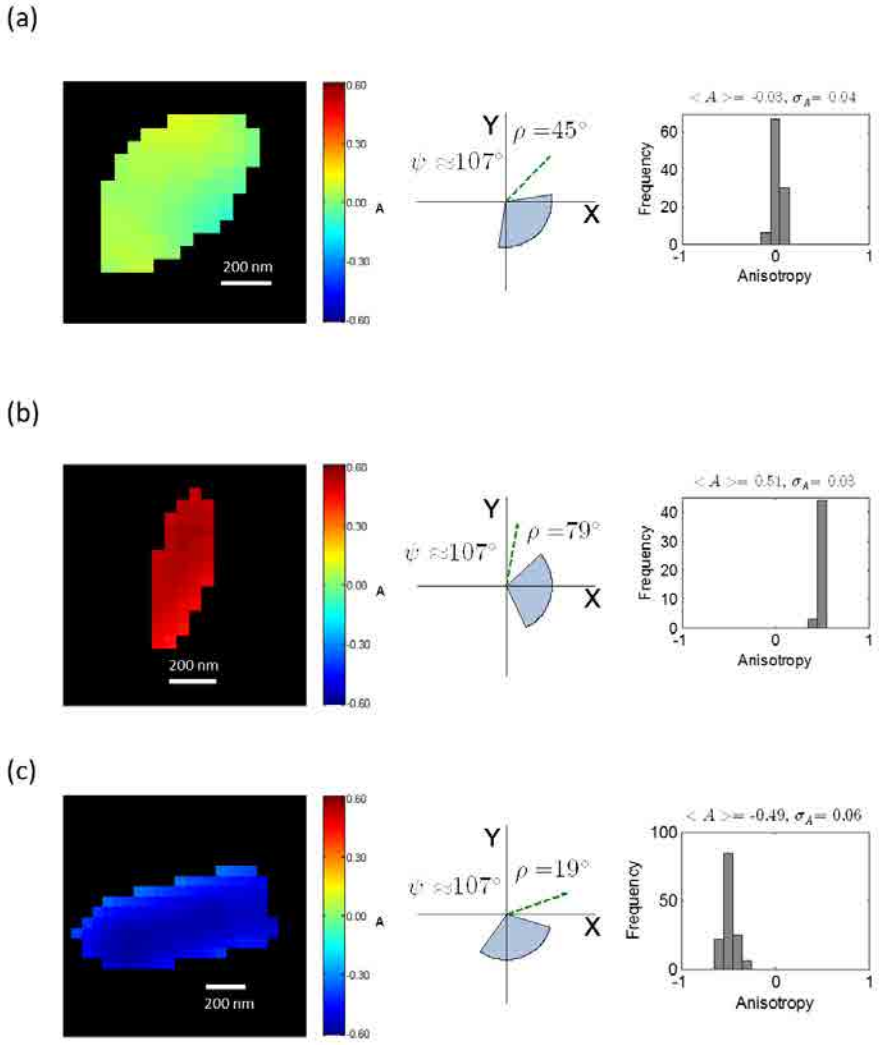

Figure 6.50: Isolated DNA fibers labelled with YOYO-1 for different ρ angles. Pixel size = 54 nm. Left: polar-SOFI image (C_2). Center: molecule distribution based on a cone model. Right: anisotropy histogram.

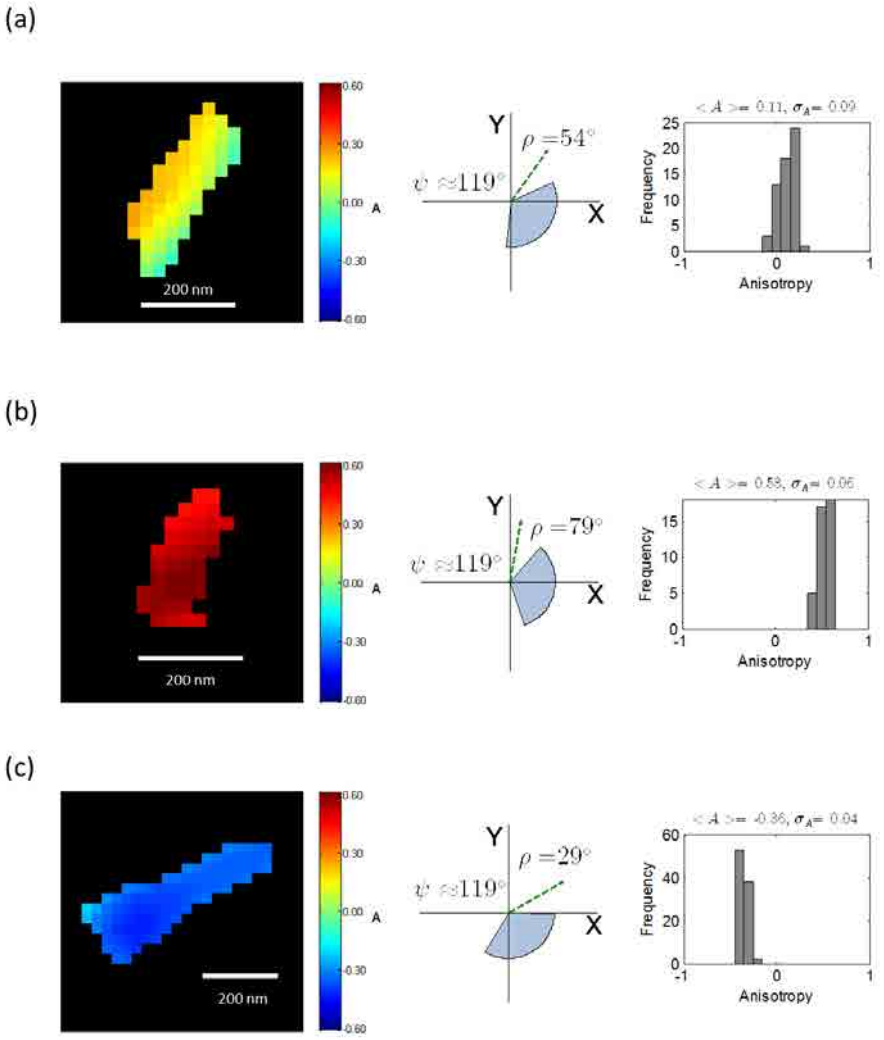

Figure 6.51: Isolated DNA fibers labelled with YOYO-1 for different ρ angles. Pixel size = 27 nm. Left: polar-SOFI Image (C_4). Center: molecule distribution based on a cone model. Right: anisotropy histogram.

6.4.5 Resolution improvement

The SOFI experimental images presented in this work show finally a spatial resolution not reaching the expected reduction of a n factor as compared to the initial PSF, and even not reaching the expected $\sqrt{n}$ reduction factor that would be obtained without the last linearization/reconvolution step. Modifications in the initial bSOFI toolbox can be performed in order to obtain a better final resolution in the cumulant images, including the increase the number of iterations of deconvolutions before linearization. We noticed however that this approach introduces artifacts and heterogeneities, which is mostly due to the low SNR quality of the images obtained in our study, introduced by the splitting into two polarized detection channels.

Due to the low SNR in our images and the fact that the last reconvolution is mostly appropriate for high SNR conditions, we made an attempt to avoid this last reconvolution step in the bSOFI Matlab toolbox. The resulting images are shown in Fig. 6.52 for tubulin COS 7 cell labeled with Alexa 647. We obtain a FWHM of respectively 199 nm and 137 nm for the second and fourth cumulants, choosing the same isolated fiber as previously. These values are much closer to the expected 198 nm and 140 nm values (assuming a $\sqrt{n}$ reduction factor). This shows that while the resolution improvement expected by the last reconvolution step is not reached, an image processing avoiding this step recovers the expected resolution in pure, not re-convolved cumulant images. However one can notice a higher degree of heterogeneities in the anisotropy values in isolated fibers, which will lead most probably to larger anisotropy histograms.

Fig. 6.53 show similar results performed on DNA labelled with YOYO-1. We obtain FWHMs of 162 nm and 88 nm for the second and fourth cumulants, which are also here closer to their theoretical expectation of 147 and 104 nm as compared to our previous approach.

Fig. 6.54 show finally the result obtained without reconvolution or amyloid fibrils. We obtain 176 nm and 121 nm of FWHM on isolated fibers for the second and fourth cumulants, which is here as well closer to the expected resolution of 142 nm and 100 nm as compared to our previous approach.

An overview of experimental and expected resolutions are summarized in Table 6.1. The theoretical resolution in this table is given by [15]:

$$r_c = \frac{0.61\lambda}{NA\sqrt{n}} \tag{6.24}$$

were λ is the emission wavelength, n is the cumulant order and NA is the numerical aperture of the used objective.

In the end avoiding the last reconvolution step has improved the experimental resolution, however at the expense of more heterogeneities in the anisotropy images. This analysis shows that the choice of operations in the signal analysis

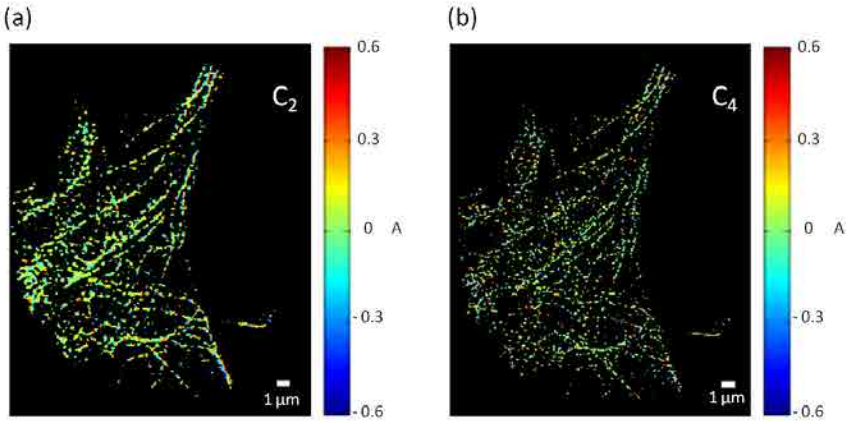

Figure 6.52: polar-SOFI anisotropy analysis of Tubulin in COS 7 cells labeled with Alexa 647 without last reconvolution of the bSOFI toolbox [99]. polar-SOFI anisotropy images (a) C_2 (pixel size = 89 nm) and (b) C_4 (pixel size = 44 nm).

Sample	Dye	λ_{em}	NA	r_d	r_{C2}	r_{C4}	F_{C2}	F_{C4}	F_{dC2}	F_{dC4}	F_{ds}
Amyloid	ThT	490	1.49	201	142	100	252	160	176	121	20
Tubulin	Alexa647	665	1.45	280	198	140	278	175	199	137	54
DNA	YOYO-1	509	1.49	208	147	104	285	170	162	88	36

Table 6.1: Comparison of resolution. λ_{em}: emission wavelength [nm], NA: numerical aperture of the used objective, r_d: Diffraction limit [nm], r_{C2}: Theoretical resolution of C_2 [nm], r_{C4}: Theoretical resolution of C_4 [nm], F_{C2}: Minimum FWHM for C_2 images [nm], F_{C4}: Minimum FWHM for C_4 cumulant images [nm] , F_{dC2}: Minimum FWHM without the last convolution step C_2 images [nm] , F_{dC4}: Minimum FWHM without the last convolution step C_4 images [nm] and F_{ds}: FWHM obtained with the polar-dSTORM method [nm].

has to be done accordingly with considerations on the SNR present in the images, as well as the goal of the analysis. In studies where a precise, quantitative estimation of the anisotropy is required, one might chose indeed rather a lower resolution approach.

6.5 Conclusion

In this chapter, we have introduced a new polarization super resolved microscopy technique that allows retrieving the molecular orientation behavior based on the

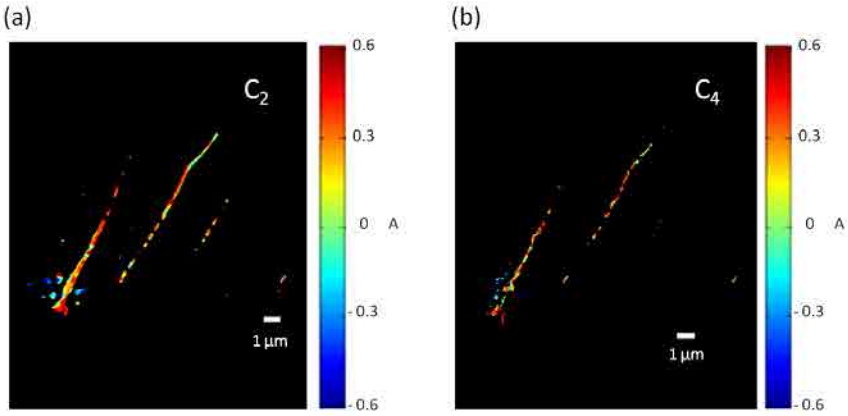

Figure 6.53: polar-SOFI anisotropy analysis of isolated DNA fibers labeled with YOYO-1 without last reconvolution of the bSOFI toolbox [99]. polar-SOFI anisotropy images (a) C_2 (pixel size = 54 nm) and (b) C_4 (pixel size = 27 nm).

stochastic fluctuation of single molecules, polar-SOFI.

As mentioned during this chapter, SOFI works in different microscopy imaging modes, including conventional widefield microscope, TIRF and confocal, without any special requirement. It is also applicable with much less stringent signal to noise condition and for different types of fluorescence fluctuations that are not necessarily based on pure blinking as required for dSTORM [101]. Nevertheless, SOFI is also a good option when short acquisition times are needed, high label density or when the on/off ratio and SNR is not optimal for localization microscopy methods [111]. This adaptability is a clear advantage of this technique. In addition, this technique is not limited to fluorescence fluctuations from on/off emission rates, and it can be used for any stochastically fluctuating signal, as it has been proved in surface-enhanced Raman scattering (SERS) measurements [111], with SERS biotags (SBTs) of dimers and trimers of metal nanoparticles that in certain conditions undergo to long-term blinking behavior [111].

Although the experimental resolution obtained by SOFI microscopy is lower than the resolution obtained by localization microscopy techniques, it is a very robust technique to isolate molecules from a rejected background.

Above these advantages, we have shown that it is also applicable to polarized measurements. In terms of quantification analysis based on the cumulant signals, the linearity between the cumulant signal and the initial intensity represents a big advantage to enlarge the possible applications of the SOFI technique such as for

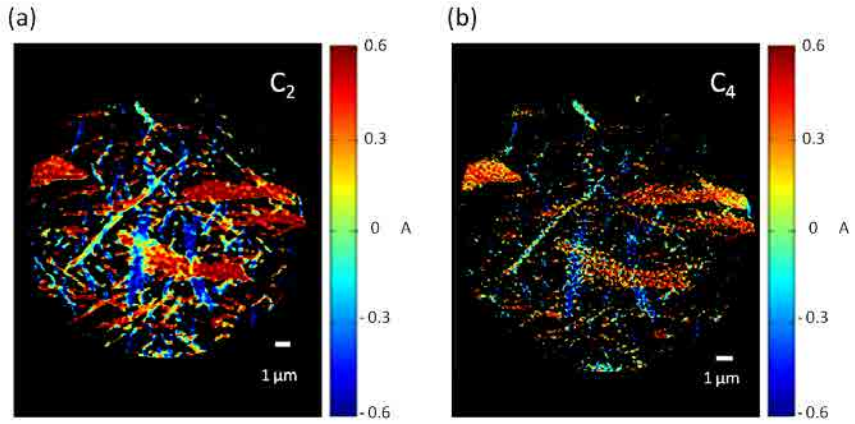

Figure 6.54: polar-SOFI anisotropy analysis of Amyloid fibrils in vitro directly labeled with ThT without last reconvolution of the bSOFI toolbox [99]. polar-SOFI anisotropy images (a) C_2 (pixel size = 54 nm) and (b) C_4 (pixel size = 27 nm).

polar-SOFI. We have shown that the polar-SOFI based on the second cumulant estimation permits to obtain in a reliable way molecular orientation behavior similar as in the case of polar-dSTORM, close to the single molecular level for low-density samples. We have also pointed-out the cases and situations which can lead to a strong bias and low precision in polar-SOFI anisotropy images.

In this chapter, polar-SOFI algorithm has been tested with different biological samples: tubulin fibers, amyloid fibrils and DNA, which gave reasonable quality of experimental conditions for imaging at sub-diffraction limit scale (Table 6.1).

We have shown for those samples that the obtained information per pixel is a good measurement of ensemble-averaged anisotropy at a sub-diffraction scale, which provides a clear idea of molecular order information.

Still, there are many questions to be addressed for the future application of SOFI microscopy and its application to polarized detection. This includes optimization of the on-off rate, the treatment of image heterogeneities by post-processing for the high order cumulants (>4) and the optimal acquisition rate. In terms of quantification use, given a SNR and blinking rate, what is the highest cumulant order that keeps the linear correspondence to the initial intensity? Also as a function of parameters estimation as brightness and molecular density, further theoretical studies should be performed in order to extend its use to quantitative applications.

Conclusion and outlooks

The aim of this PhD project was to develop a super resolution polarization-resolved microscopy technique able to image molecular orientation in static and dynamic environments at single molecule level and nanoscale resolution.

For this purpose, we proposed a combination of direct Stochastic Optical Reconstruction Microscopy (dSTORM) [2] in combination with polarized detection, called polar-dSTORM. Based on a refined signal analysis technique which provides high accuracy in the estimation of molecular anisotropies, we report nanoscale orientational behaviors of biomolecular assemblies in fixed cells. This method necessitated a thorough signal analysis of the conditions in terms of total intensity, single molecule image quality and localization precision, which we performed using Monte Carlo simulations. In addition, a model was develop to interpret anisotropy data and in particular the dynamic nature of the observed orientational behaviors.

The method proposes has allowed to quantify molecular orientation of fluorophores linked to tubulin and actin stress fibers in COS 7 cells, but also in vitro fibers structures such as isolated actin fibers, DNA and amyloid fibrils. We have also analyzed freely rotating single molecules in order to evaluate the potential of the technique in tracking conditions where molecules diffuse in space and orientation.

In addition, we have proposed a new application for the SOFI microscopy (polar-SOFI), that is able to quantify the orientational behavior at resolution below the diffraction limit. This technique is interesting for the cases when the localization microscopy algorithms as STORM or PALM are not adequate in terms of acquisition time and SNR. In a similar way as for polar-dSTORM, polar-SOFI was validated through a Monte Carlo simulation, using image analysis of second order and fourth order cumulants which are based on spatio-temporal cross-correlations of fluorescence fluctuation signals recorded in sub-pixels of the image stacks. Simulations show that the second order cumulant, even though being poorer in resolution than the fourth order cumulant, is a good option for high quality anisotropy estimation. We have applied this method to quantify

averaged molecular orientation (within sub-pixels sizes defined by the cumulant calculation) in tubulin in COS 7 cells, DNA and amyloid fibrils in vitro. The obtained results are in agreement with the expected orientational behavior measured in our polar-dSTORM experiments. Polar-SOFI, even though it does not measure single molecule orientation but rather large scale averaged information (typically 150nm resolution), complements the dSTORM approach since it is more compatible with second-time scale dynamic imaging.

The techniques explored in this work bring for the first time to the best of our knowledge, a quantitative analysis of molecular order down to nanoscale level. While this work was dedicated to proof of principles and first demonstrations, further directions of research can be defined in the field.

In terms of data analysis, more refined analysis could be performed by accounting for the possibility of off-plane tilt angles of the molecules. The tilted molecules are most probably neglected in our approach since only high fluorescence signals and symmetric 2D-Gaussian PSF shapes are selected by our signal-filtering technique. Accounting for 3D orientated emitters would require measuring lower signals but also slightly deformed PSF as mentioned in earlier works, which pointed out the degradation of localization precision when fitting single molecules' image spots by simple 2D Gaussian functions. Accounting for this change of PSF would require establishing a more refined fitting procedure and relating this deformation to the 3D off-plane orientation angle of the single molecules. This would bring richer 3D information which in some cases might be needed.

In terms of data interpretation, our data show clearly the possible presence of slow-dynamics rotational motions, at a time scales longer than the CCD integration time. It is possible to bring a finer analysis of this effect without relying only on many-molecules statistics as we perform in our work, by using more complex excitation/detection polarization schemes which have been developed by other groups. The inconvenient of projecting the fluorescence signal on more polarization states is the loss of signal, and therefore poorer precision in the analysis, however there are situations where the fluorophores are bright enough to envision such an analysis.

In terms of instrumentation development, improvements in terms of analysis time could also be performed to evaluate de possibility to obtain almost "on-live" monitoring of anisotropy. Due to the short time acquisition necessary for SOFI imaging, it allows almost "on-live" reconstruction of the anisotropy images, that represents a good alternative to observe changes in the morphology and molecular order at sub-diffraction limit.

In terms of applications, super-resolution anisotropy imaging can now be applied in the general frame of monitoring changes in the interactions between bio-molecules. An application currently undertaken is to visualize the respective

order properties of DNA and a reconstruction enzyme, at a nanoscale level, in order to visualize the possible effect of such enzyme on the DNA local conformation. For this, a 2-color super-resolved anisotropy imaging set-up is under construction to image simultaneously both molecules. It can also be extended to studies on diverse protein-protein interaction mechanisms and on actin stress fiber structural properties under different treatments perturbing its polymerization state (induced by drugs in fixed cells for instance).

Bibliography

[1] Eric Betzig, George H. Patterson, Rachid Sougrat, O Wolf Lindwasser, Scott Olenych, Juan S. Bonifacino, Michael W. Davidson, Jennifer Lippincott-Schwartz, and Harald F Hess. Imaging intracellular fluorescent proteins at nanometer resolution. *Science*, 313:1642–5, 2006.

[2] S. Van de Linde, A. Löschberger, T. Klein, M. Heidbreder, S. Wolter, M. Heilemann, and M. Sauer. Direct stochastic optical reconstruction microscopy with standard fluorescent probes. *Nature Protocols*, 6:991–1009, 2011.

[3] Digambara Patra, Ingo Gregor, and Jörg Enderlein. Image Analysis of Defocused Single-Molecule Images for Three-Dimensional Molecule Orientation Studies. *The Journal of Physical Chemistry A*, 108(33):6836–6841, 2004.

[4] Mikael P. Backlund, Matthew D. Lew, Adam S. Backer, Steffen J. Sahl, Ginni Grover, Anurag Agrawal, Rafael Piestun, and W. E. Moerner. Simultaneous, accurate measurement of the 3D position and orientation of single molecules. *Proc. Natl. Acad. Sci. U.S.A.*, 109(47):19087–92, 2012.

[5] Laurent Cognet, Gregory S. Harms, Gerhard a. Blab, Piet H. M. Lommerse, and Thomas Schmidt. Simultaneous dual-color and dual-polarization imaging of single molecules. *Applied Physics Letters*, 77(24):4052–4054, 2000.

[6] F. Perrin. La fluorescence des solutions. Polarisation. Vie moyenne des molécules dans l'état excité. *J. Phys. Radium*, 7(12):390–401, 1926.

[7] T. J. Gould, M. S. Gunewardene, M. V. Gudheti, V. V. Verkhusha, S. Yin, J. A. Gosse, and S. T. Hess. Nanoscale imaging of molecular positions and anisotropies. *Nature Methods*, 5:1027 – 1030, 2008.

[8] D. Axelrod. Carbocyanine dye orientation in red cell membrane studied by microscopic fluorescence polarization. *Biophys J.*, 26:557–573, 1979.

[9] K. Florine-Casteel. Phospholipid order in gel-and fluid-phase cell-size liposomes measured by digitized video fluorescence polarization microscopy. *Biophys J.*, 57:1199–1215, 1990.

[10] Alla Kress, Patrick Ferrand, Hervé Rigneault, Tomasz Trombik, Hai-Tao He, Didier Marguet, and Sophie Brasselet. Probing orientational behavior of MHC class I protein and lipid probes in cell membranes by fluorescence polarization-resolved imaging. *Biophys J.*, 101(2):468–76, 2011.

[11] Joseph N. Forkey, Margot E. Quinlan, and Yale E. Goldman. Measurement of single macromolecule orientation by total internal reflection fluorescence polarization microscopy. *Biophys J.*, 89(2):1261–1271, 2005.

[12] J. Borejdo and S. Burlacu. Measuring orientation of actin filaments within a cell: orientation of actin in intestinal microvilli. *Biophys J.*, 65:300–309, 1993.

[13] J. Borejdo and S. Burlacu. Orientation of actin filaments during motion in in vitro motility assay. *Biophys J.*, 66:1319–1327, 1994.

[14] J. van Mameren. *Integrating single-molecule visualization and DNA micromanipulation.* PhD thesis, VU University Amsterdam, 2008.

[15] T. Dertinger, R. Colyer, G. Iyer, S. Weiss, and J. Enderlein. Fast, background-free, 3D superresolution optical fluctuation imaging (SOFI). *Proc. Natl. Acad. Sci. U.S.A.*, 106:22287–22292, 2009.

[16] H. Lodish and A. Berk. *Molecular Cell Biology.* W. H. Freeman, 7th edition, 2012.

[17] W. E. Fowler and U. Aebi. A consistent picture of the actin filament related to the orientation of the actin molecule. *The Journal of Cell Biology*, 97(1):264–9, 1983.

[18] J. Wehland and K. Weber. Actin rearrangement in living cells revealed by microinjection of a fluorescent phalloidin derivative. *Eur J Cell Biol.*, 24(2):176–183, 1981.

[19] E. Wulf, A. Deboben, F. A. Bautz, H. Faulstich, and T. Wieland. Fluorescent phallotoxin, a tool for the visualization of cellular actin. *Proc. Natl. Acad. Sci.*, 76(9):4498–4502, 1979.

[20] T. Yanagida, M. Nakase, K. Nishiyama, and F. Oosawa. Direct observation of motion of single F-actin filaments in the presence of myosin. *Nature*, 307:58–60, 1984.

[21] J. A. Cooper. Effects of cytochalasin and phalloidin on actin. *The Journal of Cell Biology*, 105(4):1473–8, 1987.

[22] Toshiro Oda, Keiichi Namba, and Yuichiro Maéda. Position and orientation of phalloidin in F-actin determined by X-ray fiber diffraction analysis. *Biophys J.*, 88(4):2727–36, 2005.

[23] G. M. Cooper. *The Cell: A Molecular Approach.* Sinauer Associates, 2nd edition, 2000.

[24] B. Alberts. *Essential cell biology.* Garland Science, 3rd edition, 2009.

[25] J. D. Watson and F. H. C. Crick. Molecular structure of nucleic acids: a structure for deoxyribose nucleic acid. *Nature*, 171(4356):737–738, 1953.

[26] R. E. Franklin and R. G. Gosling. Molecular configuration in sodium thymonucleate. *Nature*, 171(4356):740–741, 1953.

[27] Roma N. Rambaran and Louise C. Serpell. Amyloid fibrils: abnormal protein assembly. *Prion*, 2(3):112–7, 2008.

[28] M. B. Pepys. Pathogenesis, diagnosis and treatment of systemic amyloidosis. *Philosophical transactions of the Royal Society of London. Series B, Biological sciences*, 356(1406):203–211, 2001.

[29] P. Divry and Florkin M. Sur les proprietes optiques de lámyloid. *Societe de Biologie*, 97:180–181, 1927.

[30] E. D. Eanes and G. G. Glenner. X-ray diffraction studies on amyloid filaments. *J Histochem Cytochem*, 16(11):673–677, 1968.

[31] G. G. Glenner and C. W. Wong. X-ray diffraction studies on amyloid filaments.Alzheimerś disease: initial report of the purification and characterization of a novel cerebrovascular amyloid protein. *Biochem Biophys Res Commun*, 120:885–890, 1984.

[32] J. L. Jiménez, J. I. Guijarro, E. Orlova, J. Zurdo, C. M. Dobson, M. Sunde, and H. R. Saibil. Cryo-electron microscopy structure of an SH3 amyloid fibril and model of the molecular packing. *The EMBO journal*, 18(4):815–21, 1999.

[33] Ritu Khurana, Cristian Ionescu-Zanetti, Maighdlin Pope, Jie Li, Liza Nielson, Marina Ramírez-Alvarado, Lynn Regan, Anthony L. Fink, and Sue A. Carter. A general model for amyloid fibril assembly based on morphological studies using atomic force microscopy. *Biophys J.*, 85(2):1135–44, 2003.

[34] Sean A. Hudson, Heath Ecroyd, Tak W. Kee, and John A. Carver. The thioflavin T fluorescence assay for amyloid fibril detection can be biased by the presence of exogenous compounds. *FEBS Journal*, 276:5960–5972, 2009.

[35] M. Biancalana, K. Makabe, A. Koide, and S. Koide. Molecular mechanism of thioflavin-T binding to the surface of beta-rich peptide self-assemblies. *J Mol Biol.*, 385:1052–63, 2009.

[36] Jeff W. Lichtman and José-Ángel Conchello. Fluorescence microscopy. *Nature Methods*, 2(12):910–919, 2005.

[37] J. R. Lakowicz. *Principles of Fluorescence Spectroscopy.* Kluwer Academic / Plenum Publishers, 1999.

[38] B. Valeur. *Molecular fluorescence: principles and applications.* Wiley-VCH, 2002.

[39] A. Kress. *Probing molecular orientational order of lipid reporters and MHC Class I protein in cell membranes using polarization-resolved fluorescence imaging.* PhD thesis, Aix-Marseille III Université, 2011.

[40] C. Cantor and P. Schimmel. *Biophysical Chemistry.* W. H. Freeman and Company, 1980.

[41] Josef Lazar, Alexey Bondar, Stepan Timr, and Stuart J Firestein. Two-photon polarization microscopy reveals protein structure and function. *Nature Methods*, 8:684–690, 2011.

[42] Alla Kress, Xiao Wang, Hubert Ranchon, Julien Savatier, Hervé Rigneault, Patrick Ferrand, and Sophie Brasselet. Mapping the local organization of cell membranes using excitation-polarization-resolved confocal fluorescence microscopy. *Biophys J.*, 105(1):127–136, 2013.

[43] Manos Mavrakis, Yannick Azou-Gros, Feng-Ching Tsai, José Alvarado, Aurélie Bertin, Francois Iv, Alla Kress, Sophie Brasselet, Gijsje H Koenderink, and Thomas Lecuit. Septins promote F-actin ring formation by crosslinking actin filaments into curved bundles. *Nature Cell Biology*, 16(4), 2014.

[44] Julien Duboisset, Patrick Ferrand, Wang He, Wei, Xiao Wang, Hervé Rigneault, and Sophie Brasselet. Thioflavine-T and Congo red reveal the polymorphism of insulin amyloid fibrils when probed by polarization-resolved fluorescence microscopy. *The Journal of Physical Chemistry B*, 117(3):784–788, 2013.

[45] X. Wang. *Confocal angle resolved linear dichroism microscopy for structural fluorescence imaging.* PhD thesis, École Centrale de Marseille, 2013.

[46] Stephanie a Rosenberg, Margot E. Quinlan, Joseph N. Forkey, and Yale E. Goldman. Rotational motions of macro-molecules by single-molecule fluorescence microscopy. *Acc. Chem. Res.*, 38(7):583–593, 2005.

[47] M. Sunde, L. C. Serpell, M. Bartlam, P. E. Fraser, M. B. Pepys, and C. C. Blake. Common core structure of amyloid fibrils by synchrotron X-ray diffraction. *J. Mol. Biol.*, 273(3):729–739, 1997.

[48] A. Larsson, C. Carlsson, M. Jonsson, and B. Albinssont. Characterization of the Binding of the Fluorescent Dyes YO and YOYO to DNA by Polarized Light Spectroscopy. *J. Am. Chem. Soc.*, 116(19):8459–8465, 1994.

[49] A. Agronskaia, J. M. Schins, B. G. de Grooth, and J. Greve. Polarization effects in flow cytometric DNA sizing. *Applied optics*, 38(4):714–9, 1999.

[50] J. M. Schurr and B. S. Fujimoto. The amplitude of local angular motions of intercalated dyes and bases in DNA. *Biopolymers*, 27(10):1543–69, 1988.

[51] Christina Carlsson, Anette Larsson, Mats Jonsson, Bo Albinsson, and Bengt Nordcn. Optical and Photophysical Properties of the Oxazole Yellow DNA Probes YO and YOYO. *Journal of Physical Chemistry*, 98(40):10313–10321, 1994.

[52] E. Abbe. Beiträge zur Theorie des Mikroskops und der mikroskopischen Wahrnehmung. *Archiv für Mikroskopische Anatomie*, 9(1):413–418, 1873.

[53] L. Rayleigh. On the theory of optical images, with special reference to the microscope. *Philos. Mag.*, 42:167–195, 1896.

[54] S. W. Hell and J. Wichmann. Breaking the diffraction resolution limit by stimulated emission: stimulated-emission-depletion fluorescence microscopy. *Opt. Lett.*, 19(11):780–2, 1994.

[55] Michael Hofmann, Christian Eggeling, Stefan Jakobs, and Stefan W Hell. Breaking the diffraction barrier in fluorescence microscopy at low light intensities by using reversibly photoswitchable proteins. *Proc. Natl. Acad. Sci. U.S.A.*, 102(49):17565–9, 2005.

[56] Rainer Heintzmann, Thomas M. Jovin, and Christoph Cremer. Saturated patterned excitation microscopy–a concept for optical resolution improvement. *Journal of the Optical Society of America. A, Optics, image science, and vision*, 19(8):1599–609, 2002.

[57] Mats G. L. Gustafsson. Nonlinear structured-illumination microscopy: wide-field fluorescence imaging with theoretically unlimited resolution. *Proc. Natl. Acad. Sci. U.S.A.*, 102(37):13081–6, 2005.

[58] S. A. Jones, S. Shim, J. He, and X. Zhuang. Fast, three-dimensional super-resolution imaging of live cells. *Nature Methods*, 8(6):499 – 505, 2011.

[59] S. T. Hess, T. P. Girirajan, and M.D. Mason. Ultra-high resolution imaging by fluorescence photoactivation localization microscopy. *Biophys. J.*, 91:4258–4272, 2006.

[60] Michael J Rust, Mark Bates, and Xiaowei Zhuang. Sub-driffaction-limit imaging by stochastic optical reconstruction microscopy (STORM). *Nature methods*, 3(10):793–795, 2006.

[61] Erwen Mei, Jianyong Tang, Jane M. Vanderkooi, and Robin M. Hochstrasser. Motions of single molecules and proteins in trehalose glass. *J. Am. Chem. Soc.*, 125(9):2730–2735, 2003.

[62] I. Sase, H. Miyata, S. Ishiwata, and K. Kinosita. Axial rotation of sliding actin filaments revealed by single-fluorophore imaging. *Proc Natl Acad Sci USA.*, 94(11):5646–5650, 1997.

[63] Masashi Ohmachi, Yasunori Komori, Atsuko H. Iwane, Fumihiko Fujii, Takashi Jin, and Toshio Yanagida. Fluorescence microscopy for simultaneous observation of 3D orientation and movement and its application to quantum rod-tagged myosin V. *Proc. Natl. Acad. Sci. U.S.A.*, 109(14):5294–8, 2012.

[64] M. Böhmer and J. Enderlein. Orientation imaging of single molecules by wide-field epifluorescence microscopy. *JOSA B*, 20(3):554–559, 2003.

[65] Adam S. Backer, Mikael P. Backlund, Matthew D. Lew, and W. E. Moerner. Single-molecule orientation measurements with a quadrated pupil. *Opt. Lett.*, 38(9):1521–3, 2013.

[66] Joerg Enderlein, Erdal Toprak, and Paul R. Selvin. Polarization effect on position accuracy of fluorophore localization. *Opt. Express*, 14(18):8111–20, 2006.

[67] M. D. Lew, M. P. Backlund, and W. E. Moerner. Rotational mobility of single molecules affects localization accuracy in super-resolution fluorescence microscopy. *Nano letters*, 13:3967– 3972, 2013.

[68] Ilaria Testa, Andreas Schönle, Claas von Middendorff, Claudia Geisler, Rebecca Medda, Christian a Wurm, Andre C Stiel, Stefan Jakobs, Mariano Bossi, Christian Eggeling, Stefan W Hell, and Alexander Egner. Nanoscale separation of molecular species based on their rotational mobility. *Opt. Express*, 16(25):21093–104, 2008.

[69] Mike Heilemann, Sebastian van de Linde, Anindita Mukherjee, and Markus Sauer. Super-resolution imaging with small organic fluorophores. *Angewandte Chemie (International ed. in English)*, 48:6903–8, 2009.

[70] A. Edelstein, N. Amodaj, K. Hoover, R. Vale, and N. Stuurman. Computer Control of Microscopes Using μManager. *Current Protocols in Molecular Biology*, 92:14.20.1–14.20.17, 2010.

[71] C. A. Schneider, W. S. Rasband, and K. W. Eliceiri. NIH Image to ImageJ: 25 years of image analysis. *Nature Methods*, 9:671–675, 2012.

[72] K. I. Mortensen, L. S. Churchman, J. A. Spudich, and H. Flyvbjerg. Optimized localization analysis for single-molecule tracking and super-resolution microscopy. *Nature Methods*, 7(5):377–381, 2010.

[73] A. Sergé, N. Bertaux, H. Rigneault, and D. Marguet. Dynamic multiple-target tracing to probe spatiotemporal cartography of cell membranes. *Nature Methods*, 5:687–694, 2008.

[74] S. Bonneau, M. Dahan, and L.D. Cohen. Single quantum dot tracking based on perceptual grouping using minimal paths in a spatiotemporal volume. *IEEE Trans. Image Process.*, 14:1384–1395, 2005.

[75] R. J. Ober, S. Ram, and E. S. Ward. Localization accuracy in single-molecule microscopy. *Biophys. J.*, 86:1185–1200, 2004.

[76] Samuel T. Hess, Travis J. Gould, Manasa V. Gudheti, Sarah A. Maas, Kevin D. Mills, and Joshua Zimmerberg. Dynamic clustered distribution of hemagglutinin resolved at 40 nm in living cell membranes discriminates between raft theories. *Proc. Natl. Acad. Sci. U.S.A.*, 104:17370–5, 2007.

[77] Bo Huang, Wenqin Wang, Mark Bates, and Xiaowei Zhuang. Three-dimensional super-resolution imaging by stochastic optical reconstruction microscopy. *Science*, 319(5864):810–3, 2008.

[78] M. Mlodzianoski, J. Schreiner, S. Callahan, K. Smolková, A. Dlasková, J. Santorová, P. Ježek, and J. Bewersdorf. Sample drift correction in 3D fluorescence photoactivation localization microscopy. *Opt. Express*, 19:15009–15019, 2011.

[79] M. Guizar-Sicairos, S. Thurman, and Fienup J. Efficient subpixel image registration algorithms. *Opt. Lett*, 33:156–158, 2008.

[80] Mark Bates, Bo Huang, Graham T Dempsey, and Xiaowei Zhuang. Multicolor super-resolution imaging with photo-switchable fluorescent probes. *Science*, 317(5845):1749–53, 2007.

[81] David Baddeley, Mark B Cannell, and Christian Soeller. Visualization of Localization Microscopy Data. *Microsc. Microanal.*, 16(1):64–72, 2010.

[82] S Wolter, M Schüttpelz, M Tscherepanow, S Van De Linde, M Heilemann, and M Sauer. Real-time computation of subdiffraction-resolution fluorescence images. *Journal of microscopy*, 237(1):12–22, 2010.

[83] G. S. Kaminski Schierle, S. van de Linde, M. Erdelyi, E. K. Esbjörner, T. Klein, E. Rees, C. W. Bertoncini, C. M. Dobson, M. Sauer, and C. F. Kaminski. In situ measurements of the formation and morphology of intracellular β-amyloid fibrils by super-resolution fluorescence imaging. *J. Am. Chem. Soc.*, 133(33):12902–12905, 2011.

[84] Sophie Brasselet, Patrick Ferrand, and Alla Kress. Imaging Molecular Order in Cell Membranes by Polarization-Resolved Fluorescence Microscopy. *Springer Series on Fluorescence*, 13:311–337, 2013.

[85] Melike Lakadamyali, Hazen Babcock, Mark Bates, Xiaowei Zhuang, and Jeff Lichtman. 3D multicolor super-resolution imaging offers improved accuracy in neuron tracing. *PloS one*, 7(1):e30826, 2012.

[86] H. Nyquist. Regeneration theory. *Bell Syst. Techn. J.*, 11:126–147, 1932.

[87] C. E. Shannon. Communication in the presence of noise. *Proc. Inst. Radio Eng.*, 37:10–21, 1949.

[88] Hari Shroff, Catherine G Galbraith, James A Galbraith, and Eric Betzig. Live-cell photoactivated localization microscopy of nanoscale adhesion dynamics. *Nature methods*, 5:417–423, 2008.

[89] Robert P. J. Nieuwenhuizen, Keith A. Lidke, Mark Bates, Daniela Leyton Puig, David Grünwald, Sjoerd Stallinga, and Bernd Rieger. Measuring image resolution in optical nanoscopy. *Nature methods*, 10:557–62, 2013.

[90] B. Richards and E. Wolf. Electromagnetic Diffraction in Optical Systems. II. Structure of the Image Field in an Aplanatic System. *Proc. R. Soc. Lond. A.*, 253(1274):358–379, 1959.

[91] Mark P. Warchol and Worth E. Vaughan. Dielectric relaxation by restricted rotational diffusion. *Advances in Molecular Relaxation and Interaction Processes*, 13(1274):317–330, November 1978.

[92] Ke Xu, Hazen P. Babcock, and Xiaowei Zhuang. Dual-objective STORM reveals three-dimensional filament organization in the actin cytoskeleton. *Nature methods*, 9(2):185–188, 2012.

[93] Mikael P. Backlund, Matthew D. Lew, Adam S. Backer, Steffen J. Sahl, and W. E. Moerner. The role of molecular dipole orientation in single-molecule fluorescence microscopy and implications for super-resolution imaging. *Chemphyschem*, 15(4):587–99, 2014.

[94] Johann Engelhardt, Jan Keller, Patrick Hoyer, Matthias Reuss, Thorsten Staudt, and Stefan W. Hell. Molecular orientation affects localization accuracy in superresolution far-field fluorescence microscopy. *Nano letters*, 11(1):209–13, 2011.

[95] J. N. Forkey, M. E. Quinlan, and Y. E. Goldman. Protein structural dynamics by single-molecule fluorescence polarization. *Progress in biophysics and molecular biology*, 74(1-2):1–35, 2000.

[96] G. Baffou, M. P. Kreuzer, F. Kulzer, and R. Quidant. Temperature mapping near plasmonic nanostructures using fluorescence polarization anisotropy. *Opt. Express*, 17(5):3291–8, 2009.

[97] S. Geissbüehler. *Structural and Functional Stochastic Super-Resolution Microscopy*. PhD thesis, École Polytechnique Fédérale de Lausanne, 2013.

[98] Peter Dedecker, Gary C H Mo, Thomas Dertinger, and Jin Zhang. Widely accessible method for superresolution fluorescence imaging of living systems. *Proc. Natl. Acad. Sci. U.S.A.*, 109(27):10909–14, 2012.

[99] S. Geissbüehler, N. L. Bocchio, C. Dellagiacoma, C. Berclaz, M. Leutenegger, and T. Lasser. Mapping molecular statistics with balanced super-resolution optical fluctuation imaging (bSOFI). *Optical Nanoscopy.*, 1:4, 2012.

[100] T. Dertinger, R. Colyer, R. Vogel, J. Enderlein, and S. Weiss. Achieving increased resolution and more pixels with Superresolution Optical Fluctuation Imaging (SOFI). *Opt. Express*, 18:18875–18885, 2010.

[101] S. Geissbüehler, C. Dellagiacoma, and T. Lasser. Comparison between SOFI and STORM. *Biomedical Optics Express*, 2(3):408–20, 2011.

[102] C. Dellagiacoma. *Single Molecule Sensing*. PhD thesis, École Polytechnique Fédérale de Lausanne, 2011.

[103] Jagadish Sankaran, Xianke Shi, Liang Yoong Ho, Ernst H. K. Stelzer, and Thorsten Wohland. ImFCS: a software for imaging FCS data analysis and visualization. *Opt. Express*, 18(25):25468–81, 2010.

[104] Balakrishnan Kannan, Jia Yi Har, Ping Liu, Ichiro Maruyama, Jeak Ling Ding, and Thorsten Wohland. Electron multiplying charge-coupled device camera based fluorescence correlation spectroscopy. *Analytical chemistry*, 78(10):3444–51, 2006.

[105] O. Schwartz and D. Oron. Improved resolution in fluorescence microscopy using quantum correlations. *Physical Review A*, 85(3):033812, 2012.

[106] Thomas Dertinger, Mike Heilemann, Robert Vogel, Markus Sauer, and Shimon Weiss. Superresolution optical fluctuation imaging with organic dyes. *Angewandte Chemie (International ed. in English)*, 49(49):9441–3, 2010.

[107] Sangyeon Cho, Jaeduck Jang, Chaeyeon Song, Heeyoung Lee, Prabhakar Ganesan, Tae-Young Yoon, Mahn Won Kim, Myung Chul Choi, Hyotcherl Ihee, Won Do Heo, and YongKeun Park. Simple super-resolution live-cell imaging based on diffusion-assisted Förster resonance energy transfer. *Scientific reports*, 3:1208, 2013.

[108] V. P. Leonov and A. N. Shiryaev. On a method of calculation of semi-invariants. *Theory Prob. Appl.*, IV(3):319–329, 1959.

[109] Jerry M. Mendel. Tutorial on Higher-Order Statistics (Spectra) in Signal Processing and System Theory : Theoretical Results and Some Applications. *Proc. IEEE*, 79(3):278–305, 1991.

[110] P. Thévenaz, U. E. Ruttimann, and M. Unser. A pyramid approach to subpixel registration based on intensity. *IEEE transactions on image processing : a publication of the IEEE Signal Processing Society*, 7(1):27–41, 1998.

[111] T. Dertinger, A. Pallaoro, G. Braun, S. Ly, T. A. Laurence, and S. Weiss. Advances in superresolution optical fluctuation imaging (SOFI). *Q. Rev. Biophys.*, 46(2):210–221, 2013.